Discovering a novel therapy for disorders that feature defects of the neuromuscular junction structure



Mirela-Daniela Panea

Linacre College

University of Oxford

A thesis submitted for the degree of Doctor of Philosophy

Michaelmas Term 2020

Word count: ~44,000

Impact of Covid-19 summary

The Covid-19-related lockdown resulted in Institute closure for four months, period that coincided with treatment endpoint for some subjects taking part in the study presented in **Chapter 4**. Thus, further analyses were performed later than initially planned in this instance. Immunostaining studies presented in the same chapter were initially planned to include at least 5 mice per treatment group. However, they present only 3 animals per group and that is due to restricted time allowed in the Wolfson imaging facility once reopened.

The high-dose gene therapy trial in an AChR deficiency mouse model presented in **Chapter 5** is incomplete and data is shown as an overview. Also, the neuromuscular junction fine structure studies for the same model mice in the low-dose trial were postponed. This was due to restrictions added in line with the government guidance within the Electron microscope facility, as well as the high-demand and limited availability of the microscope after four months of being unavailable whilst the Institute was closed.

Abstract

Background: Congenital myasthenic syndromes (CMS) are a group of inherited disorders that affect signal transmission at the neuromuscular junction (NMJ) and share the clinical feature of fatigable muscle weakness. Downstream of tyrosine kinase 7 (DOK7) is a cytoplasmic-adaptor protein that amplifies the signalling from the muscle-specific receptor tyrosine kinase (MuSK), which is responsible for the formation and stabilisation of the NMJ. It has recently been shown that overexpression of DOK7 protein in muscles, generates enlarged NMJs in mice, which are very efficient in signal transmission, have no reported detrimental effects and can ultimately lead to a complete recovery for disease model mice.

Aim: To study novel therapies for CMS based on DOK7 overexpression.

Results: By using an adeno-associated virus system (DOK-AAV) we generated enlarged NMJs in wild-type mice to further investigate the morphology and electrophysiology of these synapses. The DOK7-AAV gene therapy was shown to generate enlarged synapses that improved the phenotype of two animal models of CMS. In addition, 5431 small molecules from a library of muscle-specific compounds were used in screening experiments to find potential small molecules that could upregulate DOK7. Confirmatory results were performed on an assay of biological activity and revealed two potential small molecule hits. They will provide the basis for a more detailed analysis of the effects of DOK7 upregulation in cell culture biological assays and ultimately for *in vivo* testing.

Conclusion: These studies demonstrate that DOK7 upregulation would benefit differing CMS subtypes and could potentially improve signal transmission in other NMJ-associated disorders.

Acknowledgements

I would first like to thank my supervisor Professor David Beeson for giving me the opportunity to carry out my DPhil study in his laboratory. I would like to thank both of my supervisors, Professor David Beeson and Dr Judith Cossins, for their guidance and support throughout the duration of my study and writing of this thesis. Their passion for science and contribution with knowledge in regards to the topic of my DPhil, inspired and motivated me over the past four years.

I am also extremely grateful for the enormous help and training offered by Dr Richard Webster during my DPhil study and for the writing of this thesis, and I would like to thank him for his continuous encouragement. His ideas and guidance have been essential to this project but also to my scientific development.

I would like to thank Susan Maxwell for helping me gather the ultrastructural images for the low-dose study in a mouse model of AChR deficiency and for spontaneously helping me throughout the years by performing various experiments whenever I asked for help.

I would like to thank Dr Judith Cossins, Susan Maxwell, Dr Weiwei Liu, Dr Michelangelo Cao and Dr Pedro Rodriguez-Cruz for their help, guidance and training in performing various laboratory techniques.

To all current and previous members of the Beeson group for their patience to my endless questions, interesting scientific discussions and for making my time in Oxford a lot easier. Special thanks to Marie, Nicole and Esra for their friendship in and outside of the laboratory.

I also want to thank David Parr for his help in the management of my grant and for his entertaining discussions.

I am grateful to Dr Graham Wynne and Dr Angela Russell for offering access to their libraries of compounds within the Department of Pharmacology, University of Oxford.

I want to thank Nick Ward from the Biomedical Services (JR Hospital) for his help in caring for the animals.

I am grateful for the opportunity arisen to collaborate with Cristi Soitu on developing a screening technique for my project.

I would like to thank the following departments and facilities: the Weatherall Institute of Molecular Medicine, the Wolfson Imaging Centre, the Nuffield Department of Clinical Neurosciences, the Biomedical Services and the Electron microscopy facilities of the Dunn School at University of Oxford.

My DPhil project was mainly supported by a studentship offered by Myaware, a UK charity dedicated to the care and support of patients with myasthenia. I am also grateful for the travel grants received throughout my studies from the Nuffield Department of Clinical Neurosciences, Brain and Linacre College.

To my cousins Cori, Diana, and Alin for their love and support. Special thanks to Cori for teaching me how to study, be curious and always try to improve myself, without which I would have never pursued such an interesting career path.

Very special thanks to my wonderful friends Rebecca, Diana, Ana and Marco for their advice, support and patience but especially for understanding me exactly when I needed it the most. Their friendship is one of the most precious things I have!

To Tudor: Thank you for your amazing support and love during the last three years and especially for your patience during the last months while I was writing my thesis. You have contributed without doubt to my happiness and motivation that were necessary to complete this journey and I am very grateful for that! Your optimism and constant willingness to learn and improve yourself inspired me ever since I met you and continues to inspire me to become a better person and scientist. I also want to thank Tudor's family for their continuous encouragement and support.

Last but not least, I would like to thank my parents, Severius and Lucretia, from the bottom of my heart for supporting me throughout my studies and for believing in me in ways I could not imagine possible. I am eternally grateful and this is all thanks to you!

Table of contents

Abstract ……5
Acknowledgements ……7
Table of contents ……11
List of figures ……18
List of tables ……24
Abbreviations……26

1. Chapter 1: Introduction

1.1. The basis of neuromuscular transmission ……28
1.1.1. The anatomy, function and molecular architecture of the neuromuscular junction ……29
1.1.1.1. The nerve terminal ……31
1.1.1.2. Basal lamina……32
1.1.1.3. The postsynaptic region ……32
1.1.2. Principles of neurotransmission ……33
1.1.3. The development and maturation of the neuromuscular junction ……37
1.1.4. Signalling pathways at the neuromuscular junction ……40
1.1.4.1. Agrin induced AChR clustering pathway ……42
1.2. Congenital myasthenic syndromes ……50
1.2.1. Introduction ……50
1.2.2. Congenital myasthenic syndromes caused by mutations in the DOK7 gene ….53
1.2.3. AChR deficiency syndromes ……54
1.3. Overview of available treatments for CMS ……56
1.4. Possible novel therapies for CMS ……58
1.4.1. Introduction ……58
1.4.2. The potential of small molecules libraries screening……59
1.4.3. Adeno-associated virus mediated gene therapy ……62
1.5. The discovery of 'enlarged synapses' and their potential to enhance neuromuscular transmission ……66
1.6. Models of CMS used to study response to treatment ……68
1.7. Hypothesis and objectives ……70

2. Chapter 2: Materials and methods

2.1. In vivo methods ……..……..74

2.1.1. Ethical statement ……..74

2.1.2. Transgenic mouse lines used ……..……..74

2.1.2.1. A mouse model of acetylcholine receptor deficiency ($hγ^{+}mε^{-/-}$) ……..74

2.1.2.2. A mouse model for the most common DOK7-CMS patient mutation ($Dok7^{KI/KI}$)……..75

2.1.3. Mouse genotyping and breeding ……..75

2.1.3.1. AChR deficiency mouse model (hγ+mε-/-) ……..75

2.1.3.2. $Dok7^{KI/KI}$ mice ……77

2.1.4. Pilot study to test DOK7-AAV gene therapy in wild-type mice ……..……..78

2.1.5. Generation of enlarged synapses in wild-type mice ……...……..78

2.1.6. AAV gene therapy in AChR-deficient mice ……..79

2.1.7. AAV gene therapy in $DOK7^{KI/KI}$ mice ……...79

2.1.8. Evaluation of muscle strength and weight in mice ……...80

2.1.9. Repetitive nerve stimulation ……81

2.1.10. Ex-vivo diaphragm electrophysiology/ Endplate potential recordings …….…83

2.1.11. Imaging neuromuscular junctions ……...84

2.2. DNA methods ……..87

2.2.1. DNA extraction from bacterial cultures ……..…....87

2.2.2. Polymerase Chain Reaction (PCR) ……..……87

2.2.2.1. Standard PCR ……87

2.2.2.2. PCR amplification of CG-rich DNA templates ……88

2.2.2.3. High-fidelity PCR reactions ……89

2.2.3. Resolution of DNA on agarose gels ……....89

2.2.4. DNA extraction from agarose gels ……...89

2.2.5. General principle of molecular cloning ……...90

2.2.5.1. DNA digestion ……90

2.2.5.2. DNA dephosphorylation ……90

2.2.5.3. DNA ligation ……90

2.2.5.4. Plasmids ……90

2.2.5.5. pGEM®-T Easy cloning ……91

2.2.5.6. Site-directed mutagenesis ……92

2.2.5.7. Bacterial transformation ……93

2.2.6. Specific cloning ……...94

2.2.6.1. Generation of luciferase reporter construct ……94
2.2.6.2. Cloning of DOK7 cDNA into pAAV9-CMV-EGFP plasmid ……96
2.2.6.3. Cloning of EGFP tag into pBabe-DOK7-cDNA plasmid ……99
2.3. RNA methods ……101
2.3.1. RNA extraction from mouse muscle tissue ……101
2.3.2. DNA removal from RNA preparations ……102
2.3.3. Reverse-transcription ……102
2.3.4. Quantitative real-time polymerase chain reaction ……103
2.3.5. RNA sequencing ……105
2.4. Protein analysis methods ……107
2.4.1. Protein extraction from cell cultures ……107
2.4.2. Protein extraction from mouse tissue ……107
2.4.3. DOK7 Immunoprecipitation assay ……108
2.4.4. Sodium dodecyl sulphate-polyacrylamide gel electrophoresis and western blotting ……109
2.5. Cell culture methods ……112
2.5.1. Transfection methods ……114
2.5.1.1. Polyethylenimine (PEI) transfections ……114
2.5.2. Generation of recombinant agrin ……114
2.5.3. Agrin-induced AChR clustering ……115
2.5.4. Generation of C2C12 reporter stable cell line to be used in the screening of compounds ……117
2.5.5. The luciferase reporter assay ……117
2.5.6. The screening of small-molecule compounds ……118
2.5.7. pBabe retroviral system ……120
2.5.7.1. Using a retroviral system to titrate levels of DOK7 needed to mimic the formation of a synapse in vitro ……121
2.5.8. Titration of DOK7-AAV (Adeno-associated viral systems) ……122
2.6. Statistical analysis ……123
2.7. Materials ……124

3. Chapter 3: Characterisation of wild-type mice treated with DOK7-AAV gene therapy

3.1. Introduction ……..…126

3.2. Investigating the effects of an EGFP tag on DOK7's ability to induce AChR clusters using a retroviral system ……128

3.3. Generation of recombinant DOK7-AAV construct ……..131

3.4. Investigating the infectivity rate of DOK7-AAV in C2C12 myotubes ……....133

3.5. Expression of DOK7-AAV in vivo in wild-type mice ……..…135

3.5.1. Ex vivo electrophysiological recordings of hemidiaphragm-nerve preparations ……..136

3.5.2. Fluorescent immunostaining of enlarged synapses ……138

3.5.3. Investigating the transduction efficiency of DOK7-AAV gene therapy in various muscles ……..141

3.5.4. Expression of DOK7-EGFP in other muscles tissue ……....143

3.5.5. Gene expression analysis in DOK7-AAV treated mice ……144

3.5.6. Relative gene expression of Dok7, Musk, Chrna1 and Chrne in DOK7-AAV infected mice ……...144

3.5.7. Differential gene expression in gene therapy treated mice ……..146

3.6. Discussion ……..148

4. Chapter 4: DOK7-AAV gene therapy in a mouse model of DOK7-CMS

4.1. Introduction ……...157

4.1.1. DOK7-CMS mouse model ……..158

4.1.2. Experimental design ……...160

4.2. Changes in time to humane endpoint of gene therapy treated DOK7-CMS mice. ……162

4.3. Evaluation of body weight of gene therapy treated DOK7-CMS mice ……....163

4.4. Muscle fatigability of gene therapy treated model mice ……..165

4.5. Decrement of CMAP on repetitive nerve stimulation ……..166

4.6. Ex-vivo electrophysiological recordings ……...167

4.7. Analysing changes in NMJs morphology ……....169

4.7.1. Changes in the presynaptic and nerve terminal areas ……....171

4.7.2. Staining intensity between presynaptic and nerve terminal areas ……173
4.7.3. The percentage of enlarged NMJs ……...…174
4.8. DOK7 overexpression in other muscles groups ……...176
4.9. Discussion ……177

5. Chapter 5: DOK7-AAV gene therapy as a treatment for AChR deficiency CMS

5.1. Introduction ……...185
5.1.1. The AChR-deficiency model ……..186
5.1.2. Gene therapy experimental design ……....189
5.2. DOK7 gene therapy low-dose treatment ……...191
5.2.1. Evaluation of body weight during treatment trial ……192
5.2.2. Muscle fatigability of model mice during treatment trial ……193
5.2.2.1. Evaluation of muscle fatigability after pyridostigmine treatment ……..197
5.2.3. Decrement of compound muscle action potentials following repetitive nerve stimulation in model mice during treatment trial ……...198
5.2.4. Ex vivo electrophysiological recordings of neuromuscular transmission following gene therapy treatment ……..201
5.2.5. DOK7-AAV transduction efficiency in different muscles of treated model mice ……..205
5.2.6. DOK7 expression levels in other muscles tissues ……...210
5.3. A pilot study for high-dose DOK7-AAV gene therapy in AChR deficient model mice ……211
5.3.1. Evaluation of changes in body weight during high-dose treatment trial ……...213
5.3.2. Evaluation of muscle fatigability of model mice during high-dose treatment trial ……..…214
5.3.3. Decrement of compound muscle action potentials following repetitive nerve stimulation in model mice during high-dose treatment trial ……..215
5.3.4. Ex vivo electrophysiological recordings of neuromuscular transmission following high-dose gene therapy treatment ……217
5.3.5. Evaluation of NMJ structure following high-dose gene therapy treatment ...218
5.3.6. DOK7 protein expression in muscle tissues of model mice following high-dose DOK7-AAV treatment ……....220

5.4. Discussion ……..222

6. Chapter 6: Screening of small molecules that can upregulate the expression of DOK7 protein

6.1. Introduction ……...232

6.1.1. Small molecule library used ……...236

6.1.2. Using a reporter system for compound screening ……....237

6.2. Experimental design of screening assay ……..240

6.3. Generation of DOK7 luciferase reporter cell line ……...242

6.3.1. Stable transfection and single clone selection ……...244

6.4. Screening for enhanced DOK7 promoter activity using a luciferase reporter …..245

6.4.1. Screening of small molecules ……247

6.5. Validation of compound hits using an assay of relevant biology ……249

6.6. Determining dose-response patters of lead compounds ……..251

6.7. Discussion ……..255

1. Chapter 7: Conclusions and further perspectives

……...……..262

Bibliography ……270

Publication ……..……..311

Appendix…….……..312

1.1. List of buffers ……312

1.2. Reagents ……313

1.3. Drugs used in mice ……314

1.4. Antibodies used in immunohistochemistry ……...314

1.5. List of software programmes used ……..……...314

1.6. Fiji macro used for the analysis of NMJ parameters ……...316

List of figures

Figure 1.1. The NMJ structure. **30**
Figure 1.2. The schematic representation of neurotransmission at the NMJ. **36**
Figure 1.3. The structure of the AChR. **39**
Figure 1.4. Schematic representation of the AChR clustering and dispersal pathways. **41**
Figure 1.5. The structure of agrin (secreted form). **42**
Figure 1.6. Schematic representation of Agrin-LRP4-MuSK-DOK7 complex. **44**
Figure 1.7. The structure of DOK7. **46**
Figure 1.8. The structure of rapsyn. **48**
Figure 1.9. Targeted therapies for CMS. **57**
Figure 1.10. Drug discovery timeline. **61**
Figure 1.11. Adeno-associated virus gene therapy mechanism. **65**
Figure 1.12. AChR clustering assay. **69**
Figure 1.13. Hypothesis. **70**
Figure 1.14 Diagram of objectives. **72**

Figure 2.1. DOK7-AAV gene therapy study design. **80**
Figure 2.2. Inverted screen test used to measure muscle fatigability of mice. **81**
Figure 2.3. Electromyography represented on an animal. **82**
Figure 2.4. Schematic diagram of DOK7.1Kb.promoter.luciferase. reporter-pcDNA3.1 (Hygro+). **96**
Figure 2.5. Schematic representation of the workflow in generating the pAAV9-CMV-DOK7.EGFP construct. **98**
Figure 2.6. Molecular cloning workflow for generating pBabe.DOK7.EGFP-PURO.IRES-EGFP. **99**
Figure 2.7. Schematic representation of AChR clustering assay. **115**
Figure 2.8. Macro used for the analysis of the number of AChR clustered on cultures myotubes. **116**
Figure 2.9. Schematic representation of luciferase reporter assay design for the screening of small-molecule compounds. **119**

Figure 3.1. AChR clustering assay to compare between DOK7-EGFP and DOK7 wild-type (WT) transduced C2C12 myotubes. **130**
Figure 3.2. Generation of recombinant DOK7-AAV plasmid. **132**
Figure 3.3. Titration of DOK7-AAV multiplicity of infection in C2C12 mouse muscle cells. **134**
Figure 3.4. Schematic representation of study design for using DOK7-AAV in wild-type mice. **135**
Figure 3.5. Electrophysiological recordings from *ex vivo* hemi-diaphragms of 6-week-old mice treated with DOK7-AAV in comparison to control mice. **137**
Figure 3.6. NMJs properties in the diaphragm muscle of DOK7-AAV treated group in comparison to control. **139**
Figure 3.7. NMJ properties in the EDL and soleus muscles of DOK7-AAV treated group in comparison to control. **140**
Figure 3.8. DOK7 EGFP-AAV transduction efficiency. **141**
Figure 3.9. DOK7-EGFP expression in tongue and tibialis (TA) muscles. **143**
Figure 3.10. Fold increase in gene expression of key components at the NMJ in DOK-AAV treated mice compared to control. **145**
Figure 3.11. Differential gene expression as a result of DOK7 overexpression in muscle tissue of DOK7-AAV treated mice. **147**

Figure 4.1. Generation of DOK7 congenital myasthenia mouse model. **159**
Figure 4.2. Schematic representation of study design for using DOK7 gene therapy in a mouse model of DOK7-CMS. **161**
Figure 4.3. Probability of survival for DOK7-AAV gene therapy treated DOK7-CMS mice. **162**
Figure 4.4. Body weight of gene therapy treated DOK7-CMS mice in comparison to wild-type mice. **163**
Figure 4.5. Body weight of adult gene therapy treated DOK7-CMS mice. **164**
Figure 4.6. Hang period as assessed by inverted screen test. **165**
Figure 4.7. Muscle decrement following repetitive nerve stimulation in gene therapy treated myasthenic mice. **166**
Figure 4.8. Recordings of electrophysiological parameters. **168**
Figure 4.9. Fluorescent staining of NMJs. **170**

Figure 4.10. Nerve and AChRs areas analysed in muscles of gene therapy treated model mice in comparison to control. **172**
Figure 4.11. Intensity of staining of nerve and AChRs areas analysed in muscles of gene therapy treated model mice. **173**
Figure 4.12. Analysis of enlarged postsynaptic areas in gene therapy treated model mice. **175**
Figure 4.13. DOK7 EGFP protein expression in muscles of gene therapy treated model mice. **176**
Figure 4.14. Body weight of adult gene therapy treated model mice divided by gender. **180**

Figure 5.1. Generation of AChR-deficiency mouse model. **188**
Figure 5.2. Schematic representation of study design for using DOK7-AAV gene therapy in AChR-deficient mice. **190**
Figure 5.3. Schematic representation of study design for using low-dose DOK7-AAV gene therapy. **191**
Figure 5.4. Body weight of low-dose model mice during low-dose treatment trial. **192**
Figure 5.5. Muscle fatigability as assessed by inverted screen test model mice during low-dose treatment trial. **194**
Figure 5.6. Correlation between hang period and body weight in model mice during low-dose treatment trial. **195**
Figure 5.7. Hang time normalised to body weight in model mice during low-dose treatment trial. **196**
Figure 5.8. Muscle fatigability as assessed by inverted screen test in model mice during low-dose treatment trial after one-time pyridostigmine treatment. **197**
Figure 5.9. Decrement results of model mice during treatment trial. **199**
Figure 5.10. Amplitudes (A) and frequencies (B) of mEPPs recorded from diaphragm preparations of model mice following gene therapy treatment. **202**
Figure 5.11. Amplitudes of EPPs (A) and Quantal content (B) recorded from diaphragm preparations of model mice following gene therapy treatment. **204**
Figure 5.12. Fluorescent staining of model mice NMJs following DOK7-AAV gene therapy treatment trial. **207**
Figure 5.13. Areas of NMJs stained for AChR clusters in model mice following DOK7-AAV Treatment. **208**
Figure 5.14. DOK7-AAV transduction efficiency in various muscles of low-dose model mice

following gene therapy. **209**
Figure 5.15. DOK7 EGFP expression in TA and heart muscles in model mice following DOK7-AAV treatment. **210**
Figure 5.16. Schematic representation of study design for using high-dose DOK7-AAV gene therapy. **212**
Figure 5.17. Body weight of model mice during high-dose treatment trial. **213**
Figure 5.18. Muscle fatigability as assessed by inverted screen test in model mice during high-dose treatment trial. **214**
Figure 5.19. Decrement results of model mice during high-dose treatment trial. **216**
Figure 5.20. Electrophysiological parameters recorded from diaphragm preparations of model mice following high-dose gene therapy treatment. **217**
Figure 5.21. Areas of NMJs stained for AChR clusters in model mice following high-dose DOK7-AAV treatment. **219**
Figure 5.22. DOK7 EGFP expression in tibialis (TA) and heart muscles in model mice following high-dose DOK7-AAV treatment. **220**
Figure 5.23. DOK7 EGFP expression in tibialis (TA) and heart muscles in model mice following low-dose and high-dose DOK7-AAV treatment. **221**

Figure 6.1 Small molecule screening study objectives and workflow. **235**
Figure 6.2. The structure of the *Dok7/DOK7* promoter. **238**
Figure 6.3. Schematic representation of luciferase reporter assay design. **239**
Figure 6.4. The natural upregulation of DOK7 protein upon myoblasts differentiation. **241**
Figure 6.5. Generation of DOK7 luciferase reporter stable cell line. **243**
Figure 6.6. Single clone selection upon generation of stable luciferase reporter cell line. **244**
Figure 6.7. Understanding the level of DOK7 protein expression needed to induce AChR clusters on the surface of C2C12 myotubes. **246**
Figure 6.8. Screening for small molecule compounds using a stable luciferase-reporter cell line. **248**
Figure 6.9. AChR clustering assay for the compound hits resulted from the luciferase reporter assay screening. **250**
Figure 6.10. Titration of two hit compounds using the AChR clustering assay. **252**
Figure 6.11. Dose-response curve of the two compound hits generated from a series of 2-fold dilutions. **254**

Figure 6.12. Chemical structures and names of compound hits. **259**

Figure 7.1. Chemical structures and names of compound hits. **265**

Figure 7.2 Structural similarities between our compound hits and previously approved drugs that showed side effects. **266**

Figure 7.3 Similarities between the two compound hits. **267**

List of tables

Table 1.1. Classification of congenital myasthenic syndromes. **52**

Table 2.1. Primers used for genotyping $h\gamma^{+}m\varepsilon^{-/-}$ mice. **76**

Table 2.2. PCR parameters used in amplifying target genes for genotyping $h\gamma^{+}m\varepsilon^{-/-}$ mice. **76**

Table 2.3. Thermocycler parameters used for a standard PCR reaction. **88**

Table 2.4 Plasmids used in this thesis. **91**

Table 2.5. Typical reactions for pGEM®-T Easy cloning with A-tailing of the insert. **92**

Table 2.6. Antibiotics used for selection of bacterial cultures. **94**

Table 2.7. Primers used in the production of luciferase reporter construct. **95**

Table 2.8. Primers used in the cloning and sequencing of pAAV9-CMV-DOK7.EGFP construct. **97**

Table 2.9. List of TaqMan® Gene Expression Assays (Applied Biosystems). **104**

Table 2.10. Primary and secondary antibodies used for western blotting. **110**

Table 2.11. Cell lines used in this thesis and their growth conditions. **113**

Table 3.1 Differentially expressed genes in DOK7-AAV treated mice. **153**

Table 5.1. Experimental design for the two AAV studies. **224**

Abbreviations

AAV – Adeno-associated virus

ACh – Acetylcholine

AChE – Acetylcholinesterase

AChR – Acetylcholine Receptor

AGRN – Agrin

ANOVA – Analysis of variance

Cdk5 – Cyclin-dependent kinase 5

cDNA – Coding DNA

CMAP – Compound Muscle Action Potential

CMS – Congenital Myasthenic Syndrome

DNA - Deoxyribonucleic Acid

DOK7 – Downstream of Tyrosine Kinase 7

DMEM – Dulbecco's Modified Eagle's Medium

DMSO – Dimethyl sulfoxide

EDL – Extensor Digitorum Longus Muscle

EMG – Electromyography

EGFP – Enhanced green fluorescent protein

EPP – Endplate Potential

FCS – Foetal calf serum

HEK 293T – Human embryonic kidney cells

HRP – Horseradish peroxidase

HS – Horse serum

IP – intraperitoneal

IRES – Internal ribosome entry site

LB – Lysogeny broth

LRP4 – Low-density Lipoprotein receptor-related protein 4

mEPP – Miniature Endplate Potential

MUSK – Muscle-Specific Tyrosine Kinase

NMJ – Neuromuscular Junction

ns – Not significant

P – Postnatal day

PH – Pleckstrin homology domain

PTB – Phosphotyrosin binding domain

PBS – Phosphate Buffered Saline

PBS-T – Phosphate Buffered Saline (PBS) containing 0.05/0.1% Tween

PCR – Polymerase Chain Reaction

PI3K – Phosphoinositide 3-kinase

PKA – Protein Kinase A

RNA – Ribonucleic acid

RT – Room Temperature

SDS-PAGE – Sodium dodecyl sulphate polyacrylamide gel electrophoresis

SEM – Standard Error of the Mean

TA – Tibialis anterior

WT – Wild-type

95% CI – 95% Confidence Intervals

Chapter 1

Introduction

This introduction gives an overview of the neurotransmission at the neuromuscular junction. It also summarises the function and structure of the neuromuscular junction in health and disease, as well as current treatment options and the current need for new therapies. There is a recent interest in using gene therapy techniques as potential novel treatments for neuromuscular diseases. However, their efficacy depends on the molecular mechanism behind each disease as well as the gene therapy method and delivery technique, and therefore needs extensive investigations. One such therapy will be the focus of this thesis. We highlight previous similar work both experimental and clinical, present the possibilities for new therapies in the field and formulate a hypothesis with research questions addressed at the end based on these data.

1.1. The basis of neuromuscular transmission

An essential aspect of life is the ability to purposely move within an environment. In higher organisms, this is dependent on the correct functioning of various communication pathways which ultimately allow the signals sent from the brain to reach target muscle cells via the neuromuscular junction (NMJ). The NMJ is a complex synapse between the motor nerve terminal and a skeletal muscle. The following paragraphs will cover the structure, function and development of the mammalian NMJ in skeletal muscles.

1.1.1. The anatomy, function and molecular architecture of the neuromuscular junction

A fundamental unit of the neural circuitry within the nervous system is the synapse. Synapses enable communication between neurons as well as between neurons and their respective target cells (Eisenberg 1983). In the peripheral nervous system, a vital role is played by the NMJ, a chemical synapse formed between the nerve endings of a motor neuron and the motor endplate which is located on the membrane of a skeletal muscle. Impulses from the brain are transmitted to the muscles at the NMJ in a process called neurotransmission with the ultimate aim of muscle contraction (Engel 2013). This makes neurotransmission a crucial process for survival.

Upon reaching its target muscle, the myelinated motor neuron loses its myelin sheath abruptly at the last node of Ranvier and ultimately branches into 100-200 nerve endings which are called terminal boutons or nerve terminals (Jimsheleishvili and Sherman 2019). Each of these boutons is located at a motor endplate and is usually surrounded by terminal Schwann cells (tSC) that envelop them. The skeletal muscle NMJ comprises a presynaptic area represented by the nerve terminal, the synaptic cleft, and a postsynaptic region on the muscle membrane (**Figure 1.1** and **Figure 1.2**). In mammals, nearly all muscle fibres that propagate an action potential are centrally innervated by one NMJ. Examples of muscle fibres that are innervated by two or more NMJs are intrafusal fibres and a small proportion of extrafusal fibres that are linked to facial, laryngeal and lingual muscles (Engel 2013).

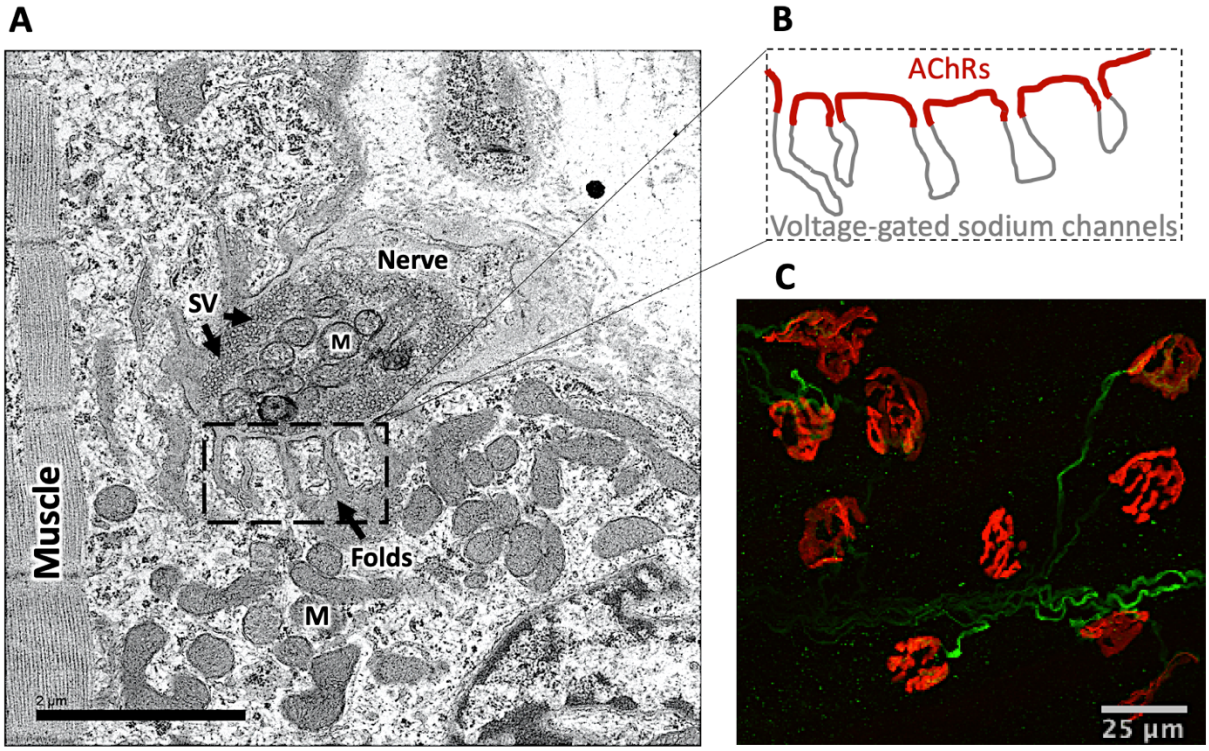

Figure 1.1. The NMJ structure. Electron micrograph of a wild-type mouse endplate region (**A**). The motor nerve terminal (Nerve) contains synaptic vesicles (SV) and mitochondria (M). The postsynaptic area of the muscle fibre contains numerous invaginations (folds) as well as mitochondria (M). The folds present on the postsynaptic membrane contain acetylcholine receptors (AChR) (red) at the top of their crests and a high concentration of voltage-gated sodium channels within their depths (grey) (**B**). Merged image showing fluorescent immunostaining of a mouse NMJ is represented in panel **C**. Neurofilament and synaptophysin antibodies were used to stain the nerve and the nerve terminal areas (green). α-bungaratoxin attached to a fluorescent fluorophore was used to label postsynaptic AChRs (red).

1.1.1.1. The nerve terminal

The nerve terminal contains numerous components such as neurofilaments, microtubules, the smooth endoplasmic reticulum and mitochondria (Engel 2013). It also contains various types of synaptic vesicles such as coated, giant, dense-core or small (50-70 vesicles/μm^2 of nerve terminal), with the small synaptic vesicles being the predominant species and therefore referred to as synaptic vesicles (SV) (**Figure 1.1** and **Figure 1.2**) (Engel 2013). Each SV stores approximatively the neurotransmitter acetylcholine (ACh), with the total amount of ACh in each vesicle being referred to as a "quantum". ACh is synthesized in the nerve terminal from choline and acetyl-CoA in a reaction that is catalysed by choline acetyltransferase (ChAT). Uptake of ACh into the SVs takes place through the vesicular ACh transporter (VAChT) and is mediated by a vacuolar proton-pump ATPase (McMahon and Nicholls 1991).

Active zones are regions on the nerve terminal membranes that define the site for docking and fusion of SVs and contain rows of voltage-gated calcium channels (Dreyer et al. 1973). There are between 600-800 evenly spaced active zones at an adult mammalian NMJ (Chen et al. 2012). The membrane of a nerve terminal contains syntaxin and synaptosomal-associated protein 25 (SNAP-25), that together with synaptobrevin, a protein found on the membrane of SVs, form a protein complex called soluble N-ethymaleimide-sensitive factor attachment protein receptor (SNARE). The SNARE complex is part of the active zone matrix network of proteins and plays a crucial role in docking and fusion of SVs to active zones, ultimately resulting in exocytosis of ACh in the synaptic cleft (Engel 2013).

1.1.1.2. Basal lamina

The synaptic, or junctional cleft represents the space between the nerve terminal and the muscle membrane into which ACh neurotransmitters are released prior to their interaction with nicotinic acetylcholine receptors (AChR) on the postsynaptic membrane (Sanes 1995; Engel 2013). It contains a structured form of extracellular matrix called basal lamina with synapse-specific components such as: certain laminins, muscle-derived collagen XIII, or nerve and muscle derived agrin and neuregulin. It is approximatively 50-70 nm wide with a length reflecting the juxtaposition of the pre- and postsynaptic membranes. Acetylcholinesterase enzyme (AChE) is localised in the synaptic cleft and catalyses the breakdown of ACh into choline and acetyl-CoA (Tuček 1983; Salpeter and Eldefrawi 1973). ColQ is a collagen-tail subunit of AChE made by association of three identical collagen-like strands that anchors and accumulates AChE at the basal lamina (**Figure 1.2**) (Massoulié et al. 1993). The tail subunit is anchored by MuSK and perlecan which binds to α-dystroglycan (Jacobson et al. 2001; Arikawa-Hirasawa et al. 2002; Cartaud et al. 2004). The high density of AChE at the synapse of 2000-3000/μm^2 is ensured by the correlation of these binding partners (Rotundo et al. 2005).

1.1.1.3. The postsynaptic region

The postsynaptic region presents multiple invaginations (or junctional folds) which increase the muscle membrane surface area eight- to ten- fold, and contain a high concentration of voltage-gated sodium channels within their depth (**Figure 1.1** and **Figure 1.2**) (Flucher and Daniels 1989; Engel 2013). The junctional folds also increase the surface area harbouring ACh receptors (AChRs), which are located at the crests of these folds, juxtaposed to the active zones of the nerve terminal (Fishman 1994; Engel 2013). This precise positioning is essential for an efficient neurotransmission.

The muscle nicotinic AChR is a ligand-activated pentamer which consists of a central channel surrounded by five subunits: α -, β-, δ- and γ- (foetal isoform) or ε-subunit (adult isoform) in a stoichiometry of 2:1:1:1 (**Figure 1.3**) (Simon et al. 1992). The synthesis and degradation of AChR takes place in the junctional sarcoplasm along with the end-plate specific species of AChE (Engel 2013). The process of assembly of the pentameric receptor extends over a period of 2 to 3 hours and only 20 to 30% of the synthesized subunits are finally assembled (Green 1999; Engel 2013). The half-life of AChRs at one mature NMJ is around 8 to 14 days and their removal occurs on a random basis at any given NMJ (Akaaboune et al. 1999; Strack et al. 2011; Rudolf et al. 2013). AChRs are internalised through endocytosis and either recycled into the membrane or transferred to lysosomes where they are degraded (Bruneau et al. 2005; Rudolf et al. 2013).

1.1.2. Principles of neuromuscular transmission

At the NMJ, an electrical signal from the nerve terminal is firstly transformed into a chemical signal, returned to an electrical signal and then transmitted along the muscle fibre to elicit muscle contraction. Effective neurotransmission depends on multiple precise processes that include the positioning of the active zones, the localisation and density of the AChRs at approximately 10,000/μm^2, the uniform distribution of AChE within the synaptic cleft but also the ability of ACh to travel within the cleft and find receptors to saturate (Engel 2013). The interaction between the ACh and the AChR happens in less than a few milliseconds, and once it dissociates, ACh diffuses into the synaptic clefts where it is hydrolysed by AChE (Albuquerque et al. 2009) (**Figure 1.2**).

Within the nerve terminal, ACh which is transported into the SVs is released from the nerve terminal at the active zones from an immediate primary release pool of ACh-containing SVs (Richards et al. 2003). A secondary release pool, also called a mobilization pool, is readily available within the nerve terminal. Each vesicle is surrounded by arrays of voltage-gated calcium channels and contains an ACh quantum of 5000-10000 molecules (**Figure 1.1** and **Figure 1.2**) (Adams et al. 2004). Distal propagation of an action potential from the motor nerve depolarises the nerve terminal and results in the opening of the voltage-gated calcium channels, which allow for an immediate calcium influx in the nerve terminal. This then activates the SNARE complex of proteins which results in the fusion between SVs and active zones on the presynaptic membrane (Söllner and Rothman 1994; Hughes et al. 2006). Between 50 to 80 active zones become 'release sites' during nerve stimulation which means that they contribute to vesicle release (Wang et al. 2004). These represent a small proportion (~5%) of the total number of active zones at a given NMJ (Badawi and Nishimune 2018). With every motor nerve discharge, around 50-200 SVs or quanta are released (Christensen and Martin 1970; Wood and Slater 2001). The total number of SVs released at one NMJ after a nerve impulse is referred to as the "quantal content". Individual vesicles often escape from the nerve terminal in the absence of a nerve impulse. The content of a single vesicle gives rise to a small postsynaptic depolarisation which is called the miniature endplate potential (mEPP) and which has an amplitude of approximatively 1 mV (del Castillo and Katz 1954). Released ACh diffuses quickly across the synaptic space.

The agrin-induced clustering pathway (discussed below) promotes dense clustering of the AChRs at the top of the junctional folds. AChRs are ligand-gated ion channels with binding sites located at the interfaces between the α- and γ/ε-subunits and the α- and δ-subunits (**Figure**

1.3) (Albuquerque et al. 2009). Upon binding of two ACh molecules, the channel opens allowing an influx of cations through the muscle membrane (Linder and Quastel 1978). This generates a local endplate potential (EPP), which leads to a depolarisation of the post-synaptic muscle membrane from around -100mV to -60mV. Once this threshold value of -60mV is reached, voltage-gated sodium channels within the depth of the junctional folds open to allow a rapid influx of sodium ions. The resulting depolarisation causes the membrane potential to become positive generating an action potential which spreads throughout the muscle fibre and causes muscle contraction. The threshold level is affected by a combination of factors including quantal content, AChR density, the structure of the postsynaptic folds and the distribution of voltage-gated sodium channels within the depth of the postsynaptic folds (Wood and Slater 1997). At a healthy NMJ, the amount of neurotransmitter released from one nerve impulse exceeds the required amount needed to depolarise the membrane above the threshold for firing of muscle action potentials (Wood and Slater 2001). This excess ability of the system to depolarise the postsynaptic membrane is referred to as 'the safety factor'. The safety factor ensures that each action potential ultimately elicits muscle contraction. Defective transmission will occur if depolarisations falls below the level required to activate the voltage-gated sodium channels.

Acetylcholinesterase terminates signal transmission by rapid elimination of released ACh, preventing it from rebinding to its receptor. After breakdown of ACh, choline is taken back in the nerve terminal making it available for re-synthesis of acetylcholine (**Figure 1.2**) (Taylor and Brown 1999; Engel 2013)

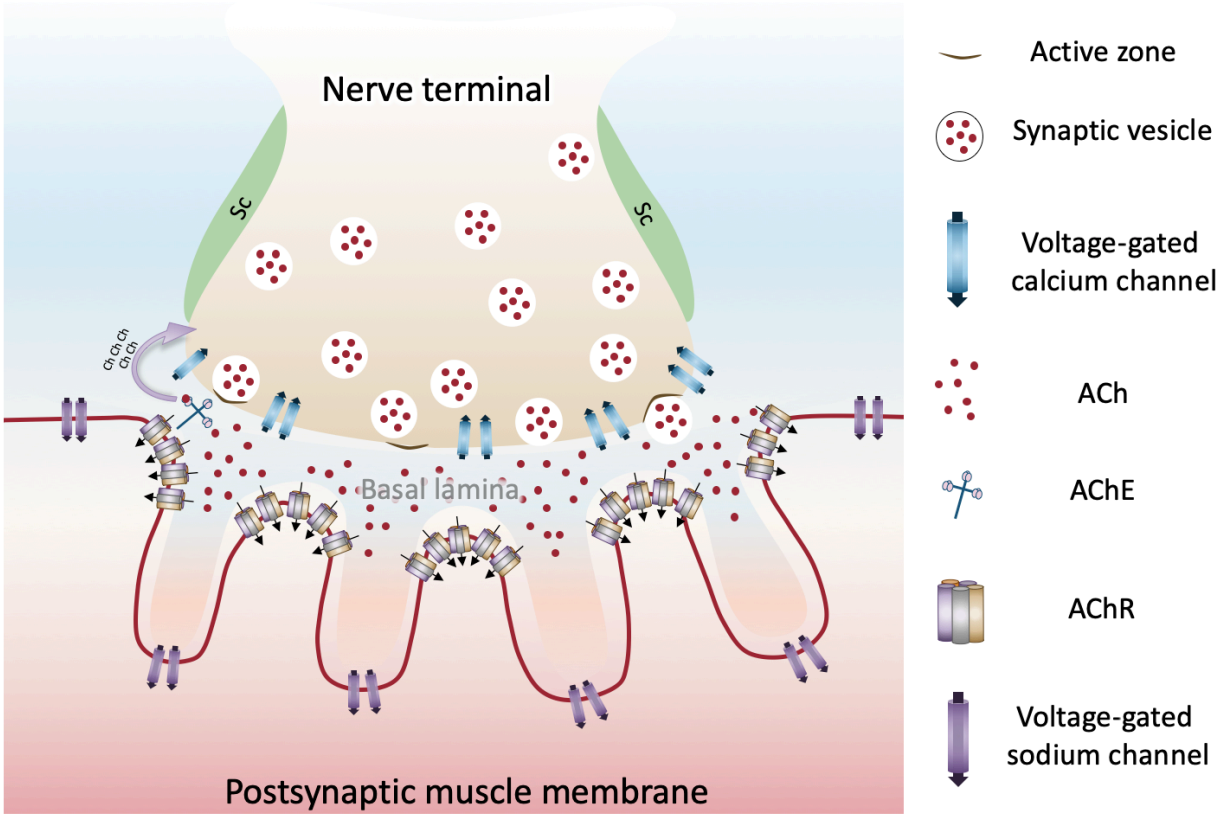

Figure 1.2. The schematic representation of neurotransmission at the NMJ. The arrival of an action potential at the nerve terminal triggers the opening of voltage-gated calcium channels which allows an influx of Ca^{+} ions into the nerve terminal and the subsequent release of acetylcholine (ACh) from the synaptic vesicles at the active zones. The ACh binds to the ACh receptors (AChRs) that cluster at the top of the crests of the postsynaptic folds. The cationic channel pore on the receptors open leading to a localized depolarization of the muscle membrane and the subsequent opening of the voltage-gated sodium channels within the depths of the folds, if the required threshold is reached. This allows for an influx of Na^{+} ions to generate an action potential that further propagates along the muscle fibre, ultimately inducing muscle contraction. Signal transmission is ceased when acetylcholinesterase (AChE), present within the basal lamina, hydrolyses ACh into choline and acetate (Sc– Schwan cell; Ch– choline).

1.1.3. The development and maturation of the neuromuscular junction

The development and maturation of the NMJ is a multistep process that requires coordinated interactions between motor nerve terminals and muscle fibres, with the aim of generating highly specialised presynaptic and postsynaptic membranes (Wu et al. 2010). Even though innervation is not needed for the development of muscle fibres, synapse formation requires reciprocal signals from both the nerve and the muscle. The development process begins during embryogenesis and is close to completion by birth in humans and during the first two weeks of life in rodents (Korneliussen and Jansen 1976; Hesselmans et al. 1993; Lanuza et al. 2002).

Following the formation of muscle fibres, AChRs concentrate in clusters in the middle of the myofibers via a nerve-independent specialisation process called "pre-patterning" (Yang et al. 2001; Wu et al. 2010). The involvement of the post-synaptic components of the agrin clustering pathway is critical in controlling synaptic specialisation. The Low-density lipoprotein Receptor-related Protein 4 (LRP4), Muscle-Specific tyrosine Kinase (MuSK), Downstream of tyrosine Kinase 7 (DOK7) and rapsyn proteins are expressed in the centre of the muscle fiber and are essential in creating a molecular scaffold for AChR pre-patterning (Gautam et al. 1995; Weatherbee et al. 2006; Kim and Burden 2008; Inoue et al. 2009). Their expression is dependent on calcium signalling within the skeletal muscles (Kaplan et al. 2018). Moreover, MuSK is known to be essential for both pre-patterning as well as precise axonal innervation (Zhang et al. 2004). Branched motor nerves, arriving subsequently at the centre of muscle fibres, release agrin which initiates the formation of a synapse through the agrin-induced AChR clustering pathway (McMahan and Wallace 1989; McMahan 1990; A. J. Denzer et al. 1997). This results in the formation and stabilisation of precisely located AChR clusters under the nerve terminal.

The motor neurons reach the muscle fibres through axonal branching and initially one fiber could be innervated by more than one nerve terminals. Through the process of 'synapse elimination', each muscle fibre ultimately remains innervated by only one motor terminal (Korneliussen and Jansen 1976; Hesselmans et al. 1993). Following innervation, AChRs make the transition from the foetal form (α2βδγ) to the adult form (α2βδε) (**Figure 1.3**) (Mishina et al. 1986; Missias et al. 1996; Yumoto et al. 2005). The two receptors differ not only in terms of structure but also in half-life duration (one day for the foetal and 8-14 days for the adult), receptor opening times (the foetal receptor is characterized by longer opening times) and the sodium channel type (Nav1.5 for foetal and Nav1.4 for adult) (Salpeter and Harris 1983; Brenner and Rudin 1989; Herlitze et al. 1996; Awad et al. 2001).

The final step in NMJ development and maturation, is the formation of junctional folds on the postsynaptic membrane. They are located to register with the active zones of the presynaptic membrane and thus, AChRs are clustered at the top of their crests. Overall, the staining of AChR clusters with either α-bungarotoxin or fasiculin gives a characteristic pretzel-like pattern of the NMJ in mice (**Figure 1.1.C**) (Marques et al. 2000; Wu et al. 2010). Both the complexity and dimensions of the junctional folds are species-specific and depend on the type of muscle fibre and innervation.

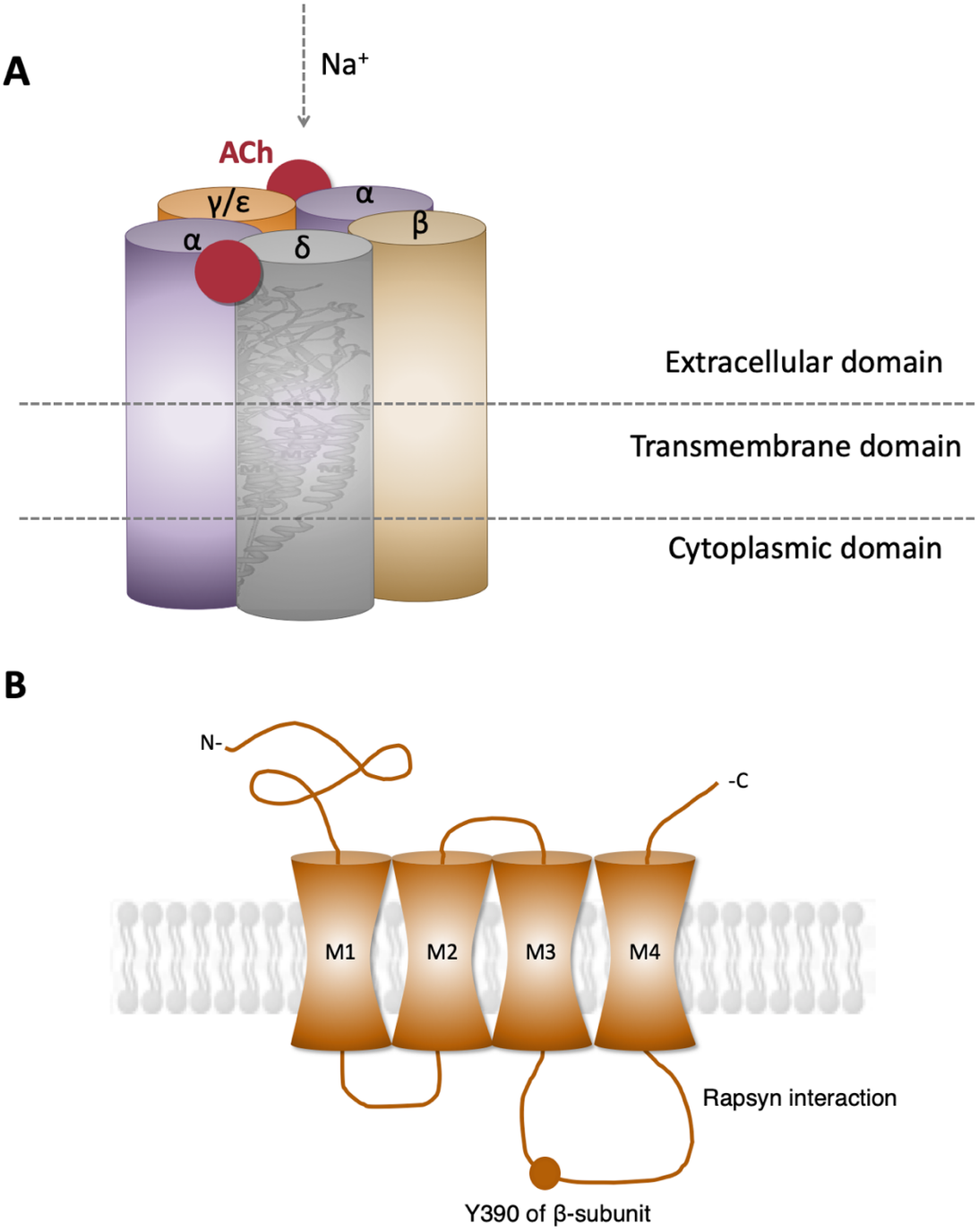

Figure 1.3. The structure of the AChR. (**A**) Foetal (γ) and adult (ε) AChR isoforms are illustrated. ACh binding sites at the extracellular domains are shown by the attachment of ACh (red). Opening of the channel allows influx of Na+ that ultimately results in depolarization of the postsynaptic membrane. (**B**) Each of the five subunits have an extracellular domain (mainly β-strands and an α-helix), four transmembrane domains (M1-M4), and a large intracellular M3/M4 linker (cytoplasmic domain) essential for interaction with rapsyn. The phosphorylation of the tyrosine residue (Y390) on the major intracellular loop of the AChRs β-subunit triggers the recruitment of rapsyn.

**adapted from the protein data bank (PDB ID: 2BG9) and Lee et al. 2009.*

1.1.4. Signalling pathways at the neuromuscular junction

The differentiation of both pre- and postsynaptic structures requires the involvement and correct interactions of many proteins (Burden et al. 2018). An important characteristic of the NMJ is the high density of AChRs on the postsynaptic membrane of approximatively 5000 to 10000 receptors per μm^2 as compared to 100 times lower at extra-synaptic sites (Salpeter and Eldefrawi 1973). The AChR concentration at a given adult NMJ is thought to be regulated by two pathways that counteract each other: a clustering pathway that works through agrin, and a dispersing pathway regulated by ACh (**Figure 1.4**) (Misgeld et al. 2005; Kummer et al. 2006). Besides inducing muscle contraction, ACh release also causes the dispersal of AChRs at extra-synaptic sites (Lin et al. 2005; Misgeld et al. 2005). The process is coordinated by the intracellular calcium elevation within the muscle that activates the calcium-dependent protease calpain and cleavage of p35 to p25 (Chen et al. 2007). p25 activates the cyclin-dependent kinase 5 (Cdk5) that induces actin cytoskeleton remodelling and ultimately AChR dispersal (Lin et al. 2005; F. Chen et al. 2007; Xu et al. 2011). The AChR clustering pathway induced by agrin promotes the stability of the postsynaptic apparatus and counteracts the destabilising influence of acetylcholine at the NMJ (Misgeld et al. 2005). The AChR dispersal pathway is thought to be important in preventing the formation of a postsynaptic apparatus that fails to make a connection (Lin et al. 2005). Moreover, a homeostatic balance between the clustering and dispersal processes is crucial for synaptic maintenance, and disruption of this balance can lead to impaired neurotransmission and disease (Kummeret al. 2006).

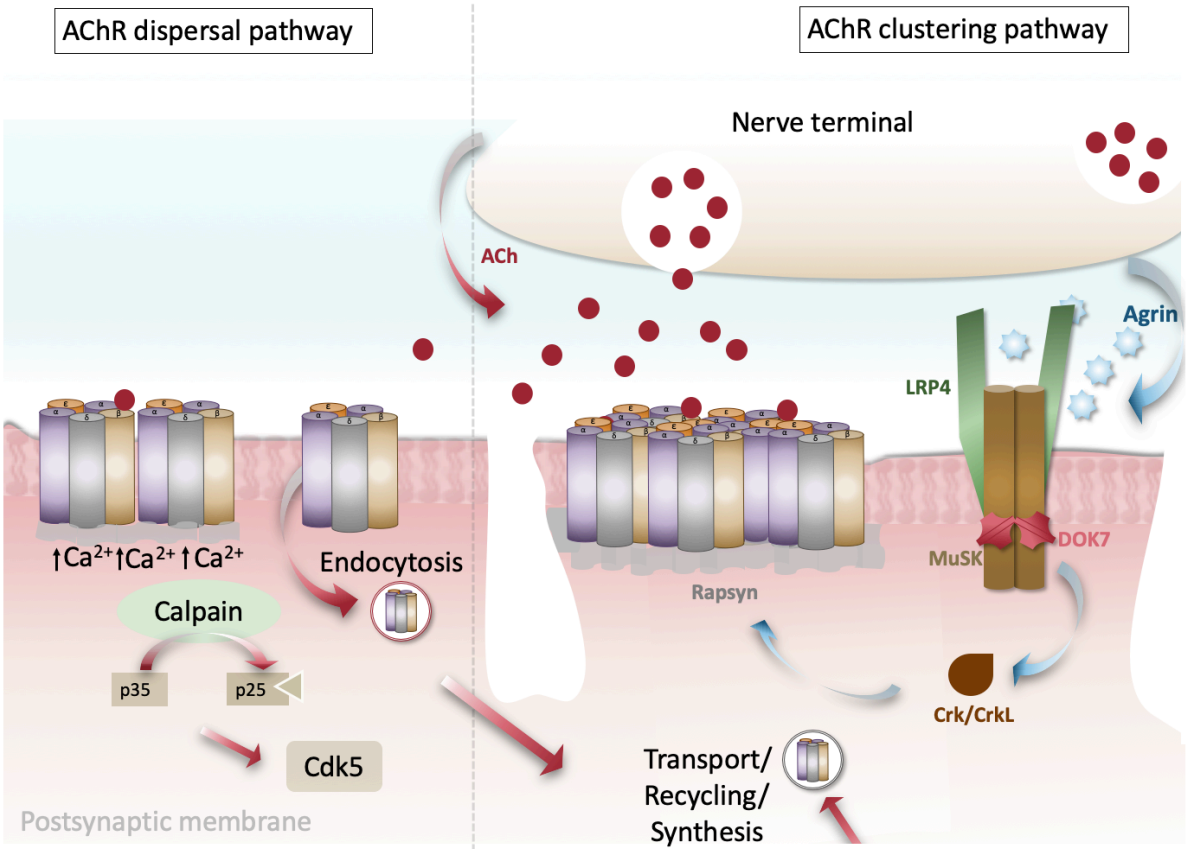

Figure 1.4. Schematic representation of the AChR clustering and dispersal pathways. Agrin binds to LRP4 upon release from the nerve terminal, resulting in MuSK activation. Further recruitment of DOK7 and Crk/CrkL stimulate MuSK activation. Subsequently, the signal is propagated downstream, ultimately resulting in the clustering of AChRs at the postsynaptic membrane with the aid of rapsyn protein. The AChR dispersal is a counteracting pathway that eliminates AChR clusters that are not stabilised by agrin and are located at extra-synaptic sites. A cyclin-dependent kinase (CdK5) mechanism is thought to drive this pathway through the interaction of rapsyn and the calcium-dependent protease calpain. While synapses specific transcription is important for achieving a high concentration of AChR clusters at the postsynaptic membrane, it is thought that spontaneous AChR clusters, endocytosed as a result of the AChR dispersal pathway, are also transported and delivered to the postsynaptic sites for insertion.

**adapted from Rodríguez Cruz et al. 2020.*

1.1.4.1. Agrin induced AChR clustering pathway

AChR clustering begins with the release of agrin from the nerve terminal. Agrin is a widely expressed multidomain extracellular matrix proteoglycan (**Figure 1.5**). Neural agrin is synthesized in the motoneurons, transported along the axons and released in the synaptic cleft (Ruegg and Bixby 1998). It is crucial for inducing the AChR clustering pathway at the NMJ and is generated by alternative splicing (Bezakova et al. 2001). Whereas agrin is not required during AChR pre-patterning, its presence at the NMJ is important in maintaining the post-synaptic structure and preventing activity-induced AChR dispersal (Misgeld et al. 2005).

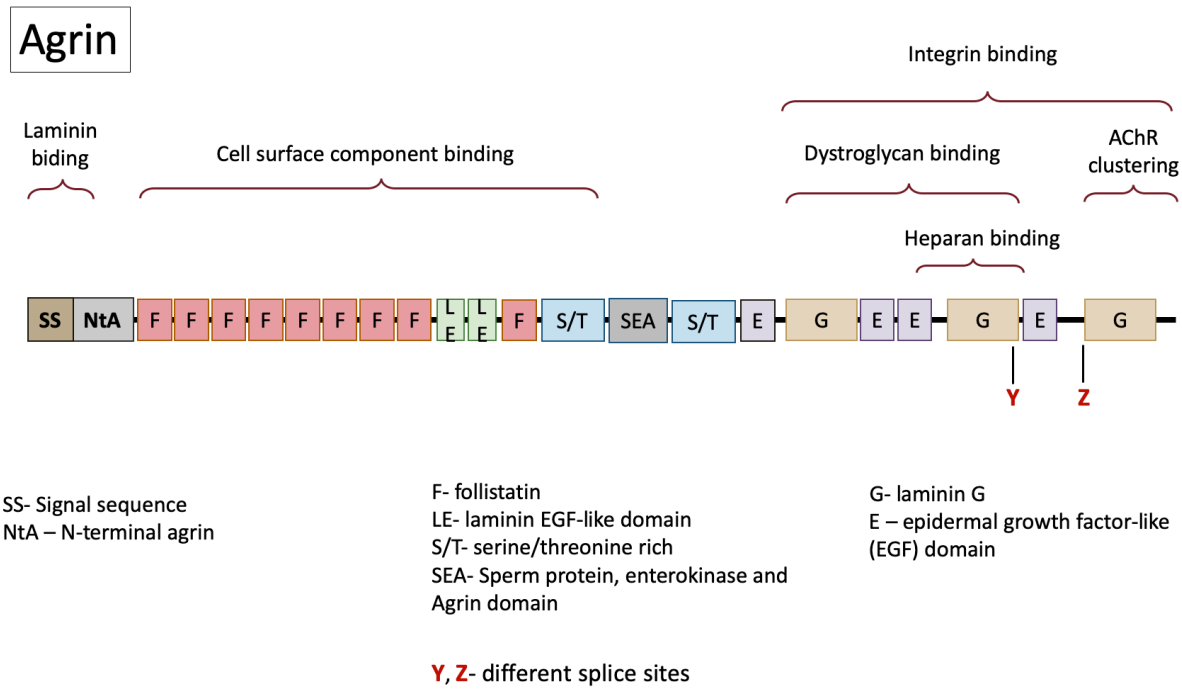

Figure 1.5. The structure of agrin (secreted form). Agrin protein contains follistatin-like cysteine-rich repeats (F), regions that are homologous to epidermal growth factor EGF (E), laminin epidermal growth factor-like (LE) and G (G) domains and two serine/threonine rich regions. There are two alternative RNA splice sites (Y,Z). Insertion of a sequence of amino acids into site Z results in the formation of neural agrin and is required for MuSK activation. **adapted from Rodríguez Cruz et al. 2020.*

Agrin binds to laminin of the basal lamina via its N-terminal region (Denzer et al. 1997). The C-terminal region of agrin is essential for the downstream signalling at the NMJ that ultimately results in aggregation of the AChRs clusters under the nerve terminal (**Figure 1.4**) (Ferns et al. 1993; Gesemann et al. 1995; Engel 2013). Upon being released from the nerve, agrin binds to the transmembrane Low-density lipoprotein Receptor (LDLR)-related Protein 4 (LRP4), forming a ternary complex with the Muscle-Specific tyrosine Kinase (MuSK) (**Figure 1.6**) (McMahan 1990; Weatherbee et al. 2006; B. Zhang et al. 2008; Kim et al. 2008). Binding of agrin to LRP4 triggers tyrosine phosphorylation of the MuSK at its juxtamembrane region (Glass et al. 1996; Kim et al. 2008; B. Zhang et al. 2008). MuSK is a receptor tyrosine kinase initially thought to be expressed only within skeletal muscles and thus to control expression of key proteins specifically at the NMJ (Valenzuela et al. 1995). However, its expression and role in the brain was shown subsequently (Garcia-Osta et al. 2006). Nevertheless, the orchestrated interactions between agrin, LRP4 and MuSK as well as the involvement of DOK7 and its downstream regulators (discussed below), make the clustering process specific for skeletal muscles.

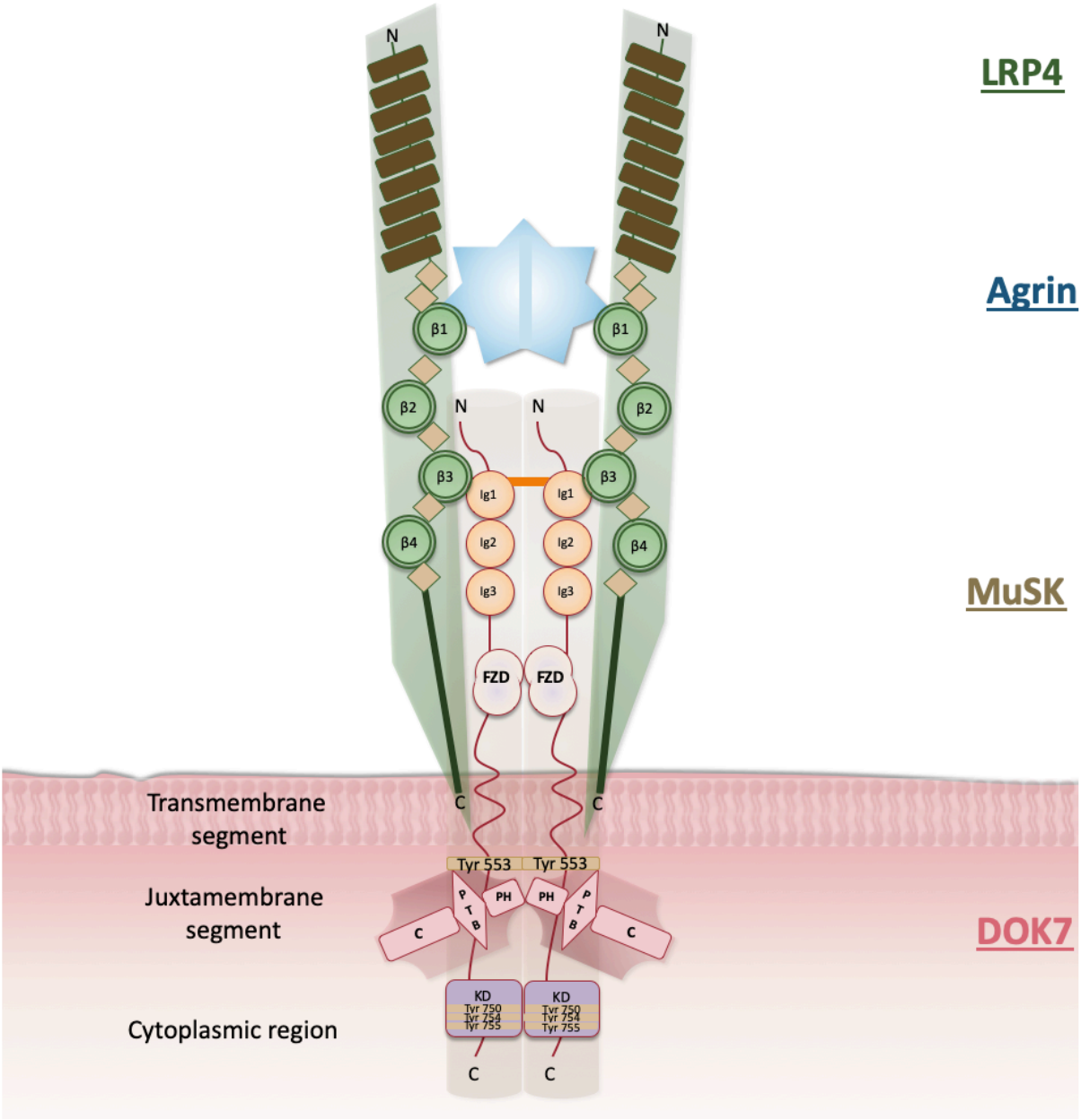

Figure 1.6. Schematic representation of Agrin-LRP4-MuSK-DOK7 complex. Once agrin binds the N-terminal region of LRP4, this undergoes conformational changes that promote the binding to the first IgG-like domain of MuSK. MuSK becomes activated via dimerization and trans-autophosphorylation of tyrosine residues within its cytoplasmic region. MuSK activation results in the recruitment of DOK7 at the active binding sites that ultimately induces full kinase activation and amplification of the downstream signal. LRP4 is composed of 8 low density lipoprotein Class A (LDLa) domains (brown) at the N terminus, 4 ß-propeller domains (green) linked by epidermal growth factor-like modules (yellow) and a C-terminal domain. MuSK contains three IgG-like domains, a frizzled domain (FZD), a transmembrane and a juxtamembrane region, a kinase domain (KD), and a short C-terminal tail. DOK7 contains a pleckstrin homology (PH) domain, phosphotyrosine-binding domain (PTB) and a C-terminus (C). **adapted from Rodríguez Cruz et al. 2020.*

After phosphorylation, MuSK recruits downstream of tyrosine kinase-7 (DOK7), a cytoplasmic adapter protein. DOK7 is a muscle-specific member of DOK-family of proteins, which are adaptor molecules that act as downstream regulators of receptor tyrosine kinases (MuSK in here). DOK7 contains an N-terminal pleckstrin homology (PH) domain important for membrane association, a phosphotyrosine binding (PTB) domain that is required to bind tyrosine phosphorylated MuSK, and a C-terminal domain (**Figure 1.6 a**nd **Figure 1.7**) (Bergamin et al. 2010). While the PH-PTB domains are needed for MuSK phosphorylation, the C-terminal plays only a partial role in the process (Hamuro et al. 2008; Ueta et al. 2017). The expression of DOK7 is restricted to the skeletal muscles and heart, even though a clear role has not been identified in the heart yet.

Once recruited, DOK7 binds to the tyrosine phosphorylated juxtamembrane region of MuSK and juxtaposes two MuSK kinase domains for trans-autophosphorylation through the dimerization of its PH and PTB domains (Bergamin et al. 2010). Agrin stimulates phosphorylation of DOK7 at the two tyrosine residues within its C-terminal domain. This also leads to the recruitment of the two adaptor proteins: Crk and Crk-like protein (CrkL) which further enhance MuSK phosphorylation (**Figure 1.4**) (Hallock et al. 2010). The precise mechanism through which the two adaptor proteins enhance MuSK phosphorylation is not yet well understood.

The complete activation of MuSK is ultimately followed by the phosphorylation of the tyrosine Y390 residue on the major intracellular loop of the β-subunit of AChRs, which triggers the recruitment of rapsyn (**Figure 1.3**) (Hopf and Hoch 1998; Borges and Ferns 2001; Borges et al. 2008). Signalling events downstream of MuSK remain poorly understood, except for rapsyn (receptor-associated protein at synapse) that may serve as an effector.

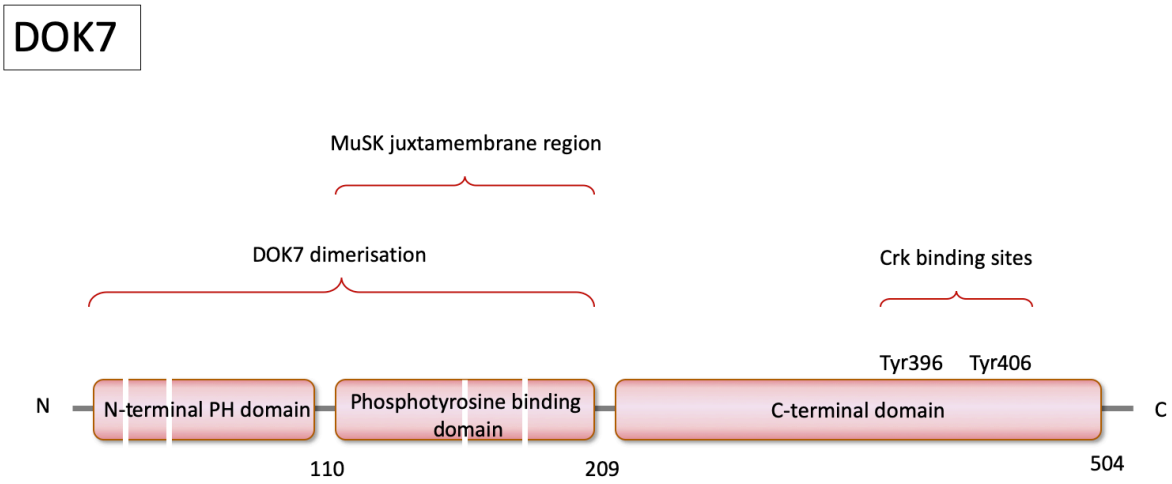

Figure 1.7. The structure of DOK7. DOK7 protein contains an N-terminal pleckstrin homology (PH) domain, a phosphotyrosine-binding (PTB) domain involved in MuSK interaction and a C-terminal domain needed for DOK7 interaction with the adaptor proteins (all coloured in light red). The white lines are used to delimitate the 7 exons.
**adapted from Cossins et al. 2012.*

Rapsyn is a membrane protein within the skeletal muscles that is essential for the clustering and precise positioning of AChRs at the postsynaptic membrane and binds to the major intracellular loops of the α-, β- and ε/γ-subunits of the AChRs (Gautam et al. 1995; Maimone and Merlie 1993; Ramarao and Cohen 1998; Lee et al. 2009). Rapsyn is estimated at 1:1 stoichiometry with the AChRs, and upon tyrosine phosphorylation of receptors' β-subunit loop, additional rapsyn molecules are recruited to the AChRs complex (Ramarao et al. 2001; Borges and Ferns 2001). Thus, absence of AChR β-subunit tyrosine phosphorylation inhibits the additional recruitment of rapsyn without completely blocking AChRs clustering at the postsynaptic membrane (Borges and Ferns 2001).

The dystrophin glycoprotein complex (DGC) spans the postsynaptic membrane and connects the actin cytoskeleton to the myofiber's basement membrane, being involved in the stabilisation of the AChR clusters at the NMJ (Xing et al. 2020). Rapsyn interacts with the cytoskeleton by binding directly to actin, and it is believed to bridge AChRs to the DGC via its association with β-dystroglycan (Apel et al. 1995; Bartoli et al. 2001; Antolik et al. 2007). The proteins of the DGC are linked together by utrophin and include β-dystroglycan, α-dystrobrevin and α-syntrophin (Apel et al. 1995; Campanelll et al. 1994; Cartaud et al. 1998; Aittaleb et al. 2017). Besides AChR, β-dystroglycan also binds to the extracellular α-dystroglycan, which interacts with laminin within the synaptic basal lamina (Banks et al. 2003). Laminin is involved in the AChR clusters maturation and interacts with agrin, influencing its correct localisation at the NMJ (Kummer et al. 2004; Mazhar and Herbst 2012).

The filamentous (F)-actin cytoskeleton is associated with the postsynaptic membrane at the NMJ (Bloch 1986). It is believed that cytoskeleton remodelling is involved in the formation and stabilisation of AChR clusters, and this is highlighted by the fact that preventing F-actin assembly results in reduced number of clusters at the postsynaptic membrane (Dai et al. 2000).

Recent studies have postulated a novel enzymatic function of rapsyn besides its role as a scaffold protein. The amino acid sequence of rapsyn includes a consensus sequence for N-myristoylation, seven tetratricopeptide repeats (TPRs), and a coiled-coil (CC) and RING domains (**Figure 1.8**) (Frail et al. 1988). The RING domain was shown to ubiquitinate itself and presents the C3H2C3 motif which are two characteristics of an E3-like enzyme (Li et al. 2016; Xing et al. 2020). As an E3 ligase, rapsyn may promote post-translational modifications (protein ubiquitination, neddylation, SUMOylation) that play an integral part in mediating various cellular functions (Deshaies and Joazeiro 2009). The second cysteine within the C3H2-

C3 motif of the RING domain is known to be necessary to maintain the activity of RING finger-dependent ubiquitin protein ligases. Mutating this residue (C366A) results in abolished activity (Thien et al. 2001). Also, knockout mice carrying a mutation of this residue fail to form AChR clusters, present extensive nerve arborisation and die shortly after birth (L. Li et al. 2016). Moreover, mutation of a major neddylation site (K397) of the δ-subunit was shown to reduce agrin-induced AChR clusters in muscle cells by reducing interaction with rapsyn (L. Li et al. 2016). Together, these observations suggest a vital role for the E3 ligase function of rapsyn in the structural organisation of the NMJ.

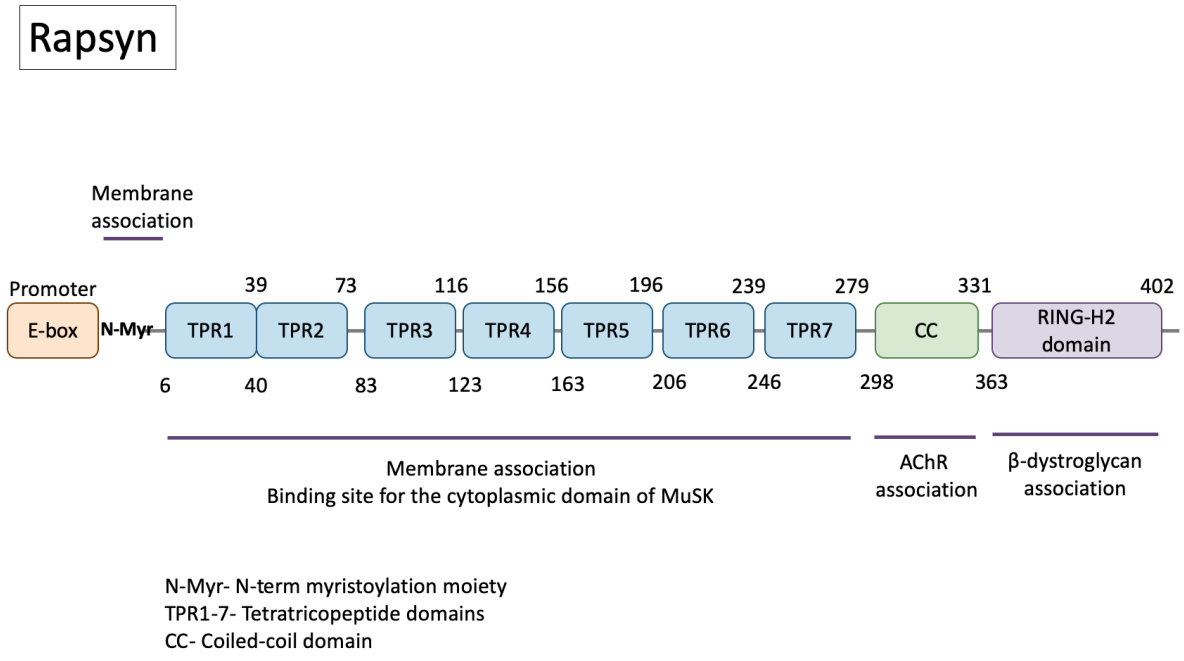

Figure 1.8. The structure of rapsyn. Rapsyn contains an N-terminal myristoylation moiety (N-Myr) necessary for submembrane association, 7 tetratricopeptide (TRP) domains responsible for rapsyn self-association and MuSK binding, a coiled-coil domain that binds to the cytoplasmic loops of the AChRs, and a RING-H2 domain that interacts with the dystroglycan complex and subsequently with the cytoskeleton.
**adapted from Rodríguez Cruz et al. 2020.*

Myristoylation, a post-translational lipidation modification of rapsyn, allows for protein-lipid interactions and tethers rapsyn to the membrane (Musil et al. 1988; Ramarao et al. 2001). The association of rapsyn with lipid rafts has been shown to be important in the formation of AChR clusters (Marchand et al. 2002; Zhu et al. 2006; Willmann et al. 2006). Lipid rafts are microdomains enriched in sphingolipids and cholesterol, serving as floating shuttles that bring together activated receptors and transducers. Ultimately, AChR clustering pathway results in the formation of a postsynaptic protein scaffold that connects freely diffusing AChRs into high-density clusters at the postsynaptic membrane.

MuSK is known as the 'concert master' of the AChR clustering, however, many other kinases and phosphatases are known to play a role at the NMJ. Amongst these, Ab1 and src are activated upon agrin stimulation. While src kinase activity is required (but not essential) for the stabilisation of mature AChR clusters, Ab1 has been shown to be involved in the NMJ assembly (Smith et al. 2001; Finn et al. 2003). In addition, Protein kinase A and C (PKA and PKC) have been shown to be involved in regulating the equilibrium between the removal and insertion of AChRs that ultimately influence the formation of stable postsynaptic receptor densities over time (Martinez-Pena et al. 2013). Activation of PKA and inhibition of PKC prevent the removal of pre-existing AChRs and promote the recycling of receptors. On the other hand, inhibition of PKA and stimulation of PKC induce the removal of postsynaptic AChRs and inactivate AChR recycling.

1.2. Congenital myasthenic syndromes

1.2.1. Introduction

Myasthenic disorders underlie defects at the neuromuscular junction (NMJ) that impair the neuromuscular transmission. Compromised neurotransmission can be either acquired, as in myasthenia gravis, or inherited, causing a congenital myasthenic syndrome.

In myasthenia gravis or autoimmune myasthenia, defects at the NMJ are caused by autoantibodies targeting specific antigens of the muscle membrane components (Spillane et al. 2010; Gilhus 2012; Gilhus et al. 2016). In the majority of cases, the autoimmune response is mediated by antibodies against AChRs, with a varying proportion of ~5-10% of the seronegative cases being caused by antibodies against MuSK (depending on ethnic background and location), and very few patients presenting with antibodies against LRP4 (Souto et al. 2019). Congenital myasthenic syndromes (CMS) are a heterogeneous group of rare genetic disorders characterized by fatigable muscle weakness due to one or more molecular pathophysiological mechanisms (Cruz et al. 2014; Engel et al. 2015; Beeson 2016). In the UK, the prevalence of myasthenia gravis is 77.67 cases /million people, while the prevalence of CMS is around 9.2 cases/ million children (Carr et al. 2010; Parr et al. 2014). The following paragraphs will focus on the CMS.

CMS are usually classified according to the site at the NMJ where function is impaired, pre-synaptic, synaptic or post-synaptic (**Figure 1.9**), and they share the clinical feature of fatigable muscle weakness. However, age at onset, level and pattern of weakness, as well as response to treatment vary depending on the molecular mechanism behind each genetic defect (Cruz et al.

2014). CMS are rare disorders with a low prevalence that is slowly increasing as new CMS-causative genes are identified due to next-generation sequencing (Vanhaesebrouck and Beeson 2019). This has led to rapid advances in our understanding of the disease mechanism of CMS, as well as to improving personalised treatments offered to patients.

Mutations in at least 31 genes are currently known to cause CMS as follows: 10 encode presynaptic proteins, 5 encode proteins located at the basal lamina, 11 code for postsynaptic proteins and 5 encode proteins involved in the glycosylation pathway (**Table 1** and **Figure 1.9**) (Cruz et al. 2014; Finsterer 2019). A few of the most commonly found causative genes are: *CHAT*, *COLQ*, *CHRNE*, *DOK7*, and *RAPSN*. The majority of the CMSs are caused by mutations in the genes encoding post-synaptic proteins.

The most common syndrome, representing ~40% of all cases, is due to AChR deficiency (Engel et al. 2018). AChR deficiency can be caused by mutation in the genes encoding any of the AChR subunits. This results in either lower or null expression of the receptor. Some mutations in the AChR can also induce altered channel properties causing rapid closure (fast channel syndrome), or slow closure (slow channel syndrome). Mutations in ~18% of diagnosed CMS patients have been reported in the *DOK7* gene (Beeson et al. 2006; Cossins et al. 2012). The majority of these patients harbour a common frameshift duplication (c.1124_1127 dupTGCC) on at least one allele. While most CMS are autosomal recessive diseases, the slow channel syndrome and syndromes due to mutations in *SYT2* and *SNAP25B* show dominant inheritance patterns (Herrmann 2014; Shen et al. 2014; Engel et al. 2015). The two most relevant syndromes for this thesis are discussed below.

Table 1.1. Classification of congenital myasthenic syndromes.

MECHANISM	GENE	REFERENCE
PRESYNAPTIC		
Defects in axonal transport of proteins	*MYO9A*	(O'Connor et al. 2016)
Defects in loading of ACh in synaptic vesicles	*SLC18A3*	(GL O'Grady 2016)
Defects in ACh synthesis	*CHAT*	(Ohno et al. 2001)
Defects in ACh recycling	*SLC5A7*	(H Wang 2017)
Defects in synaptic vesicle docking, priming, fusing and endocytosis	*PREPL*	(Régal et al. 2014)
	SYT2	(DN Herrmann 2014)
	VAMP1	(V Salpietro 2017)
	SNAP25	(XM Shen 2014)
	UNC13A	(Engel et al. 2016)
SYNAPTIC		
Defects of AChR clustering pathway	*AGRN*	(Huzé et al. 2009)
Synaptic basement membrane defects	*COL13A1*	(Logan et al. 2015)
Acetylcholinesterase deficiency	*COLQ*	(Ohno et al. 1998)
Laminin deficiency	*LAMB2*	(Maselli 2009)
	LAMA5	(J Maselli 2017)
POSTSYNAPTIC		
AChR deficiency with reduced numbers of AChR	*CHRNE*	(Sieb et al. 2000)
	CHRND	(JS Müller 2006)
Kinetic changes in AChR function (slow channel syndrome)	*CHRNA1*	(R Brugnoni 2010)
	CHRNB1	(Mihaylova et al. 2010)
Escobar syndrome	*CHRNG*	(K Hoffmann 2006)
DOK7 myasthenia	*DOK7*	(Beeson et al. 2006)
Rapsyn deficiency	*RAPSN*	(Ohno et al. 2003)
MuSK deficiency	*MuSK*	(Chevessier et al. 2005)
LRP4 myasthenia	*LRP4*	(Ohkawara et al. 2014)
Defects in skeletal muscle voltage-gated sodium channel	*SCN4A*	(Tsujino et al. 2003)
Plectin deficiency	*PLEC*	(Forrest et al. 2010)
UBIQUITOUS		
Defects of the glycosylation pathway	*GFPT1*	(Senderek et al. 2011)
	DPAGT1	(Belaya et al. 2012)
	ALG2	(Cossins et al. 2013)
	ALG14	(Cossins et al. 2013)
	GMPPB	(Belaya et al. 2015)
Mitochondrial citrate carrier	*SLC25A1*	(Chaouch et al. 2014)
Defective function of an inner nuclear membrane protein	*TOR1AIP1*	(Cossins et al. 2020)

1.2.2. Congenital myasthenic syndromes caused by mutations in the DOK7 gene

DOK7 plays an important role in the AChR clustering pathway, therefore pathogenic mutations within the *DOK7* gene result in impaired pre-patterning and postsynaptic assembly and maintenance (Okada et al. 2006; Beeson et al. 2006).

Screening of genomic DNA from patients with CMS revealed frameshift, missense or splice site autosomal recessive mutations along the 7 coding exons of *DOK7*. The most common variant is the c.1124_1127dupTGCC, a frameshift mutation that results in the truncation of the C-terminal domain due to a premature stop codon (Beeson et al. 2006). A transgenic mouse model homozygous for the frameshift mutation c.1124_1127dupTGCC has been generated to mimic the mechanism and symptoms of the most common patient mutation (Arimura et al. 2014). Truncations of the C-terminal region partially maintain protein function. However, mutations that result in truncations of the other two domains (PH and PTB) are not functional and are lethal when homozygous (Vogt et al. 2009; Hamuro et al. 2008).

The clinical spectrum of symptoms is wide, most commonly being characterized by a limb-girdle pattern of weakness with walking difficulties after reaching normal motor milestones (Palace et al. 2007). Other clinical symptoms are ptosis, mild facial weakness, moderate to severe bulbar symptoms and laryngeal stridor. Proximal muscles are usually more affected than distal muscles.

From a molecular point of view, in patients with *DOK7* mutations, the endplates appear smaller in size, present reduced postsynaptic folding and are therefore ineffective in ensuring a correct transmission of signal to the muscle (Slater et al. 2006). All in all, pathogenic changes of *DOK7*

result in defects of pre-patterning and postsynaptic assembly (Beeson et al. 2006; Okada et al. 2006). *DOK7* gene is highly polymorphic containing many non-pathogenic variants which makes it difficult to predict which of the variants are pathogenic mutations (Cossins et al. 2012). The impact of DOK7 mutations on the AChR clustering pathway can be observed by overexpressing DOK7 mutants in comparison to DOK7 wild type in cell culture. Overexpression of DOK7 in myotubes is known to induce AChR clustering in the absence of agrin (Beeson et al. 2006). Thus, this is a good model system that allows for visualisation of AChR clusters by fluorescent staining (**Figure 1.12**).

1.2.3. AChR deficiency syndromes

Mutations in the genes encoding the AChR subunits are a major cause of CMS and AChR deficiency due to mutations in *CHRNE* is the most common cause of CMS accounting for up to 40% of all cases (Cruz 2014; Parr et al. 2014; Engel et al. 2018).

AChR deficiency mutations lead to 70-80% loss of endplate AChRs, formation of immature endplates, NMJ fragmentation and loss of postsynaptic folding (Ohno et al. 1997; Sieb et al. 2000; Croxen 2001; Webster 2018). Cases may present from birth to early childhood, with symptoms of weakness of eye movement (ophthalmoplegia), eyelid ptosis and distal and proximal muscle weakness from moderate to severe (Engel et al. 2015). Homozygous null mutations in genes encoding α, β and δ subunits are lethal. However, null or low-expressing mutations in the gene encoding the ε subunit are not usually lethal, and it is thought that a low level of expression of the foetal γ subunit can partially compensate for the loss of the ε subunit (Ohno et al. 1997; Croxen 2001; Engel et al. 2008).

The switch between the foetal and adult subunits has been studied in depth using AChR ε-subunit knockout mice and was shown to be complete at the mRNA level by P21 (Witzemann et al. 1996; Missias et al. 1997). Expression of the foetal γ subunit in humans is maintained at low levels throughout life, which is not the case for mice (Croxen 2001). In accordance, ε-subunit knockout mice which are born with no obvious phenotype develop muscle weakness and die by 3 months of age (Witzemann et al. 1996; Missias et al. 1997). Therefore, to best mimic the human AChR deficiency syndrome, a mouse model was generated to constitutively express the human AChR γ-subunit in an AChR ε-subunit knockout background (Cossins et al. 2004). These mice present a moderate level of muscle weakness but have a normal lifespan and can be used to study disease mechanisms and to test various therapies.

1.3. Overview of available treatments for CMS

Congenital myasthenic syndromes are rare diseases for which personalised medicine matters. As severity varies between patients, clinical observations as well as genetic diagnosis are both critical in deciding the treatment.

Before the identification of CMS caused by mutations in the *DOK7* gene (Beeson et al. 2006), the standard treatment for CMS was mainly based on therapies using cholinesterase inhibitors (such as pyridostigmine), with occasional use of the potassium channel blocker 3,4 diaminopyridine or AChR 'open channel' blockers (fluoxetine or quinidine) (Rodríguez Cruz et al. 2018). After a close examination of a cohort of patients with *DOK7* mutations, it was shown that cholinesterase inhibitor medication had a detrimental effect on their health but they could benefit from treatment with β2-adrenergic receptor (β2-ADR) agonists, such as ephedrine and salbutamol (Lashley 2010). Following this observation, the combination of clinical and research studies revealed other CMS subsets that can benefit from this therapy or combination therapies. For example, salbutamol and ephedrine significantly improved symptoms of AChR deficiency in patients on pyridostigmine treatment, over a period of six to eight weeks (Rodríguez Cruz et al. 2015).

Although this is an important step for the treatment of CMS, the degree of muscle weakness depends on the molecular mechanism behind each genetic defect, therefore the response to treatment varies significantly between patients. Current advances in therapeutic strategies present a huge potential for the field of neuromuscular disease. For example, studies based on DOK7 and protein-anchoring (COLQ) therapy, antisense oligonucleotides therapy or systemic administration of agrin have shown improvement of neuromuscular disorders symptoms in

animal models (Mann 2001; Arimura et al. 2014; Hettwer et al. 2014; Miyoshi, Tezuka, et al. 2017; Ito and Ohno 2018). DOK7 gene therapy is discussed in more detail below.

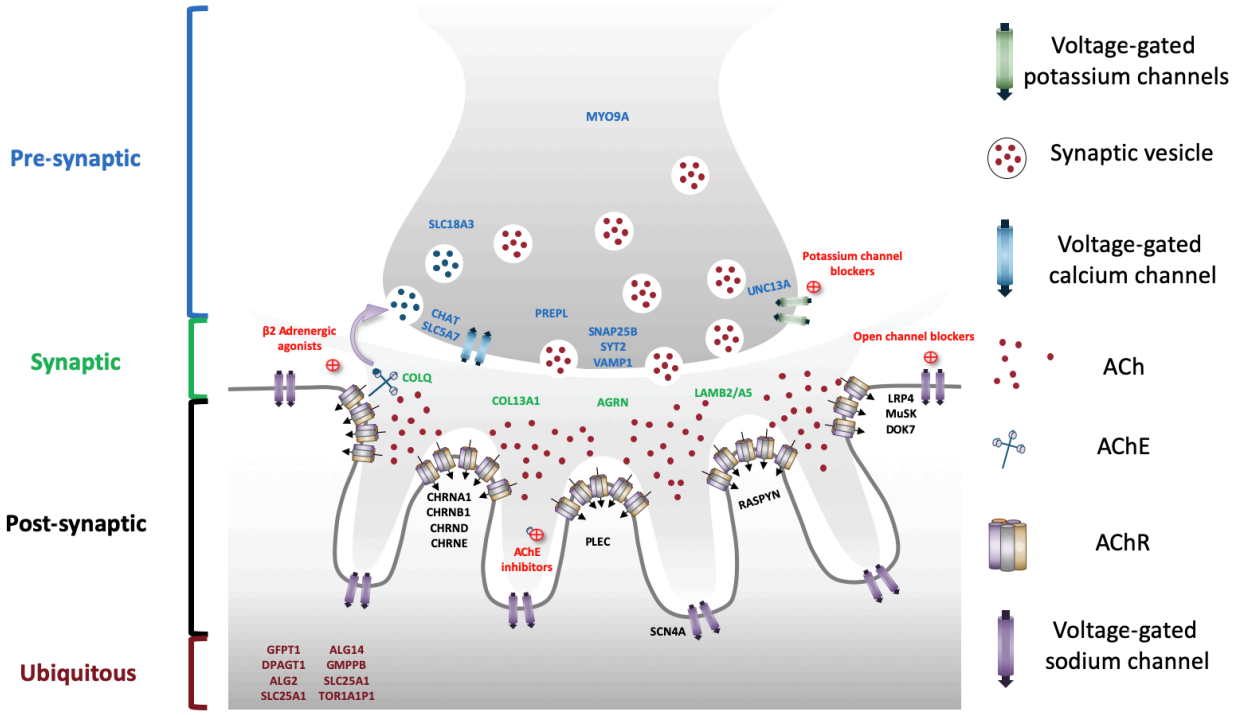

Figure 1.9. Targeted therapies for CMS. **adapted from Rodríguez Cruz et al. 2018.*

1.4. Possible novel therapies for CMS

1.4.1. Introduction

Therapeutic discovery is one of the most costly, intricate and lengthy scientific undertakings and it requires expertise from many different science disciplines. Current advances are not only focusing on the discovery process itself, but also on developing innovative methodologies to speed up the drug discovery process in the search for novel drugs and personalised therapeutics.

For a long time, drug discovery was largely based on the target- and mechanism-agnostic approach, mainly using ligands and chemotypes derived from naturally found substances or discovered through ethnobotanical knowledge and often driven by luck (Eder and Herrling 2016). However, drug discovery has witnessed rapid advances within the last few decades due to numerous scientific advances in molecular biology and chemistry, as well as in computing and data analysis (e.g. the human genome project). Consequently, drug discovery has changed to a more hypothesis driven "target-based" approach. Furthermore, current collaborations between academia and pharmaceutical industries increase the chances of discovering breakthrough medicines by taking advantage of large institutes capturing both biological and technological synergies (Eder and Herrling 2016). Thus, target-based drug discovery has contributed to an increase in the availability and diversity of pharmacophores, chemotypes and therapeutic strategies.

A novel therapeutic discovery study is justifiable when there is an unmet clinical need or a constant demand for a more suitable drug to fit personalised medicine. Initial research may begin in academic laboratories with a formed hypothesis based on scientific data that suggests

modification of a pathway or protein could result in a therapeutic effect. Taking a successful candidate therapy into preclinical tests and, if proven effective into clinical trials, can take up to 15 years or more (**Figure 1.10**) (Silber 2010; Hughes et al. 2011; Eder and Herrling 2016; Berdigaliyev and Aljofan 2020).

More than 6000 rare or orphan diseases have been described to date (Dawkins et al. 2018). CMS is one such rare neuromuscular genetic disease for which symptomatic treatment is available. However, these treatments have various side effects, are required life-long and do not provide a cure for the disability.

1.4.2. The potential of small molecules libraries screening

Notably, the development of high-throughput screening and diversified drug libraries have contributed to a tremendous progress within the field of drug discovery. Generally, the libraries are designed to comprise compounds synthesized by the same company, sometimes with a similar structure or mode of action (Hughes et al. 2011; Berdigaliyev and Aljofan 2020). The most commonly used sources to find new drugs are:

- Natural sources
- Small molecule compound libraries
- Computer-aided drug design (CADD) methods
- Biological sources
- Drug repurposing approach

Many challenges are encountered on the way to finding new drug leads as for example the limitations due to the large and complex structures of biological agents, the difficulties linked to the purification and characterisation of natural products or the fact that drugs designed by CADD require extensive testing and are not necessarily active in the biological system as a whole (Berdigaliyev and Aljofan 2020). Drug repurposing can make a very appealing and cost effective alternative to drug development, however, from a commercial point of view it might not be attractive enough for pharmaceutical collaborators due to a lack of intellectual property laws to protect them (Oprea and Overington 2015).

Small molecule synthesis has emerged as a complementary strategy to the traditional drug discovery process from the idea that smaller molecules (usually with a molecular weight of maximum 500 Da) are simpler and more likely to fit into the desired binding sites than complex molecules (Hannet al. 2001; Eder and Herrling 2016; Berdigaliyev and Aljofan 2020). High molecular weight molecules are also characterised by poor absorption, distribution and metabolism as well as high affinity binding which can lead to many but unspecific interactions. While larger molecules tend to be more difficult to develop into effective compounds without altering their drug-like properties and potency, small molecule hits can be more readily optimised into potent lead compounds, thus providing the starting point in drug discovery (Murray and Rees 2009). Typically, a small molecules screen involves testing thousands of compounds against a certain biological target. Once a small molecule that can modulate a particular biological process is found, this will be developed into a drug lead that will further guide the production of similar large-scale molecules to be further tested (**Figure 1.10**).

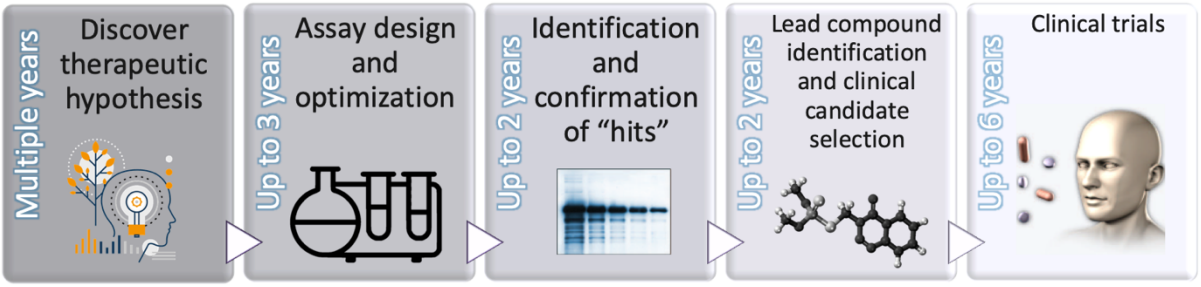

Figure 1.10. Drug discovery timeline. Discovery of novel drugs begins with the development of a therapeutic hypothesis for which the assay design and optimisation is the first crucial step and is followed by the screening for potential hit compounds. The process can take more than 5 years. Once hits are identified and confirmed, their structure can be chemically modified for improved physiochemical characteristics and pharmacokinetics profiles. They next become lead compounds that are further tested in pre-clinical and clinical trials.

High-throughput screening has become the standard method for discovering novel drug leads for various diseases (Inglese et al. 2007; Thorne et al. 2012; Silber 2010; Eder and Herrling 2016; Berdigaliyev and Aljofan 2020). It is based on collections of hundred thousand of compounds that are usually tested in an automated format, and can be introduced at any stage of the drug development process such as to screen for hit molecules or to find similar lead compounds. Moreover, CADD is a useful technique to evaluate the physiochemical properties of known ligands. This can provide guidance on potential structural modifications of compound hits to enhance their activity and avoid undesirable properties such as poor absorption, distribution, metabolism, excretion or toxicity.

Over the past few years, small molecules have led over biologics accounting for more than 50% of recent drug approvals ("Compilation of CDER New Molecular Entity (NME) Drug and New Biologic Approvals | FDA" n.d.; "Small Molecules Lead in Recent New Drug Approvals" 2020). With more than 1500 unique drugs developed from small molecules which

are currently FDA approved, many known disease targets are already covered (Kinch et al. 2014; "Orange Book: Approved Drug Products with Therapeutic Equivalence Evaluations," n.d.). Their discovery has changed the outcome for many diseases which are now curable or at least symptomatically controlled (Eder and Herrling 2016; Berdigaliyev and Aljofan 2020).

1.4.3. Adeno-associated virus mediated gene therapy

The concept of gene therapy began with the idea that introduction of exogenous nucleic acids within cells of a living organism could results in a therapeutic effect. The selection of the delivery system which can be via viral or non-viral vectors depends on various aspects such as the size of the genomic material to be inserted, the type of tissue that needs to be targeted and more importantly the period needed for the transgene to be expressed in order to achieve a therapeutic effect.

Due to its low pathogenicity, relatively long-lasting expression from a single delivery and its ability to transduce both dividing and quiescent cells, adeno-associated virus (AAV) provides an effective gene delivery vehicle (Weinberg et al. 2013; Haggerty et al. 2020). AAV is a replication-defective parvovirus that was first observed in 1965 as a contaminant of an adenovirus preparation (Atchison et al.1965). It consists of a single stranded DNA genome and its replication depends on a helper virus (e.g. adenovirus or herpes simplex virus) (Atchison et al. 1965; Rose et al. 1969; Lotfinia et al. 2019). The AAV genome is 4.7 kb long and contains open reading frames (ORFs) encoding genes for various proteins involved in viral replication (*rep*), viral capsid formation (*cap*) and assembly of structural proteins involved in capsid formation (*aap*). Based on the protein components that make up the capsid, various serotypes with different tissue tropisms and transduction efficiencies have been reported (Lisowski et al.

2015). The ORFs are flanked all together by two inverted terminal repeat sequences (ITRs) (Daya and Berns 2008; Colella et al. 2018). Depending on the existence or absence of a helper virus, the AAV can undergo either lytic or lysogenic cycles respectively. In the absence of the required helper genes, AAV develops latency by integrating within the host genome into a specific site in chromosome 19 and requires to be rescued by a helper virus to shift to its lytic state (Cheung et al. 1980; Drouin and Agbandje-Mckenna 2013). During a lytic cycle, AAV is able to replicate its genome by making use of its host's DNA polymerase. This is ultimately followed by virus production.

Since 1984, when the concept of recombinant AAV-based vectors (rAAV) was first described, rAAV gene therapy has demonstrated huge potential (**Figure 1.11**) (Hermonat and Muzyczka 1984). Development of rAAV as a gene therapy method involved eliminating its ability to integrate into the host chromosome and allowing it to exist in the host cell as episomal DNA with insignificant integrative rates. rAAV vectors elicit a very mild immune response from the host in comparison with adenoviruses or retroviruses.

The first ever FDA-approval for AAV gene therapy for an inherited condition was in 2017 (for patients with Leber's congenital blindness) and marked an immense achievement for the field (Shaberman 2017). This was followed by other reported successes in the AAV gene therapy field, with promising clinical trials for Parkinson's disease, Becker muscular dystrophy and most recently the FDA authorization for Spinal muscular atrophy (Kotterman et al. 2015; Mendell et al. 2015; Schorling et al. 2020).

Recombinant AAV plasmids, used in gene therapy, are constructed in such a way that the region of interest replaces all the original AAV ORFs while maintaining both ITRs needed to guide genome replication and packaging (Zhang et al. 2001; Wang et al. 2019). Thus, to ultimately produce a recombinant AAV carrying the region of interest, a packaging cell line (HEK293 cells) is transfected with the helper virus that provides the essential *rep, cap* and *aap* genes. The packaged virion can then be used to transduce target cells.

AAV gene therapy provides an option for precise targeted treatment strategy for CMS, especially since it has proved promising in other neuromuscular disorders (D. Wang et al. 2014).

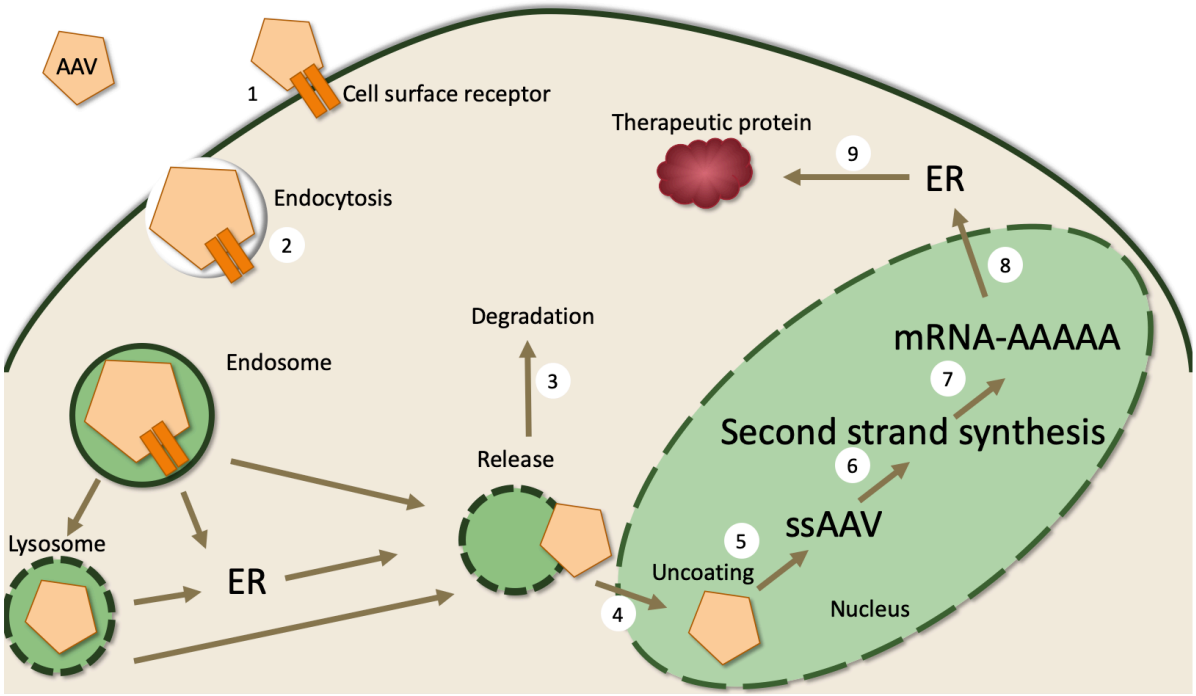

Figure 1.11. Adeno-associated virus gene therapy mechanism. Adeno-associated virus (AAV) virions bind to receptors on the surface of targeted cells (1). They are further taken into endosomes within the cytoplasm of these cells through endocytosis (2). Upon endosomal release, the AAV could be ubiquitylated and targeted for degradation (3) or transported to the nucleus through intracellular trafficking (4). In the nucleus, the virions are uncoated for the DNA to be released (5), the AAV single stranded DNA to be converted into double stranded DNA (6) and the mRNA to be transcribed (7). Next, the mRNA is transported out of the nucleus (8) for the functional therapeutic protein to be finally produced (9).

**adapted from C. Li and Samulski 2020.*

1.5. The discovery of 'enlarged synapses' and their potential to enhance neuromuscular transmission

A study focusing on the biology and function of DOK7 protein, showed that when DOK7 is expressed at high levels in differentiated myotubes, it induces the formation of multiple clusters of AChRs, which can ultimately be used to mimic the formation of a synapse *in vitro* (Inoue et al. 2009). A transgenic mouse model was then generated to express the human *DOK7* gene uniformly throughout the muscles, under the control of the human skeletal α-actin promoter (HSA) (Inoue et al. 2009). Overexpression of DOK7 in skeletal muscles induced enhanced MuSK activation and synaptogenesis and caused the formation of markedly enlarged NMJs. To facilitate DOK7 mediated NMJ formation in muscles, a recombinant AAV vector carrying the human *DOK7* gene that was tagged with EGFP was generated (Arimura et al. 2014). Wild-type mice injected with this DOK7-AAV vector developed enlarged synaptic structures after one week. These mice had normal muscle strength and, although they exhibited enhanced neuromuscular transmission, the numbers of active zones and synaptic vesicles were reduced, which may represent the balance needed to avoid overactivation of AChRs in these oversized synapses (Eguchi et al. 2020).

To test the efficiency of DOK7-AAV as a gene therapy candidate, a DOK7-CMS mouse model was generated to contain the most common patient mutation c.1224_1227dupTGCC (described in **Section 1.2.1**) (Arimura et al. 2014). This mutation is extremely severe when introduced into mice which fail to thrive and die by P20. Injection of this mouse model with DOK7-AAV caused the formation of super synapses and had a drastic effect on the phenotype, enabling the symptomatic mice to completely recover and survive above 1 year (Arimuras et al. 2014). To

demonstrate its potential in other neuromuscular disorders, the authors have also shown reverse phenotypes in animal models of Emery-Dreifuss muscular dystrophy and Amyotrophic lateral sclerosis (Arimura et al. 2014; Miyoshi et al. 2017).

Given the potential of the DOK7-AAV gene therapy in these mouse models, overexpression of DOK7 could become a therapeutic option in other forms of CMS.

1.6. Models of CMS used to study response to treatment

Neuromuscular transmission at the NMJ is based on a series of complex mechanisms working in precise harmony. The use of *in vitro* cell culture and *in vivo* mouse models of CMS to study both disease mechanisms and response to treatment is a pre-requisite to allow for the development of more potent tailored therapies with fewer side effects.

The clustering of AChRs on myotubes can be replicated and visualised *in vitro* in differentiated muscle cells (Okada et al. 2006). Myotubes can be differentiated from their precursor myoblasts to fully mature multinucleated myotubes in ~ 5 to 9 days. Neural agrin added overnight to the culture or overexpression of DOK7, will induce the formation of AChR clusters on the membrane of myotubes which, can be visualised by fluorescent staining or quantified using a radiolabelled ligand (**Figure 1.12**).

Various animal models have been used in studies aiming to understand the structure, organisation and function of the NMJ. These include *C. elegans* nematodes, fruit fly *Drosophila*, zebrafish and rodents. The mouse model is the most informative, with NMJs presenting phenotypic and molecular similarities to human NMJs (Webster 2018). Mice can be used to study neurotransmission *in vivo* and *in vitro* and thus determine functional pathogenic changes in more detail. Several CMS-related mutant mouse models have been designed to replicate aspects of disease phenotype. The two models used in this thesis are: a mouse model with a DOK7 mutation and a mouse model of AChR deficiency. Detailed description of these mouse models is presented in respective chapters.

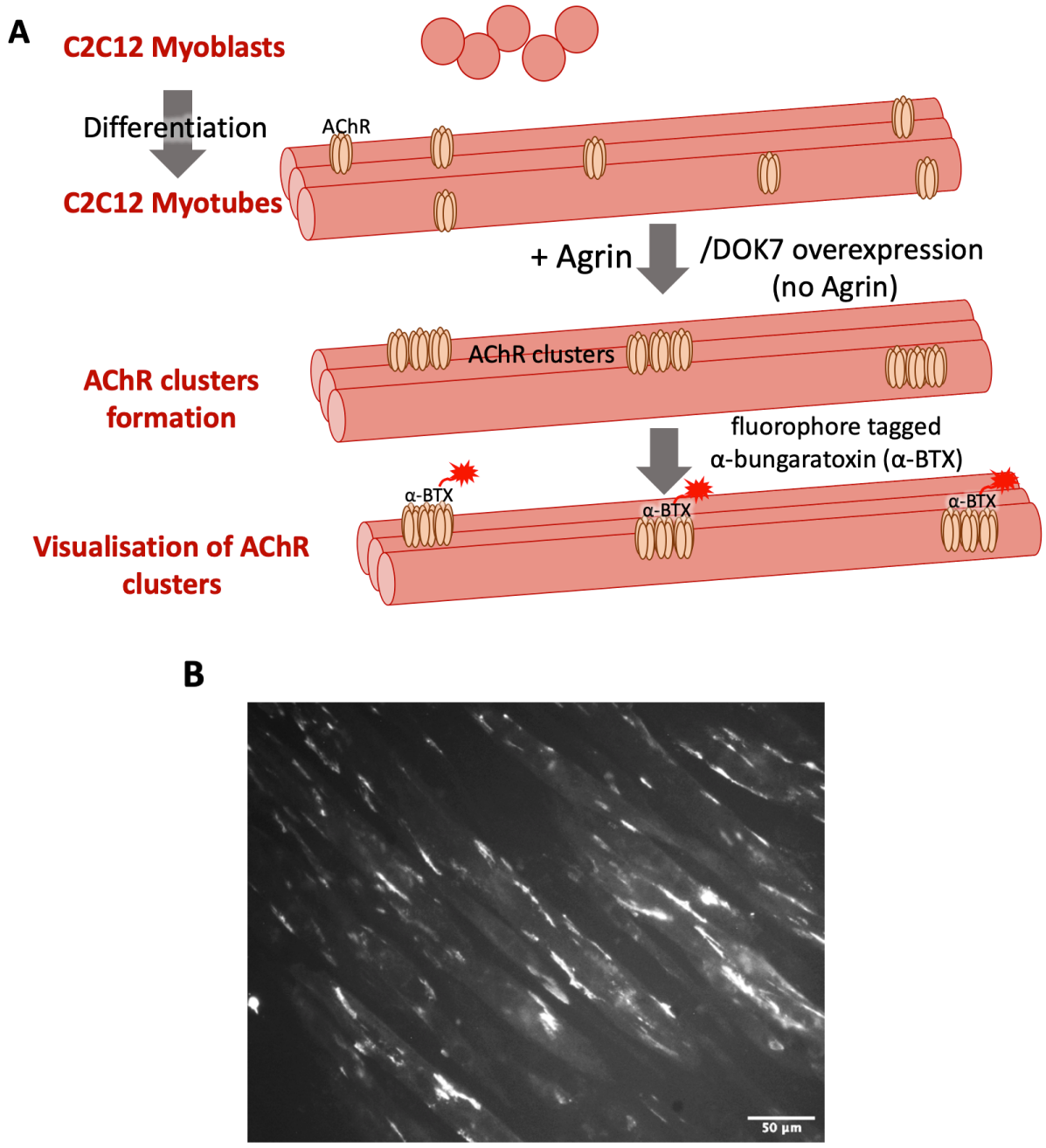

Figure 1.12. AChR clustering assay. A schematic representation of the AChR clustering assay is shown in panel **A**. When agrin is added to the myotubes, or DOK7 is overexpressed, AChR clusters are formed. These can be stained with α-bungaratoxin (a snake venom that binds AChRs) attached to a fluorophore or a radiolabelled ligand. **B** represents an image of AChR clusters stained on myotubes that were visualised with a fluorescence microscope.

1.7. Hypothesis and objectives

The work in the presented thesis is based on the observation that DOK7 overexpression induces the generation of functional enlarged synaptic structures, which are precisely located at the original synaptic sites (Arimura et al. 2014; Eguchi et al. 2020). MuSK plays a crucial role in the organisation and maintenance of the NMJs (L. Li et al. 2018). Because DOK7 acts by amplifying MuSK signal, as long as MuSK is located correctly, overexpression of DOK7 will generate enlarged synapses, all located in the correct position on muscle fibres.

Our hypothesis proposes that such enlarged neuromuscular junctions, characterised by increased AChR clusters size, can ultimately enhance neuromuscular transmission. Therefore, overexpression of DOK7 can be harnessed as a novel therapy in many different forms of CMS or other neuromuscular disorders (**Figure 1.13**). Two treatment approaches will be explored, and the work is divided into four parts (**Figure 1.14**):



Figure 1.13. Hypothesis.

1) Explore the impact of DOK7 overexpression on the structure and function of NMJ by using DOK7-AAV gene therapy in wild-type mice

Although it has previously been shown that overexpression of DOK7 triggers the increase of pre- and post-synaptic areas in diaphragm muscles, the exact mechanism behind this process

has not yet been described (Inoue et al. 2009; Arimura et al. 2014; Eguchi et al. 2020). Analyses were performed on muscles of DOK7-AAV treated wild-type mice to gain further insights. This study also aimed to confirm the formation of enlarged synapses in other muscles in addition to the diaphragm as shown previously.

2) Investigate the effects of DOK7 gene therapy on neuromuscular transmission in an animal model of DOK7-CMS

DOK7-AAV therapy restored motor activity and increased survival in DOK7-CMS mice (Arimura et al. 2014). These mice presented increased MuSK activity, enhanced AChR phosphorylation and enlargement of NMJs. However, the effects of DOK7 overexpression on neuromuscular transmission has not been investigated. This study aimed to explore electrophysiological properties of NMJs in DOK7-CMS mice.

3) Test the DOK7 gene therapy in an animal model of AChR deficiency

AChR deficiency due to mutations in the *CHRNE* gene is the most common form of CMS and is characterised by a reduction in the number of AChR clusters. To investigate the potential of DOK7-AAV therapy in a different form of CMS, we tested it in an animal model of AChR deficiency.

4) Screen for small molecules that can specifically upregulate the expression of DOK7

Modifying protein production as a potential treatment of human disease is the basis for many promising gene therapies. Having shown that DOK7 overexpression can become a therapeutic target for CMS and potentially other NMJ related diseases, a study was designed to screen for small molecule compounds that can specifically upregulate the production of DOK7.

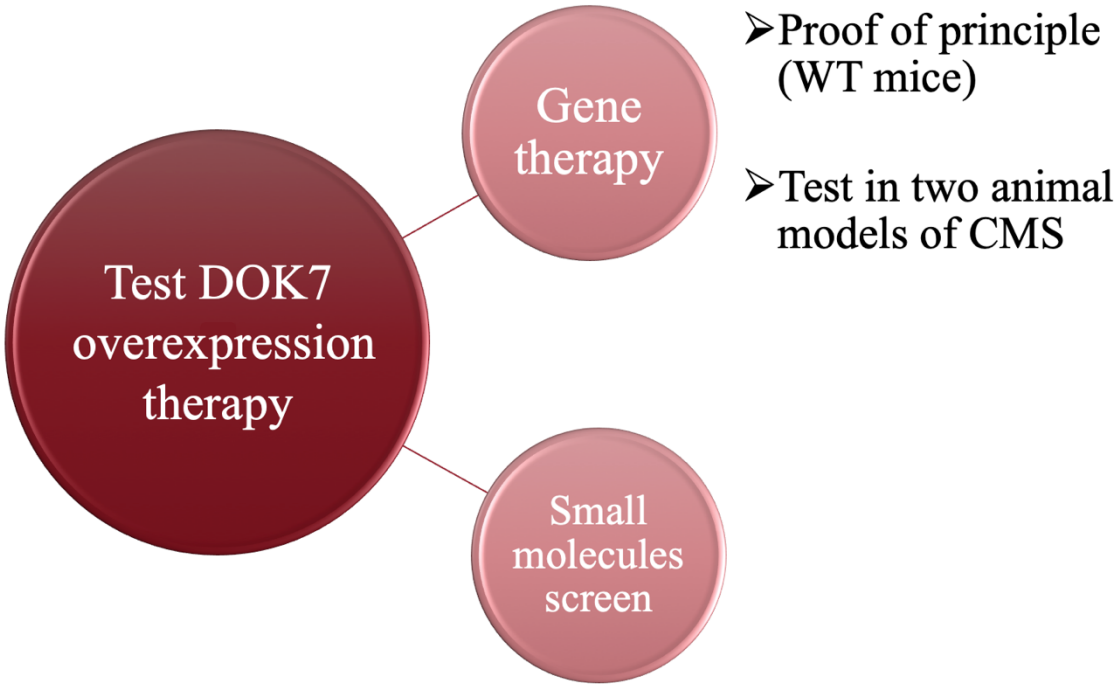

Figure 1.14 Diagram of objectives. (WT- wild-type)

Chapter 2

Materials and methods

2.1. In vivo methods

The work was performed in collaboration with Dr Richard Webster and Miss Susan Maxwell, therefore only short summaries of electrophysiological analysis, decrement tests and Dok7$^{KI/KI}$ genotyping will be presented.

2.1.1. Ethical statement

Animal experiments described in this thesis were conducted under the authority of UK Home Office project and personal licenses in accordance with the Animals (Scientific Procedures) Act 1986 at the University of Oxford. All the experiments were performed at the Biomedical Services (John Radcliffe) under the project license number PPL30/3455 and personal license number I2D301E0E. Mice were housed in individually ventilated cages and fed ad-libitum with standard diet unless stated otherwise. C57BL/6 mice were purchased locally from Biomedical Services.

2.1.2. Transgenic mouse lines used

2.1.2.1. A mouse model of acetylcholine receptor deficiency (hγ^{+}mε$^{-/-}$)

The hγ^{+} mε$^{-/-}$ mouse model was designed to constitutively express the human AChR γ-subunit (hγ^{+}) under the control of the human skeletal muscle α-actin promotor in an AChR ε-subunit

'knock-out' background ($m\varepsilon^{-/-}$) (Cossins et al. 2004). This model reflects the human condition of AChR deficiency.

2.1.2.2. A mouse model for the most common DOK7-CMS patient mutation (Dok7$^{KI/KI}$)

Dok7$^{KI/KI}$ is a knock-in (KI) mouse model homozygous for the frameshift mutation (c.1124_1127dupTGCC) which is the most common *DOK7* mutation found in human CMS patients. The model was kindly provided to us by Yuji Yamanashi's research group and was designed by Arimura and colleagues (Arimura et al. 2014).

2.1.3. Mouse breeding and genotyping

2.1.3.1. AChR deficiency mouse model ($h\gamma^{+}m\varepsilon^{-/-}$)

Progeny harbouring $h\gamma^{+}m\varepsilon^{+/-}$ were mated with siblings of the same genotype to generate litters containing mice with the human γ-subunit transgene in an $\varepsilon^{-/-}$ background ($h\gamma^{+}m\varepsilon^{-/-}$). Mouse genotyping was performed by Polymerase Chain Reaction (PCR) analysis of genomic DNA as performed by Cossins and colleagues (Cossins et al. 2004). Mice were ear-clipped and 0.2 cm size ear tissue was digested overnight at 55°C with 100 µl DirectPCR (ViagenBiotech, 401-E) containing Proteinase K (1µg; Sigma Aldrich 70663). The following day, samples were incubated at 95°C for 45 minutes, followed by a 10 minutes incubation at room temperature. Standard PCR was performed using MegaMix-Blue (Microzone, 2MMB-25), which contains recombinant Taq polymerase in reaction buffer, 2.75 mM $MgCl_2$, 220 µM deoxyribonucleotide triphosphates (dNTPs), blue agarose loading dye and stabilizer. 25 µl Mega-Mix Blue was mixed with 1 µl of primer mix (containing 0.5 µl each primer) from 100 µM primer stock and 1 µl DNA template for each sample. Human AChR γ-subunit was detected using primers that are specific for the human AChR γ-subunit gene and amplify the genomic DNA sequence between exons 11 and 12, mouse ε-subunit gene was detected

using primers that amplify the cDNA between exons 2 and 4, and presence of neomycin resistance gene was used as a marker indicating the disruption of a mouse allele within the targeted mouse ε-subunit gene (**Table 2.1**). The PCR reactions were carried out in Veriti thermal cyclers (Applied Biosystems) (**Table 2.2**).

Table 2.1. Primers used for genotyping hγ^{+}mε$^{-/-}$ mice

Target gene	Primer name	Primer sequence 5'-3'
Human AChR γ-subunit	hγ-F	GAGTTAGGGCTGAGCCAGTTCTGTG
	hγ-R	GTCTGGTGAGGGCAGGTAGGGGCGTG
Neomycin resistance gene	neo-F	CAACAGACAATCGGCTGCTCT
	neo-R	GAATGGGCAGGTAGCCGGAT
Mouse AChR ε-subunit gene	mε-F	CTCTTCGACAATTATGATCCAGA
	mε-R	GAGCCGATAGTCGTGCCAGT

Table 2.2. PCR parameters used in amplifying target genes for genotyping hγ^{+}mε$^{-/-}$ mice

Number of cycles	Step		Temperature	Duration
Initial denaturation				
1			95ºC	3 min
Amplification				
30	Denaturation		95ºC	40s
	Annealing	neomycin resistance gene	66ºC	40s
		ε-subunit and γ-subunit genes	62ºC	
	Extension		72ºC	1 min/Kb
Final extension				
1			72ºC	5 min
1	Cooling		4ºC	∞

PCR products were separated on a 0.8% agarose gel which was stained with UltraPure™ Ethidium Bromide (Thermo Fisher Scientific; Cat. No. – 15585011) at a final concentration of 0.5 μg/ml. The gels were run in 1xTBE buffer at 50V and DNA was visualized using a UV light. The 100 bp DNA Ladder (Thermo Fisher Scientific; Cat. No. - SM0243) was used as a size marker to check for the amplified γ-subunit (290bp), the neomycin resistance gene (333bp) and the ε-subunit gene (352bp).

2.1.3.2. Dok7$^{KI/KI}$ mice

Progeny harbouring Dok7$^{+/KI}$ were mated to siblings of the same genotype to generate litters containing mice homozygous for the frameshift mutation c.1124_1127dupTGCC. Mouse genotyping, carried out by Miss Susan Maxwell, was performed by restriction digest of PCR products. Mice were ear-clipped at around 3 weeks old by Mirela Panea or Dr Richard Webster. An approximatively 0.2 cm ear tissue was digested with 100 μl of DirectPCR Extraction Reagent (ViagenBiotech 401-E) containing Proteinase K (0.5–2 μg; Sigma Aldrich 70663) by incubating overnight at 55ºC. The following day, the samples were incubated at 95ºC for 45 minutes and then kept at room temperature for 10 minutes to cool down. Amplified and digested PCR products were separated on a 0.8% agarose gels which was stained with UltraPure™ Ethidium Bromide (Thermo Fisher Scientific; Cat. No. – 15585011) at a final concentration of 0.5 μg/ml and visualized under the UV light.

2.1.4. Pilot study to test DOK7-AAV gene therapy in wild-type mice

C57BL/6 mice of 3 weeks old were injected intraperitoneally as follows: three with $1x10^{12}$vg/animal of the DOK7-AAV (Vigene Biosciences; custom made) gene therapy treatment and one with saline solution (Sodium Chloride for Injections 0.9% w/v; Hameln). 3 weeks after the injections mice were sacrificed and the hemidiaphragm, extensor digitorum longus (EDL), tibialis anterior (TA) and tongue muscles were harvested for histological, protein and mRNA studies. Electrophysiological recordings were performed by Richard Webster on *ex vivo* hemidiaphragms.

2.1.5. Generation of enlarged synapses in wild-type mice

8 C57BL/6 mice were injected intraperitoneally at 3 weeks old with a $4x10^{11}$vg/animal, as follows: 5 with the DOK7-AAV (Vigene Biosciences; custom made) gene therapy treatment and 3 with a control treatment containing EGFP-AAV (Vigene biosciences; Cat. No. CV10009). At 6 weeks old mice were sacrificed and tissue was harvested for further studies (histological, fine structure, protein expression and mRNA expression studies). Electrophysiological recordings were performed by Dr Richard Webster on *ex vivo* hemidiaphragms.

2.1.6. AAV gene therapy in AChR-deficient mice

$h\gamma^{+}m\varepsilon^{-/-}$ mice were genotyped at around 2 weeks old. Intraperitoneal injections of 3 weeks old mice were performed with $4x10^{11}$vg/animal of either DOK7-AAV (Vigene Biosciences; custom made) or saline solution (Sodium Chloride for Injections 0.9% w/v; Hameln) for 10 males and 12 females per treatment group, in a blinded fashion. From 6 weeks old, their muscle strength and weight were monitored weekly for a minimum of 10 weeks. Following, decrement test, electrophysiological recordings and tissue harvesting were performed. An additional study with a higher dose of injected treatment ($1x10^{12}$gc/animal) was performed in a similar manner for a group of 8 mice: 3 males and 1 female with DOK7-AAV gene therapy at a dose of 1x1012vg/mouse, and 2 males and 2 females with saline solution as a negative control (SHAM).

2.1.7. AAV gene therapy in $DOK7^{KI/KI}$ mice

$DOK7^{KI/KI}$ mice and their littermates were monitored from birth day for overall appearance and weight gain. All pups with a weight of 2.2 g or below at P3 were considered model mice and received intraperitoneal injections with $4x10^{11}$gc/animal of DOK7-AAV (Vigene Biosciences; Custom made). Their weight was monitored daily for 3 to 4 weeks. The mice that failed to gain weight or lost 0.1g over a period of 48 hours were humanely euthanized. Once weaned, the injected mice were genotyped to confirm that they were indeed $DOK7^{KI/KI}$ model mice. Inverted screen tests to asses hang time were performed starting at 12 weeks of age for a period of 6 weeks for $DOK7^{KI/KI}$ DOK7-AAV treated mice and also for $DOK7^{+/KI}$ as a positive control. Decrement tests were performed at the end of the 5 weeks period. Finally, the

mice were sacrificed for protein expression analysis, histological studies, and electrophysiological recording of hemidiaphragms (decrement tests and electrophysiology recordings were performed by Dr Richard Webster).

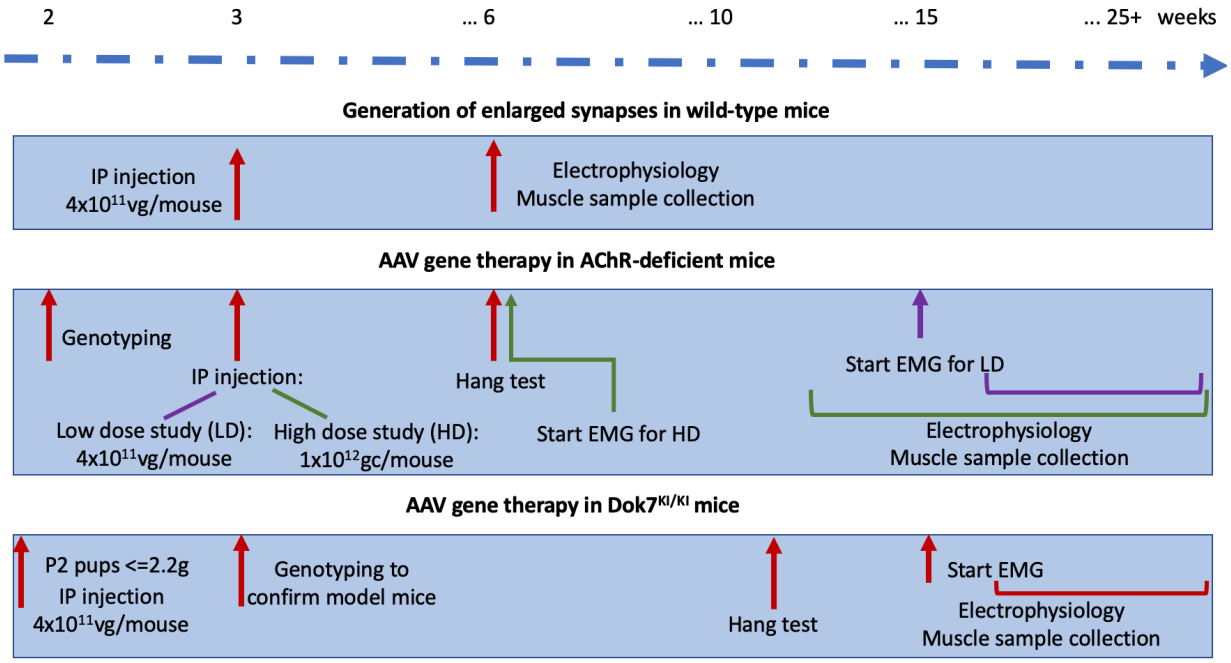

Figure 2.1. DOK7-AAV gene therapy study design. Firstly, the treatment was tested and optimised in wild-type mice. Following, gene therapy was used on two myasthenic animal models as shown in the figure. Low dose (LD) and high dose (HD) studies were designed for the AChR-deficiency mice *P2- post natal day 2.

2.1.8. Evaluation of muscle strength and weight in mice

Muscle fatigue of mice were monitored once per week. Muscle strength was evaluated using an inverted screen test as described by Cossins et al. (Cossins et al. 2004). A 50 cm^2 screen of wire mesh consisting of 12 mm^2 of 1 mm diameter wire surrounded by a 5 cm deep wooden

frame was used. The mouse was placed in the centre of the screen and immediately as the screen was rotated to the inverted position, the timer was started. The screen was supported on a solid base 50 cm above a padded surface. When the mouse fell off, the timer was paused, the time recorded, and the mouse was immediately placed back on the screen. The test was repeated for 2 subsequent attempts without resting in between. Finally, the cumulative hang-time was used for analysis.



Figure 2.2. Inverted screen test used to measure muscle fatigability of mice. The figure shows a representation of an inverted screen test. Three continuous attempts were recorded for each animal without rest in between.

2.1.9. Repetitive nerve stimulation

Compound muscle action potential decrement (CMAP) on repetitive nerve stimulation is a commonly used technique to detect defective neuromuscular transmission in myasthenic patients considering that decremental muscle response is a cardinal feature of myasthenia. We used this technique to evaluate the effect of DOK7-AAV gene therapy on neurotransmission

in myasthenic mice. The procedure was performed entirely by Dr Richard Webster on anesthetized mice in a blinded fashion (Webster et al. 2013). In brief, the right sciatic nerve was stimulated via 2 mono-polar needles (Viasys Healthcare, UK) at an intensity above the level that generates the maximal compound muscle action potential (CMAP) amplitude (Dual bio amp/stimulator, AD Instruments UK). Recording of the CMAP decrement was done using two mono-polar needle electrodes (anode and cathode) that were positioned within the gastrocnemius muscle to achieve maximal CMAP amplitude. Data was acquired using Powerlab 4/25 (AD Instruments, UK) with a sampling frequency of 200 kHz filtered at 5 kHz low pass and 1 Hz high pass. The CMAP amplitude was measured peak to peak, and the decrement was defined as the decrease in percentage in CMAP amplitude between the 1st and 10th stimuli in a train of 10 stimulations (with at least 30s rest in between each train) at various frequencies, repeated 3 times for each frequency (pClamp 9, Molecular Devices, USA). The results from at least three animals/ group were analysed.

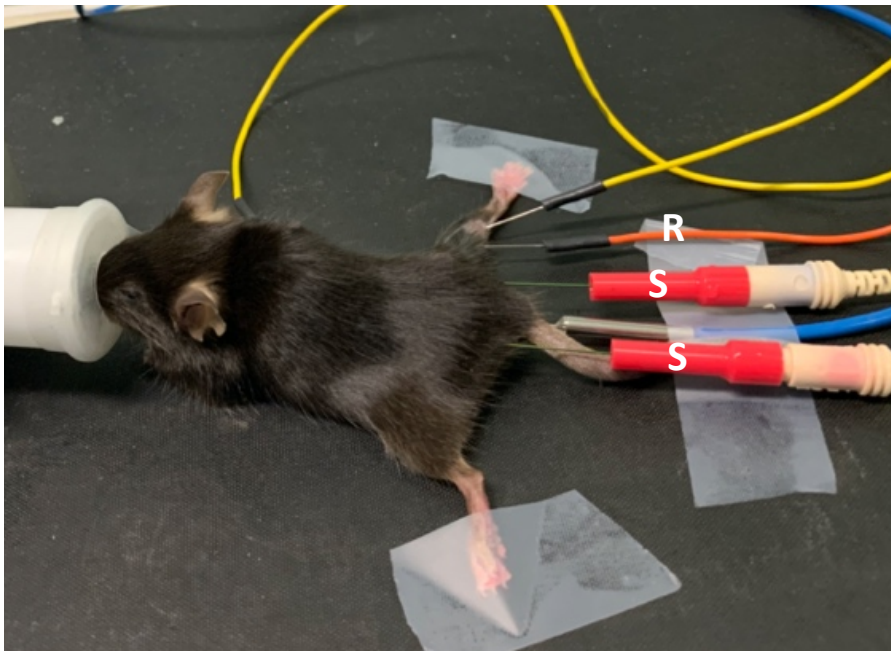

Figure 2.3. Electromyography represented on an animal. The right hind limb contains recording electrodes (R) within the belly of the gastrocnemius muscles. The sciatic nerve is stimulated by stimulating (S) electrodes.

2.1.10. Ex-vivo diaphragm electrophysiology/ Endplate potential recordings

Effects of DOK7-AAV gene therapy on neuromuscular transmission were also assessed by performing electrophysiological recordings on hemi-diaphragm-phrenic nerve preparations. Recordings were performed by Dr Richard Webster following the previously described protocol (Cossins et al. 2004).

In brief, phrenic nerve/hemi-diaphragm preparations were dissected and bathed in Krebs solution, bubbled with 95% O2 / 5% CO2. Preparations were pinned out in Sylgard-coated Petri dishes containing bubbled Krebs solution. The phrenic nerve was pulled into a suction electrode coupled to a pulse generator (GRASS instruments S48 solid-state square wave stimulator, Quincy, USA) with an associated stimulus isolation unit. To allow for the measurement of evoked potentials preparations were incubated with 2.5 μM μ-conotoxin GIIIB (Peptide Institute, Japan). The toxin is a blocker of the sodium channel Nav1.4, thus it was used to block muscle action potential and contraction. Recordings were made at RT after the preparation was incubated for 30 minutes with the toxin and then washed.

Depolarisation at an endplate was recorded intracellularly using a sharp electrode filled with 3M KCl, which was positioned above the endplate zone using a stereomicroscope (Olympus BX51WI) under micromanipulator control (Scientifica, UK). Spontaneous (mEPPs- miniature endplate potentials) and nerve-evoked (EPP- endplate potentials) depolarisations were measured. Data signals were passed through a Humbug 50 Hz noise eliminator (Quest Scientific via Digitimer, Welwyn Garden City, UK), in order to reduced electrical noise on

recordings. For an approximate recording time of 1 hour, up to 30 MEPPs followed by up to 30 EPPs (stimulated at 1 Hz) were recorded/ individual endplate, from 15-30 endplates/ animal. Quantal content was calculated for each endplate to estimate the number of synaptic vesicles released by the nerve terminal with each stimulation. Mean quantal content (QC) was calculated using the formula:

$$QC = \text{mean}(AMP_{EPP})/\text{mean}(AMP_{mEPP})$$

*AMP_{EPP} =corrected amplitude of the EPP; AMP_{mEPP} =the amplitude of the MEPP

In the above calculations, EPPs (evoked at 1 Hz) were corrected for nonlinear summation using the formula:

$$AMP_{EPP} = AMP_{EPP(measured)} / ((1-0.8AMP_{EPP(measured)})/E)$$

In the latter formula, E is the resting membrane potential (-80mV) and 0.8 represents the correction factor for mouse endplates (McLachlan and Martin 1981). Data was grouped according to each individual study and was represented as mean +/−SEM.

2.1.11. Imaging neuromuscular junctions

To further investigate the effect of DOK7-AAV gene therapy on the structure of the neuromuscular junction, we used immunostaining of AChRs and nerve terminals and studied these in whole-mount hemidiaphragm preparations and teased muscle fibres of extensor digitorum longus (EDL) and soleus muscles. EDL, soleus and diaphragm muscles were quickly dissected and bathed in Krebs buffer (appendix) previously bubbled with 95% O_2/5% CO_2. The leg muscles were partially teased into 2 bundles. All muscles were pinned out in Sylgard-coated petri dishes containing bubbled Krebs solution, and immediately fixed for 30 minutes at RT in 1% formaldehyde in PBS.

Following, the muscles were washed three times in PBS and kept in PBS at 4ºC until further processing. Post-synaptic AChRs were labelled with α-Bungaratoxin Alexa Fluor™ 549 conjugate (Invitrogen, B13423) diluted 1:150 in PBS by incubating the muscles overnight at 4ºC. The following day, all samples were washed with 12 changes of PBS for approximatively 2 hours.

To observe the nerve terminals, samples were further stained for neurofilament and synaptophysin as follows (Webster et al. 2013b). All muscles were dehydrated by sequential incubations in ice-cold ethanol for 2 minutes and ice-cold methanol for 5 minutes (7 minutes for DOK7 KI mice) at -20ºC, followed by two washes in PBS. Next, samples were blocked at RT in PBS-Tween (PBS containing 0.05% Tween 20) with 3% goat serum and 0.1% triton-X for 30 minutes. After brief washes in PBS-Tween, the muscles were incubated overnight at 4ºC with PBS-Tween containing 3% goat serum, chicken anti-neurofilament antibody (ab-4680, Thermo Fisher Scientific, 1:1000) and rabbit anti-synaptophysin antibody (ab-4, Thermo Scientific, 1:100). The following day, samples were washed for 1 hour at RT in PBS-Tween with 6 changes and then incubated for 3 hours at RT in PBS-Tween containing 3% goat serum, goat anti-chicken and goat anti-rabbit Alexa Fluor™ 488-conjugated secondary antibodies (Invitrogen, 1:100; Cat. No. A-11039, R37116). Next, muscles were washed for 1 hour at RT with 6 changes of PBS-Tween and teased out into single fibres for EDL and soleus. All samples were mounted using SlowFade™ Diamond Antifade Mountant (Thermo Fisher Scientific; Cat. No. S36963) and No. 1.0 glass coverslips sealed with nail varnish.

Fluorescence was observed with a Zeiss LSM 780 Upright confocal microscope and images were captured with ZEN 2.3 LSM software. For all samples belonging to the same study, identical settings were used (such as: laser power, gain, offset, magnification, image resolution,

scan speed, z-stack interval, etc.). Seven to ten z-stacks with 1.44 μm steps from each animal were acquired using both a 10x and a 25x oil objective. Sections were chosen randomly around regions with lots of nerve boutons capturing as many NMJs as possible and each image was an average of 4 scans. Images were quantitatively analysed in a blinded fashion using Fiji. Single images of the maximum intensity projections were generated by collapsing respective z-stacks.

In images of NMJs obtained during experiments of AChR-deficiency mice, a minimum of 10 AChR-stained endplates per 10x microscopic field were counted. Using an semi-automated custom macro with the Fiji software, the area of AChR stained clusters was analysed (**Appendix 1.6**). A mask and a binary image were generated to account for the background noise and endplates were selected by surrounding their area with a freehand shape. Area was analysed using the Analyse Particle tool and contrast and brightness were adjusted for maximal visualization of AChR-stained NMJs without altering the data of the image. A minimum intensity threshold was applied. This was carried out for DOK7-AAV gene therapy treated mice in comparison to untreated mice for EDL, soleus and diaphragm muscles. The percentage of enlarged synapses for each muscle was taken as an indicator of the transduction efficiency.

For images of NMJs obtained during experiments of DOK7-CMS mice, the following parameters were recorded: the number of AChR stained NMJs per 25X field, and their area and intensities. A minimum of 5 AChR-stained NMJs per 25x field were counted using a semi-automated macro for the Fiji software as described above. Similarly, 10x magnification images, that cover a larger area of stained tissue, were used to calculate the percentage of enlarges synapses.

The measurements in unit pixels were automatically converted into μm^2 by the ZEN software.

2.2. DNA methods

Chemicals were purchased from Sigma-Aldrich or Promega. Sanger sequencing of plasmid DNA or PCR-amplified product was done in-house at the Sequencing facility provided by the Weatherall Institute of Molecular Medicine (WIMM). Oligonucleotides used for sequencing or to generate PCR products were designed using SnapGene software and synthesized by Invitrogen.

2.2.1. DNA extraction from bacterial cultures

DNA was extracted from bacterial cultures using the QIAprep Spin Miniprep Kit (Qiagen – Cat. No. 27106) for small preparations or PureLink® HiPure Plasmid Filter Maxiprep Kit (Invitrogen ™ - Cat. No. - K2100-17) for larger cultures, according with the manufacturer's protocol.

2.2.2. Polymerase Chain Reaction (PCR)

2.2.2.1. Standard PCR

PCR was performed on Veriti thermal cyclers from Applied Biosystems®. The settings and parameters were optimised for each individual reaction. For a standard PCR reaction MegaMix-Blue (Microzone™) containing recombinant *Taq* polymerase in 1 x reaction buffer with 2.75 mM $MgCl_2$, 220 µM dNTPs (deoxyribonucleotide triphosphates), blue loading dye and stabiliser was used. A typical reaction mixture contains 18 µl of MegaMix-Blue, 2 µl of a primer mix (from a 10 µM stock) and DNA template (10-100ng/µl depending on the quality of

DNA). The parameters for a PCR reaction with the MegaMix-Blue used are shown in **Table 2.3**.

Table 2.3. Thermocycler parameters used for a standard PCR reaction.

Number of cycles	Step	Temperature	Duration MegaMix-Blue/ AccuPrime™ GC-Rich/ PfuUltra II
Step 1 Initial denaturation			
1		95ºC	5 min/ 3 min/ 2min
Step 2 Amplification			
~ 30	Denaturation	95ºC	30 s/30s/20s
	Annealing	Tm- 5ºC	30 s/30s/20s
	Extension	72ºC	1 min/Kb
Step 3 Final extension			
1		72ºC	10 min/10 min/3 min
1	Cooling	4ºC	∞

2.2.2.2. PCR amplification of CG-rich DNA templates

Invitrogen™ AccuPrime™ GC-Rich DNA Polymerase (Thermo Fisher Scientific; Cat. No. - 12346086) was used for the amplification of DNA templates with a high GC content. This is a thermostable DNA polymerase that allows efficient amplification with high accuracy. Typically a 50 µl PCR amplification reaction contained 36 µl of distilled water, 10µl of 5x AccuPrimeTM GC-Rich Buffer A, 1µl of DNA template (100ng/µl), 2µl of primer mix (10µM stock) and 1 µl of AccuPrime™ GC-Rich DNA Polymerase. The cycling parameters for PCR amplification are shown in **Table 2.1.**

2.2.2.3. High-fidelity PCR reactions

PfuUltra II Fusion HS DNA polymerase (Agilent Technoologies; Cat. No. - 600670) was used when high fidelity PCR reactions were performed. A typical 50 µl PCR reaction mix was made of 40.5µl distilled water, 5 µl of 10x *PfuUltra II* reaction buffer, 0.5 µl of dNTP mix (25mM of each dNTP), 1 µl of DNA sample (100ng/µl), 2µl of primer mix (10µM each) and 1 µl of *PfuUltra II* Fusion HD DNA polymerase. Cycling parameters are shown in **Table 2.3**.

2.2.3. Resolution of DNA on agarose gels

Agarose gel electrophoresis was used to resolve DNA fragments. The standard percentage of agarose used was 0.8-1.5% agarose (UltraPure™ agarose; Thermo Fisher Scientific; Cat. No. 16500500) in 1X TBE buffer (90mM Tris base, 90mM boric acid and 2mM EDTA) with UltraPure™ Ethidium Bromide (Thermo Fisher Scientific; Cat. No. – 15585011) at a final concentration of 0.5 µg/ml. Samples of DNA were prepared in a mixture with 5x Loading Buffer Blue (Bioline; Cat. No. - BIO-37045) and electrophoresis was carried out in 1X TBE buffer at 50-90 V. The gels were analysed with a GelDoc-It®2 Imaging system and the VisionWorks® Acquisition and Analysis software (UVP).

2.2.4. DNA extraction from agarose gels

Bands of desired DNA were visualised using a UV transilluminator and excised from the gel with a clean scalpel under a UV transilluminator and DNA was purified using the QIAquick gel extraction kit (Qiagen; Cat. No. - 28706) following the manufacturer's protocol.

2.2.5. General principle of molecular cloning

2.2.5.1. DNA digestion

Digestion of DNA was performed with restriction enzymes that were purchased from New England Biolabs (NEB) and were used according to the manufacturer's protocol.

2.2.5.2. DNA dephosphorylation

When only one restriction enzyme was used to digest a plasmid, the linearized plasmid was dephosphorylated using the Antarctic phosphatase (NEB, Cat. No. -M0289). One reaction mix typically included 1-5 µg of DNA, 1µl of phosphatase, 2 µl of 10x Antarctic Phosphatase Reaction Buffer, and nuclease-free water up to a total volume of 20 µl. The reaction was incubated for 30 minutes at 37°C followed by 2 minutes at 80°C to heat-inactivate the enzyme.

2.2.5.3. DNA ligation

DNA ligations were performed using T4 DNA ligase (Roche; Cat. No. - 10481220001) in a reaction mixture incubated overnight at RT as recommended by the manufacturer, using a 3:1 molar ratio of insert to vector for compatible sticky ends ligation and 5:1 for blunt ends ligation.

2.2.5.4. Plasmids

Plasmids used in this thesis are summarised in **Table 2.4**. Molecular cloning and site-directed mutagenesis were performed on selected plasmids as mentioned below.

Table 2.4 Plasmids used in this thesis.

Plasmid	Description
pGL3-Basic	Expression plasmid that encodes the firefly luciferase gene, a commonly used reporter gene.
pcDNA3.1-DOK7promoter	Expression plasmid containing 1 KB sequence of the DOK7 promoter.
pcDNA3.1-DOK7-Luciferase	Expression plasmid containing 1 KB sequence of the DOK7 promoter, a start codon and the firefly luciferase gene immediately after the start codon → luciferase reporter construct.
pSectagB-ratAgrn	Expression plasmid that encodes C-terminal rat agrin.
pBabe-PURO-DOK7	Retroviral plasmid for the expression of the human DOK7 protein. It contains an internal ribosome entry site (IRES) so that the fluorescent marker (the enhanced green fluorescent protein- EGFP) is also expressed under the same promoter but not tagged to the protein.
pBabe-PURO-DOK7.EGFP	The previously presented retroviral plasmid, containing a sequence to produce an EGFP- tagged version of the human DOK7 protein.
pAAV9-CMV-EGFP	Adeno-associated virus expression plasmid for the AAV9 serotype containing a CMV promoter and the EGFP encoding gene.
pAAV9-CMV-DOK7.EGFP	Previously presented adeno-associated virus expression plasmid containing a gene encoding for an EGFP tagged DOK7 protein.
pBabe-EGFP	Retroviral plasmid used as control (empty retrovirous).

2.2.5.5. pGEM®-T Easy cloning

PCR amplicons were sub-cloned into the pGEM®-T Easy Vector System (Promega; Ast. No. – A1380) following the manufacturer's protocol, to facilitate cloning into the final plasmid. A-tailing was performed on blunt-ended PCR products as pGEM®-T Easy vector supplied in the kit is a linearized plasmid containing a 3' thymidine overhang at both ends. A typical reaction

of A-tailing followed by the insert ligation into the pGEM®-T Easy vector is shown in **Table 2.5**. 2µl of reaction mixture containing the ligated plasmid were transformed into Top10 competent cells. The transformed cells were plated on LB agar plates containing ampicillin (Table), 0.5 mM IPTG (isopropyl ß-D-1-thigalactopyranoside; Sigma, Cat. No.367-93-1) and 80 µg/ml X-Gal (5-bromo-4-choro-3-indoly-ß-galactopyranoside; Sigma, Cat. No. 7240-90-6), and incubated overnight at 37°C. Recombinant clones were picked considering the blue/white screening system, that allows for the rapid detection of a successful cloning via insertional inactivation of the ß-galactasidose enzyme's alpha-peptide region from the vector, with the PCR fragment. White-positive colonies were cultured overnight and the DNA was then extracted and sent for sequencing.

Table 2.5. Typical reactions for pGEM®-T Easy cloning with A-tailing of the insert.

Reaction components	Amount (µl)	Incubation details
A-tailing of PCR products		
DNA (PCR product)	13	72°C for 10 minutes
10x Taq Buffer	2.5	
dATP (2 nM)	2.5	
$MgCl_2$ (50 mM)	0.75	
Taq polymerase	1	
ddH_2O	2.25	
Ligation of PCR insert into pGEM®-T Easy vector		
pGEM®-T Easy vector (50 ng)	1	RT for ~16 hours
A-tailed PCR insert	3/5:1 molar ratio to vector	
2x Ligation buffer	10	
T4 ligase	1	
ddH_2O	Up to 20µl total volume	

2.2.5.6. Site-directed mutagenesis

Site-directed mutagenesis was performed using the QuikChange® Multi Site-Directed Mutagenesis Kit (Agilent Technologies; Cat. No. – 200514) to generate single base substitutions in various plasmids when needed. For each substitution, specifically designed

mutagenic primers having the desired change situated centrally were designed using SnapGene software following the manufacturer's protocol (**Table 2.7**). *PFuTurbo* DNA polymerase was used to generate dsDNA that harbours the desired change. Following, the reaction was incubated with *Dpn*I enzyme for 30 minutes at RT to digest the parental DNA template. *Dpn*I is an endonuclease that cuts specific sequences of methylated and hemi-methylated DNA, and because *dam+ E. coli* strains were used to generate the original plasmids used as templates, they were methylated and thus susceptible to *Dpn*I digestion. The DNA was transformed into either XL1—Gold (provided with the kit) or *Top10* competent cells (Thermo Fisher Scientific; Cat. No. – C404006) that were then cultured on LB agar plates containing the appropriate antibiotic and incubated overnight at 37ºC. Successful mutagenesis was confirmed by sequencing of purified plasmid.

2.2.5.7. Bacterial transformation

Chemically competent *Escherichia coli* (E. coli) bacterial cells used in this thesis are: NEB®10-beta (NEB; Cat. No. C3019I), XL10-Gold® Ultracompetent Cells (Provided with the QuikChange Multi Site-Directed Mutagenesis Kit) and One Shot® TOP10 (Thermo Fisher Scientific; Cat. No. – C404010).

50 µl of competent cells per reaction were thawed on ice for 10 minutes. 10-100 ng of DNA was added and the mix was incubated on ice for a further 20 minutes. Following, the cells were heat shocked at 42ºC for exactly 30 seconds and then incubated on ice for 5 min. Next, lysogeny broth (LB) medium without antibiotic was added to a total volume of 500µl. The cells were then incubated for 1 hour at 37ºC with shaking. Around 100-150 µl cells were cultured on LB agar plates containing the appropriate antibiotic (**Table 2.6)** and incubated

overnight at 37ºC. Plasmid DNA was extracted from bacterial cultures using plasmid miniprep or maxiprep kits.

Table 2.6. Antibiotics used for selection of bacterial cultures.

Antibiotic	Concentration used	Provider
Ampicillin	100 μg/ml	Sigma; Cat. No. A0166

2.2.6. Specific cloning

2.2.6.1. Generation of luciferase reporter construct

A luciferase reporter construct containing approximately 1kb of the human *DOK7* promoter upstream of firefly luciferase was generated to be further used in a luminescence assay for the screening of small compounds. First, firefly luciferase (1653 bp) was PCR amplified from the pGL3-Basic plasmid using *PFuUltra II* Fusion HD DNA polymerase and the primers listed in **Table 2.7**. The PCR product was A-tailed and sub-cloned into the pGEM®-T Easy vector to generate pGEM®-T Easy-Luc.

In order to clone the firefly luciferase into the pcDNA3.1-DOK7promoter plasmid (previously generated by Dr Judith Cossins), an *Age*I restriction site was introduced at the 3' end of the DOK7 promoter by site-directed mutagenesis using the Mutagenesis.AgeI.site.Rv primer. The resulting plasmid, and pGEM®-T Easy-Luc were digested with *Age*I and *Xba*I restriction enzymes and analysed by gel electrophoresis. A 1673 bp DNA band corresponding to firefly luciferase and the 7573 bp linearized vector backbone were excised and purified for subsequent ligation. The ligation was then transformed into *Top10* competent cells and positive clones were confirmed by PCR analysis using the luciferase amplification forward and reverse

primers. One positive clone was picked for DNA purification and ultimately confirmed by DNA sequencing using the same luciferase primers.

Table 2.7. Primers used in the production of luciferase reporter construct.

Target	Primer name	Primer sequence (5' to 3')	Comments
Luciferase gene	Forward_Luciferase	AAATACCGGTATGGA AGACGCCAAAAACATAAAGAAAGG	To include *Age*I restriction site
	Reverse_Luciferase	GACTCTAGAATTACACGGCGATCTTTCC	To include *Xba*I restriction site
Introducing *Age*I restriction enzyme site	Mutagenesis,AgeI.site.Rev	CTCGCCCTTGCTACCGGTCTTCTGTCA	

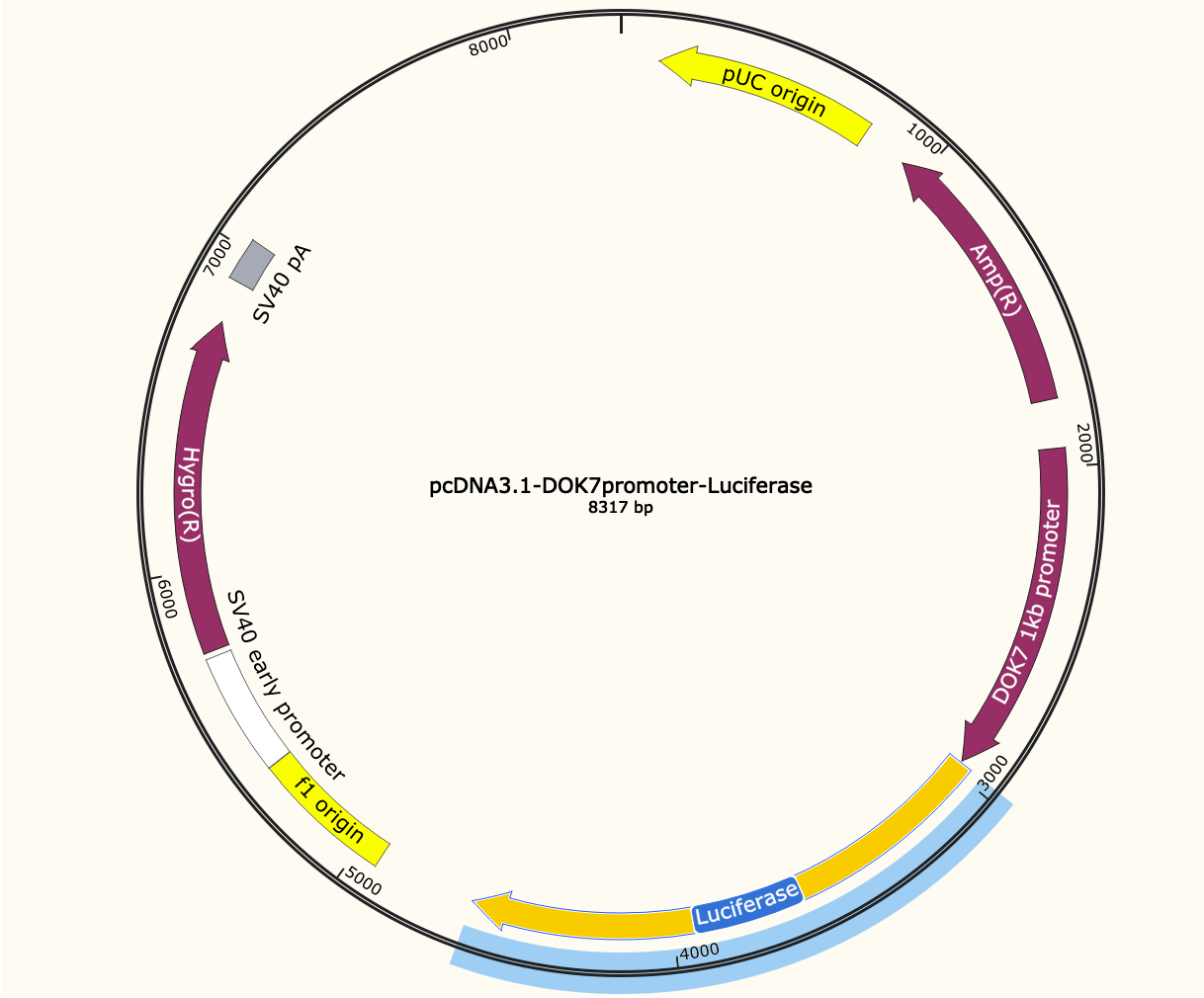

Figure 2.4. Schematic diagram of pcDNA3.1-DOK7promoter. Luciferase sequence was cloned immediately after the 1 kb sequence of the DOK7 promoter to produce a reporter construct.

2.2.6.2. Cloning of DOK7 cDNA into pAAV9-CMV-EGFP plasmid

Human *DOK7* cDNA was PCR amplified from pBabe-PURO-DOK7 vector (previously generated by Dr W. Liu) using AccuPrime™ GC-Rich DNA Polymerase and the primers listed in **Table 2.8**, which include *Asi*SI and *Xho*I restriction enzymes recognition sites. The *DOK7* cDNA amplicon was first ligated into the pGEM®-T Easy vector upon A-tailing and then cloned into the pAAV9-CMV-EGFP plasmid (Vigene Biosciences) via its *Asi*SI and *Xho*I restriction digest sites.

The *Xho*I restriction site within the reverse primer used to amplify the DOK7 cDNA sequence was designed to replace the three nucleotides corresponding to the its stop codon. Thus, in the final plasmid *DOK7* cDNA and EGFP will be transcribed within the same open reading frame, generating an EGFP fluorescently tagged DOK7 protein.

The ligated plasmid was then transformed into *Tpo10* competent cells and the final product, pAAV9-CMV-DOK7.EGFP, was confirmed by diagnostic restriction enzyme digest and then by DNA sequencing using DOK7f4_118, DOK7r1_119, DOK7f8_127, and mid_EGFP.rev primers.

Table 2.8. Primers used in the cloning and sequencing of pAAV9-CMV-DOK7.EGFP construct.

Target	Primer name	Primer sequence (5' to 3')	Comments
DOK7 cDNA	DOK7.cDNA.AsisI. Forward	GCGATCGCAGCCGCCATGAC CGAGGCGGCGCTGGTGGA	To include *Asi*SI restriction site
	DOK7.cDNA.XhoI. Reverse	AAGCTTACTCGAGTGGAGG GGGGTTTACCTT	To include *Xho*I restriction site
Tagged DOK7.EGFP gene	DOK7f4_118	TGCTGGTCTACAAGGACAAG TCGG	Sequencing primer
	DOK7r1_119	GCAATGATGTCCTCGTCTTG	
	DOK7f8_127	AGGCCAGTCACTTGGACGTC A	
	mid_EGFP.rev	AGTTCGAGGGCGACACCCTG GT	

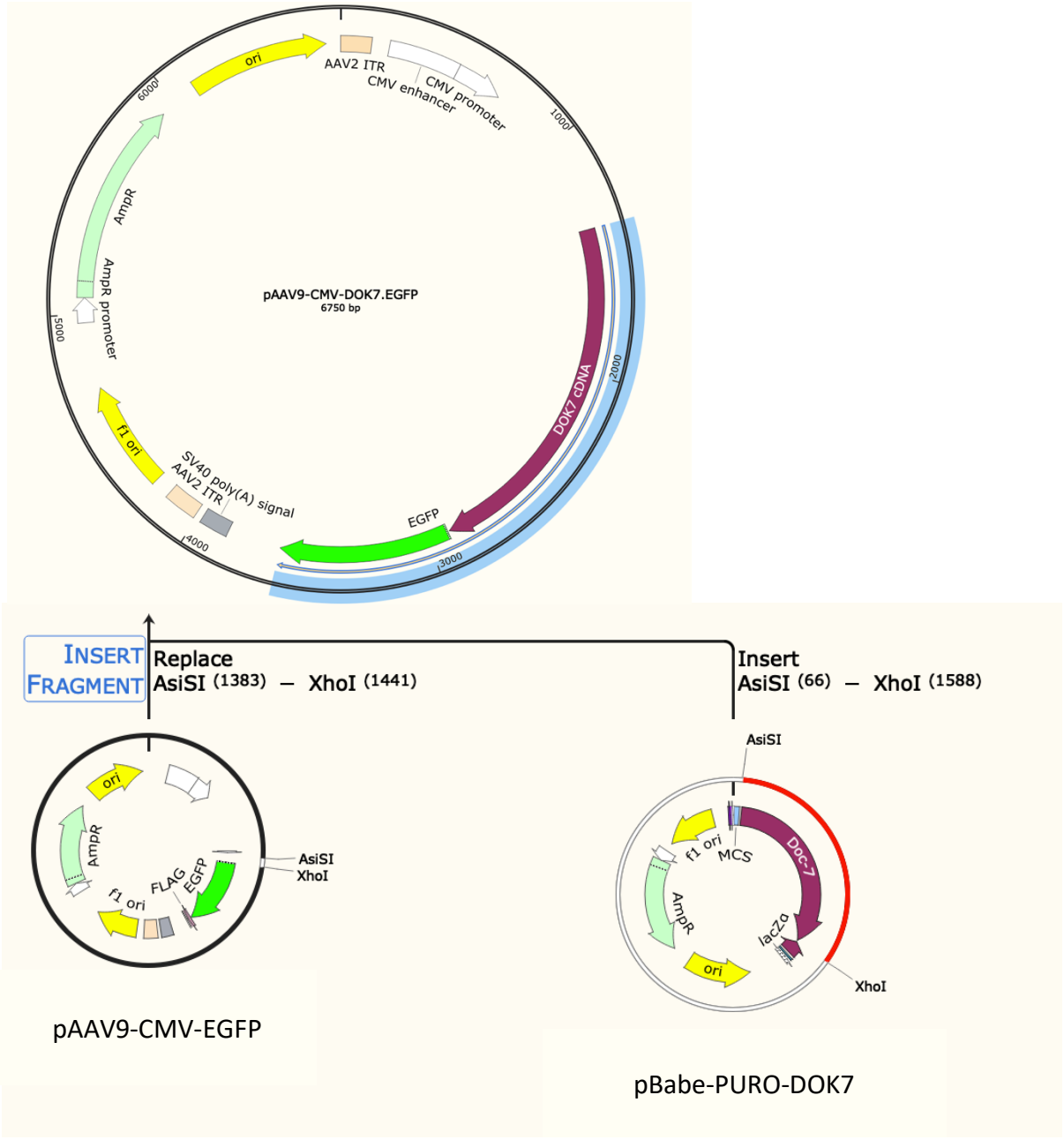

Figure 2.5. Schematic representation of the workflow in generating the pAAV9-CMV-DOK7.EGFP construct. *AsiS*I and *Xho*I restriction sites are shown in both plasmids. DOK7 cDNA sequence was inserted into the final plasmid without a stop codon to generate a fluorescently tagged DOK7 EGFP protein.

2.2.6.3. *Cloning of EGFP tag into pBabe-DOK7-cDNA plasmid*

The previously generated pAAV9-CMV-DOK7.EGFP plasmid was digested simultaneously with *Xcm*I and *Mfe*I restriction enzymes to generate a 1351 bp insert made of the final 406 bp of the DOK7 cDNA coding sequence tagged with the EGFP sequence. Following, the pBabe-PURO-DOK7 was digested with *Xcm*I and *Ecor*I restriction enzymes to excise out the same 406 bp sequence of the DOK7 cDNA.

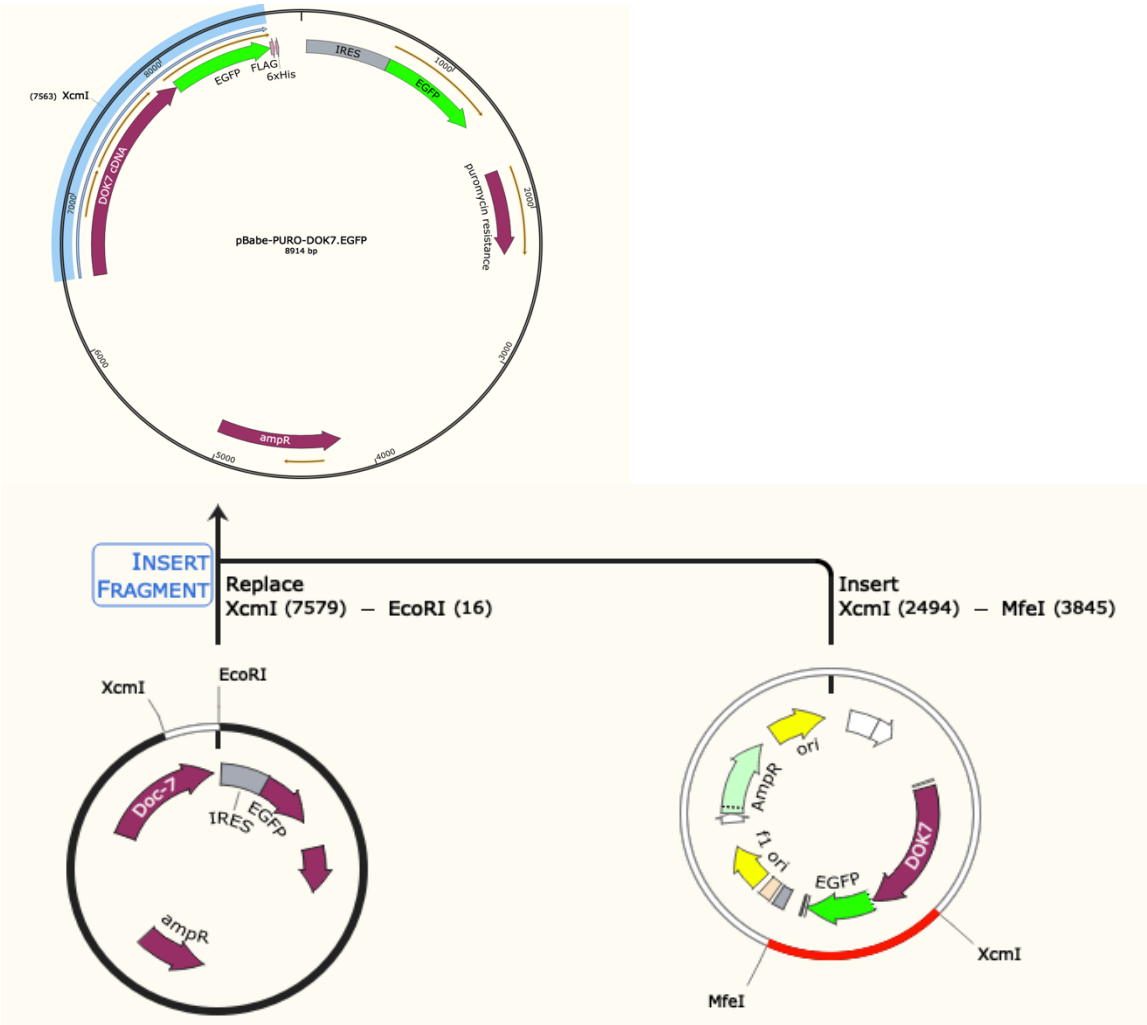

Figure 2.6. Molecular cloning workflow for generating pBabe-PURO-DOK7.EGFP. A 1351 bp sequence (red) was inserted into the final plasmid via *Xcm*I and the compatible *Mfe*I and *Ecor*I restriction enzymes sites.

Both plasmids were then analysed by electrophoresis and the correct bands were excised and gel-purified for subsequent ligation. The ligation of a 1351bp insert into the 7563bp vector backbone was possible due to the compatible cohesive ends between the two *Mfe*I and *Ecor*I restriction enzymes used at one site, and the same *Xcm*I restriction enzyme used for the other. The reaction products were then transformed into *Top10* competent cells and 10 clones were chosen and grown overnight at 37ºC. The correct sequence of the pBabe-PURO-DOK7.EGFP was confirmed first by diagnostic PCR using DOK7f8_127 and mid_EGFP.rev (**Table 2.8**) primers and finally by DNA sequencing.

2.3. RNA methods

2.3.1. RNA extraction from mouse muscle tissue

RNA isolation was performed either immediately after sample collection or from samples that were snap-frozen in LN_2 immediately after dissection and stored at -80ºC until further processing.

Total RNA was isolated from tibialis anterior (TA) muscle using TRIzol™ Reagent (Invitrogen). Between 50-100 mg of tissue was homogenized at 4ºC in 1 ml/sample of ice-cold reagent using Precellys® 24 system from Bertin Instruments (VWR) at 6000 rpm using a 30-5 seconds program twice. Samples were than centrifuged for 5 minutes at 12000 x g at 4ºC to remove fats and cell debris, and the clear supernatant was transferred to a new tube. In order to permit the complete dissociation of the nucleoprotein complex, samples were further incubated for 5 minutes at RT. 0.2 ml of Chloroform per 1 ml of TRIzol™ Reagent was added to each tube. Samples were vortexed for 15 seconds, incubated for 2-3 minutes and centrifuged for 15 minutes at 12000 x g at 4ºC. At this stage, the mixture segregated into two layers separated by an interphase: a lower red phenol-chloroform layer and a colourless upper aqueous phase that contained the RNA. To precipitate the RNA, 0.5 ml of isopropanol per 1 ml of TRIzol™ Reagent was added and samples were mixed and incubated for 10 minutes at RT, followed by centrifugation at 12000 x g at 4ºC. The supernatant was discarded and the total RNA pellet was washed in 1 ml of 75% ethanol by a brief vortex of the tube followed by centrifugation at 7500 x g and 4ºC. Next, the supernatant was removed and the RNA pellet was left to airdry for 5-10 minutes. To solubilize the RNA, the pellet was then resuspended in 20 µl of RNase-free water and incubated in a heat block at 55ºC for 10 minutes. Once dissolved

or after the approximatively 10 minutes, RNA concentration was measured using a NanoDrop™ 2000 Spectrophotometer (Thermo Fisher Scientific). To determine sample purity, the A260/280 and 260/230 ratios were calculated providing that absorbance at 260 nm provides total nucleic acid content.

2.3.2. DNA removal from RNA preparations

TURBO DNA-free™ (Ambion Life Technologies; Cat. No. AM1907) procedure was next used to remove traces of contaminating DNA from the RNA preparations. To each RNA sample 0.1 volume of 10x TURBO DNase Buffer and 1 µl of TURBO DNase was added. The samples were then mixed gently and incubated at 37°C for 30 minutes. 2µl of DNase Inactivation Reagent was then added which was followed by a 5 minutes incubation at RT with occasional mixing. Finally, the samples were centrifuged at 10000 x g for 1.5 minutes and the supernatant containing the RNA was transferred to a fresh tube.

2.3.3. Reverse-transcription

Reverse transcription was performed using High-Capacity RNA-to-cDNA™ Kit (Thermo Fisher Scientific; Cat. No. 4387406). Reaction mixtures of 20 µl volume were prepared as follows: 10 µl of 2x RT Buffer Mix, 1µl of 20x RT Enzyme Mix, 2µg of RNA sample (up to 9 µl) and the required quantity of Nuclease-free H_2O for each sample to reach 20 µl. Each round of experiments were designed to have two control samples: one containing no RNA and a different one containing RNA but no RT Enzyme Mix. The samples were incubated at 37°C for 1 hour followed by 5 minutes at 95°C in a Verti thermocycler. The cDNA was then stored at -20°C until further use.

2.3.4. Quantitative real-time polymerase chain reaction

Quantitative real-time polymerase chain reaction (qRT-PCR) was performed using TaqMan Gene Expression Master Mix and TaqMan Expression Assays specific for the genes of interest (**Table 2.9**) following the manufacturer's protocol. Reactions were performed in technical duplicates in MicroAmp™ Fast Optical 96-well plates (Thermo Fisher Scientific – Cat. No. 4346907) covered with MicroAmp™ Optical Adhesive Film (Thermo Fisher Scientific – Cat. No. 4311971). Plates were handled and prepared with minimum light, and each reaction contained TaqMan® Gene Expression Assay, TaqMan® Gene Expression Master Mix, 100 ng of cDNA template and RNase-free water in a 10 μl/reaction. For each individual gene tested, a no RNA template control (NTC) was prepared to rule out any reagent contamination or primer-dimer formation, but also a no reverse transcriptase control (NRT) was used to exclude genomic DNA contamination. *Hprt1* (encoding Hypoxanthine-guanine phosphoribos yltransferase) was used as an endogenous control gene for mouse muscle tissue and ultimately qPCR was performed in a 96-well plate format using the QuantStudio™ 7 Flex Real-Time PCR system (Thermo Fisher Scientific) and its associated software.

Table 2.9. List of TaqMan® Gene Expression Assays (Applied Biosystems)

Protein	Species	Gene	Assay code
Hypoxanthine-guanine phosphoribosyltransferase	Mouse	*Hprt1*	Mm01324427_m1
Acetylcholine receptor gamma subunit	Mouse	*Chrng*	Mm00437419_m1
Acetylcholine receptor epsilon subunit	Mouse	*Chrne*	Mm00437411_m1
Acetylcholine receptor alpha-1 subunit	Mouse	*Chrna1*	Mm00431629_m1
Muscle-specific kinase	Mouse	*Musk*	Mm01346929_m1
Downstream of tyrosine kinase 7 (mouse)	Mouse	*Dok7*	Mm00554697_m1
Downstream of tyrosine kinase 7 (human)	Human	*DOK7*	Hs00543534_m1

Differences in gene expression between wild-type mice and DOK7-AAV gene therapy treated mice, were analysed using the comparative Ct (cycle threshold) method for relative quantification (Schmittgen and Livak 2008). ΔCt was the Ct measurement for the gene of interest normalised to the Ct value of *Hprt1,* the internal control housekeeping gene (Kozera and Rapacz 2013). ΔΔCt was used to compare the fold difference in gene expression between DOK7-AAV gene therapy treated and control (EGFP-AAV) mice after normalisation. This was calculated as 2 to the power of – ΔΔCt as follows:

$$2^{-\Delta\Delta Ct} = [(Ct_{\text{gene of interest}} - Ct_{\text{housekeeping gene}})\text{DOK7-AAV} - (Ct_{\text{gene of interest}} - Ct_{\text{housekeeping gene}})\text{EGFP-AAV}]$$

2.3.5. RNA sequencing

Total RNA was extracted from previously dissected and snap-frozen TA mouse muscles as described in **Section 2.3.1**, and contaminant DNA was digested in each sample (**Section 2.3.2**). RNA concentration was measured using a NanoDrop™ 2000 Spectrophotometer (Thermo Fisher Scientific). To determine sample purity, the A260/A280 and A260/A230 ratios were calculated considering that absorbance at 260 nm provides total nucleic acid content. For samples with ratios below 2, RNA was considered pure enough to be further processed. RNA integrity was further analysed using the automated electrophoresis platform Agilent RNA ScreenTape System (Agilent 2200 TapeStation; Agilent Technologies) following the manufacturer's protocol. In brief, all reagents were allowed to equilibrate at RT for 30 minutes. Samples were then prepared in new tubes containing 1.5 µl RNA Sample Buffer with 1.5 µl RNA Sample. A reaction containing an RNA Ladder was also prepared. The tubes were heated at 72°C for 3 minutes, placed on ice for 2 minutes, and then loaded into the 2200 TapeStation instrument. Reactions with an RIN^{e} (RNA integrity number) value higher than 6 were sent to Novogene for library preparation and RNA sequencing.

Samples were sequenced using 150 base-pair reads, paired-end RNA-sequencing technology (Q30≥80% PE150; Illumina HiSeq 2000, Illumina, San Diego, CA), and data was analysed as follows. The Ilumina sequence reads FASTQ files were aligned against the mouse genome mm10 using the Spliced Transcripts Alignment to a Reference (STAR) software (Dobin et al. 2013). Reads were counted using the featureCounts module on the output SAM (Sequence Alignment Map) files. The expression level of transcripts can be measured by the number of reads that map to the transcript. Data was then arranged in descending order considering -log(p value) values, meaning that the list will start with the gene that has the smallest *p* value. Analysis of 40 differentially expressed genes was done by plotting the log(Fold Change) values

against the negative log(p value) using a volcano plot. The significance threshold was set at a p value of 0.05. Variations in gene expression were compared between DOK7-AAV gene therapy treated mice and the control group (EGFP-AAV) form 3 mice per treatment group, and significantly upregulated or downregulated genes were color-coded on the volcano plot.

2.4. Protein analysis methods

2.4.1. Protein extraction from cell cultures

C2C12 cells previously cultured in 6, 24 or 96-well culture plates were trypsinised (**Section 2.5**) and washed with PBS and resuspended in 100-500 µl of lysis buffer (10 mM Tris, 100 mM NaCl, 1 mM EDTA, 1%Triton X-100, pH 7.4) supplemented with Protease inhibitor cocktail (Sigma – Cat No. P8340) used at 1:100 dilution. The cells were incubated for 1 hour at 4°C with gentle rotation, and then centrifuged at 13000 rpm for 10 minutes at 4°C. The supernatant was transferred into a new tube and used in further experiments or stored at -20°C until further use.

2.4.2. Protein extraction from mouse tissue

Mouse muscle tissue (TA, EDL or heart) that was previously dissected and snap-frozen in LN_2, was transferred on ice into 2 ml tubes containing steel beads (Precellys® Steel kit 2,8 mm; VWR – Cat No.432-0364). 250 µl of ice-cold lysis buffer (10 mM Tris, 100 mM NaCl, 1 mM EDTA, 1%Triton X-100, pH 7.4) containing 1:100 Protease inhibitor cocktail (Sigma – Cat No. P8340) was added in each sample tube. The tissue was next homogenized using the Precellys® 24 system from Bertin instruments (VWR – Cat. No. 432-3750) at 6000 rpm using 30-5 seconds program twice. The samples were then incubated for 2-3 hours at 4°C rotating, transferred into new tubes without the beads and centrifuged at 13000 rpm for 10 minutes at 4°C to. The supernatant was then collected and used in subsequent experiments or stored at -20°C for further experiments.

2.4.3. DOK7 Immunoprecipitation assay

Mouse tissue was previously dissected and processed to extract proteins as described in **Section 2.4.2**. Dynabeads™ Protein G (Thermo Fisher Scientific – Cat. No. 10003D) magnetic beads were used to separate Dok7 from a tissue lysate. For each sample, 50 µl of previously resuspended beads was transferred into a tube for each sample and placed in a magnet rack. 2 washes in PBS were followed by one-hour incubation of the beads with 5 µg of mouse monoclonal DOK7 antibody (diluted in PBST) at 4°C with rotation. PBST was discarded and previously thawed or freshly centrifuged tissue lysate was added to the beads and incubated overnight at 4°C with rotation. The following day the beads were washed 2 times in lysis buffer (washes were kept at -20°C).

4x NuPAGE™ LDS Sample Buffer (Thermo Fisher Scientific – Cat. No. NP0007) and 10x NuPAGE™ sample reducing agent (Thermo Fisher Scientific – Cat. No. NP0004) together with lysis buffer were added to the samples up to a total volume of 45 µl. From each sample two aliquots were made, one to be stored at -20°C and one heated at 95°C for 10 minutes.

For protein samples that were to be analysed using western blotting (not including samples for immunoprecipitation), protein concentration was determined using the colorimetric Pierce™ BCA Protein assay Kit (Thermo Fisher Scientific – 23225) according to the manufacturer's protocol. Samples within the same experiment were adjusted to contain equal amounts of protein, with no more than 50 µg of total protein/ sample.

Protein samples were then subjected to SDS-PAGE electrophoresis, transferred to nitrocellulose membrane transferring and analysed (**Section 2.4.4**). Densitometry of bands was analysed with Fiji software.

2.4.4. Sodium dodecyl sulphate-polyacrylamide gel electrophoresis and western blotting

Samples were denatured at 95ºC for 5-10 minutes in 4x NuPAGE™ LDS Sample Buffer (Thermo Fisher Scientific – Cat. No. NP0007) and 10x NuPAGE™ sample reducing agent (Thermo Fisher Scientific – Cat. No. NP0004). Denatured samples were then loaded into 10, 12 or 15 wells NuPAGE™ 4-12% Bis-Tris protein gels (1.0 mm; Thermo Fisher Scientific – Cat. No. NP0321, NP0322, NP0323), together with the SeeBlue™ Plus2 Pre-stained Protein Standard marker (Thermo Fisher Scientific – Cat. No. LC5925) and resolved by Sodium dodecyl sulphate-polyacrylamide gel electrophoresis (SDS-PAGE). The gels were run in 1x NuPAGE™ MOPS SDS Running Buffer (Thermo Fisher Scientific – Cat. No. NP0001) at 150V using a XCell *SureLock*™ Mini-Cell Electrophoresis System (Thermo Fisher Scientific – Cat. No. EI001). Following, the proteins were electro-transferred at 30V for at least 2 hours onto nitrocellulose membranes (0.45 μm; Thermo fisher Scientific; Cat. No. 88018). The transfer was carried out at RT in 1x NuPAGE™ Transfer Buffer (Thermo Fisher Scientific – Cat. No. NP0006) containing 10% Methanol absolute using an XCell *SureLock*™ XCell II™ Blot Module (Thermo Fisher Scientific – Cat. No. EI002). To avoid non-specific binding of antibodies, the membranes were blocked for 1 hour at RT with 5% Marvel Dried Skimmed Milk Powder in PBST (Phosphate Buffer Saline with 0.1% Tween®20). Next, the membranes were incubated with a primary antibody followed by a horseradish peroxidase (HRP)-conjugated secondary antibody, both diluted to reach desired concentrations in 1% Marvel Dried Skimmed Milk Powder in PBST. Each antibody incubation was carried out at RT for 1

hour and was followed by 30 minutes of PBST washing with 3 changes of buffer. **Table 2.10** provides a summary of the antibodies used and, host species, dilution and provider.

Table 2.10. Primary and secondary antibodies used for western blotting.

Primary antibody			
Antigen	**Clone**	**Dilution**	**Provider**
α-tubulin	Mouse monoclonal	1:10000	Sigma T5168
DOK7	Mouse monoclonal	1:250	Sc-390856
EGFP	Mouse monoclonal	1:1000	Ab184601
HRP-conjugated Secondary antibody			
Antigen	**Clone**	**Dilution**	**Provider**
Mouse IgG	Goat polyclonal	1:1000	Dako P0447
Mouse IgG (preferentially for non-reduced form of mouse IgG)	Rat	1:1000	ab131368

Amersham™ ECL™ (enhanced chemiluminescence) or Amersham™ ECL™ Prime reagents (Cytiva– Cat. No. RPN2106, RPN2232) were used to detect the HRP-conjugated bound antibodies by exposing the membranes to autoradiography films (SLS – Cat. No. MOL7016). For the detection of a second different protein on the same blot, the blot was incubated with

harsh stripping buffer (20 ml SDS 10% SDS), 12.5 ml Tris HL pH 6.8 0.5 M, 67.5 ml H_2O and 0.8 ml of β-mercaptoethanol), washed thoroughly in water for two hours and then blocked and re-probed with desired primary and secondary antibodies.

Images of the developed films were acquired using the GelDoc-It2 310 imaging system and its associated VisionWorks®LS image acquisition software (UVP). To quantify the relative intensities of the protein bands, densitometry analysis was performed using Fiji software. The whole process of protein denaturation, gel electrophoresis and electro-transfer of proteins on a membrane to finally visualize them separated is referred to as western blotting.

2.5. Cell culture methods

The cell lines used in this thesis were cultured in Corning tissue culture plasticware in Dulbecco's modified Eagle medium (DMEM; Sigma-Aldrich) supplemented with 1% of antibiotic-antimycotic solution (PSA-Penicillin, Streptomycin and Amphotericin; Gibco) and various amounts of foetal calf serum (FCS) (PAA Cell Culture Ltd) as shown in **Table 2.11**. Cells were usually passaged at the desired dilution every 2-4 days.

To passage cells, the existing media was removed by aspiration and cells were washed, once, with a sufficient volume of PBS to cover the flask, prior to adding a covering volume of trypsin (1ml / T25cm^2, 2ml / T75 cm^2, 5ml / T175cm^2) with short incubation at 37°C. Once the cells were fully detached, the trypsin solution was neutralised by addition of fresh culture medium, the cell suspension was diluted at the desired fraction in fresh culture medium and re-plated into a new culture flask or plate. For all cell culture-based experiments described below, cells in suspension were stained with 0.4% Trypan Blue and counted using a Countess automated cell counter system

To maintain stocks of cell lines, cells were frozen and stored in -80°C or liquid nitrogen. Initially, cells were detached as described above, resuspended in fresh culture medium, and centrifuged at 1,500 rpm for 5 minutes. The resulting cell pellet was resuspended in cell freezing medium (FCS+10 DMSO) and was aliquoted in CryoTube vials. Vials were frozen at -80°C for short term storage, after which they were transferred to liquid nitrogen for long term storage.

As shown in **Table 2.11**, for the C2C12 cells to differentiate into myotubes, the medium was changed to contain a lower percentage of FCS upon reaching 100% confluency. The fusion medium was refreshed every day for at least 5 days or until mature myotubes were formed.

Table 2.11. Cell lines used in this thesis and their growth conditions

Growth conditions			
Cell lines		DMEM +1% PSA supplemented with	Incubation conditions:
C2C12 (Mouse muscle cells)	Myoblasts	15% FCS	37° C 5-10% CO_2 95%humidity
	Myotubes	2% FCS + 10% HS* (fusion/differentiation medium)	
HEK 293 T cells (Human embryonic Kidney cells)		10% FCS	
Phoenix™ -ECO cells		10% FCS	
*HS- horse serum (Sigma) C2C12 and Phoenix cells were purchased from ATCC, HEK293 T cells were purchased from ECACC			

2.5.1. Transfection methods

2.5.1.1. Polyethylenimine (PEI) transfections

HEK 293T ($3x10^5$ cells/well of a 6-well plate) were transiently transfected with desired DNA plasmids using PEI (linear MW 25,000 Da) (prepared as 45mg PEI in 8ml distilled water, pH 7.2) in transfection mixtures containing 3 µg of DNA, 1.25 µl of 20% glucose (in H_2O), 1.5 µl PEI and H_2O up to 7.5 µl. 12 to 16 hours post-transfection, the transfection mixtures were replaced by fresh culture medium and the cells were cultured until subsequent procedures.

2.5.2. Generation of recombinant agrin

Inducing the formation of AChR clusters on the surface of mature C2C12 myotubes upon incubation with agrin is one way of modelling a synaptic structure *in vivo*. To produce recombinant agrin, HEK 293T cells were grown in a T175 flask to 90% confluency. A transfection mix containing PEI (**Section 2.5.1**) was then added onto their growth medium. The DNA construct was designed to express a soluble c-terminal splice form of rat neural agrin that lacks the heparin binding site thus preventing the molecule from attaching to the extracellular matrix. The construct was kindly donated to our group by Dr Werner Hoch (Ferns et al. 1993).

After 24 hours, the medium was replaced with HEK cells growth medium and after incubation for a further 48 hours, the medium was collected, centrifuged at 2000 rpm for 10 minutes at RT and the supernatant was aliquoted and stored at -20°C. Before using recombinant agrin in further experiments, a titration was performed to determine the most efficient concentration in generating AChR clusters on C2C12 myotubes.

2.5.3. *Agrin-induced AChR clustering*

To induce the formation of AChR clusters, mature C2C12 myotubes were either incubated overnight with recombinant agrin (produced as described above) or were transfected (**Section 2.5.1**) to overexpress DOK7. The following day, myotubes were incubated with α-bungarotoxin conjugated to Alexa Fluor 594 at 1:1000 dilution in differentiation medium for one hour at 37ºC. The toxin was washed away three times with differentiation medium and cells were then then fixed for 20 minutes in 3% PFA in differentiation medium at 37ºC. Finally, to wash the phenol red from the medium, the cells were washed and stored in Phosphate Buffer Saline (PBS) at 4ºC until further imaging.

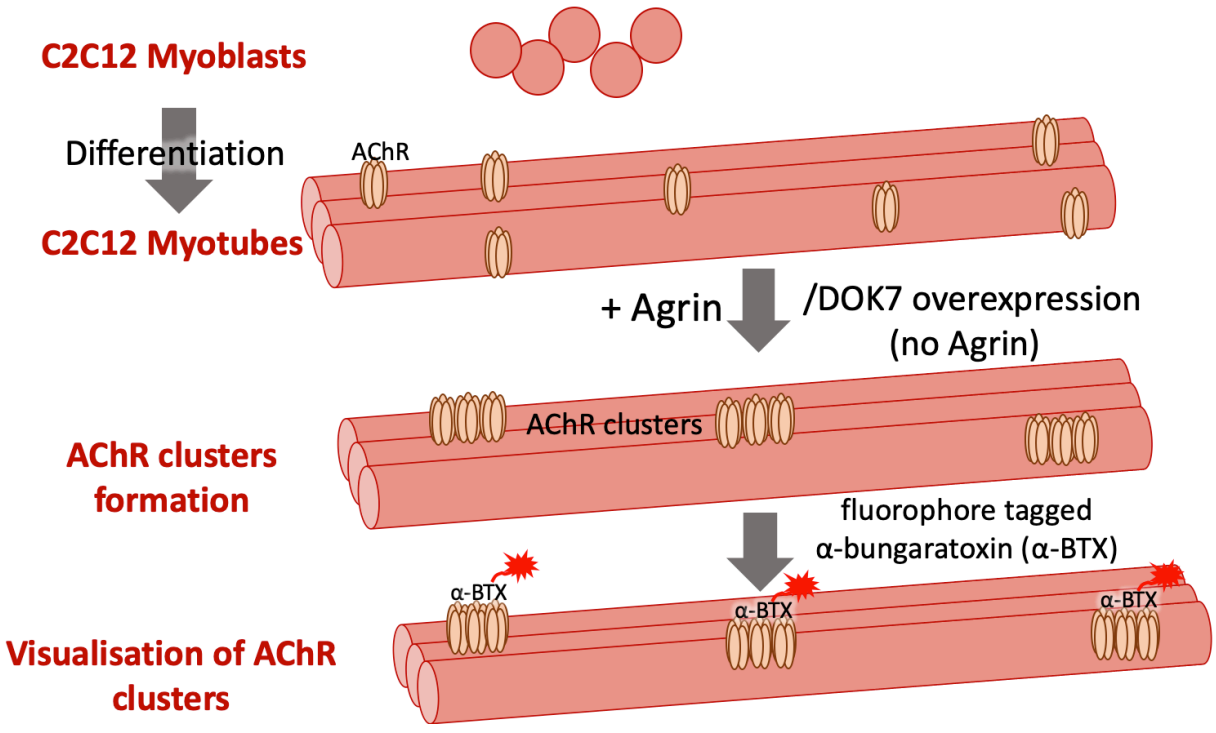

Figure 2.7. Schematic representation of AChR clustering assay. C2C12 myoblasts were differentiated into myotubes and either incubated with Agrin overnight or stained with fluorescently labelled α-bungaratoxin directly for DOK7 overexpressing myotubes. AChR clusters were visualised using a fluorescence microscope.

10 to 20 images (from 2 to 3 wells) at 20x magnification per condition were acquired using an IX71 Olympus microscope (and Simple PCI software) using the same settings within an experiment. The number of AChR clusters per field was counted either manually or by using an automated macro designed for the Fiji software by a previous student in the lab (**Figure 2.8**). Calibration values of the Hamamatsu camera at desired magnifications were used to convert pixels to μm^2 (3.12pixels/μm for 20x).

```
title = getTitle();
run("Colors...", "foreground=black background=white selection=yellow");
roiManager("reset");
run("Set Scale...", "distance=312 known=100 pixel=1 unit=um");
run("8-bit");
run("Duplicate...", "title=image-2");
run("Duplicate...", "title=image-1");
run("Gaussian Blur...", "sigma=x");
imageCalculator("Subtract create", "image-2","image-1");
setThreshold(x, 255);
run("Convert to Mask");
run("Analyze Particles...", "size=2.5-Infinity circularity=0.00-1.00 show=[Overlay
Outlines] display summarize add");
selectWindow("image-2");
roiManager ("Show All");
roiManager ("Measure");
run("Flatten");
```

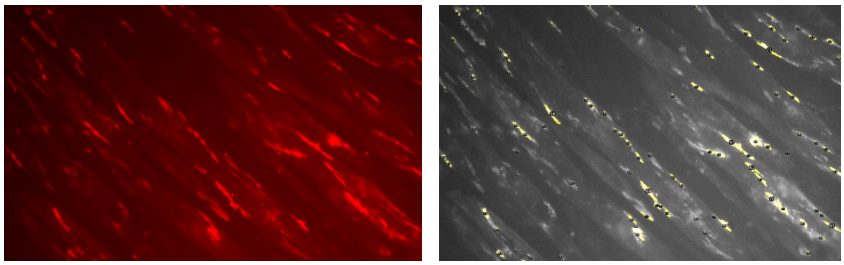

α-BTX Automated software

Figure 2.8. Macro used for the analysis of the number of AChR clustered on cultured myotubes. The shown macro was used in Fiji to perform the analysis. Gaussian blur and threshold values marked in here by x were optimised for each individual experiment (α-BTX—α-bungaratoxin).

2.5.4. Generation of C2C12 reporter stable cell line to be used in the screening of compounds

C2C12 were transfected by electroporation with the DOK7-Luciferase construct. To generate stable cell lines from single clones, the cells were seeded at a concentration of one third of a cell/well in a 96-well plate. Approximatively 45 single clones were grown for 1.5-3 weeks, but only 16 clones were able to differentiate from myoblasts to myotubes.

The luciferase reporter assay (**Section 2.5.5**) was performed on both myoblasts and myotubes. The natural upregulation of DOK7 that occurs when C2C12 differentiate from myoblasts into myotubes was used as a positive control. The clone with the highest increase in Luciferase expression level from myoblasts to myotubes was chosen for further experiments.

2.5.5. The luciferase reporter assay

ONE-Glo™ Luciferase Assay System (Promega; Cat. No. - E6110) was used to detect firefly luciferase reporter gene expression under various conditions in C2C12 cells following the manufacturer's protocol. In brief, the ONE-Glo™ Luciferase Assay Buffer was added onto the ONE-Glo™ Luciferase Assay lyophilized substrate. C2C12 cells were incubated for 5 minutes in the dark with a lysing solution of 1:1 growth medium to ONE-Glo™ Luciferase Assay Buffer. Cells were then transferred into white opaque 96-well microplates OptiPlate-96 (PerkinElmer; Cat. No. – 6005290), and the luminescence was detected using a GloMax®-Multi Detection System (Promega).

2.5.6. The screening of small-molecule compounds

5431 small-molecule compounds were provided by the Department of Chemistry at the University of Oxford. The compounds were provided in DMSO (Dimethyl sulfoxide) at a final concentration of 10 mM and stored at 4°C (or at -20°C for long term storage). Before being added to the cells, the compounds were equilibrated at RT with gentle shaking for 10 minutes.

DOK7.promoter-luciferase stable C2C12 cells (**Section 2.5.4**) were seeded in 96-well plates at a density of 4x10^{4} cells/well. Upon reaching 90% confluency, medium was changed to differentiate the cells for 5-8 days or until mature myotubes were formed. Cells were then incubated overnight with the compounds at a final concentration of 100 μM in growth medium. The following day, the cells were assayed for increased luciferase expression using the ONE-Glo™ Luciferase Assay System (**Section 2.5.**5). Each 96-well plate included a column of cells incubated with vehicle control. The data was represented as the fold increase in Luciferase intensity normalised to the mean vehicle control (taken from 8 wells/plate) for each plate.

Based on the above luciferase reporter results, 37 compounds were chosen to be tested for their ability to induce AChR clusters on C2C12 myotubes. 100 μM of each compound was used for this assay, and agrin was used as a positive control (**Section 2.5.3**). Background was subtracted (cells incubated with DMEM) and data was normalised to the vehicle control (cells incubated with DMSO and growth medium). Dose/response curves were generated in both cases.

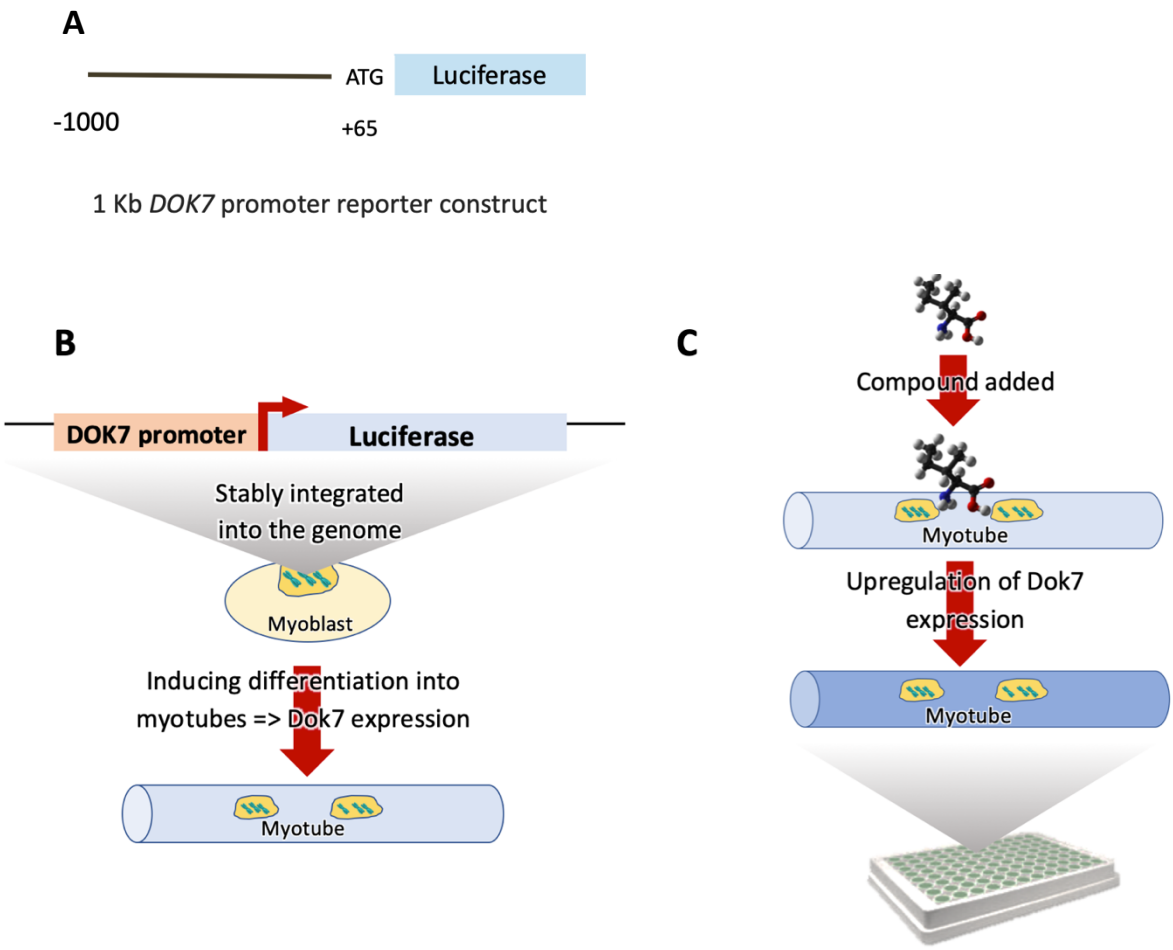

Figure 2.9. Schematic representation of luciferase reporter assay design for the screening of small-molecule compounds. A 1 kb DOK7 promoter (-1000bp) construct was designed to contain the sequence of luciferase immediately after the ATG start codon (**A**). The construct was stably integrated into the genome of C2C12 myoblasts (**B**), and the natural upregulation in the expression of DOK7 protein upon differentiation of C2C12 myoblasts into myotubes was used as a baseline control for the screening of compounds. Compounds that generated at least a 2-fold increase in DOK7 protein expression on top of the baseline control were investigated further (**C**). ATG +65 represents the position of the start codon.

2.5.7. pBabe retroviral system

Phoenix™ -ECO cells were used along with the pBabe retroviral expression vector system to generate retrovirus subsequently used to infect C2C12 myoblasts. $2x10^6$ Phoenix™ -ECO were seeded in one Corning® T25 tissue culture flask per condition. The following day the cells were PEI-transfected with 10 μg of desired DNA plasmid: pBabe-PURO-DOK7, pBabe-PURO-DOK7-EGFP or pBabe-EGFP which was used as a control (empty vector). The cells were cultured in normal growth medium, and after 72 hours the medium was harvested, centrifuged (1200rpm for 5 minutes) to remove the cell debris, and stored in aliquots at -80ºC until further use.

To infect C2C12 cells with the desired retrovirus, $5x10^4$ cells were seeded in a Corning® T25 tissue culture flask for each condition. The following day, the cells were incubated with 1 ml of retrovirus-containing medium supplemented with 1μM of polybrene (Sigma-Aldrich) at 37ºC overnight. The next morning, the medium was replaced with growth medium and the cells were transferred to a Corning® T75 flask. 48 hours after infection, the growth medium was supplemented with 1% puromycin (5μg/ml) to start cell selection.

2.5.7.1. Using a retroviral system to titrate levels of DOK7 needed to mimic the formation of a synapse in vitro

C2C12 myoblasts previously seeded in 6 individual Corning® T25 tissue culture flasks were infected with increasing percentages of DOK7 using retroviral systems for both pBabe-PURO-DOK7 and pBabe-PURO (empty vector) variants as follows:

0% DOK7 100% empty vector	**20% DOK7** 80% empty vector	**40% DOK7** 60% empty vector	**60% DOK7** 40% empty vector	**80% DOK7** 20% empty vector	**100% DOK7** 0% empty vector

After an approximatively 4 days selection with puromycin, the cells were seeded in 24-well plates. Upon reaching 90% confluency, the medium was replaced with differentiation medium. Myotubes were stained for AChR clusters with fluorescently conjugated α-bungarotoxin (α-BuTx) for an hour, washed three times with PBS, fixed for half an hour in 3% PFA at 37ºC and imaged using an IX71 Olympus microscope and a Hamamatsu camera (20 images taken for each). The number of AChR clusters per field was counted either manually (if high background levels were observed) or by using an automated macro designed for the Fiji software (Reference explication and image). Calibration values of the at desired magnifications were used to convert pixels to μm^2 (3.12pixels/µm for 20x).

2.5.8. Titration of DOK7-AAV (Adeno-associated viral systems)

Large-scale DOK7-AAV packaging was produced by Vigene Biosciences and sent to our laboratory. Prior to using the DOK7-AAV *in vivo*, a titration was performed in C2C12 cells to determine the multiplicity of infection. C2C12 cells were transduced with 10^5, 10^6, and 10^7 viral genomes (vg) per cell, each amount in a well of a 6-well plate. Cells were then grown until 90% confluency was reached and differentiated for 5-8 days. Because the DOK7 was tagged with EGFP, 20 fluorescent images were taken for each titration using an IX71 Olympus microscope and a Hamamatsu camera. The number of positive cells was recorded by manual counting using Fiji software, and the amount of DOK-AAV that gave the highest number of EGFP-positive cells with an insignificant observed cell death was chosen to be used in an AChR clustering assay as described in **Section 2.5.3**.

2.6. Statistical analysis

The required number of animals for each condition of one experiment was decided based on previous experience of performing similar experiments using the same mouse strains and data from the pilot study in wild-type mice (**Chapter 3**). Experimental mice of the same genotype, age and sex were grouped together. The investigators were blinded to the genotypes of the mice during experiments and data analysis.

Graphic design and statistical analysis were performed using Prism 8 (GraphPad Software, La Jolla, California). Specific statistical details and tests used are presented in the figure legends. Levels of statistical significance were set at threshold $p< 0.05$.

If means of only two groups were compared, an unpaired 2-tailed t-test was used. To compare between means of three groups, a one-way Analysis of variance (ANOVA) was used. Two-way ANOVA was used to compare experiments with 2 independent variables (e.g. treatment group and body weight/age/gender). One-way or two-way ANOVA with Dunnett (using saline or negative control as a reference group), or Sidak/Tukey corrections (no reference groups) were used to assess differences at given timepoints with treatment and weight (or age/gender/differentiation stage) as independent variables. Two-way repeated measurements ANOVA with Sidak's correction (to compare between different frequencies) was used to compare percentages of muscle decrement between DOK7-AAV treated or control mice.

For analysis of time to humane endpoint performed in **Chapter 4**, Kaplan Meier curves were computed and a log-rank test was used to compare time to humane endpoint between groups.

In **Chapter 6**, a dose-response curve ([Agonist vs. normalised response] variable slope) was generated to calculate EC_{50} values for the two lead compounds. The response was normalised tot the baseline control, transformed in percentages and represented as log[dose].

2.7. Materials

See Appendix

Chapter 3

Characterization of wild-type mice treated with DOK7-AAV gene therapy

3.1. Introduction

Adeno-associated viruses (AAVs) are a vast collection of naturally replication-deficient parvoviruses which attracted significant interest over the years due to their non-pathogenic nature and ability to persist in tissues for long durations. The AAV vector is a powerful tool that can be used in delivering therapeutic genes to many tissues including skeletal muscles (Bulaklak and Xiao 2017; Aguti et al. 2018; Wang et al. 2019).

AAV-vector mediated gene delivery has been recently approved for the treatment of Spinal muscular atrophy showing therefore strong evidence of its potential for other congenital neuromuscular disorders (C. Li and Samulski 2020).

A critical aspect of translating a recombinant AAV vector into a potential gene therapy treatment is finding an adequate target. While aiming to understand the biology of the DOK7 protein and its function in synaptogenesis, Inoue and colleagues observed that overexpression of DOK7 induced a significant increase in the AChR-positive area in fluorescently labelled diaphragm muscles of mouse embryos (Inoue et al. 2009). A few years later, Arimura and colleagues showed that DOK7 overexpression induced the formation of enlarged neuromuscular junctions (NMJs) in wild-type mice without having detrimental effects on the organism (Arimura et al. 2014). By using an AAV to overexpress DOK7 in skeletal muscles, they showed prolonged survival and enhanced motor activity of DOK7-CMS model mice

carrying the most common patient mutation in the *DOK7* gene (Beeson et al. 2006; Palace et al. 2007; Selcen et al. 2008; Cossins et al. 2012). Using the same treatment, they showed some beneficial effects for enlarged neuromuscular synapses in a mouse model of autosomal Dominant Emery-Dreifuss muscular dystrophy (AD-EDMD) in the same study and in a model of Amyotrophic lateral sclerosis (ALS) a few years later (Miyoshi et al. 2017). Thus, upregulation of the DOK7 protein became a potential therapeutic strategy that goes beyond simple gene replacement for DOK7-CMS patients.

Recently it was demonstrated that enlarged NMJs lead to increased neuromuscular signal transmission and ultrastructural changes of the NMJ in transgenic mice (Eguchi et al. 2020). DOK7 overexpression through DOK7-AAV gene therapy is used later in this thesis in two mouse models of CMS to gain in depth understanding of the technique and its mechanism of action, as well as to better assess its benefits. The aim of this chapter was to further explore NMJ structure and function as well as differential gene expression in muscles of wild-type mice when DOK7 is delivered using an AAV. It was important to carry out these initial experiments because DOK7-AAV was then tested as a potential gene therapy in two mouse models of CMS. Thus, the work outlined in this chapter provides the basis for the studies described in **Chapters 4** and **5**.

3.2. Investigating the effects of an EGFP tag on the ability of DOK7 to induce AChR clusters using a retroviral system

Ahead of the design of a DOK7-AAV construct to be further used *in vitro* and then *in vivo* in wild-type mice and animal models of CMS, a retroviral system was used to investigate the implications of tagging the DOK7 protein. Fusion of fluorescent tags to proteins of interest can reveal a wealth of data including information of its distribution, steady-state, dynamics and association with other proteins (Lippincott-Schwartz et al. 2001; Snapp 2005). Moreover, a protein of interest can be identified in cells and animal tissue without subsequent labelling or purification. Thus, a DOK7 wild-type and DOK7-EGFP tagged constructs were designed and produced, and a retrovirus vector system was used to transduce C2C12 myoblasts. A retrovirus system is an infectious virus used to deliver a non-viral transgenic gene into *in vitro* or *in vivo* mitotic cells (Lech and Somia 2008). This system proved to be the most efficient method to deliver single DNA expression constructs to C2C12 myotubes and generate stably expressing cell lines in our laboratory.

As mentioned in Chapter 1 (**Section 1.6**), overexpression of wild-type DOK7 protein in myotubes induces agrin-independent AChR clustering. C2C12 myoblasts were infected with a retrovirus previously generated to express either the human DOK7 with an EGFP tag at its carboxyl terminus or the untagged human DOK7. An empty retrovirus was used as a negative control. Myoblasts were then differentiated into myotubes over a period of 6-10 days in three wells of a 6 well plate for each construct. When mature myotubes were fully formed, AChR clusters on the membrane of the cells were stained with fluorescently labelled α-bungarotoxin (conjugated to Alexa Fluor 594). α-bungarotoxin is derived from a snake venom (bungarus multicinctus) that specifically binds AChR. Following fixation of myotubes, the cells were imaged using a fluorescence microscope. Representative images of stained AChR clusters for

the two DOK7 harbouring vectors and the negative control are shown in **Figure 3.1C**. Average number of AChR clusters per microscopic field as well as the average size of these clusters were measured from 20 microscopic fields per infection, from three separate infections for each condition. Both DOK7-EGFP and DOK7 robustly stimulated AChR clustering compared with the negative control and there was no significant difference in the number or length of AChR clusters between the DOK7-EGFP and the untagged DOK7 (**Figure 3.1**). AChR cluster size was similar for DOK7 induced clusters and the few clusters generated in the control sample wells.

The data indicate that an EGFP tag at the carboxyl terminus does not interfere with the ability of DOK7 protein to induce the formation of AChR clusters on the surface of C2C12 myotubes.

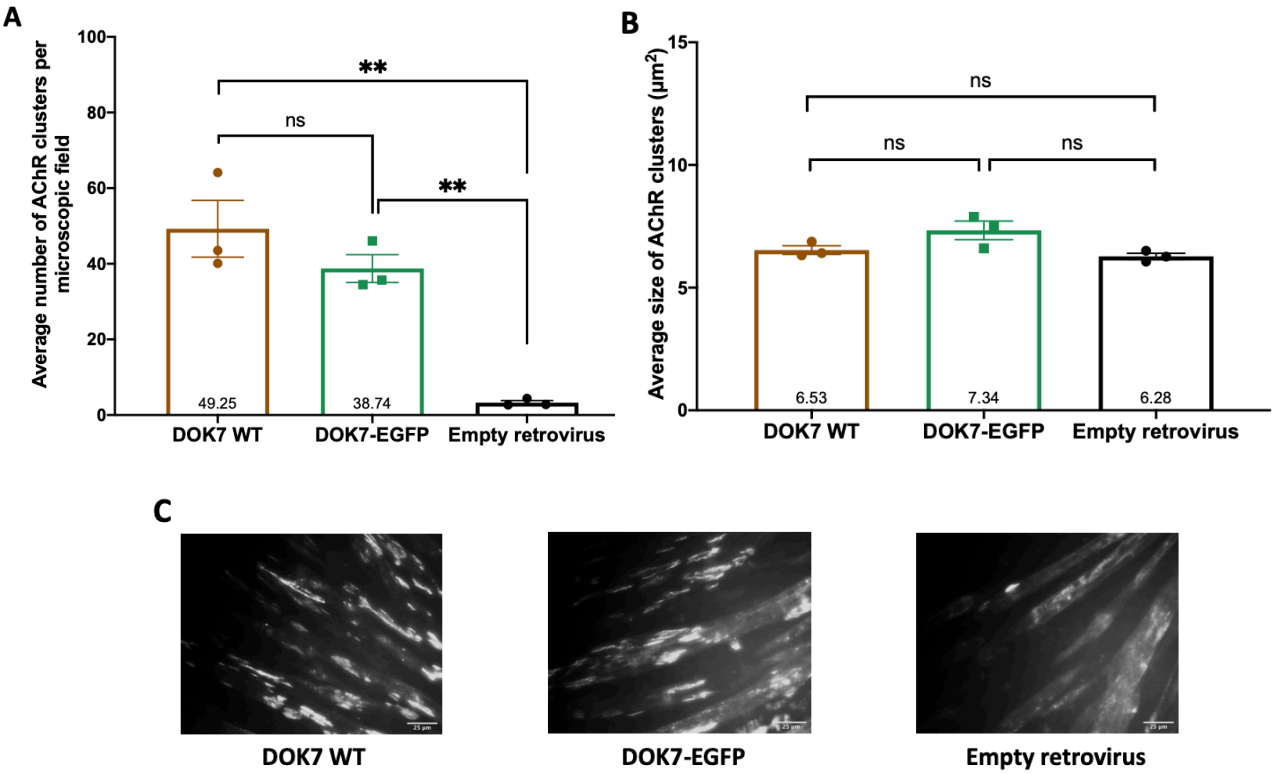

Figure 3.1. AChR clustering assay to compare between DOK7-EGFP and DOK7 wild-type (WT) transduced C2C12 myotubes. C2C12 myoblasts were infected with a retrovirus expressing either an EGFP tagged or untagged human DOK7 protein. C2C12 infected with an empty vector retrovirus were used as transfection control. Average number (**A**) and size (**B**) of AChR clusters per microscopic field were analysed for the two conditions and the control using a one way ANOVA with Tukey's multiple comparisons test (ns.- non significant *p<0.05; **p<0.01; ***p<0.001; mean +SEM). Representative images for the conditions are shown in panel **C**. (n=20 microscopic fields/infection for 3 individual retrovirus infections per condition). Scale bar: 25µm.

3.3. Generation of recombinant DOK7-EGFP AAV construct

A recombinant AAV plasmid containing an EGFP tagged DOK7 (at the C-terminus) was next generated (DOK7-AAV). The plasmid construct was further used in generating an AAV9 serotype packaged virus that induces the expression of DOK7 EGFP in the host cell or organism. The plasmid backbone (pAV-C-EGFP) used was an AAV plasmid containing the CMV promoter, an SV40 poly(A) signal, an Ampicillin resistance marker, two AAV2 inverted terminal repeats (ITRs) and the EGFP sequence. The human *DOK7* cDNA was cloned to be expressed in an open reading frame with EGFP to generate therefore the EGFP tagged protein (**Figure 3.2**). The sequence of interest was designed to be flanked by the 2 AAV2 ITR sequences (145bp) which contain the only necessary information needed in *cis* for an efficient virus production when a helper plasmid is added to supply genes needed for replication and packaging in *trans* (Wilmott et al. 2019). AAV2 have shown the highest levels of AAV ITR expression *in vivo*, and the ITRs of AAV2 serotype present a high degree of homology with other ITRs' serotypes (Rabinowitz et al. 2002; Earley et al. 2020). Thus AAV2 ITRs were chosen in here.

The DOK7-EGFP AAV plasmid was sent to Vigene Biosciences (Rockville, MD, USA) to generate the packaged DOK7-AAV virus to be further used *in vitro* and *in vivo.*

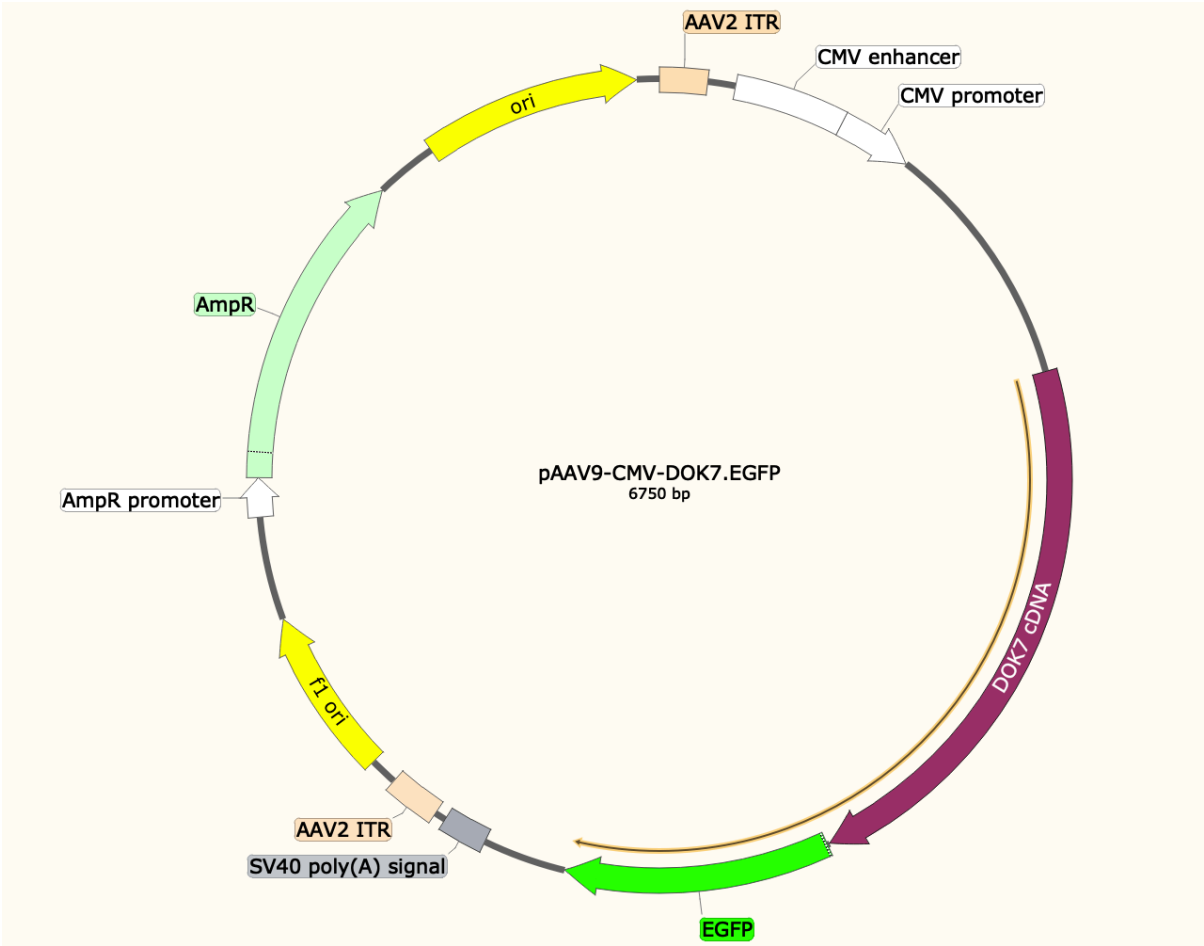

Figure 3.2. Generation of recombinant DOK7-AAV plasmid. The recombinant AAV plasmid was designed to express the human DOK7 cDNA (purple) sequence tagged with EGFP (green) fluorescent tag in the same open reading frame (black/yellow highlighted arrow). The gene of interest is flanked by two ITR sequences and the plasmid contains a CMV promoter, and a SV4- poly(A) sequence to signal the transcription termination site.

3.4. Investigating the infectivity rate of DOK7-AAV in C2C12 myotubes

To understand the ability of DOK7-AAV to transduce mouse muscle cells prior to using it *in vivo*, a titration of the virus was first performed. C2C12 myoblasts were transduced with 10^5, 10^6 and 10^7 viral genomes (VG) per cell, and differentiated into myotubes over a period of 6-10 days. Once fully mature myotubes were formed, the cells were fixed and imaged using a fluorescence microscope. The average number of EGFP-positive myotubes per microscopic field as well as their mean fluorescence intensity were compared between the three conditions. As expected, a significant increase was observed in the number of fluorescent cells with increasing viral titre (**Figure 3.3A**). Increasing the dose from 10^5 to 10^6 resulted only in a slight increase (30%) in fluorescence intensity, but increasing from 10^6 to 10^7 led to a dramatic increase of 77% (**Figure 3.3B**). Representative images with cells transduced with the three titres are shown in **Figure 3.3C**. 10^7 VG/cell titre showed the highest EGFP-positive cell number and fluorescent intensity, and it was further tested for AChR clustering activity in comparison to the baseline control (**Figure 3.3D**). Representative images of EGFP-positive cells labelled with α-bungarotoxin conjugated to Alexa Fluor 594 (red) are shown in **Figure 3.3E**.

In conclusion, DOK7-AAV induced the expression of biologically active EGFP-tagged DOK7 protein in C2C12 myotubes.

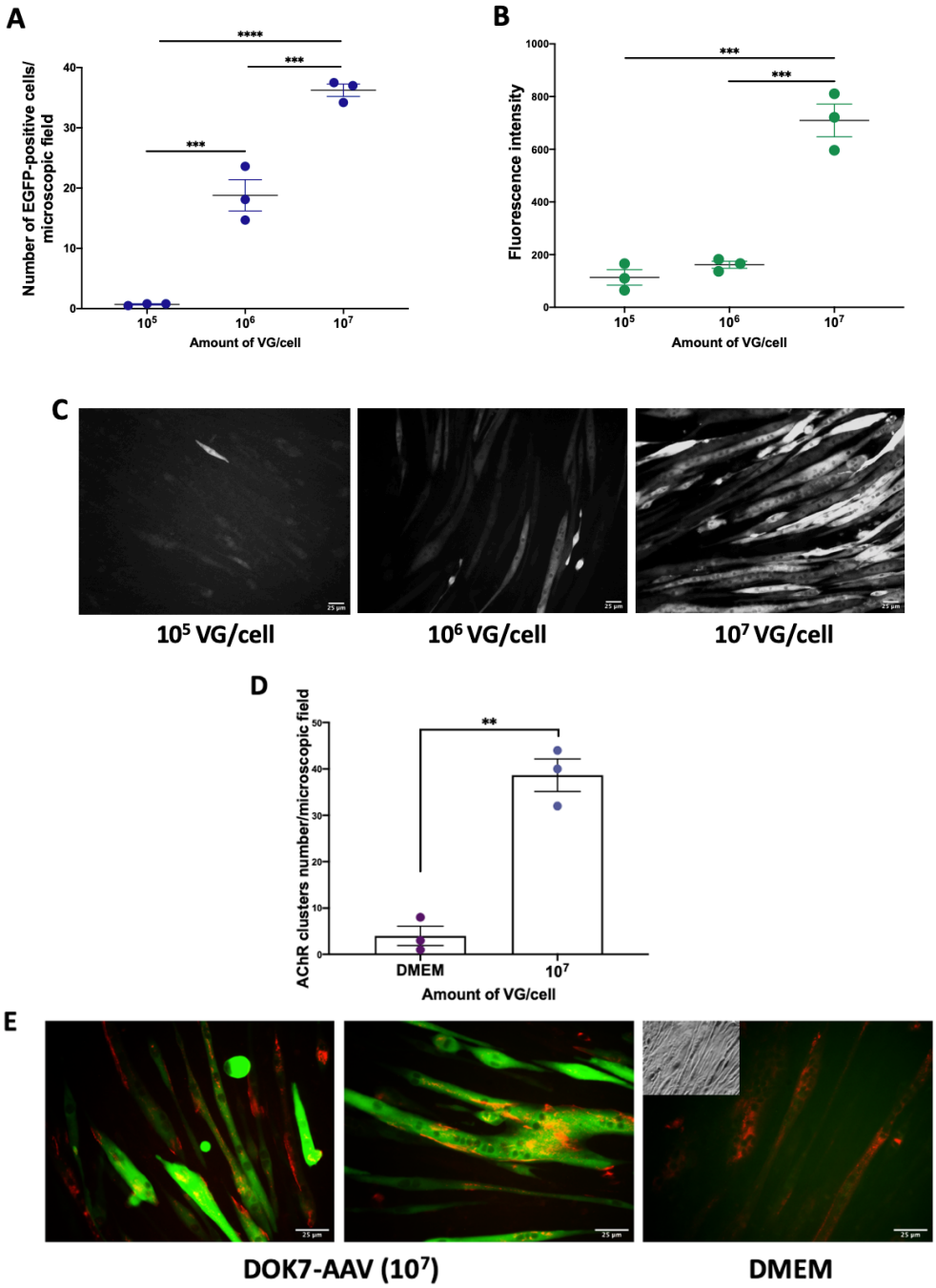

Figure 3.3. Titration of DOK7-AAV multiplicity of infection in C2C12 mouse muscle cells. C2C12 myoblasts were transduced with 10^5, 10^6 and 10^7 viral genomes per cell in 24-well plates and differentiated over a week. A one-way ANOVA with Tukey's multiple comparison tests was used to compare the number of EGFP-positive cells (**A)** and their fluorescence intensity (**B**) for the three conditions (images shown in panel **C**). The amount of VG/cell that resulted in the highest number of fluorescently positive cells was chosen for an AChR clustering assay (unpaired t test) (**D**). EGFP-positive cells with AChR clusters (red) are shown in panel **E**. DMEM was used as the baseline control (bright field shown in grey) (n=3 separated infections with 10 microscopic fields/infection; **p<0.01; ***p<0.001; ****p<0.0001; mean +SEM). Scale bar 25µm. VG- viral genomes;

3.5. Expression of DOK7-AAV in vivo in wild-type mice

Wild-type male mice were used to test the efficiency of DOK7 EGFP-AAV expression *in vivo* before using it in animal models of CMS. Five 3-week old mice were injected intraperitoneally with $4x10^{11}$ VG/mouse DOK7-AAV and three with EGFP-AAV as a negative control. The mice were sacrificed after 3 weeks for *ex vivo* electrophysiological recordings of hemidiaphragm-phrenic nerve preparations and tissue collection. Gene expression studies and tissue labelling were then performed (**Figure 3.4.**). Upon fluorescent immunolabelling of dissected tissue, one of the DOK7-AAV treated mice did not present enlarged synapses or diffused EGFP staining across muscle fibres and was therefore excluded from further analysis.

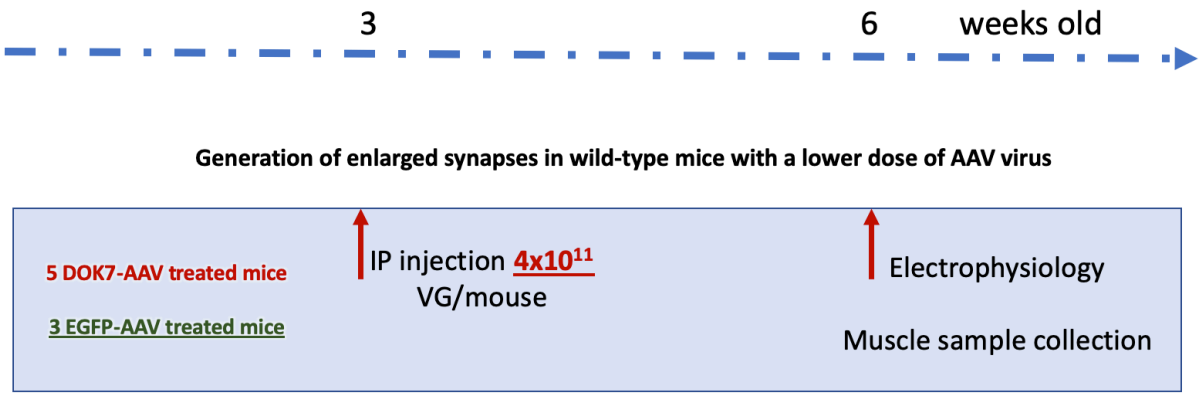

Figure 3.4. Schematic representation of study design for using DOK7-AAV in wild-type mice. Mice were injected intraperitoneally with $4x10^{11}$ vg/mouse at 3 weeks of age as follows: 5 mice were injected with DOK7 -AAV and 3 mice with EGFP-AAV control virus. 3 weeks later, the mice were euthanized for electrophysiology and muscle sample collection to perform various further studies.

3.5.1. Ex vivo electrophysiological recordings of hemidiaphragm-nerve preparations

Endplate potential recordings can give important insights with respect to the neuromuscular function since they provided detailed information about the functionality of both pre- and post-synaptic components of the NMJ. The miniature endplate potentials (mEPPs) and the endplate potentials (EPPs) were recorded from the hemidiaphragm-phrenic nerve preparations, upon blocking of the muscle action potential. The mEPPS are represented by the postsynaptic membrane depolarisation when a single synaptic vesicle is spontaneously released from the nerve terminal. EPPs represent the postsynaptic membrane depolarisations that result from the release of many synaptic vesicles upon nerve stimulation. Quantal content was calculated as the ratio between the EPP amplitude (stimulated at 1 Hz) and mEPP amplitude to estimate the number of vesicles released in response to a nerve impulse.

Two mEPP parameters, the EPP amplitude (stimulated at 1 Hz) and the quantal content were recorded for each individual mouse (**Figure 3.5**). Significantly higher mEPP frequency and quantal content of 6% and 12% respectively were recorded for the DOK7-AAV treated mice in comparison to the control mice. This likely reflects an increase in the nerve terminal area and number of release sites or probability of release.

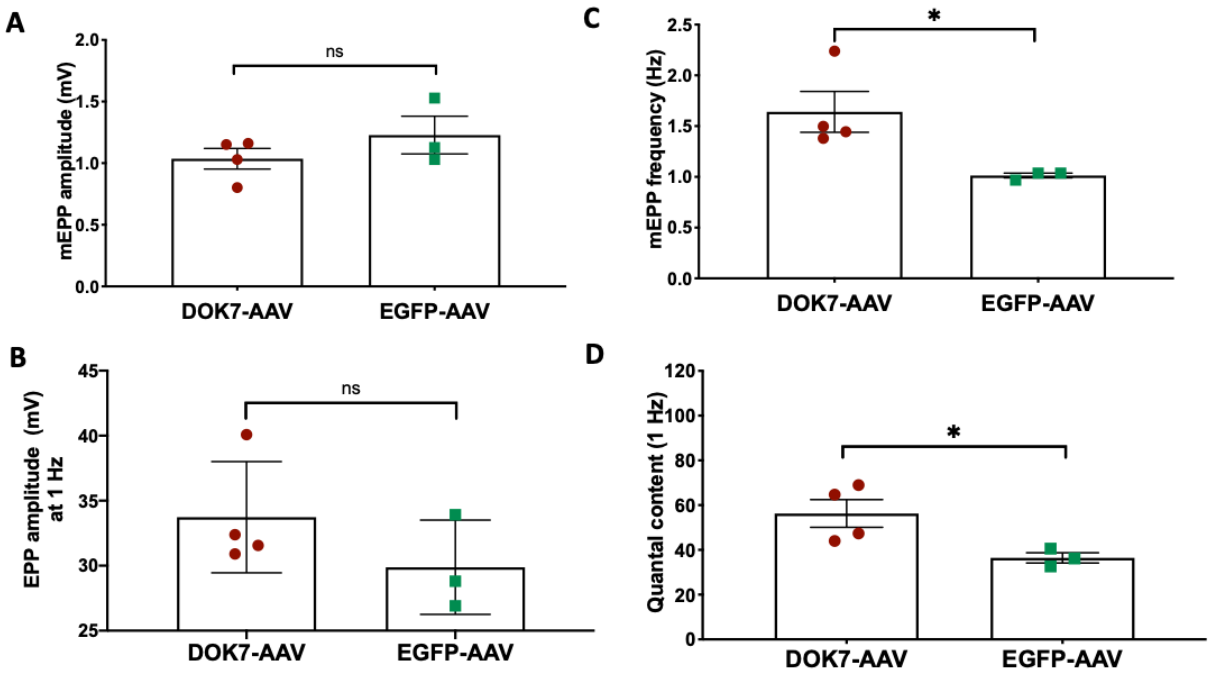

Figure 3.5. Electrophysiological recordings from *ex vivo* hemi-diaphragms of 6-week-old mice treated with DOK7-AAV in comparison to control mice. The electrophysiological recordings were performed on dissected hemidiaphragm-phrenic nerve preparations. Data point represent mean values from at least 15 recording for each mouse. Significant difference between the two treatment groups was assessed with an unpaired t-test (mean ±SEM; *p< 0.05; n=4 DOK7-AAV treated mice and 3 EGFP-AAV treated mice).

3.5.2. Fluorescent immunostaining of enlarged synapses

We next investigated whether the increase recorded for some electrophysiological parameters was related with changes in the NMJ morphology. NMJ of diaphragm, extensor digitorum longus (EDL) and soleus muscles were stained using fluorescently labelled α-bungarotoxin and compared between the DOK7-AAV group and control. Whole-mount preparations of diaphragm muscles were used to image NMJs while the EDL and soleus muscles fibres were teased and subsequently mounted. Postsynaptic sites of NMJs were visualised by labelling the AChRs with α-bungarotoxin. The nerve and nerve terminals were stained by using primary antibodies against synaptophysin (a synaptic vesicle protein) and neurofilament (intermediate filament of the neuron) followed by fluorescent secondary antibodies. Representative images of AChR and nerve terminal region immunostaining of NMJs are shown in panel **A** of **Figure 3.6** for diaphragm muscle and **Figure 3.7** for the two leg muscles. Area of neuromuscular junctions stained for AChRs and presynaptic area were measured using a Fiji software.

Figure 3.6 and **3.7** show a significant increase in the AChR clustering area of the enlarged synapses when compared to the wild-type synapses, for all three muscles (**B**). For diaphragm muscles the synapses of the DOK7-AAV treated mice appeared three times bigger in area. A smaller increase was observed for the leg muscles with 15% increase in area for the EDL muscle and approximatively 7% for the soleus muscle. An increase in the nerve/nerve terminal area in DOK7-AAV treated mice for all three muscles was also observed when compared to control, however this was significant only for the diaphragm muscle (38% in diaphragm- **Figure 3.6C**; 6% in EDL- **Figure 3.7C**; 8% in soleus- **Figure 3.7F**). For all three muscles and independently of the treatment group, presynaptic and postsynaptic areas precisely overlap.

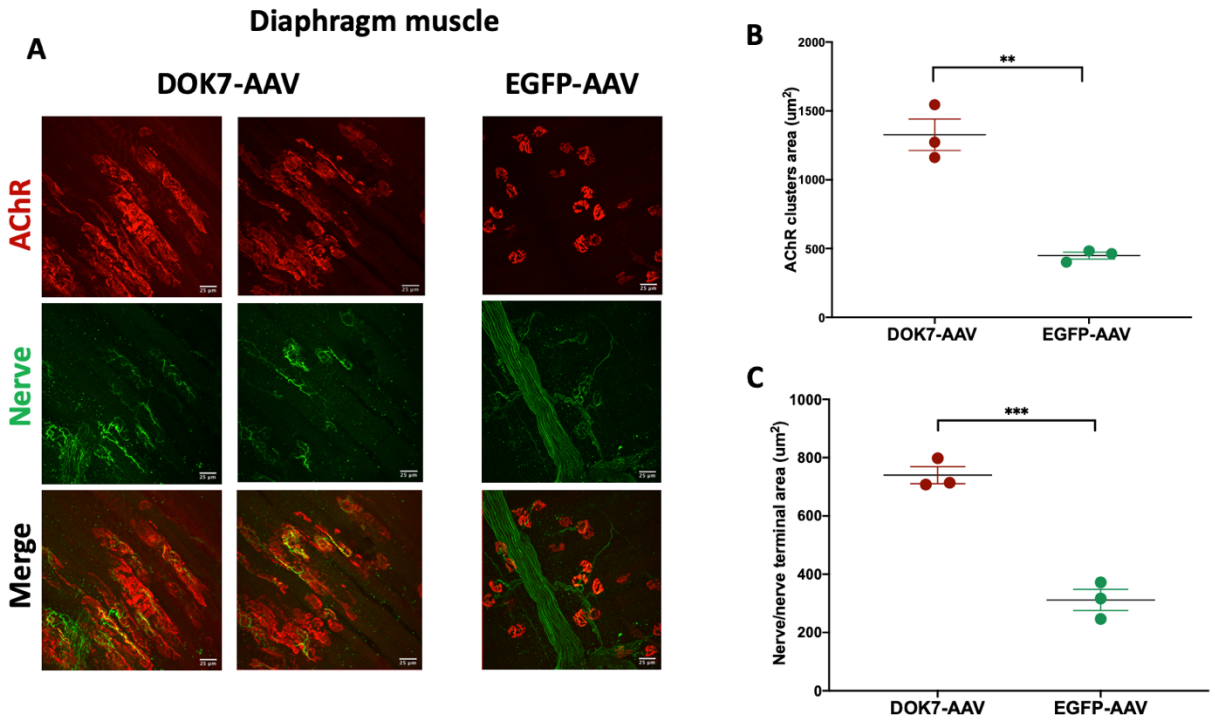

Figure 3.6. NMJs properties in the diaphragm muscle of DOK7-AAV treated group in comparison to control. Dissected diaphragm tissue was stained with fluorescent α-bungarotoxin for the AChR (red), and neurofilament and synaptophysin for the nerve and nerve terminal area (green) (**A**). Unpaired t-tests were used to analyse the differences in AChR cluster area (**B**) and nerve/nerve terminal area (**C**) between the two groups. Individual data points represent the mean values for each mouse of 50-70 individual NMJs. (ns.- non-significant; **p<0.01; ***p<0.001; n= 3 mice per treatment group; 50-70 NMJs per mouse) Scale bar: 25μm

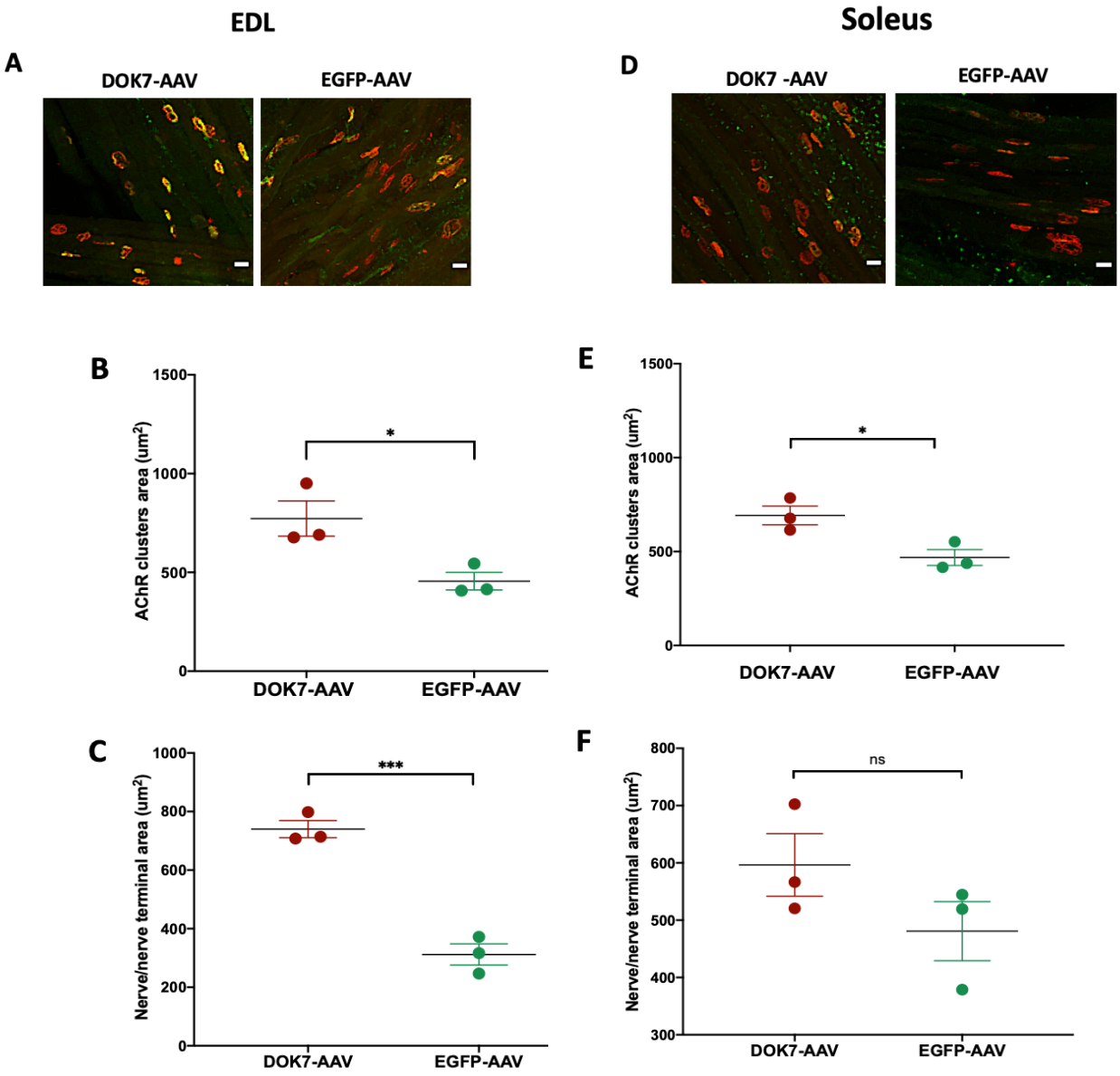

Figure 3.7. NMJ properties in the EDL and soleus muscles of DOK7-AAV treated group in comparison to control. Tissue (EDL-left; Soleus-right) was stained with fluorescent α-bungarotoxin for the AChR (red), and neurofilament and synaptophysin for the nerve (green) (**A**, **D**). Unpaired t-tests were used to analyse the differences in AChR cluster area (**B**, **E**) and nerve and nerve terminal area (**C**, **F**) between the two groups. Individual data points represent the mean values for each mouse of 40-56 individual NMJs (ns.- non-significant; *p<0.05; **p<0.01; ***p<0.001; n= 3 mice per treatment group; 40-56 NMJs per mouse). Scale bar: 25μm.

3.5.3. Investigating the transduction efficiency of DOK7-AAV gene therapy in various muscles

The transduction efficiency in the DOK7-AAV treated mice was examined by comparing the number of enlarged synapses of these mice, with the number of enlarged synapses designated by the upper end of the 95% confidence interval (CI) of the control group (EGFP-AAV treated mice). The number of NMJs with an area greater than the upper end of the 95%CI was then represented as a percentage from the total number of analysed NMJs for each mouse. 100% of the analysed synapses in the diaphragm muscles of the DOK7-AAV treated mice were bigger than the control synapses (**Figure 3.8**). A lower percentage of enlarged synapses was observed for the EDL (~67%) and soleus muscles (~48%).

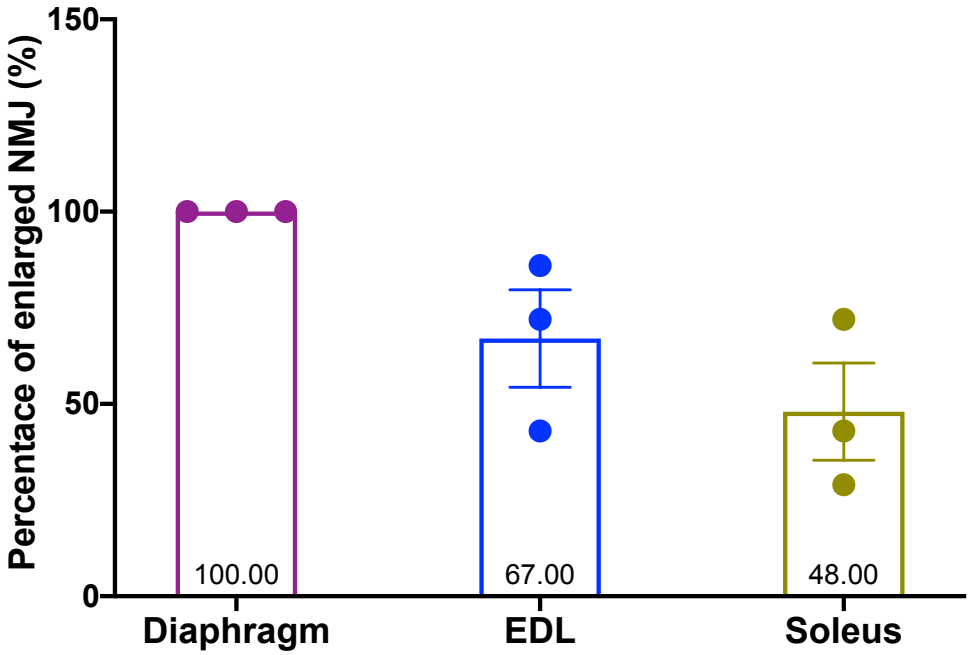

Figure 3.8. DOK7 EGFP-AAV transduction efficiency. Tissue was collected from wild-type mice treated with DOK7-AAV and immunolabeled to visualize AChRs and the nerve/nerve terminal area in Diaphragm (purple), EDL (blue) and Soleus (green) muscles. AChR area of 40-70 NMJs was measured and the percentage of enlarged synapses in the DOK7-AAV treated mice was analysed (mean ± SEM).

To conclude, by fluorescent labelling of NMJs, the formation of enlarged synapses due to overexpression of DOK7 was confirmed in the diaphragm, EDL and soleus muscles of DOK7-AAV treated mice. Both pre- and postsynaptic staining overlap indicating an alignment and thus enlargement of the whole synaptic apparatus, with the diaphragm muscle showing the highest percentage of enlarged NMJs.

3.5.4. Expression of DOK7-EGFP in other muscles tissue

To acquire a broader view of the transduction efficiency in different muscle tissues, DOK7-EGFP protein expression was analysed by western blotting in two additional muscles: tongue and TA. Muscles were homogenised and DOK7-EGFP was immunoprecipitated from the whole muscle lysates using a mouse monoclonal Dok7 antibody, subjected to SDS PAGE and western blotting. The protein was then detected with a mouse anti-EGFP primary antibody and a rat anti-mouse IgG secondary antibody (**Table 2.8**, Section **2.4.5**). The signal intensity was analysed by Fiji software.

DOK7 expression was observed in both muscles of treated animals (**Figure 3.9**). TA muscle appears to be transduced more efficiently than the tongue muscle, showing therefore the variability of AAV transduction at two different sites of the body upon intraperitoneal administration of the treatment.

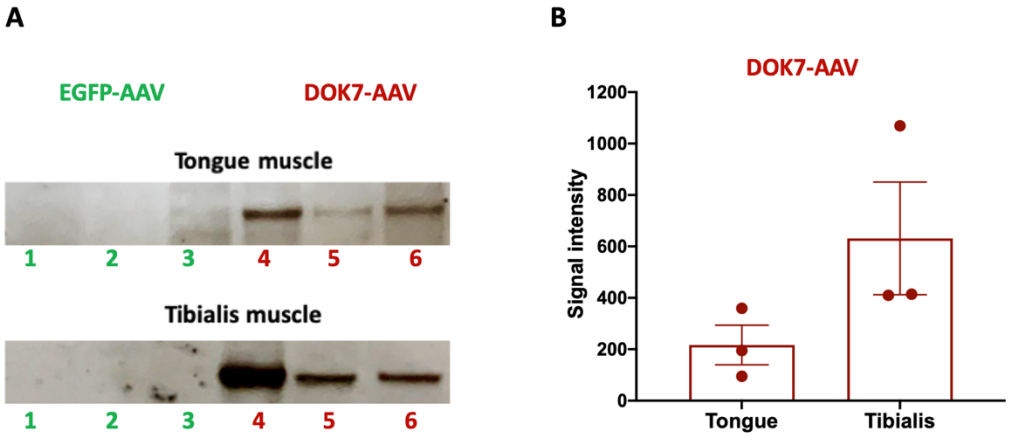

Figure 3.9. DOK7-EGFP expression in tongue and tibialis (TA) muscles. Muscles were dissected and homogenized in cold lysis buffer and the tagged protein was purified from the whole lysate by immunoprecipitation using a mouse monoclonal Dok7 antibody from both DOK7-AAV (red; 4,5,6) treated and controls samples (EGFP AAV; green; 1,2,3). Samples were run in parallel for both muscles in a western blot (**A**) and an ~80.9 kDa DOK7-EGFP protein was detected (n=3 individual animals).

3.5.5. Gene expression analysis in DOK7-AAV treated mice

During the formation and maintenance of the neuromuscular junction, the signalling evoked by the activation of MuSK regulates the transcription of key components such as the AChR subunits (Lacazette et al. 2003; Strochlic et al. 2004). Since DOK7 is an activator of MuSK, we next examined whether DOK7 overexpression leads to changes in gene expression of NMJ components.

3.5.6. Relative gene expression of Dok7, Musk, Chrna1 and Chrne in DOK7-AAV infected mice

TA muscles were homogenised and the mRNA was extracted and transcribed into cDNA. Primers specific for *Dok7*, *Musk*, *Chrna1* and *Chrne* were used to detect fold changes in gene expression in DOK7-AAV treated mice in comparison to control. The primers for Dok7 were specific to the mouse sequence and should not have cross-hybridised to human sequence. The overexpression of the human *DOK7* in muscles of DOK7-AAV treated mice was confirmed with an estimated 5-fold increase relative to the endogenous control (*Hprt1*) (**Figure 3.10A**). No significant differences in expression were observed for any of the NMJ components when comparing the two treatment groups. However, slightly increased expression was observed for *Chrna1* (2.02-fold increase) and *Chrne* (1.05-fold increase). The expression of endogenous mouse *Dok7* appeared significantly lower in DOK7-AAV treated mice.

These results suggest that there could be slight changes in the expression of some major NMJ components due to overexpression of DOK7.

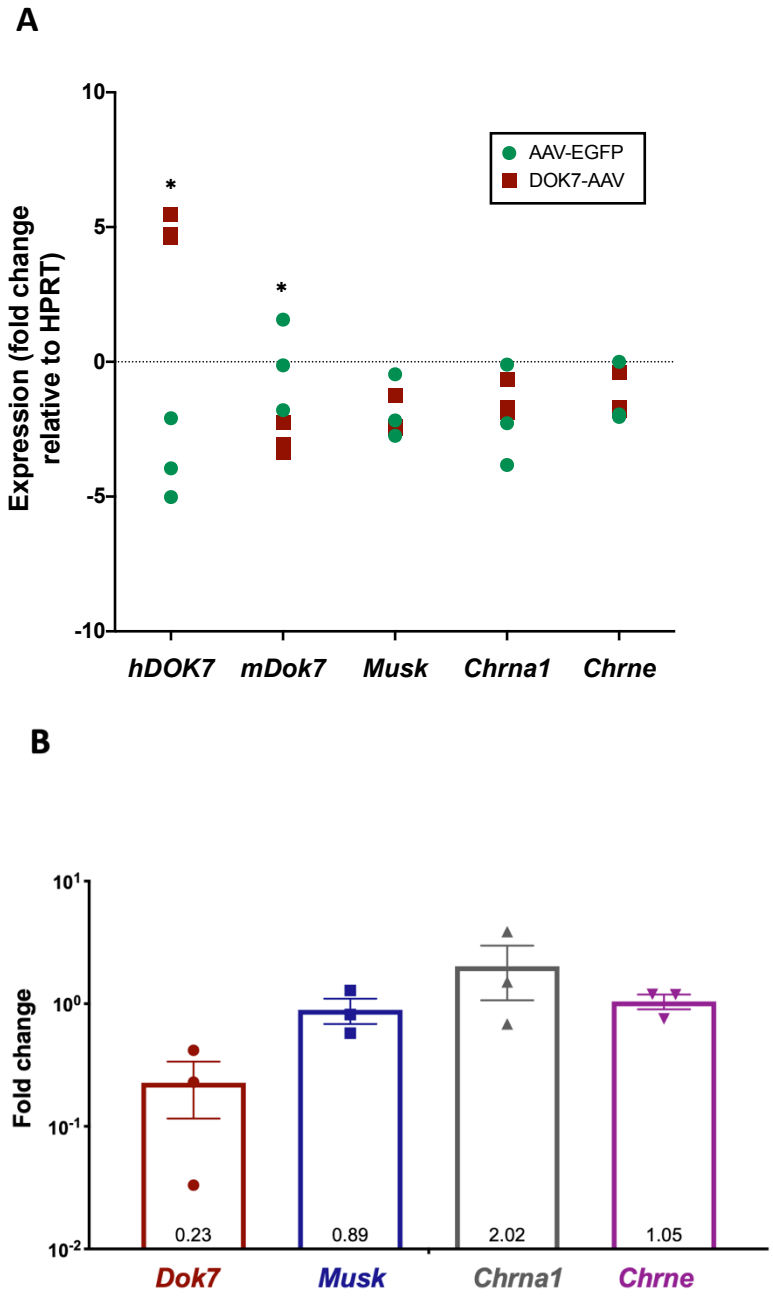

Figure 3.10. Fold increase in gene expression of key components at the NMJ in DOK-AAV treated mice compared to control. Tibialis muscle was chosen for qPCR analysis. (**A**) Data points represent expression levels in muscles from individual mice normalized to the endogenous control (*Hprt1*). Expression of human *DOK7* gene is also shown (*hDOK7*). An unpaired t-test was used to compare the fold increase in gene expression between DOK7-AAV treated animals and controls. (**B**) Fold change in gene expression upon DOK7-AAV expression, relative to *Hprt1* was analysed for some of the NMJ genes: *Dok7, Musk, Chrna* and *Chrne* (*p< 0.01; n=3 individual animals).

3.5.7. Differential gene expression in gene therapy treated mice

To further investigate the gene expression profiles, lysates from TA muscles of DOK7-AAV treated mice as well as control mice were prepared and used for RNA sequencing. Changes in the mRNA levels of 40 genes were revealed by RNA sequencing (**Figure 3.11**). 37 genes were upregulated and amongst these, *Chrna1*, *Chrne*, *Chrnd* and *Colq* were the major NMJ-related genes. Other upregulated genes were either related to transcription activation and regulation (e.g. *Etv4*, *Cda*, *Cited1*, *Gal3st3, Mapk11*) or involved in cytoskeleton organisation (*Krt18*). Four of the upregulated genes are linked to a possible role in neurotransmission and muscle contraction: *Ncam1*- neuronal cell adhesion, *Tnn1*- skeletal muscle contraction, *Tac4*- neurotransmission and *Rrad*- calcium channel regulation. The gene of a potential muscle component also appeared upregulated (*Mybph*). Downregulations of gene expression was observed for *Irf5*, *Adamts8* and *Cdc14a*, each having a potential distinctive role (**Figure 3.11-** annotations).

To conclude, these results suggest that the expression of genes involved in a variety of pathways were modified due to overexpression of DOK7. However, the specificity and biological relevance of these changes are yet to be determined.

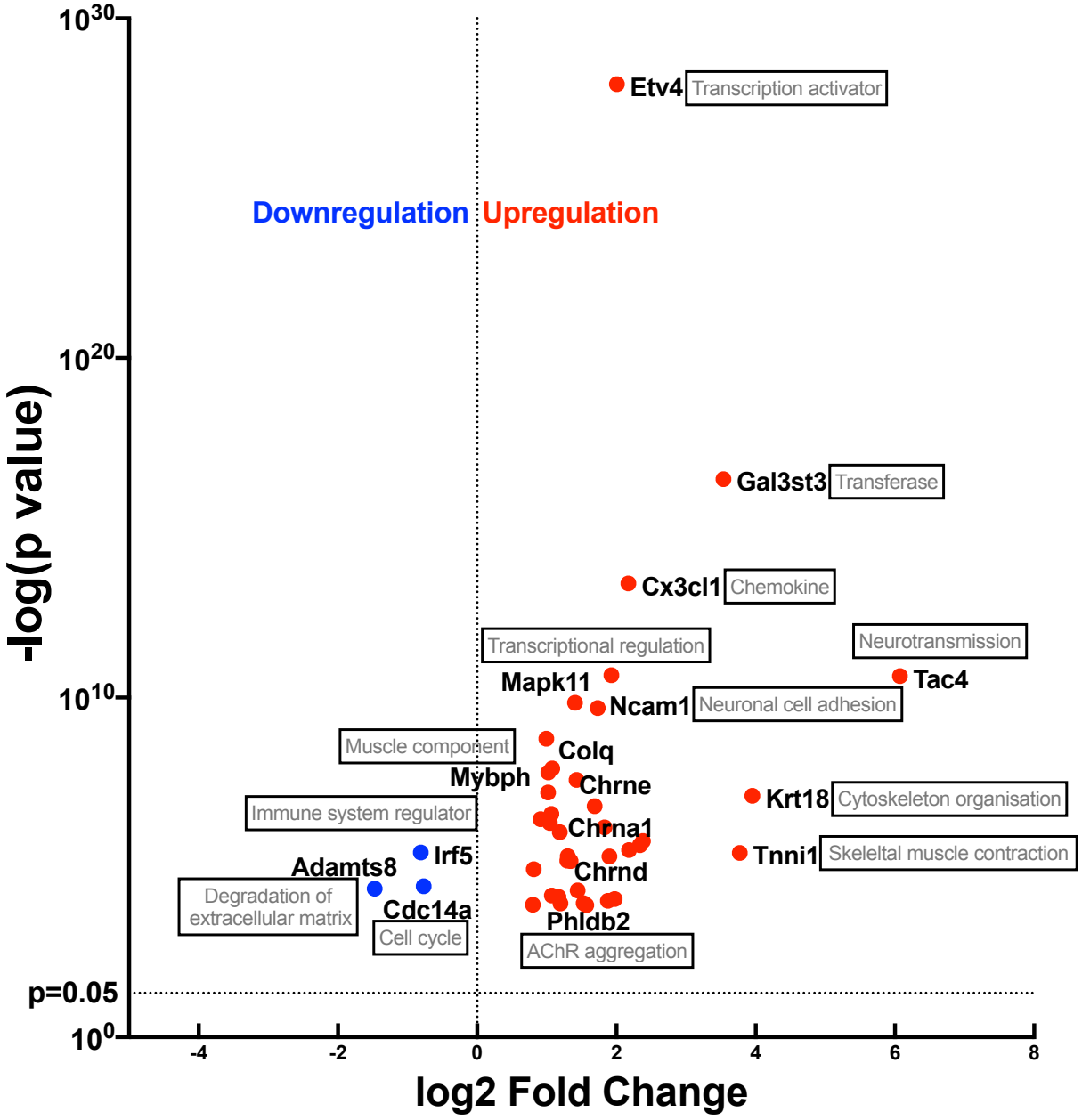

Figure 3.11. Differential gene expression as a result of DOK7 overexpression in muscle tissue of DOK7-AAV treated mice. RNA sequencing revealed changes in the expression of 40 genes. P value was transformed to -log(p value) to allow for a better visualisation of data points. Data was arranged descending according to the -log(p value) and plotted against the log2(Fold Change). The genes above the horizontal dotted lane are above the significance threshold which was set at a p value of 0.05. Genes that are upregulated are plotted to the right side of the graph (red) and gene that are downregulated to the left side (blue) (tibialis muscle; n=3 mice/ treatment group; unpaired t-test).

3.6. Discussion

This chapter aimed to investigate in more depth modifications to some aspects of neuromuscular transmission caused by DOK7 overexpression in wild-type mice, building on work originally described in 2014 (Arimura et al. 2014). As previously described by Arimura and colleagues, the overexpression of DOK7 in wild-type mice resulted in enlarged neuromuscular junctions with no detrimental effects on the body phenotype or overall wellbeing. We confirmed the formation of enlarged synapses by immunofluorescent labelling of AChRs and nerve areas in the diaphragm and two leg muscles, and we showed that:

1. Gene therapy treated mice showed significant increase in the miniature endplate potential frequency and quantal content
2. AChR stained synaptic area was significantly enlarged in the diaphragm, EDL and soleus muscles
3. The AAV transduction efficiency appeared to be higher in the diaphragm muscles; this is likely associated with the route of IP application which facilitates a direct path across the diaphragm; following IP administration, substances get absorbed by lymphatic vessels which are especially enriched around the diaphragm in most mammals (Al Shoyaib et al. 2020); thus, the diaphragm becomes the first immediately affected muscle, resulting in better transduction as compared to various muscles across the body
4. mRNA levels of *Chrna1* and *Chrne* appeared slightly increased in DOK7-AAV overexpressing animals, as well as *Chrnd*, *Colq* and some other genes potentially related to the NMJ as shown by gene profiling studies
5. While expression levels of human DOK7 protein appeared to be ~5 fold increased in the AAV-treated mice as compared to the endogenous control, variable transduction efficiencies are seen between gene therapy treated mice, most likely due to technical variability

To assess whether an EGFP tag would affect the ability of DOK7 to induce AChR clustering and possibly its function, a retroviral system was used to infect C2C12 muscle cells and induce the expression of both tagged and untagged versions of DOK7 protein. No changes were seen in AChR clusters number or length between the tagged and untagged DOK7 proteins, suggesting that an EGFP tag would most likely not interfere with its ability to induce the formation of AChR clusters *in vivo* either (**Figure 3.1**). This confirms the previous study that showed the formation of enlarged synapses in mice by using an EGFP-tagged version of DOK7 (Arimura et al. 2014). The reasoning behind using an EGFP-tagged protein was to potentially enable the quantification of transduction efficiency of DOK7-AAV *in vivo*, but also to distinguish the overexpressed protein from the endogenous mouse Dok7 in mouse muscle samples used for western blotting. It only proved useful for the latter, as the EGFP appeared diffused within the cytoplasm of muscle fibres and seemed to be expressed at levels that were difficult to distinguish from the background fluorescence.

A recombinant AAV construct containing an EGFP-tagged DOK7 was next produced. The vector was packaged in an AAV9 capsid since that serotype shows the highest transduction efficiency in skeletal muscles (Domenger and Grimm 2019). Prior to using the DOK7-AAV *in vitro*, its ability to infect mouse cells was confirmed in C2C12 myotubes (**Figure 3.2**). DOK7-AAV also induced the formation of AChR clusters (**Figure 3.2D,E**). Moreover, not having an empty AAV available to be used as negative control, the number of AChR clusters was compared to the baseline control (DMEM).

The DOK-AAV construct, designed for later use as gene therapy in CMS mouse models, was next tested in 3 week old wild-type mice. NMJ function and structure were assessed using

electrophysiological recording and NMJ immunostaining. Changes in gene expression triggered by the formation of enlarged synapses were assessed by mRNA expression studies. Frequencies of mEPPs and quantal content were increased in gene therapy treated mice, consistent with a recent study reported (**Figure 3.5**) (Eguchi et al. 2020). The results suggest an increased nerve terminal area and thus the potential for increased acetylcholine release. At variance from the study, no significant differences were seen in mEPP and EPP amplitudes. mEPP amplitude reflects the density of AChRs precisely where ACh reaches the postsynaptic membrane (Engel et al. 2015). Similarly, EPP amplitude is dependent on the density and distribution of the AChRs, the NMJs geometry and the electrophysiological properties of the sarcolemma (Engel et al. 2015). Under normal circumstances (wild-type mice), these parameters and especially AChR density are likely close to a maximum which is perhaps difficult to increase.

A significant increase in the AChR area was observed in diaphragm muscles, consistent with previous reports (Arimura et al. 2014; Eguchi et al. 2020). Here we showed that a similar increase in the postsynaptic area is also present in two leg muscles: EDL and soleus (**Figure 3.7**). Enlargement of the synaptic apparatus is also confirmed by fluorescent immunostaining of nerve area for both a synaptic vesicle protein and the neurofilament. The staining showed an overlap of the nerve terminal area with the enlarged postsynaptic region and thus the enlargement of the entire apparatus (**Figure 3.6** and **3.7**). Increase in nerve area was not significant in the soleus muscle, most likely due to the variability in transduction efficiency between mice, muscle tissue and individual muscle fibres as shown by immunostaining and protein expression studies (**Figure 3.6**, **3.7** and **3.8**). Consistent with this, the lowest AAV transduction efficiency was observed in the soleus muscle (**Figure 3.9**).

DOK7 has been shown to move between the cytoplasm and the nucleus by the aid of the PH domain-dependent nuclear import, and the nuclear export signal identified in its COOH-terminal moiety (Hamuro et al. 2008). Since DOK7 can enter the nucleus and thus, potentially influence gene expression, mRNA studies were performed to further our understanding in regards to changes due to DOK7 overexpression.

To asses changes in gene expression of some key components at the NMJ, mRNA levels for mouse *Dok7*, *Musk*, *Chrne* and *Chrna1* were analysed in DOK7-AAV treated mice in comparison to control (EGFP-AAV) by qPCR. Slightly increased expression levels were observed for *Chrna1* and *Chrne* but not *Musk* (**Figure 3.10**). The enlarged NMJ may be due to the over-activation of MuSK phosphorylation as a result of a higher amount of DOK7 recruited to the NMJ, without large changes in endogenous NMJ gene and protein expression. The DOK7-AAV treated mice showed less expression of mouse *Dok7*. This could be explained by the high level of similarities between the human and mouse sequences which could lead to unspecific binding of the primers. Thus, it is very likely that some of the endogenous *Dok7* was registered in fact as human *DOK7*. The overexpression of human *DOK7* was confirmed with an approximate 5-fold increase as compared to the endogenous control, although this would be expressed all along the muscle fibre and not just restricted to the NMJ (**Figure 3.10A**). Only three mice were used in this experiment and expression of some genes showed high variability between different animals, which is likely to reflect underlying variability in the experimental technique.

RNA sequencing was next used to assess gene expression profiling upon overexpression of DOK7 in tibialis muscle (**Figure 3.11**). Three genes that encode the AChR subunits, *Chrna1*, *Chrne* and *Chrnd* were found to show upregulation of mRNA expression (similar to the qPCR

results). This is also consistent with tissue immunostaining results indicating enlarged AChRs area in different muscles, although at the NMJ the level of mRNA expression does not necessarily correspond to the level of AChRs that are assembled and transported into the muscle surface membrane (Green 1999; Engel 2013). An increase in the expression of *Colq* was also observed. This gene encodes a multidomain functional protein of the NMJ that anchors the enzyme AChE to the basal lamina (J Arredondo 2014). Besides its structural function, it has been suggested that it can modulate AChR mRNA levels at the NMJ through interactions with MuSK (Sigoillot et al. 2010). The increase in *Colq* expression might suggest an adaptable mechanism to control increased AChRs gene expression at the NMJ.

Many of the upregulated genes are thought to play a role in transcriptional activation and regulation, most likely linked to the production of the DOK7 therapeutic gene (**Table 3.1**). Some genes involved in cytoskeleton organisation were also upregulated. *Krt18* encodes a protein called Keratin 18 that was recently shown to play a role in skeletal muscles assembly of keratin-based filaments as well as in transducing a contractile force (Muriel et al. 2020). Myosin binding protein H (*Mybph*) was also found to be upregulated and is known to be a component of the skeletal muscles, suggesting a potential link to increased muscle mass upon DOK7 upregulation (Vaughan et al. 1993; Barefield et al. 2017). Moreover, three genes that showed increased expression could play a potential role in neurotransmission and muscle contraction. *Ncam1* (neural cell adhesion molecule 1 precursor) is known to be involved in myogenesis (Lyons et al. 1992). However, the presynaptic Ncams have been shown to potentially be involved in nerve sprouting. Possibly, this reflects the increase in presynaptic nerve terminal area (Chipman et al. 2014). Troponin I (*Tnn1*), a myofibrillar protein, and the GTP-binding protein RAD (*Rrad*) also appeared upregulation. They are known to be involved in the calcium-mediated muscle contraction and calcium channel regulation respectively

(Wade et al. 1990; Gaudet et al. 2011). Three genes showed downregulation: *Cdc14a*, *Adamts8* and *Irf5* (**Figure 3.11** and **Table 3.1**). No specific correlation with the NMJs components has been described so far. However, they might be involved in establishing a counteractive response to the upregulated genes to achieve a balance at the NMJs.

Table 3.1 Differentially expressed genes in DOK7-AAV treated mice. (Information collated from genecard.org and uniport.org; accessed on 20th December 2020)

Gene	Log2 Fold Change	p value	Encoded protein; potential function
Tac4	6.07059095	2.34E-11	member of the tachykinin family of neurotransmitter-encoding genes; activates tachykinin receptor 1 and regulate endocrine and paracrine functions
Krt18	3.9508745	7.76E-08	encodes the type I intermediate filament chain keratin 18; related to cytoskeleton remodelling neurofilaments pathway
Tnni1	3.77131531	3.75E-06	Troponin I1, Slow Skeletal Type; associates with tropomyosin and regulates calcium sensitivity of the myofibril apparatus of striated muscles
Gal3st3	3.53659843	3.68E-17	member of the galactose-3-O-sulfotransferase protein family; catalyses sulfonation by transferring a sulphate group to the 3' position of galactose in N-acetyllactosamine
Rrad	2.37939678	1.68E-06	Ras Related Glycolysis Inhibitor And Calcium Channel Regulator; involved in the Angiopoietin Like Protein 8 Regulatory Pathway
Cited1	2.33534139	2.21E-06	member of the CREB-binding protein/p300-interacting transactivator with Asp/Glu-rich C-terminal domain (CITED) family of proteins
Msln	2.18178244	3.08E-06	Preproprotein; potential pathways: adhesion and metabolism of proteins
Cx3cl1	2.17021163	4.35E-14	C-X3-C Motif Chemokine Ligand 1; play a role in inflammatory diseases, neuropathies, cancer, HIV infections
Etv4	2.00619562	8.74E-29	ETS Variant Transcription Factor 4; GPCR signalling
Gprc5a	1.97508363	8.55E-05	Type 3 G protein-coupling receptor; may play a role in cellular growth and differentiation
ORF63	1.92812321	2.19E-11	Immediate-early protein 63; transcriptional regulator of viral mRNAs
Col19a1	1.89831111	4.75E-06	Collagen Type XIX Alpha 1 Chain; might be involved in maintaining the integrity of extracellular matrix
Plekhh2	1.87754476	9.64E-05	Pleckstrin Homology Domain-Containing Family H Member 2; might play a role in actin binding

Cda	1.830806	6.65E-07	Cytosine Nucleoside Deaminase; metabolism of nucleotides
Ncam1	1.7297282	2.04E-10	Neural Cell Adhesion Molecule 1; cell-to-cell and cell-to matrix interactions during development and differentiation within the nervous system
Crym	1.68704288	1.57E-07	Crystallin Mu; involved viral mRNA translation
Arc	1.56690722	0.00012 901	Activity Regulated Cytoskeleton Associated Protein; regulator of synaptic plasticity
Ndrg4	1.52707401	0.00011 282	Vascular Smooth Muscle Cell-Associated Protein 8; regulates mitogenic signalling
Sema3a	1.44301393	4.80E-05	Semaphorin-3A; vital for neuronal pattern development
Nes	1.42831924	2.66E-08	Nestin protein; member of intermediate filament protein family; expressed primarily in nerve cells
Mapk11	1.406039	1.42E-10	Mitogen-Activated Protein Kinase 11; role in cell proliferation and transcriptional regulation;
Gramd1b	1.34090684	6.57E-06	GRAM Domain Containing 1B; involved in ectoderm differentiation and mediates non-vesicular transport of cholesterol from the plasma membrane
Chrnd	1.30141992	4.68E-06	Cholinergic Receptor Nicotinic Delta Subunit; ligand-gated ion channel activity
M1ap	1.29308571	6.38E-06	Meiosis 1 associated protein; likely involved in the progression of meiosis
Sfn	1.19625964	0.00011 493	Epithelial Cell Marker Protein 1; regulator of translation by binding of initiation factors
Chrna1	1.18545023	9.17E-07	Cholinergic Receptor Nicotinic Alpha 1 Subunit; ligand-gated ion channel activity
Cpne2	1.16630324	7.40E-05	Calcium-dependent membrane-binding family of proteins; regulation of molecular events at the interface of the cell membrane and cytoplasm
Chrne	1.07723896	1.23E-08	Cholinergic Receptor Nicotinic Epsilon Subunit; ligand-gated ion channel activity
Fzd10	1.07231144	6.78E-05	Frizzled Class Receptor 10; G protein-coupled receptor activity
Lmo2	1.0644527	2.66E-07	LIM Domain Only 2; hematopoietic stem cell differentiation, chromatin binding
Dusp6	1.04238104	4.94E-07	Dual Specificity Phosphatase 6; cell proliferation and differentiation
Colq	1.02226691	1.60E-08	Collagen Like Tail Subunit Of Asymmetric Acetylcholinesterase; anchoring the catalytic subunit of asymmetric AChE to the synaptic basal lamina
Mybph	1.0172843	6.25E-08	Myosin Binding Protein H; structural constituent of muscle
Prkar1a	0.99298593	1.63E-09	Protein Kinase CMAP-Dependent Type I Regulatory Subunit Alpha; involved in CMAP signalling
Ufsp1	0.90997111	3.83E-07	Ubiquitin-fold modifier 1 Specific Peptidase 1; human form predicted to be non-functional
4930544D05Rik	0.8130407	1.14E-05	RIKEN cDNA 4930544D05; unknown function

Phldb2	0.80029113	0.00012594	Pleckstrin Homology Like Domain Family B Member 2; may play a role in AChR aggregation in the postsynaptic membrane (by similarity)
Cdc14a	-0.7681844	3.62E-05	Cell Division Cycle 14A; phosphatase activity; role in cell cycle control
Irf5	-0.8091926	3.67E-06	Interferon Regulatory Factor 5; modulation of cell growth, potential regulation of apoptosis and immune system activity
Adamts8	-1.4720456	4.22E-05	ADAM Metallopeptidase With Thrombospondin Type 1 Motif 8; degradation of the extracellular matrix and metabolism of protein

The increased NMJ size demonstrates that overexpressed DOK7 protein can indeed be recruited to the NMJ and have its effects on the size of the synaptic apparatus. It would be of interest to investigate whether the recruitment of DOK7 protein to the NMJ, happening exclusively as a result of the DOK7-AAV treatment, is derived from myonuclei in the extra-synaptic and peri-synaptic regions. These could be playing an essential role in the formation of the enlarged synapses.

In conclusion, the research presented in this chapter confirms some of the previous reported results in regards to enlarged NMJs. It also presents preliminary results on potential variability in AAV transduction efficiency between different muscles when given by IP injection. Remarkably, few changes in gene expression of known NMJ proteins were found overall.

Chapter 4

DOK7-AAV gene therapy in a mouse model of DOK7-CMS

4.1. Introduction

Congenital myasthenic syndromes (CMS) are genetic diseases defined by abnormal neuromuscular transmission at the neuromuscular junction (NMJ) (Spillane et al. 2010). Besides key players linked with neurotransmission, the size and organisation of an NMJ are also important determinants of its function (Slater 2008). Structural alterations of the NMJs have been previously observed with various neuromuscular disorders such as muscular dystrophy (MD), amyotrophic lateral sclerosis (ALS) or spinal muscular atrophy (SMA) (Fischer et al. 2004; Kariya et al. 2008; Ghedini et al. 2008). In many forms of CMS, functional deficits in neuromuscular transmission are interconnected with alterations to synaptic structure and vice versa. For instance, in DOK7-CMS myasthenic weakness is associated with smaller NMJs and simplified synaptic structures (Slater et al. 2006; Selcen et al. 2008).

Arimura et al. emphasised for the first time the potential of gene replacement at the NMJ as a therapy for DOK7 congenital myasthenia (Arimura et al. 2014). They showed that overexpression of a functional human DOK7 protein in skeletal muscles of DOK7-CMS model mice, induced the formation of enlarged NMJs structures and restored their motor functions resulting in prolonged lifespan. However, no electrophysiological data is available for this mouse model.

In this study we aimed to analyse in more depth the effects of the DOK7-AAV gene therapy in a DOK7-CMS mouse model by using a similar approach to Arimura and colleagues (Arimura et al. 2014). We used inverted screen hang tests, decrement tests, *ex vivo* electrophysiological recordings and analysis of the NMJ morphology to characterise these effects and ultimately establish the potential of using this therapeutic intervention in other types of congenital myasthenic syndromes.

4.1.1. DOK7-CMS mouse model

The DOK7-CMS mouse model was designed as a 'knock-in' model, homozygous for the most prevalent DOK7 frameshift mutation in patients: c.1124_1127dupTGCC (KI) (**Figure 4.1.**) (Beeson et al. 2006; Palace et al. 2007; Cossins et al. 2012; Arimura et al. 2014). The majority of DOK7 patients reported carry at least one allele with a frameshift mutation in exon 7 of the *DOK7* gene. The c.1124_1127dupTGCC is the most common of these and results in truncation of the C-terminus region of DOK7 protein. Since the C-terminus of the DOK7 protein plays an important role in recruiting adaptor proteins that may contribute to MuSK activation, its truncation influences MuSK activity resulting in impaired downstream signalling within this pathway and thus defective neuromuscular transmission at the NMJ (Hallock et al. 2010; Ueta et al. 2017).

Patients with DOK7-CMS are characterised by progressive limb-gridle weakness often presenting with walking difficulties (Palace et al. 2007; Selcen et al. 2008). DOK7-CMS model mice show a far more severe phenotype than humans with a short lifespan (13-20 days),

significantly reduced body weight, and walking difficulties apparent from 9th day of life (Arimura et al. 2014). Similar to human patients, these mice show abnormally small NMJs (Slater et al. 2006; Beeson et al. 2006; Selcen et al. 2008; Arimura et al. 2014). In this study, the mouse model will further be referred to as DOK7-CMS mouse model.

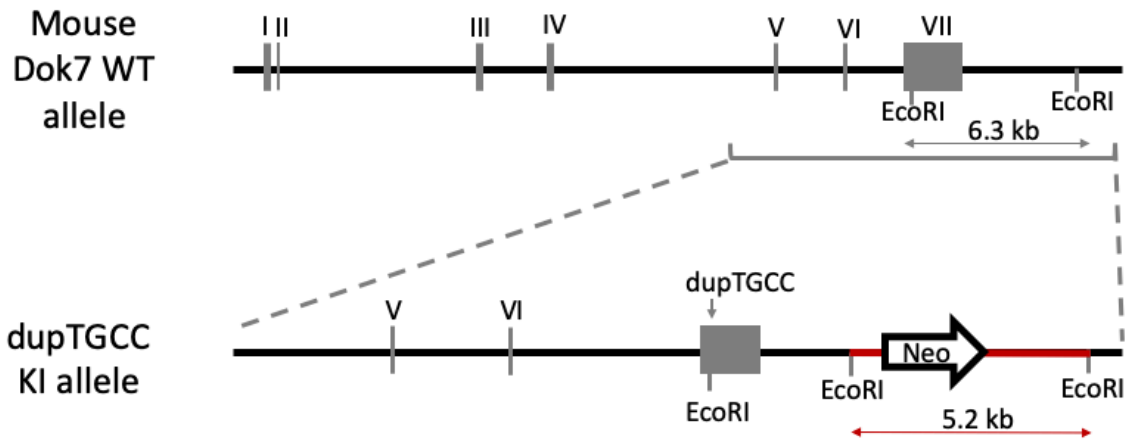

Figure 4.1. Generation of DOK7 congenital myasthenia mouse model. The targeting vector was designed to contain a mutation in exon 7 which corresponds to the most prevalent mutation in the *DOK7* gene in patients with DOK7 congenital myasthenia (c.1124_1127dupTGCC). Neomycin resistance gene was introduced downstream of exon 7 to facilitate embryonic stem (ES) cells selection after electroporation of linearized vector. Chimeras were then generated by injecting a positive ES clone into a blastocyst. Germ-line chimeric males where then crossed with wild-type females to generate heterozygotes mice that were further used to generate knock-in mouse models (KI) (Arimura et al. 2014).

4.1.2. Experimental design

Dok7$^{+/KI}$ males were crossed with females of the same genotype to generate DOK7-CMS mice homozygous for the 1124_1127dupTGCC mutation. Genotyping was not feasible in the first few days of life, and to deliver the gene therapy treatment in time, the body weight of new-born pups was monitored from day of birth (P0). Pups that weighed 2.2g or less by postnatal day 4 (P4) received a one-time DOK7 gene therapy treatment intraperitoneally ($4x10^{11}$vg/mouse) (**Figure 4.2.**). Because gender was difficult to be determined at such an early age, the study was performed on mixed sexes (no gender-related differences were later observed as response to treatment during the trial). Subsequently, their body weight was monitored daily for ~4 to 5 weeks and genotyping was performed at around 3 weeks of age to confirm the genotype of DOK7-CMS model mice. In case a humane endpoint was reached, which was defined as either loss of weight of at least 0.1g in 24h, or no weight gain over 48h (as per Home Office License), mice were humanely euthanised and removed from the study. Beginning with week 12 of age, their muscle fatigability was assessed weekly for 6 weeks. Following, EMG decrement was recorded on anesthetised mice, beginning with 18 weeks of age, and mice were then humanely euthanised for *ex vivo* electrophysiological recordings and tissue collection. EMG and electrophysiological recordings were performed by Richard Webster. Due to unforeseen circumstances, that culminated with institute closure for approximatively 3 months, EMG and electrophysiology were performed between 26-32 weeks for some of the mice (3 males and 1 female per treatment group). No age differences were observed during the analysis.

As the phenotype of heterozygous littermates was indistinguishable from the homozygous wild-type mice (with the same genetic background), these mice were considered wild-type and were used as controls (Arimura et al. 2014).

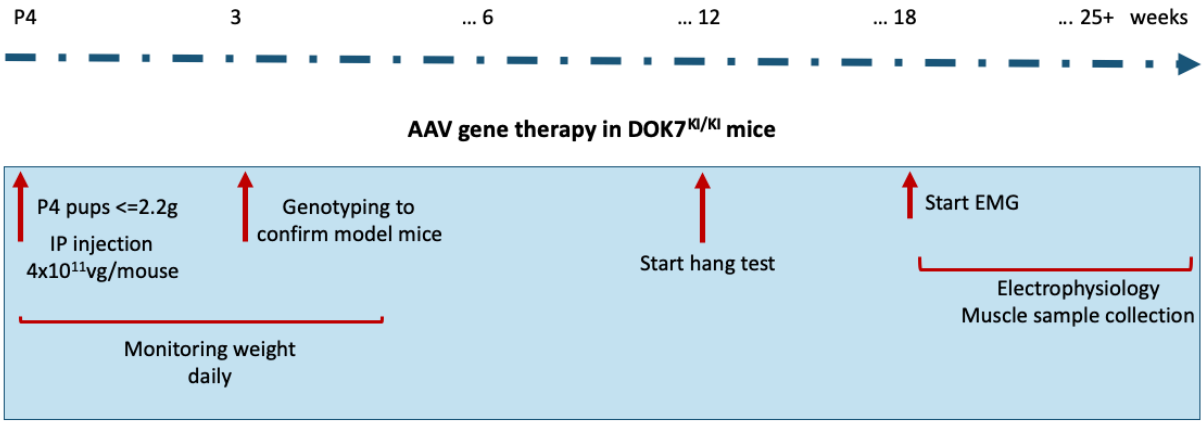

Figure 4.2. Schematic representation of study design for using DOK7 gene therapy in a mouse model of DOK7-CMS. Dok7$^{+/KI}$ littermates were crossed with mice of the same genotype. All pups from any new litter that by P4 weighed less than or equal to 2.2g were considered DOK7-CMS mice (DOK7$^{KI/KI}$ mice) and were injected intraperitoneally with DOK7 gene therapy (4x10^{11}vg/mouse). Their body weight was then monitored daily for at least 4-5 weeks, and at around 3 weeks of age the genotype of injected mice was confirmed. Beginning with 12 weeks of age the muscle strength of these mice was assessed for a period of 6 weeks. A decrement test following repetitive nerve stimulation (EMG) was performed beginning with 18 weeks old. This procedure was followed by tissue harvesting to further perform *ex vivo* electrophysiological recordings and other studies.

4.2. Changes in time to humane endpoint of gene therapy treated DOK7-CMS mice

To assess whether DOK7 gene therapy has an influence on the lifespan of DOK7-CMS mice, the probability of survival was analysed for gene therapy treated mice in comparison to untreated mice. Untreated mice failed to gain weight and had to be humanely euthanised between P7-P10 (as per Home Office License) (**Figure 4.3.**). 80% of treated mice survived until ~ P17 and this percentage decreased to 57% from 20 days of age onwards. These mice survived beyond 100 days and were used for further assessments.

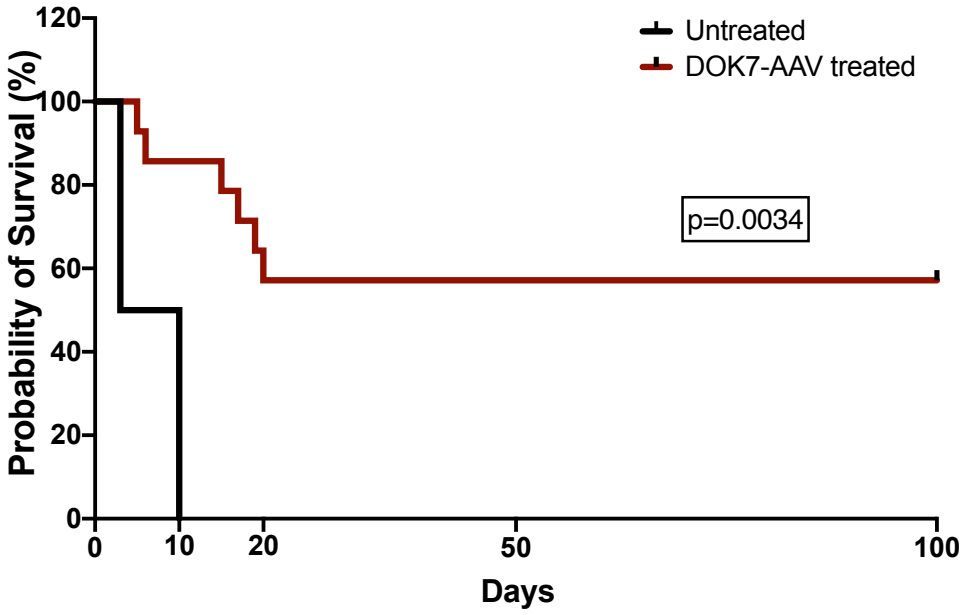

Figure 4.3. Probability of survival for DOK7-AAV gene therapy treated DOK7-CMS mice. Pups were injected at P4 with DOK7-AAV gene therapy. The body weight of both treated (red) and untreated (black) DOK7-CMS mice was used to assess response to treatment. Humane endpoints were reached by untreated mice by P10. 57% of treated mice survived past 100 days and were further used in the study. Kaplan-Meier analysis and log-rank test were performed to compare the percentages of survival between the two treatment groups (n=2 untreated mice and 14 treated mice).

4.3. Evaluation of body weight of gene therapy treated DOK7-CMS mice

In neonatal mice, body weight was used as an indicator for effectiveness of treatment with DOK7-AAV gene therapy. During the course of the treatment, 6 pups from the gene therapy treated group reached humane endpoints by postnatal day 20 (**Figure 4.4.A**). Body weight of the other 8 gene therapy treated model mice slowly increased over the course of the trial, reaching ~50% of the body weight of age-matched wild-type mice at 29 days of age (**Figure 4.4.A,B**). **Figure 4.4.B** illustrates 10 days old DOK7-CMS treated mice next to wild-type mice of the same age for reference.

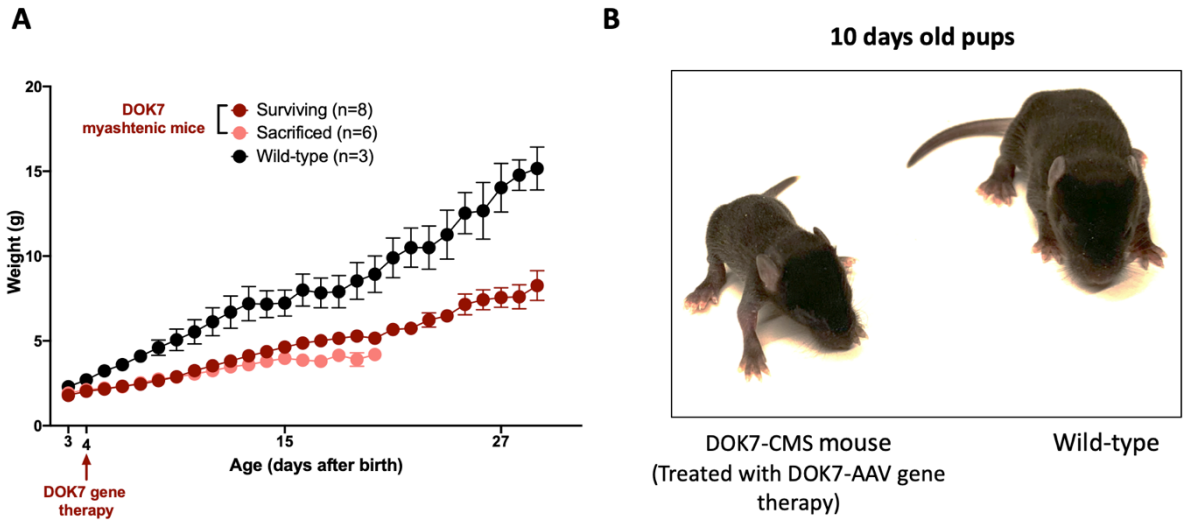

Figure 4.4. Body weight of gene therapy treated DOK7-CMS mice in comparison to wild-type mice. Model mice were injected at P4 with DOK7-AAV gene therapy (dark and light red). Body weight of both treated and wild-type (black) mice was monitored daily for at least 4 weeks (**A**). 6 of the treated mice reached humane endpoints by 20 days of age and were euthanized (light red). 8 of the treated mice survived past 100 days of age and were further used to evaluate the effects of gene therapy treatment. 10 days old pups are shown in panel **B** for reference (n=3 wild-type and 14 model mice).

Out of all the DOK7-AAV gene therapy treated model mice, 8 mice of mixed sexes survived past 100 days of life. Their genotype was confirmed at ~ 3 weeks, and beginning with 12 weeks of age, their weight was monitored again for 6 weeks. Model mice reached only ~86% of body weight of age-matched wild-type mice by 18 weeks of age, and they were visibly smaller than the wild-type (**Figure 4.5.**). An overall significant difference was observed between the two treatment groups which was constant over the course of the 6 weeks.

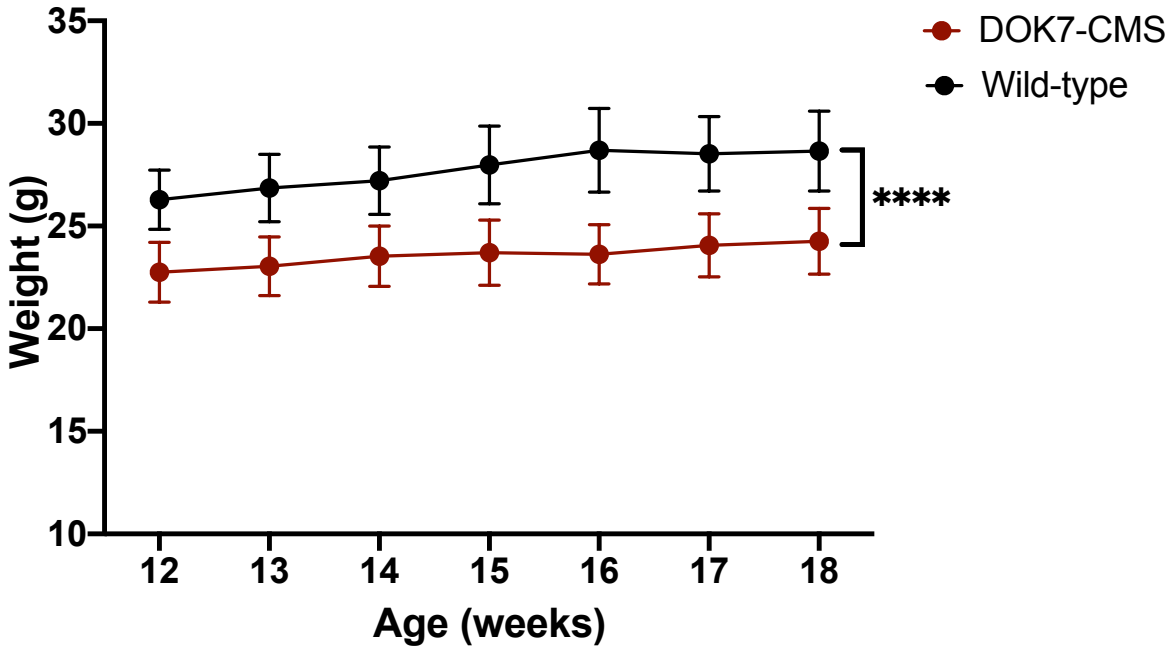

Figure 4.5. Body weight of adult gene therapy treated DOK7-CMS mice. Body weight of mice from both gene therapy treated and control groups was monitored once a week for a 6-week period. Data and error bars are represented as means ± SEM over a period of 6 weeks starting with week 12 of age. A two-way ANOVA with Sidak's multiple comparison test was performed to compare the two groups overall and considering each timepoint (****$p<0.0001$; n=5 female mice and 3 male mice/treatment group).

4.4. Muscle fatigability of gene therapy treated model mice

Subsequently, muscle fatigability was assessed for the gene therapy treated model mice in comparison to the wild-type mice as evaluated by an inverted screen test. This was done once a week for 6 weeks, around the same time of the day (for consistency). With a cut-off of 10 minutes applied, gene therapy treated model mice appeared to perform significantly better than the wild-type mice (**Figure 4.6.A**).

It was clear that wild-type mice were significantly heavier than the model mice (**Figure 4.5**), and therefore the data was normalised to body weight for each mouse at each different timepoint (**Figure 4.6.B**). This analysis revealed no significant differences in muscle fatigability between the two groups, and similar fluctuation patterns for both treatment groups.

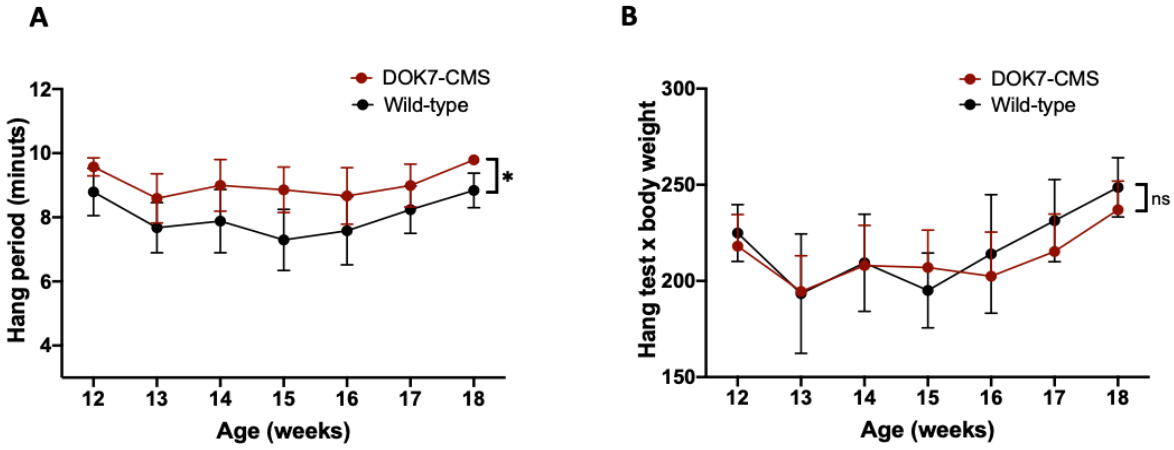

Figure 4.6. Hang period as assessed by inverted screen test. To account for any changes caused by body weight difference, hang time data **(A)** was normalised to body weight (by multiplication). Data and error bars are represented as means ± SEM over a period of 6 weeks starting with 12 weeks of age **(B)**. A two-way ANOVA with Sidak's multiple comparison test was performed to compare the two groups overall and considering individual time points of the trial (ns.- non significant; *$p<0.05$; n=5 female mice and 3 male mice/treatment group).

4.5. Decrement of CMAP on repetitive nerve stimulation

Since DOK7-AAV gene therapy increased the lifespan of DOK7-CMS mice that also showed muscle strength comparable to wild-type mice, we next investigated muscle fatigability upon repetitive nerve stimulation. Gene therapy-treated model mice showed significantly increased muscle decrement in comparison to the wild-type mice (**Figure 4.7.**). With less than 10% decrement at 1Hz, a continuous increase in muscle decrement was observed until it reached ~30% at 20Hz. No decrement was observed for the wild-type mice at any frequencies.

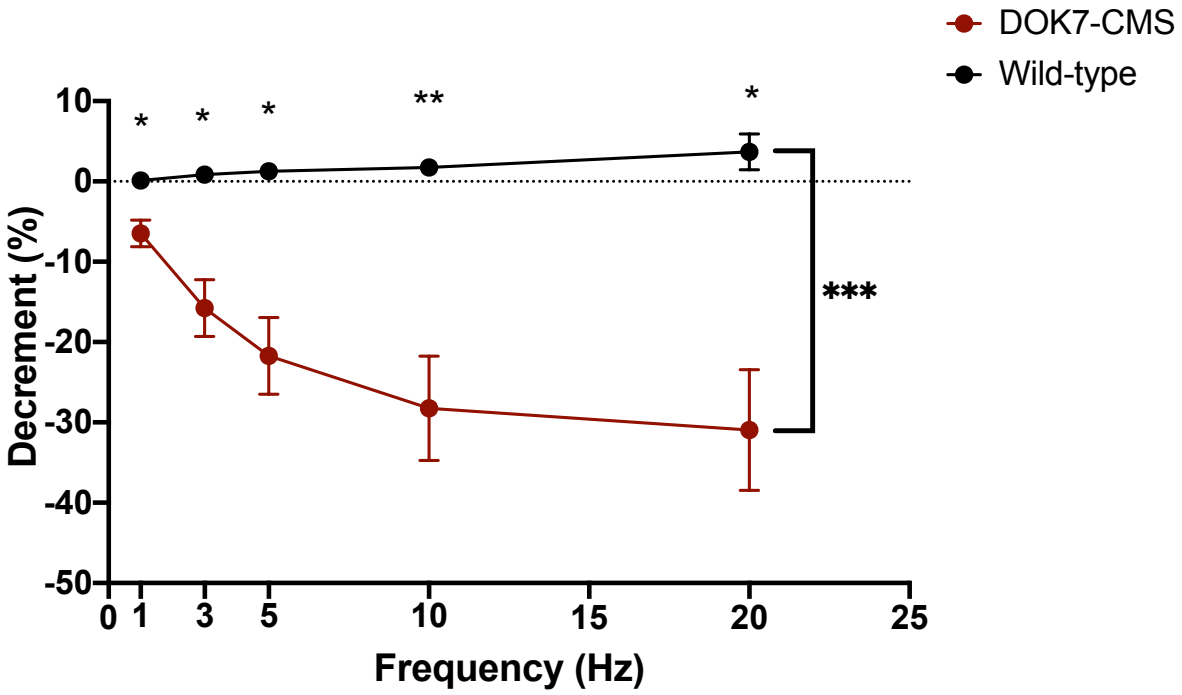

Figure 4.7. Muscle decrement following repetitive nerve stimulation in gene therapy treated myasthenic mice. Mice from both the gene therapy treated and control groups were anesthetised and prepared for decrement test. Individual data points represent the mean ±SEM at different frequencies. Repeated measurements two-way ANOVA with Sidak's multiple comparison tests were performed to compare between wild-type and gene therapy treated mice overall as well as at different frequencies (*p<0.05; **p<0.01; ***p<0.001; n=5 female mice and 3 male mice/treatment group).

4.6. Ex vivo electrophysiological recordings

The gene therapy treated mice demonstrated fatigable muscle strength on an inverted screen similar to the wild-type mice but the EMG recordings indicated at least some impairment of neuromuscular transmission. Thus, a more detailed assessment of neuromuscular transmission was undertaken. This was done by electrophysiological analysis of *ex vivo* hemidiaphragm-phrenic nerve preparations in mice of 18-32 weeks old. Upon blockage of skeletal muscle action potentials with μ-conotoxin, miniature endplate potentials (mEPP) and endplate potentials (EPP) were recorded. The diaphragm-nerve preparation of one wild-type mouse failed, so no recordings were collected from this mouse. 7-15 endplates were analysed for each animal.

Changes were seen in both presynaptic and postsynaptic measurements. mEPPs are the small depolarisations of the resting membrane potentials caused by the spontaneous release of a single acetylcholine containing vesicle from the nerve terminal, and its subsequent binding to the AChRs. Significant lower mEPP amplitudes (16%) were recorded for the gene therapy treated model mice (**Figure 4.8.A**). However, the frequency at which these mEPPs occurred was significantly higher in the gene therapy treated DOK7-CMS mice, with wild-type mice showing only ~50% of the values recorded for the model mice (**Figure 4.8.B**).

EPPs are evoked by pulses at 1 Hz applied to the phrenic nerve which result in ACh release from the nerve terminal ultimately leading to large depolarisations of the postsynaptic membrane. Mean EPP amplitudes were approximatively 25% higher in gene therapy treated model mice in comparison to wild-type (**Figure 4.8.C**). Also, the quantal content, which is representative to the number of vesicles released in response to a single nerve impulse, was

recorded as 48% higher in gene therapy treated DOK7-CMS mice and that was significant (**Figure 4.8.D**).

In summary, electrophysiological recordings showed increased mEPP frequencies, EPP amplitudes and quantal content but decreased mEPP amplitudes in gene therapy treated mice in comparison to controls.

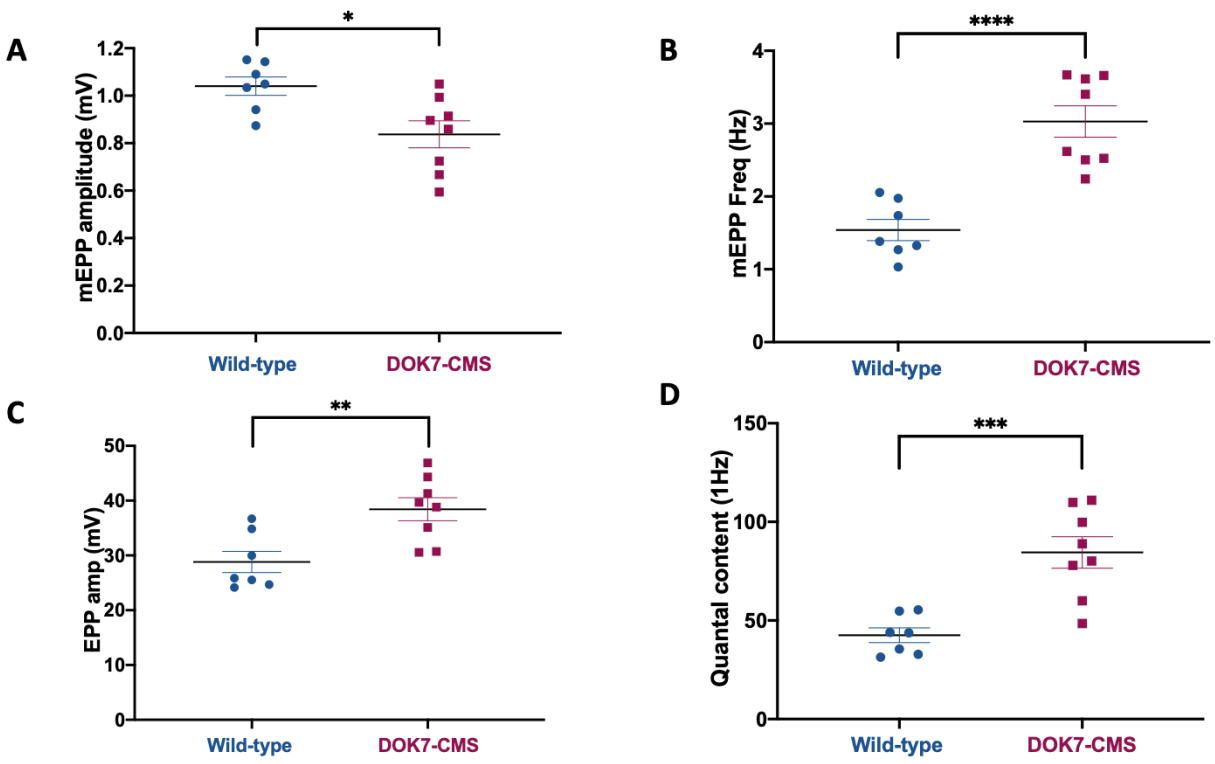

Figure 4.8. Recordings of electrophysiological parameters. *Ex vivo* hemidiaphragm-phrenic nerve preparations were used to record mEPP amplitudes (**A**) and frequencies (**B**) as well as EPP amplitudes (**C**) and quantal content (**D**). Average values from 7-15 recordings for each individual animals are represented as single data points. Data is overall represented as mean ±SEM. Unpaired t tests were used to compare between the two groups (*p<0.05; **p<0.01; ***p<0.001; ****p<0.001; n=7 wild-type (4 female mice and 3 male mice) and 8 model mice (5 female mice and 3 male mice)).

4.7. Analysing changes in NMJs morphology

We next investigated whether there are any changes considering the neuromuscular junction morphology in response to DOK7 gene therapy treatment. This was investigated at the end of the treatment, on mice of 18-32 weeks old. Whole-mount diaphragm muscles and teased fibres of the extensor digitorum longus (EDL) and soleus muscles were stained using α-bungarotoxin for the AChRs and neurofilament and synaptophysin antibodies for the axons and nerve terminals. Z-stack of at least 15 NMJ areas per mouse were taken using a 25x objective, and areas, intensity of staining and number of enlarged NMJs were analysed using Fiji software. All images were taken using the same settings. Representative images for each muscle are shown in **Figure 4.9**.

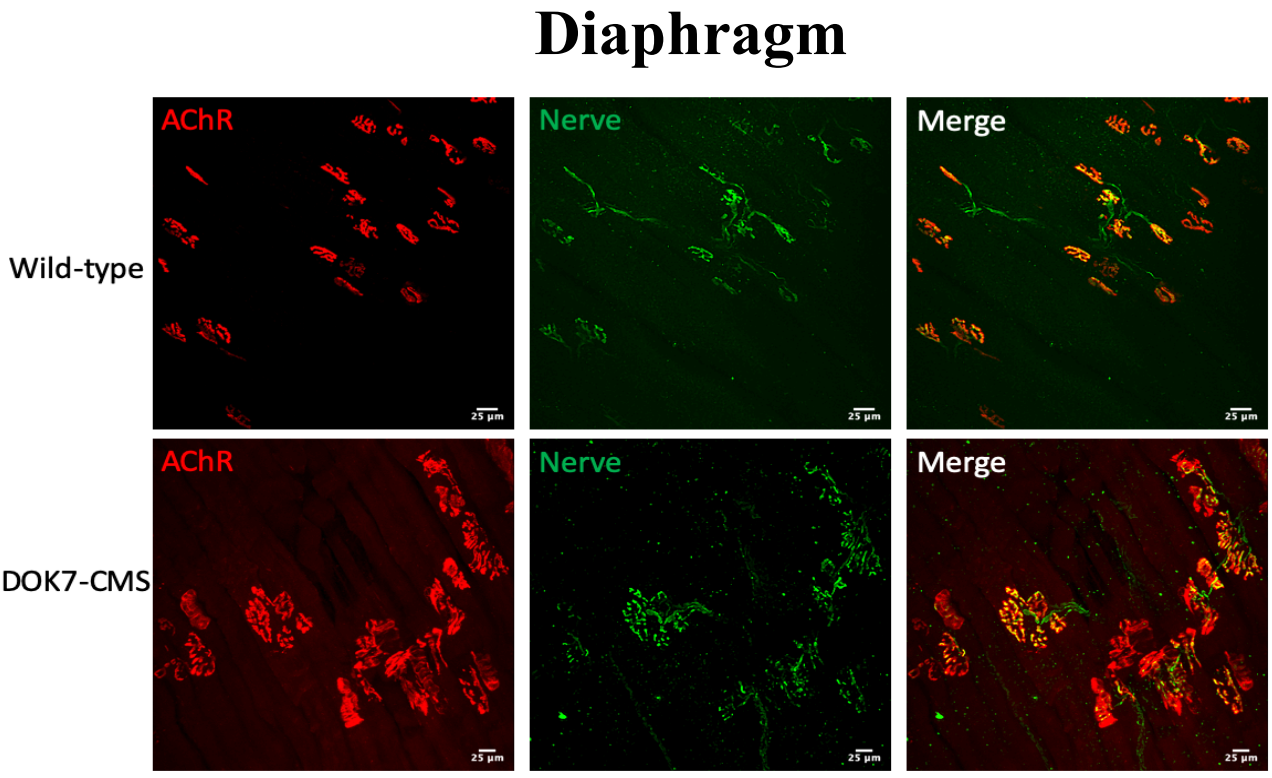

*Image continues on the next page

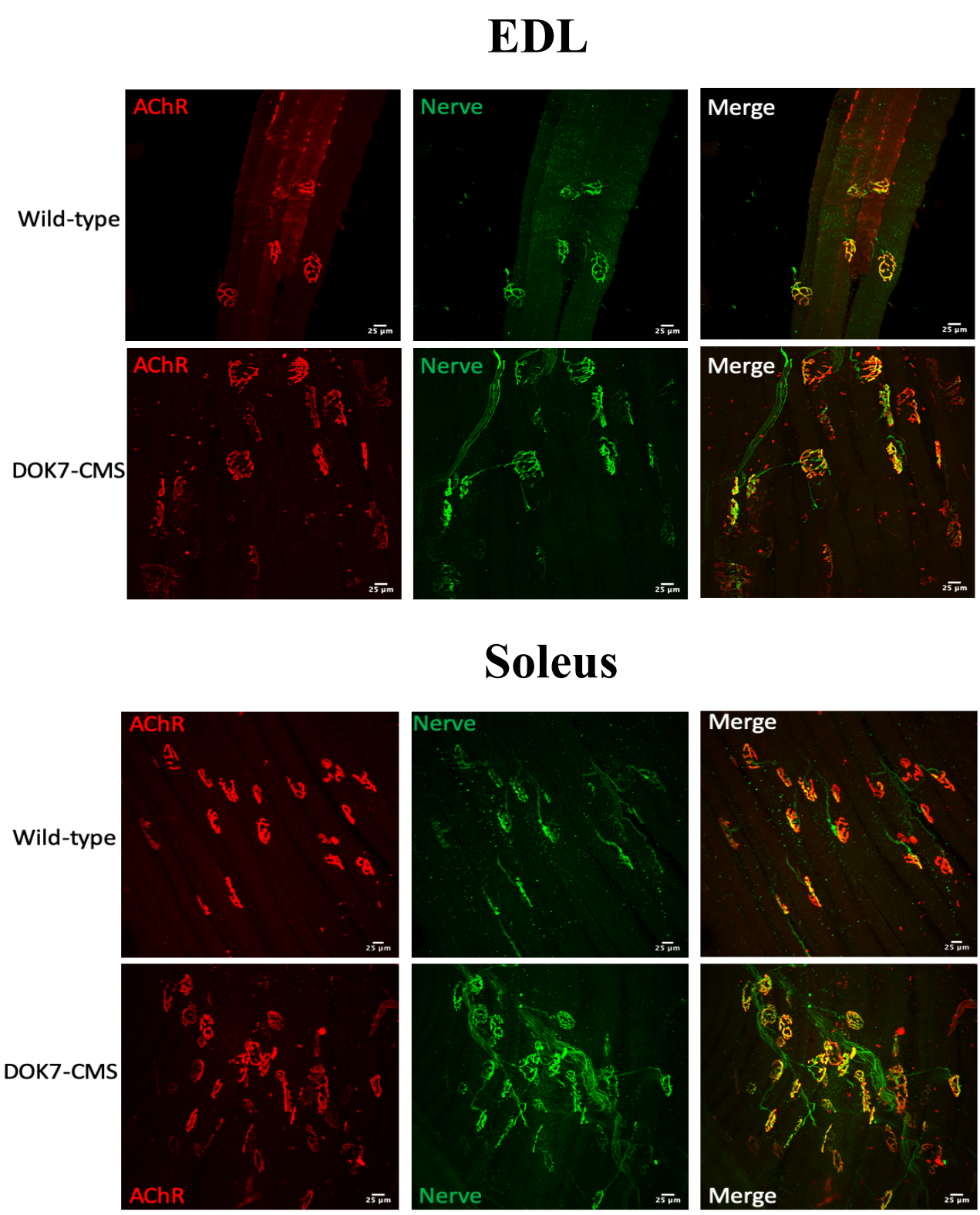

Figure 4.9. Fluorescent staining of NMJs. Dissected diaphragm, EDL and soleus muscles were stained with fluorescent α-bungarotoxin for the AChR (red) and neurofilament and synaptophysin for the nerve and presynaptic area (green). Merged pictures are shown in the panels on the right. (Scale bar: 25μm)

4.7.1. Changes in the presynaptic and nerve terminal areas

We first compared the postsynaptic and nerve terminals stained regions in all three muscles for both wild-type mice and DOK7 gene therapy treated model mice. Areas of both AChRs and nerve were significantly bigger in gene therapy treated mice in comparison to the controls for diaphragm and EDL muscles (**Figure 4.10**). An approximatively 75% increase was seen in the diaphragm muscle for both regions (**Figure 4.10.A**). EDL muscles of gene therapy treated mice presented NMJs with 53% increase in the AChR area, and 45% increase in the nerve terminal region in comparison to control muscles (**Figure 4.10.B**). For the soleus muscles the only significant changes were observed for the AChR area with 20% increase (**Figure 4.10.C**).

We next assessed the α-bungarotoxin/nerve coverage ratio to establish the extent to which the postsynaptic and nerve terminal areas overlap considering the diaphragm, EDL and soleus muscles. This was represented as the ratio between the AChRs and nerve areas. Ratios above 1 would suggest an enlarged postsynaptic area as compared to the nerve region. An overall tendency of increased AChR areas was observed in the gene therapy treated model mice as shown by ratios above 1 for all three muscles in **Figure 4.10.D**. This was overall significant for all three muscles ($p=0.0072$) and more marked in the diaphragm and EDL muscles. No significant differences were seen between the three muscles for the two treatment groups (**Figure 4.10D**).

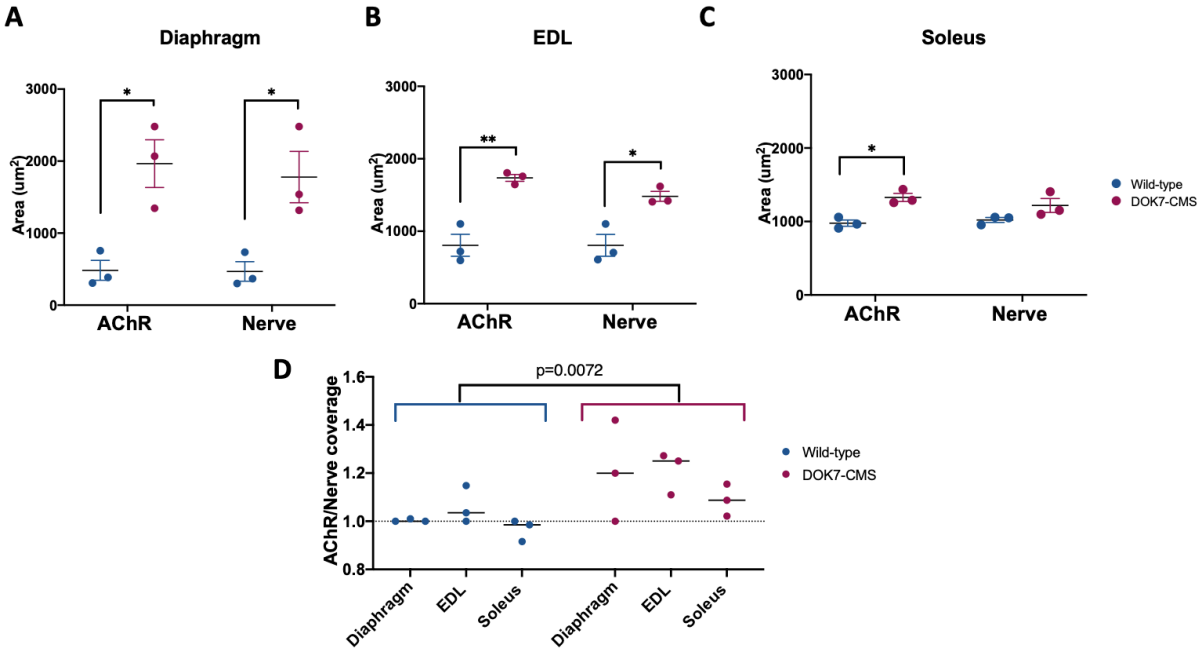

Figure 4.10. Nerve and AChRs areas analysed in muscles of gene therapy treated model mice in comparison to control. Tissue was collected and immunolabeled to visualize AChRs and the presynaptic area in the diaphragm (**A**) EDL (**B**) and soleus (**C**) muscles. Parameters were measured for both control (blue) and treated (red) mice. Data points represent average values of at least 15 NMJs. The values of the two treatment groups were compared using a two-way ANOVA with Tukey's multiple comparison tests. AChR/Nerve coverage ratios for the three muscles were compared between the two treatment groups and were analysed using a two-way ANOVA with Sidak's multiple comparison tests (**D**) (*$p<0.05$; **$p<0.01$; mean ± SEM; n= 3 wild-type (2 female; 1 male) and 3 DOK7-CMS treated mice (2 females; 1 males)).

4.7.2. Staining intensity between presynaptic and nerve terminal areas

While analysing NMJs parameters overall, intensity of staining for the nerve terminal areas appeared faint for certain samples, so we next assessed quantitatively changes in fluorescence intensity between the two treatment groups. Staining intensities are represented by the mean grey value for each fluorescent NMJ area, normalised to the mean grey value of the background control per each microscopic field. A slight decrease in staining intensity for the nerve area as compared to postsynaptic region was observed in the diaphragm muscle independent of the treatment group and this was significant (p=0.03) (**Figure 4.11.A**). No significant changes were seen between the gene therapy treated mice and wild-type mice for any of the muscles (**Figure 4.11**).

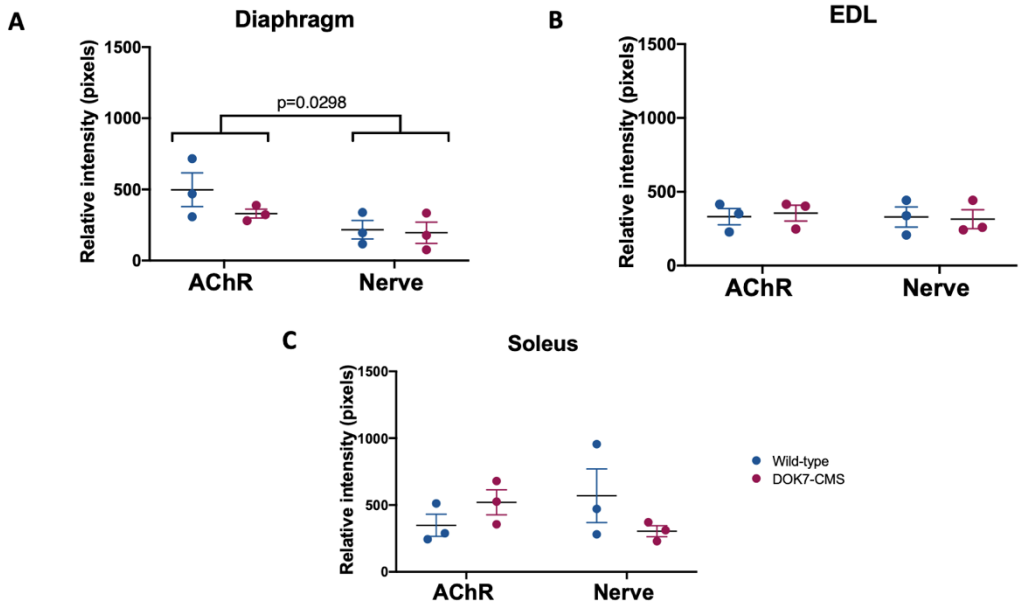

Figure 4.11. Intensity of staining of nerve and AChRs areas analysed in muscles of gene therapy treated model mice. Tissue was collected and immunolabeled to visualize AChRs and the nerve in the diaphragm (**A**), EDL (**B**), and soleus (**C**) muscles. Parameters were measured for both control (blue) and treated (red) mice. Data points represent average values of at least 15 NMJs ± SEM. The intensity of each individual NMJ (average grey value of pixels) was normalized to the mean background control. The values of the two treatment groups were compared using a two-way ANOVA with Tukey's multiple comparison tests (n=3 wild-type (2 female; 1 male) and 3 DOK7-CMS treated mice (2 females; 1 males)).

4.7.3. The percentage of enlarged NMJs

Having shown an increase in AChR areas in the muscles of gene therapy treated mice for diaphragm and EDL muscles, we next looked at the postsynaptic staining in all three muscles for both treatment groups using lower magnification confocal images (10x) to comprise more NMJs/field, and be able to calculate the percentage of enlarged NMJs (gene therapy efficiency). Increased staining area, corresponding with increased postsynaptic areas, was seen in all muscles of the gene therapy treated mice (DOK7-CMS), with ~1.7-fold increase in the diaphragm and soleus muscles and 1.4 in EDL (**Figure 4.12**). No significant differences were seen in the number of AChR areas per microscopic field as analysed by a two-way ANOVA test (**Figure 4.12.D**).

Also, more than half of the analysed NMJs were larger in the gene therapy mice with 62% in the diaphragm muscle, 69% in the EDL and 76% in the soleus muscle (**Fig.12E**). The 95% confidence interval (CI) for the wild-type groups considering each muscle were calculated, and all NMJs that had the AChR area bigger than the upper limit of the 95% CI of the wild-type group, were considered enlarged. The percentage of enlarged NMJs for each muscle were calculated from 10x microscopic fields, from a total of at least 90 NMJs/field in the diaphragm and 40 NMJs/field in the leg muscles, for each individual mouse.

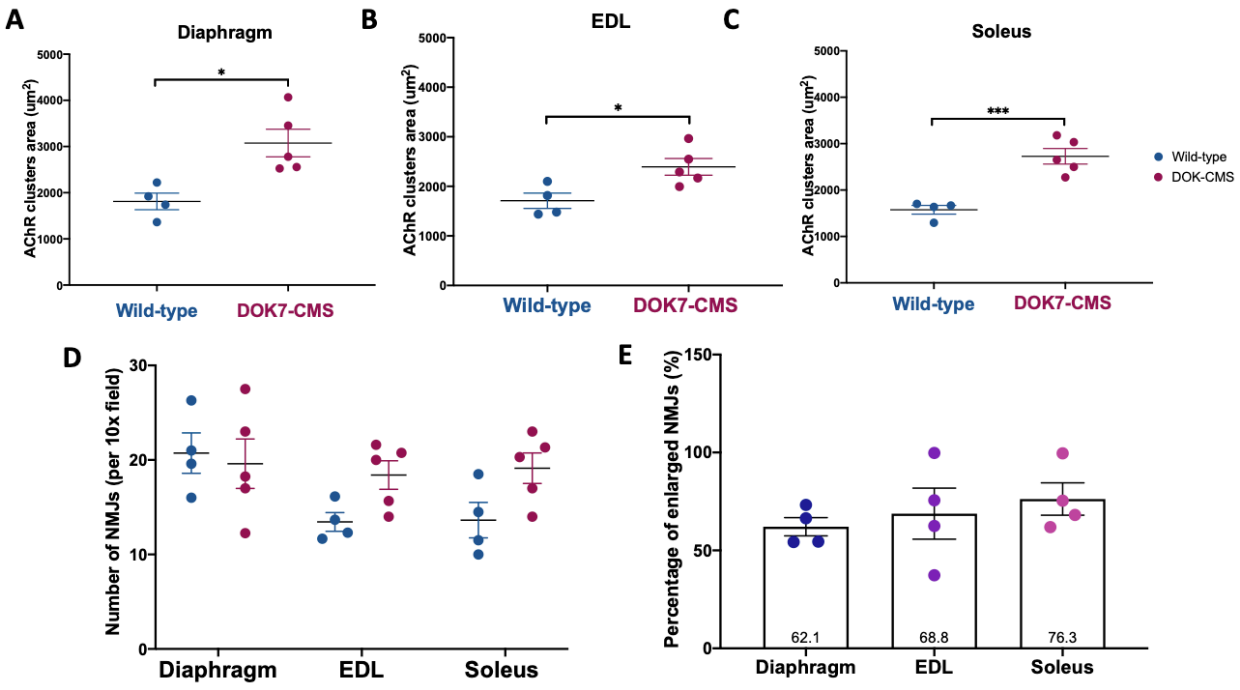

Figure 4.12. Analysis of enlarged postsynaptic areas in gene therapy treated model mice. Tissue was collected and immunolabeled to visualize AChRs in the diaphragm (**A**) EDL (**B**) and soleus (**C**) muscles. Parameters were measured for both control (blue) and treated (red) mice. Data points represent average values of at least 40 NMJs per animal. Unpaired t tests were used to compare the two treatment groups considering all three muscles (**A**, **B**, **C**). A two-way ANOVA with Tukey's multiple comparison test was performed to compare the number of NMJs per microscopic field overall, as well as for each individual muscle (**D**). Percentages of enlarged NMJs for the three muscles are shown in panel **E**. (mean ± SEM; n=4 wild-type (2 female; 2 males) and 5 DOK7-CMS treated mice (3 females; 2 males))

4.8. DOK7 overexpression in other muscle groups

DOK7 overexpression induces the formation of enlarged synaptic structures. Having shown that treated mice present enlarged AChR areas in diaphragm, EDL and soleus muscles but with a certain amount of variability between individual tissues and animals, we next analysed expression in other skeletal muscles. We used tissue from an alternative leg muscle (tibialis anterior-TA) and heart. Tissue was homogenised and used to purify the human DOK7 EGFP tagged protein by immunoprecipitation using a mouse monoclonal Dok7 antibody. Samples from both gene therapy treated model mice as well as controls were then subject to SDS-PAGE and western blotting (using the same mouse monoclonal Dok7 antibody) (**Figure 4.13.A**). Signal intensities, analysed using Fiji software, showed DOK7 EGFP expression only in gene therapy mice as expected (**Figure 4.13**).

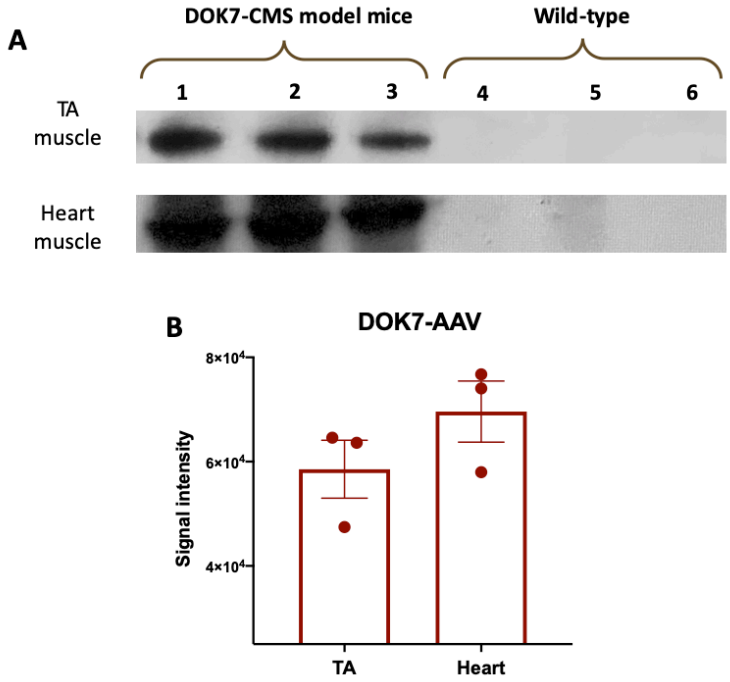

Figure 4.13. DOK7 EGFP protein expression in muscles of gene therapy treated model mice. Heart and tibialis anterior (TA) muscles were dissected and homogenized in lysis buffer. DOK7 EGFP tagged protein was purified from the whole lysate by immunoprecipitation using a mouse monoclonal Dok7 antibody from both gene therapy (1,2,3) and control tissues (4,5,6). Western blotting (**A**) was used to detect the 85.7 kDa DOK7 protein (53 kDa DOK7 protein +32.7 kDa EGFP). The signal intensities for the two muscles were measured by Fiji (**B**) (n=3 mice per group).

4.9. Discussion

This study brings additional information to the previously reported study of using DOK7 gene therapy in a mouse model of DOK7 congenital myasthenic syndrome (Arimura et al. 2014). DOK7 gene therapy was shown to increase the lifespan and improve motor functions of these mice. By use of decrement test, *ex vivo* electrophysiological recordings and analysis of NMJ morphology, we showed that DOK7 gene therapy provides sufficient human DOK7 protein to compensate for the endogenous mutant Dok7 and thus restore neuromuscular junction function. Indeed, sufficient DOK7 is synthesised to induce enlarged NMJs with implications for therapy in alternative conditions.

DOK7 is a key muscle-intrinsic activator of MuSK and plays a crucial role in the formation and maintenance of NMJs (Okada et al. 2006; Inoue et al. 2009). The importance of this protein is also observed in our DOK7-CMS model mice that reach humane endpoints shortly after birth (by P7-10). This is likely due to respiratory failure that could be caused by disorganised innervation and decreased numbers of AChR-stained NMJs in neonatal DOK7 myasthenic mice as shown previously (Webster et al. 2020).

DOK7 gene therapy improved the probability of survival in the DOK7 myasthenic mice with 57% still alive by day 20 of age (**Figure 4.3**). This is different from the previous study that showed 100% survival of the DOK7 gene therapy treated pups with a one-time dose between P9 to P12 (Arimura et al. 2014). Even though the same mouse model was used, in our hands the untreated pups fail to gain enough weight to be able to survive for the same amount of time as shown in the study (P13-P20), and need to be euthanised between P7-P10. Also, the phenotype of DOK7-CMS mice only becomes obvious from ~P4.

This has brought some constraints to the experimental design of our study, emphasizing the need of an early administration of the gene therapy which at the same time had to be late enough to allow us to identify potential model mice. Thus, the decrease in survival percentage is likely linked to the short timeframe available for DOK7 gene therapy administration, as well as the challenges associated with performing intraperitoneal injections on 4 days old pups. Six of the injected mice survived past P15, however, they failed to gain weight post-treatment and had to be humanely euthanised (**Figure 4.4**). This suggests an insufficient effect of the gene therapy treatment, likely linked to the possibility that the administered treatment was leaking through the IP puncture wound which was visible on the thin skin of neonatal mice. Another possibility for losing these mice is that the injections could have punctured into internal organs leading to damage. Perhaps an intravenous way of administration could be considered for future studies, providing that the myasthenic mice could be identified early enough (Lampe et al. 2014).

Mutations in the DOK7 gene cause a limb-gridle CMS characterised by abnormal neurotransmission due to impairment of the AChR clustering pathway (Beeson et al. 2006; Selcen et al. 2008; Cossins et al. 2012). The phenotype of the DOK7-CMS model mice used in this study is more severe than the phenotype of humans carrying the same mutation as mentioned (1124_1127dupTGCC). The unexpected level of severity puts limits on the use of this mouse model in future studies. However, overexpression of DOK7 resulting from DOK7 gene therapy was previously shown to restore the phenotype (Arimura et al. 2014). In our hands, the model mice showed improved lifespan, and motor function comparable to age-matched wildtype counterparts as assessed by the inverted screen hang test (**Figure 4.6**).

Besides being considered a parameter of general wellbeing, body weight was monitored as response to gene therapy treatment in neonatal mice and was also taken into account for the inverted screen assay (**Figure 4.4A** and **Figure 4.5**). Even though the treatment has a remarkable effect on survival, the DOK7 gene therapy treated model mice appeared smaller than the wild-type mice (~14% lower body weight at 18 weeks of age independently of the gender) (**Figure 4.5** and **Figure 4.14**). The observation is in contrast with the study done by Arimura and colleagues, who showed that at P56 there was no difference in weight between DOK7-AAV treated model mice and wild-type littermates. This is likely due to variability of the DOK7 gene therapy efficiency across muscle fibres. Also, we showed in the protein expression studies and NMJs fluorescent staining that DOK7 gene therapy reached similarly various muscles across the body, however it did vary between individual animals (**Figure 4.12E** and **Figure 4.13**). This may be linked to the fact that the treatment was given at a very early age. Synapse elimination happens approximately in the first two weeks of life in mice (Ribchester 1988). During the early stages of development, most of the muscle fibres are innervated by many neurons and present multiple areas of AChRs. Once axons withdraw, the non-innervated AChRs disappear leaving only one motor endplate per muscle fiber, which could very well be the least affected by the gene therapy treatment (Balice-Gordon and Lichtman 1993). It is also possible that the process of synapse elimination could be affected by the overexpression of DOK7 to some extent.

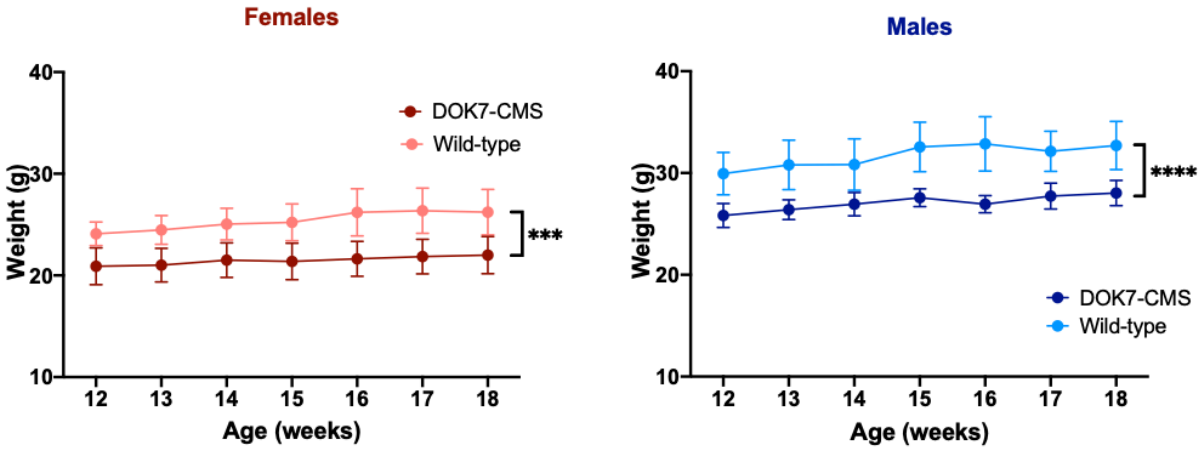

Figure 4.14. Body weight of adult gene therapy treated model mice divided by gender. Data and error bars are represented as means ± SEM over a period of 6 weeks. A two-way ANOVA with Sidak's multiple comparison test was performed to compare the two groups overall and considering each timepoint (***p<0.001; ****p<0.0001; n=5 females and 3 males/treatment group).

Decrement of CMAP on repetitive nerve stimulation was recorded in gene therapy treated DOK7-CMS model mice as assessed by EMG. It was found to be ~30% at the highest frequency tested (**Figure 4.7**). This contrasts with the results of the muscle strength test that showed no differences between the treated model mice and wild-types (**Figure 4.6.B**). DOK7 protein plays an important role in pre-patterning as well as axon pathfinding during development (Beeson et al. 2006; Okada et al. 2006; Arimura et al. 2014). Both of these features are impaired in the DOK7-CMS neonatal mice as shown previously, and probably the DOK7 gene therapy cannot restore the effects on the NMJs completely (Arimura et al. 2014; Webster et al. 2020). This might also be an explanation for the 6 treated mice that were given gene therapy treatment, survived longer than non-treated animals, but were lost during the treatment protocol. A 10 minutes cut-off was applied to the inverted screen test, and therefore it is possible that we could have seen significant changes in fatigable muscle strength between

the wild-type and treated mice if the time was extended to 20 or 30 minutes. It would be of interest to test this in the future.

Reduced EPP amplitude and quantal content are the main electrophysiological changes characteristic to the DOK7-CMS patients as reported before (Beeson et al. 2006; Slater et al. 2006). In a study using neonatal DOK7-CMS model mice, lower mEPP frequencies were observed amongst their active fibres (Webster et al. 2020). Here we found a significant increase in EPP amplitudes and quantal content for the gene therapy treated myasthenic mice in comparison to the wild-type mice (**Figure 4.8.C**,**D**). Even though mEPP amplitudes were lower in the gene therapy treated DOK7-CMS mice, the frequencies of these mEPPs were significantly higher (**Figure 4.8.A**,**B**). In summary, for the functional properties of neuromuscular transmission following DOK7 gene therapy of the DOK7-CMS model mice our results demonstrate a marked improvement.

Given that some of the electrophysiological parameters of the DOK7-CMS model mice showed not only improvement but were significantly increased when compared to the wild-type mice, we next investigated NMJs morphology (**Figure 4.9**). Electrophysiological changes following DOK7 gene therapy correlated with an increase in NMJs area in diaphragm, EDL and soleus muscles of model mice (**Figure 4.10** and **Figure 4.12**). Also, there was an overall tendency of larger postsynaptic area in comparison to the nerve terminal area as shown by the AChR/Nerve coverage ratios analysis in these mice (**Figure 4.10D**). Moreover, we showed that more than 60% of the postsynaptic areas appeared enlarged in the diaphragm, EDL and soleus muscles (**Figure 4.12E**). Neonatal DOK7-CMS model mice show reduced number of AChR aggregates in diaphragm muscles (Okada et al. 2006; Webster et al. 2020). This was restored in our model mice as the number of analysed NMJ areas per 10x microscopic field were similar to the ones

of wild-type mice (**Figure 4.12.D**). A tendency of reduced staining of the nerve areas was observed in the diaphragms of DOK7-CMS model mice (**Figure 4.11**). However, this was also seen in the wild-type mice, suggesting that it could be a characteristic of the genetic background of this mouse strain. Perhaps this observation could explain the fact that one of the wild-type phrenic nerve hemidiaphragm preparations failed (mentioned above). However, this observation needs further investigations but has inherent difficulties since the mouse model was not originally generated in our laboratory.

The treated model mice were relatively strong, slightly underweight and they presented with considerable muscle decrement. Besides being influenced by the time of treatment administration and the transduction efficiency of DOK7-AAV therapy treatment across different animals, this might suggest a small residual effect of altered neurotransmission. The *ex vivo* electrophysiological recordings support this statement by showing obvious differences in neurotransmission as compared to the wild-type mice. We and others have also shown that the ratio of nerve to postsynaptic membrane coverage was altered in such way that not all of the enlarged AChRs are aligned with potential AChR release sites (**Figure 4.10D**) (Eguchi et al. 2020). This might suggest that altering the size and shape of the NMJs is not ideal for the tissue and requires the presence of an adaptive mechanism to limit excessive transmission. This limitation of neurotransmission could end up being excitotoxic and that might be more evident while assessing CMAP by high frequency repetitive nerve stimulation than muscle fatigability by a hang screen test.

DOK7 gene therapy improves motor function and lifespan of DOK7-CMS model mice while the overexpression of DOK7 also induces the formation of enlarged AChR areas. Our results support the use of DOK7-AAV gene therapy in a mouse model of DOK-CMS, and highlights

the potential of DOK7 overexpression as a therapeutic approach for CMS and other neuromuscular disorders. A key question to be addressed in the future is the role of the enlarged synaptic size and what precisely are the advantages and disadvantages of this fundamental biological alteration, as well as if indeed the synaptic enlargement could be transposed to other species including humans.

Chapter 5

DOK7-AAV gene therapy as a treatment for AChR deficiency CMS

5.1. Introduction

One of the most common forms of CMS in patients is the Acetylcholine receptor (AChR) deficiency, which is usually due to homozygous or heteroallelic mutations in the AChR ε-subunit (Parr 2014). These mutations lead to various levels of impaired neurotransmission caused by reduced AChR expression at the postsynaptic membrane.

It is well known that patients with AChR deficiency benefit from treatment with acetylcholinesterase inhibitors. However, long-term treatment can lead to a reduced therapeutic effect (Engel 2007). In a recent report, β2–adrenergic agonists were shown to improve long-term response to pyridostigmine in patients, thus showing the potential for combined treatment for AChR deficiency (Rodríguez Cruz et al. 2015). This was later emphasised in a study done by Vanhaesebrouck et al. that confirmed the reduction of pyridostigmine treatment benefits, in an AChR deficiency mouse model over time, and showed that these can be recovered by salbutamol, a β2–adrenergic receptor agonist (Vanhaesebrouck et al. 2019).

DOK7 is an important component of the AChR clustering pathway at the NMJ, and its upregulation induces enlarged AChR cluster areas in various muscles of wild-type mice, as

shown in **Chapter 3** (Okada et al. 2006; Beeson et al. 2006; Arimura et al. 2014). Given the fact that mutations causing AChR deficiency result in low expression of AChRs, we hypothesised that DOK7 overexpression could induce AChR upregulation at the NMJ, ultimately improving neurotransmission and thus the myasthenic phenotype. DOK7-AAV gene therapy could become an alternative one-time treatment for AChR deficient patients in the future, avoiding therefore the need for long-term combined treatments and possible side effects. The potential of DOK7-AAV gene therapy in a mouse model of DOK7-CMS was shown in **Chapter 4**.

In order to address this hypothesis, we investigated the efficiency of DOK7-AAV gene therapy in an AChR-deficiency mouse model previously generated in the laboratory (discussed below) (Cossins et al. 2004). The study aims to ultimately provide evidence and rationale for the use of DOK7 gene therapy in most CMS.

5.1.1. The AChR deficiency mouse model

An ε-subunit knock-out muse model was previously designed to study AChR deficiency (Witzemann et al. 1996; Missias et al. 1997). The phenotype of these mice appeared much more severe as compared with their human counterparts, as model mice presented with limited lifespan of only 8-14 weeks of age. While the foetal AChR γ-subunit expression persists at low levels throughout human life, in mice this is not the case (Croxen 2001). The γ-subunit still expressed in humans is thought to be incorporated into the adult AChRs expressed at the postsynaptic membrane, thus compensating for the loss of ε-subunit.

An AChR deficiency mouse model that constitutively expresses the human AChR γ-subunit in an ε-subunit knockout background was subsequently generated to address this problem (**Figure 5.1A,B**) (Cossins et al. 2004). The transgene containing a skeletal muscle promotor α-actin and the human AChR γ-subunit, was inserted into the genome of an AChR ε-subunit knockout mouse model on the X-chromosome. This mouse model reflects the human AChR deficiency condition, having a less severe myasthenic phenotype. The homozygous mice presents a characteristic myasthenic phenotype of reduced weight, fatigable muscle weakness and reduced miniature endplate potentials (mEPPs) and endplate potentials (EPPs) (Cossins et al. 2004). Thus, with a well characterised phenotype and normal lifespan, this mouse model represents an adequate choice for assessing the benefits of the DOK7-AAV gene therapy as a treatment of AChR deficiency.

Transgenic mice were identified by PCR with specific primer pairs to detect the human transgene (AChR γ-subunit), the neomycin cassette that confirms the complete or partial (on one allele) knockout of the ε-subunit, and the AChR ε-subunit DNA. Heterozygous mice ($h\gamma^{+}\varepsilon^{+/-}$) were crossed to generate AChR deficiency model mice ($h\gamma^{+}\varepsilon^{-/-}$), which were identified by the absence of the ε-subunit PCR band and the presence of neomycin and AChR γ-subunit amplicons (**Figure 5.1C**).

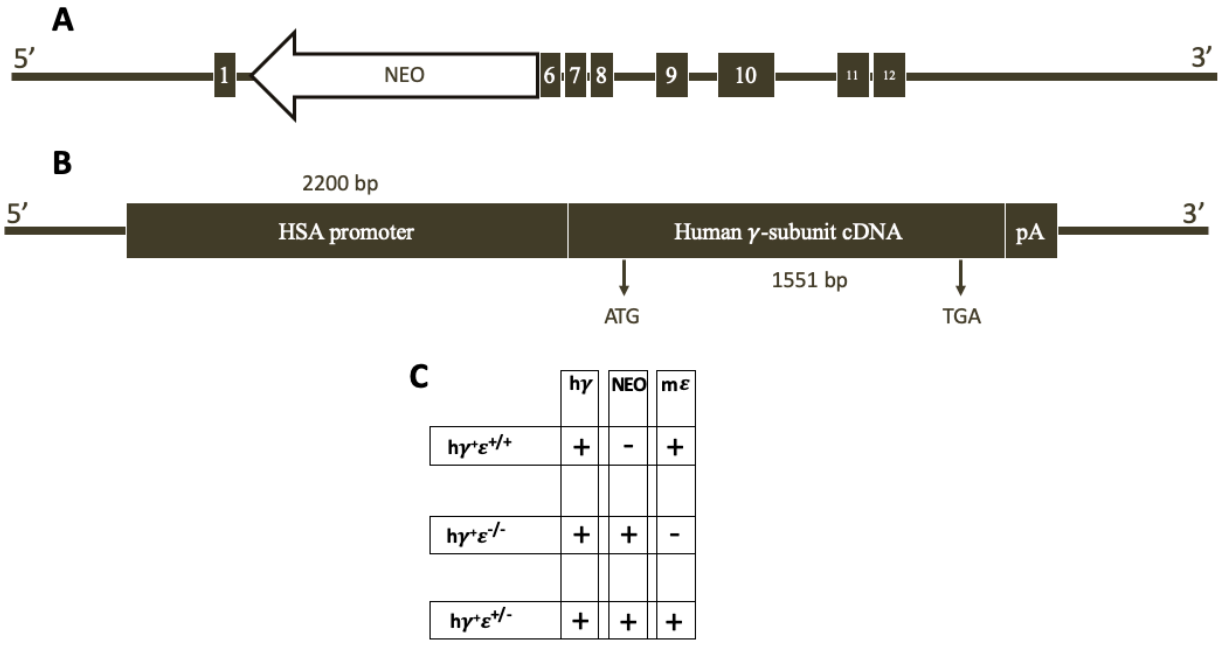

Figure 5.1. Generation of AChR-deficiency mouse model. The location of the neomycin cassette in the mouse ε gene is shown in panel **A** (Missias et al. 1997). Brown boxes indicate exons and the arrow shows the direction of transcription for the neomycin cassette. Exons 2 to 5 of the AChR ε-subunit gene (encoding 150 amino acids of the mature protein's N-terminal) were replaced by the neomycin resistance gene. The AChR deficiency mouse model was designed using the ε-subunit knockout mouse model by adding a transgene cassette containing a 2.2 kb sequence of the human α-actin promoter with its regulatory regions followed by the human muscle AChR γ-subunit cDNA (+ the SV40 large T poly(A) site) **(B)**. Genotyping of the progeny from $h\gamma^{+}\varepsilon^{+/-}\times h\gamma^{+}\varepsilon^{+/-}$ mice is shown in panel **C**. Genomic DNA was used as a template for the PCR amplifications. Specific primers were used to detect the human AChR γ-subunit DNA (hγ, 290 bp), the neomycin resistance gene (NEO, 333 bp), and the mouse AChR ε-subunit gene (ε, 352 bp)**.** Examples of each genotype are shown: wildtype mice expressing human γ - $h\gamma^{+}\varepsilon^{+/+}$, model mice- $h\gamma^{+}\varepsilon^{-/-}$ and heterozygote mice- $h\gamma^{+}\varepsilon^{+/-}$.

5.1.2. Gene therapy experimental design

Experiments were conducted in AChR-deficiency model mice for two treatment groups: DOK7 EGFP-AAV gene therapy and SHAM (vehicle control). Genotyping was performed on 2 weeks old mice and treatment was administered intraperitoneally (IP) at 3 weeks old. Dosage and route of administration were decided based on previous work done by Arimura and colleagues and the work presented in **Chapter 3**. Given the fact that AAV9 systemic transduction in intraperitoneally (IP) injected adult mice was shown to be achieved at comparable levels to intravenous administration, IP was used in this study (Inagaki et al. 2006; Bostick et al. 2007). Two doses were tested (**Figure 5.2**):

- low dose- $4x10^{11}$vg/mouse (same as in **Chapter 3**)
- high dose- $1x10^{12}$vg/mouse

Muscle fatigability was assessed once a week by an inverted screen hang tests beginning with 6 weeks of life at identical times of the day. A cut-off of 10 minutes was applied for the inverted screen test. Tests of decrement on EMG were performed at various ages depending on the dose group. A gradual loss of strength that plateaued at around 12 weeks of age was previously noticed in this mouse model (J. Cheung, unpublished data). This time-dependent reduction in hang time is thought to be linked to the gradual loss of the endogenous mouse γ-subunit expression and thus of the mouse foetal AChRs.

A small number of one-time pyridostigmine add-on experiments were also performed towards the end of the protocol to assess for combination treatments. Based on a pilot study done on

AChR deficiency mice by Dr An Vanhaesebrouck (data not published), 14 mg/kg/day of pyridostigmine was given via drinking water at least 24 hours prior to the muscle fatigability assessment. To assess whether the effect of the drug was removed from the system prior to performing other experiments, an inverted screen test was performed 72 hours after last administration.

At the end of each study trial, mice were humanely euthanised for *ex vivo* analysis of NMJ function and morphology. Electrophysiological recording and decrement of CMAPs following repetitive nerve stimulation were performed by Richard Webster. AChR-deficient mice are further referred to as model mice.

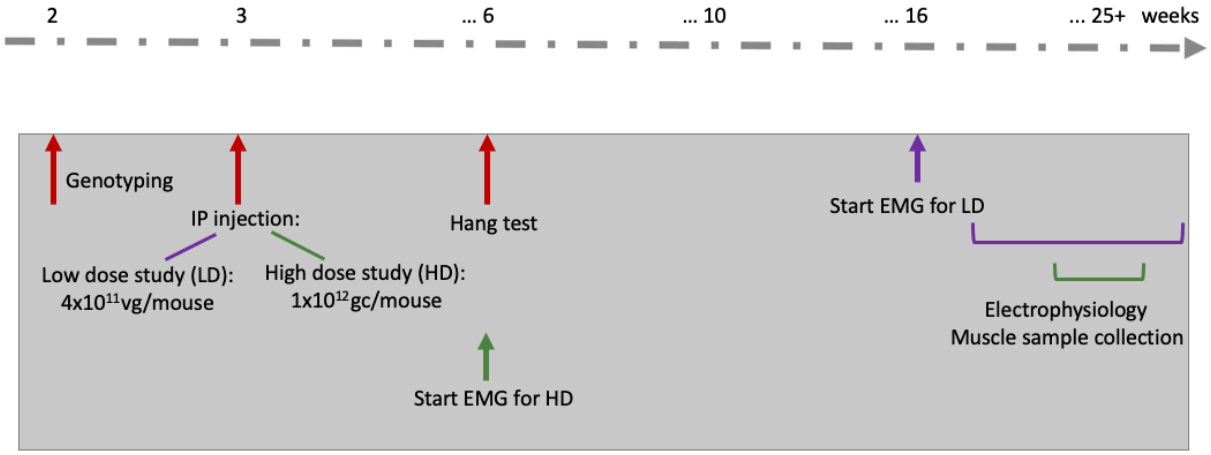

Figure 5.2. Schematic representation of study design for using DOK7-AAV gene therapy in AChR-deficient mice. To test the efficiency of DOK7-AAV gene therapy in AChR deficiency mice, two trials were designed: low-dose (purple) and high-dose (green). Model mice were injected intraperitoneally at 3 weeks of age with the gene therapy treatment or saline solution (SHAM).

5.2. DOK7 gene therapy low-dose treatment

Twelve female and ten male mice were injected intraperitoneally as follows: six females and five males with DOK7-AAV gene therapy ($4x10^{11}$vg/mouse), and six females and five males with vehicle control (SHAM) (**Figure 5.3**). Starting at 6 weeks of age, their muscle fatigability was assessed by an inverted screen test once a week for a period of 10-24 weeks until they were sacrificed for *ex vivo* electrophysiological recordings and tissue collection. One week before study endpoint, an electromyography (EMG) CMAP decrement test was performed. To asses if treatment effect was sustained over time, mice were divided into two age groups: 15-18 weeks of age and 27-30 weeks of age. Experiments and analysis were done in a blinded fashion.

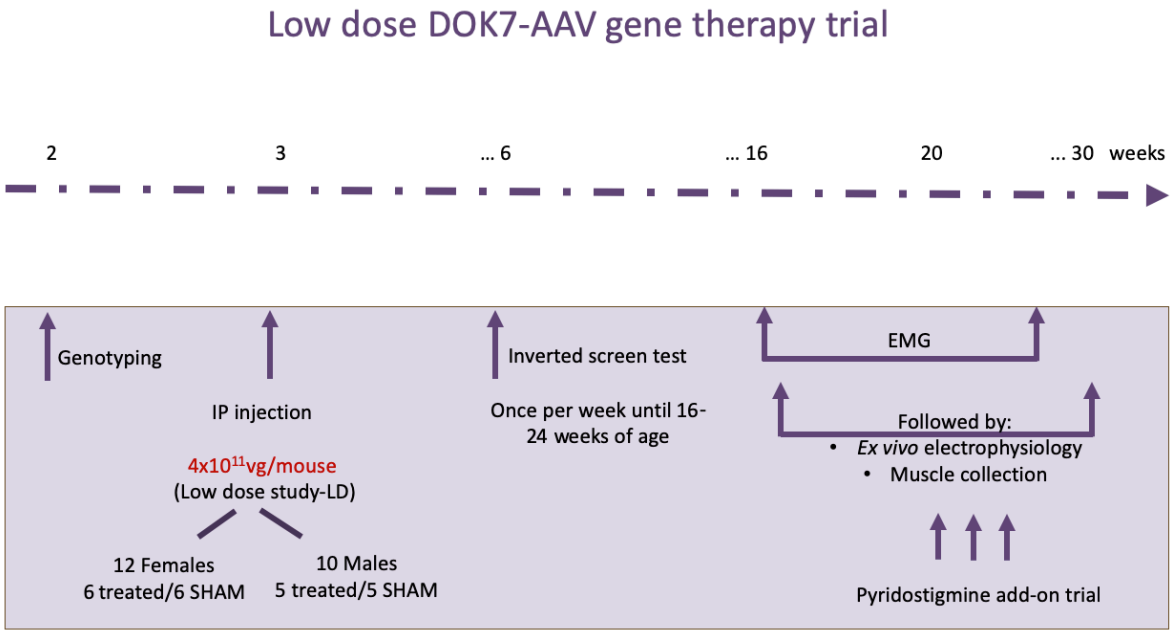

Figure 5.3. Schematic representation of study design for using low-dose DOK7-AAV gene therapy. Model mice were injected intraperitoneally at 3 weeks of age with $4x10^{11}$vg/mouse or vehicle control. Inverted screen hang tests started at 6 weeks old, once a week up until 16-24 weeks of age. Decrement tests were performed starting at 16 weeks of age (EMG). Pyridostigmine was used as a one-time add-on treatment towards the end of the trial. Animals were ultimately euthanised for *ex vivo* electrophysiology and muscle collection.

5.2.1. Evaluation of body weight during treatment trial

To investigate whether the gene therapy treatment affected body weight, model mice were weighed once a week during the trial. For consistency, this was measured at the same time every week. DOK7 gene therapy treated model mice overall gained more weight during the trial than the SHAM treated mice (females-7% and males-5%) (**Figure 5.4**). A slight drop in weight was observed at 16 weeks of age independent of gender or treatment group. The weight gain was more significant for females.

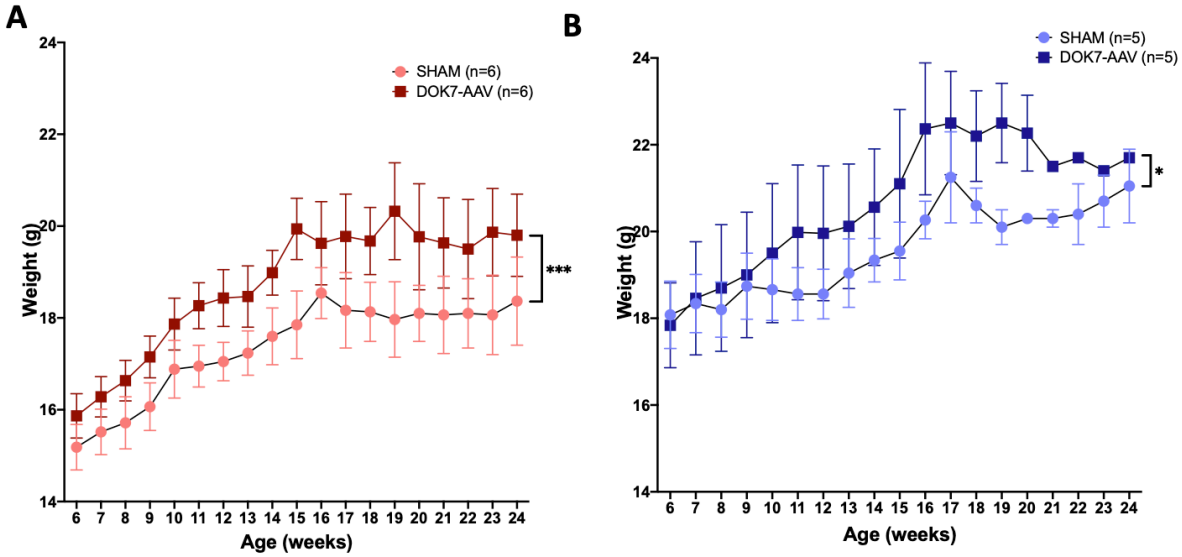

Figure 5.4. Body weight of low-dose model mice during low-dose treatment trial. Body weight of mice from both gene therapy treated and SHAM groups were monitored for the whole period of treatment trial for females (**A**) and males (**B**). Data was collected over a period of 18 weeks starting with 6 weeks of age. Each data point represents the mean hang time from all mice in a treatment group with the same age as shown by x axis, ±SEM. A two-way ANOVA test was performed to compare the two treatment groups, and Sidak's multiple comparison were used to compare between individual timepoints (age) (*p<0.05; ***p<0.001; n=5 male and 6 female mice per treatment group).

5.2.2. Muscle fatigability of model mice during treatment trial

To evaluate the clinical response to treatment, muscle fatigability of treated and control model mice was assessed once weekly during treatment trial by an inverted screen test. **Figure 5.5** shows results for both females (**A**) and males (**B**). The gradual decrease in strength mentioned above was observed until 12 weeks of age for model mice independent of gender or treatment group.

A marked improvement in hang time was observed for gene therapy treated model mice. Overall during treatment trial this was ~30% in females (**A**) and ~68% in males (**B**).

A gradual worsening in performance was observed for females from week 16 to 22 of age. Male model mice treated with DOK7-AAV gene therapy showed a higher significance in hanging times than the females. A multiple comparison test with Sidak's correction was used to compare between the two treatment groups for both genders at different timepoints (age) throughout the trial. No significant differences were observed, most likely due to high variability between animals within each treatment group at given timepoints.

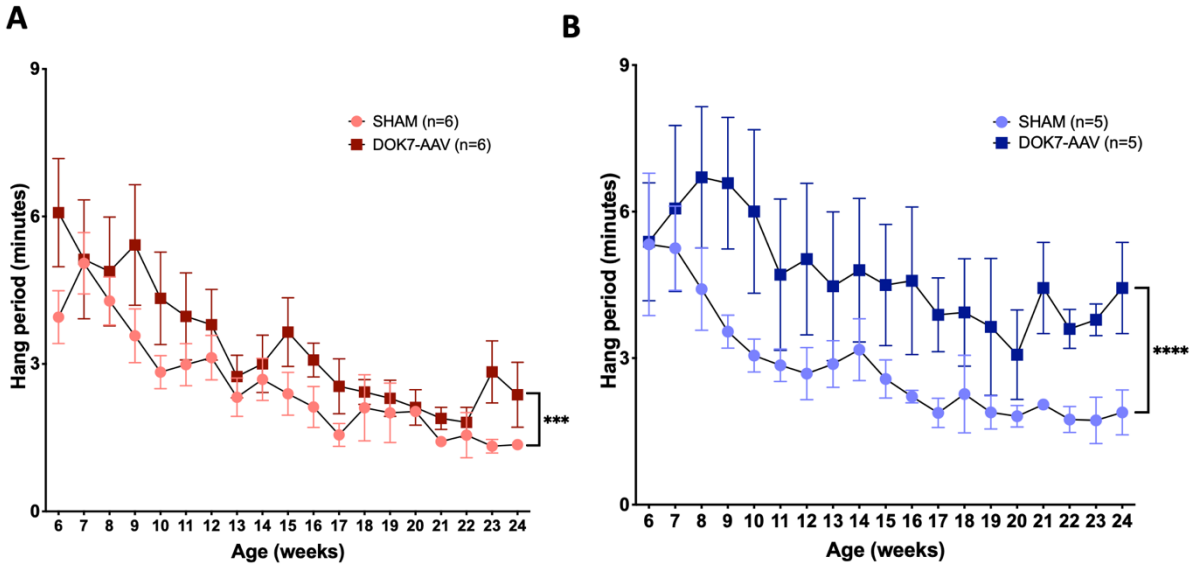

Figure 5.5. Muscle fatigability as assessed by inverted screen test model mice during low-dose treatment trial. Mice from both the gene therapy treated and SHAM groups were assessed using an inverted screen test. Data was collected over a period of 18 weeks starting with 6 weeks of age. Each data point represents the mean hang time from all mice in a treatment group with the same age as shown by x axis, ±SEM. A two-way ANOVA test with Sidak's multiple comparison test was performed to compare the two groups overall and considering individual ages for both females **(A)** and males **(B)** (***p<0.01; ****p<0.0001; n=5 male and 6 female mice per treatment group).

A significant difference in body weight was observed between DOK7-AAV-treated and SHAM-treated mice in **Figure 5.4** for both males and females. To assess for a relationship between the body weight and inverted screen hang time, correlation analyses were performed on average values for individual timepoints (age). A negative correlation was observed between body weight and hang time for both males and females of each treatment group as shown in **Figure 5.6**, and this was significant.

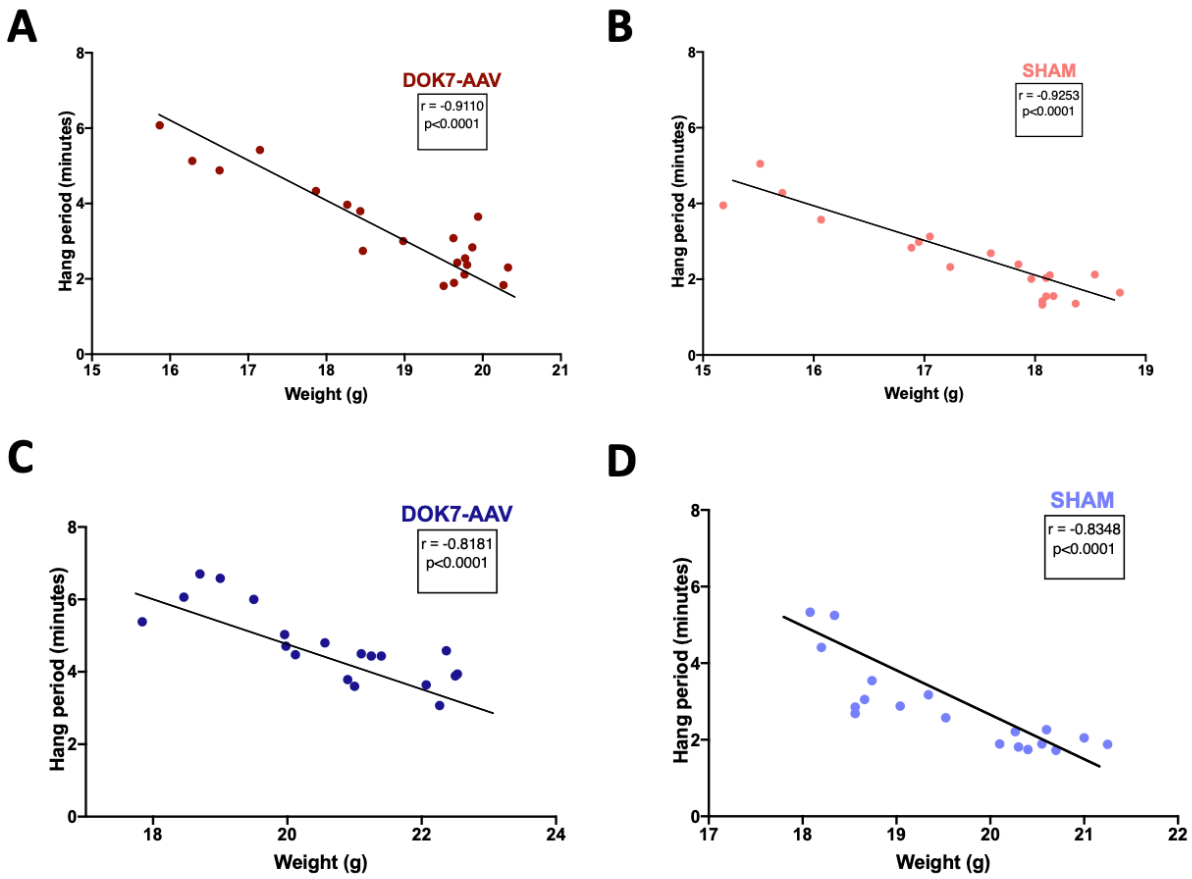

Figure 5.6. Correlation between hang period and body weight in model mice during low-dose treatment trial. Mean results of hang time and bodyweight for each individual age timepoint were correlated. Correlation graphs for females are shown in **A** and **B** and for males in **C** and **D** (**B** and **D** showing the control groups). A negative correlation (negative r) was seen for all animals independently of gender or treatment group (individual p values are shown for each graph; n=5 male and 6 female mice per treatment group).

To account for the negative correlation between hang time and body weight of model mice, data collected from the inverted screen test was normalised to body weight for each individual mouse (**Figure 5.7**). Given the fact that females showed a higher significant difference in body weight than males when comparing DOK7-AAV-treated mice with SHAM-treated mice (**Figure 5.4A**), the overall difference in hang time appeared slightly higher after normalisation.

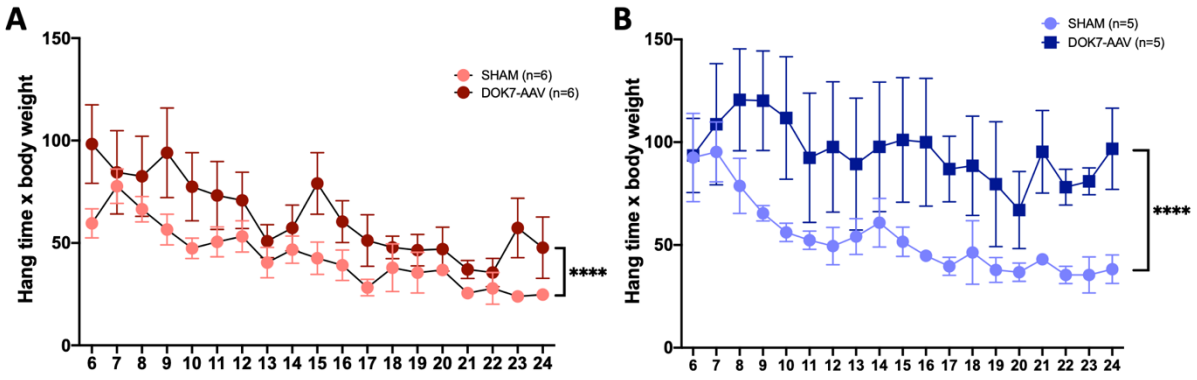

Figure 5.7. Hang time normalised to body weight in model mice during low-dose treatment trial. Data was collected over a period of 18 weeks starting with 6 weeks of age for females **(A)** and males **(B)**. Each data point represents the mean hang time from all mice in a treatment group with the same age as shown by x axis, ±SEM. A two-way ANOVA with Sidak's multiple comparison test was performed to compare the two groups overall and considering individual time points of each week (****$p<0.0001$; n=5 male and 6 female mice per treatment group).

5.2.2.1. Evaluation of muscle fatigability after pyridostigmine treatment

Pyridostigmine treatment was added towards the end of the trial to test the efficiency of short-time combination treatments. Improvements in hang time were recorded for model mice independent of the treatment group as expected. However, the model mice treated with DOK7-AAV gene therapy showed a greater increase in hang time with 73% for females and 55% for males when a cut-off of 10 minutes for the hang time was applied (**Figure 5.8**).

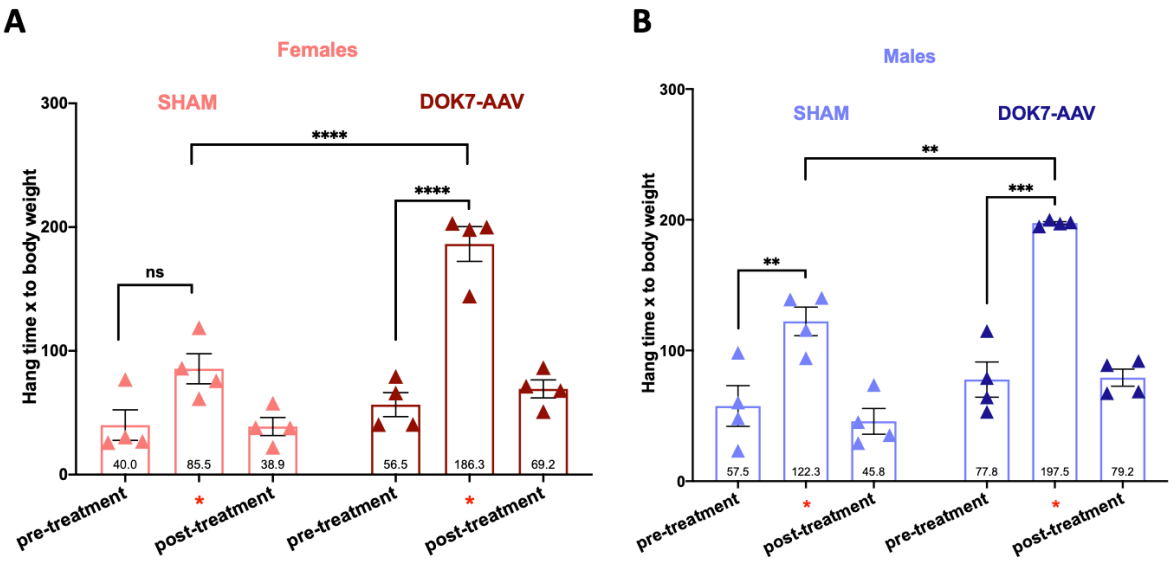

Figure 5.8. Muscle fatigability as assessed by inverted screen test in model mice during low-dose treatment trial after one-time pyridostigmine treatment. Mice from both the gene therapy and SHAM treated groups were assessed for muscle strength using an inverted screen. Data and error bars are represented as means ± SEM for both females **(A)** and males **(B)** for before, during (*) and after the treatment (assessed 72h after last dose received). A two-way ANOVA with Tukey's multiple comparison test was performed to compare between treatment groups at different timepoints during pyridostigmine treatment trial (*p<0.05; ***p<0.001; ****p<0.0001; n=4 mice per treatment group).

In conclusion, gene therapy treated animals showed improved muscle strength for both males and females. The improvement was more accentuated when pyridostigmine was used as an add-on treatment.

5.2.3. Decrement of compound muscle action potentials following repetitive nerve stimulation in model mice during treatment trial

Having shown a clear difference in muscle fatigability during treatment trial in model mice, we next examined whether these differences coincided with a corresponding improvement in decrement of compound muscle action potential (CMAPs) on EMG, as a measure of overall neurotransmission efficiency. To do this, measurements of decrement following repetitive nerve stimulation were used to compare the two treatment groups at the end of the treatment trial. Mice were anaesthetised, the sciatic nerve was repetitively stimulated and CMAPs were successively recorded from the gastrocnemius muscles.

The decrement was calculated as the difference between the 1st and the 10th CMAP recordings, and the percentage of reduction was used to compare the decrement between the two treatment groups. Stimulation frequencies varied between 1 to 20 Hz and muscle decrement increased concomitantly with stimulation frequencies for model mice independent of the treatment and gender (**Figure 5.9**). No significant differences in muscle decrement were observed overall or at different frequencies between the two treatment groups for either females (**Figure 5.9A**) or males (**Figure 5.9B**).

As mentioned in **Section 5.2**, model mice were divided into two age groups to evaluate changes in treatment efficiency over time. Higher decrement (females -13%; males -11%) was observed in mice of 15-18 weeks as compared to 27-30 weeks of age, for gene therapy treated males and females (**Figure 5.9C,E**). No age-related differences were observed for the control groups (**Figure 5.9D,F**).

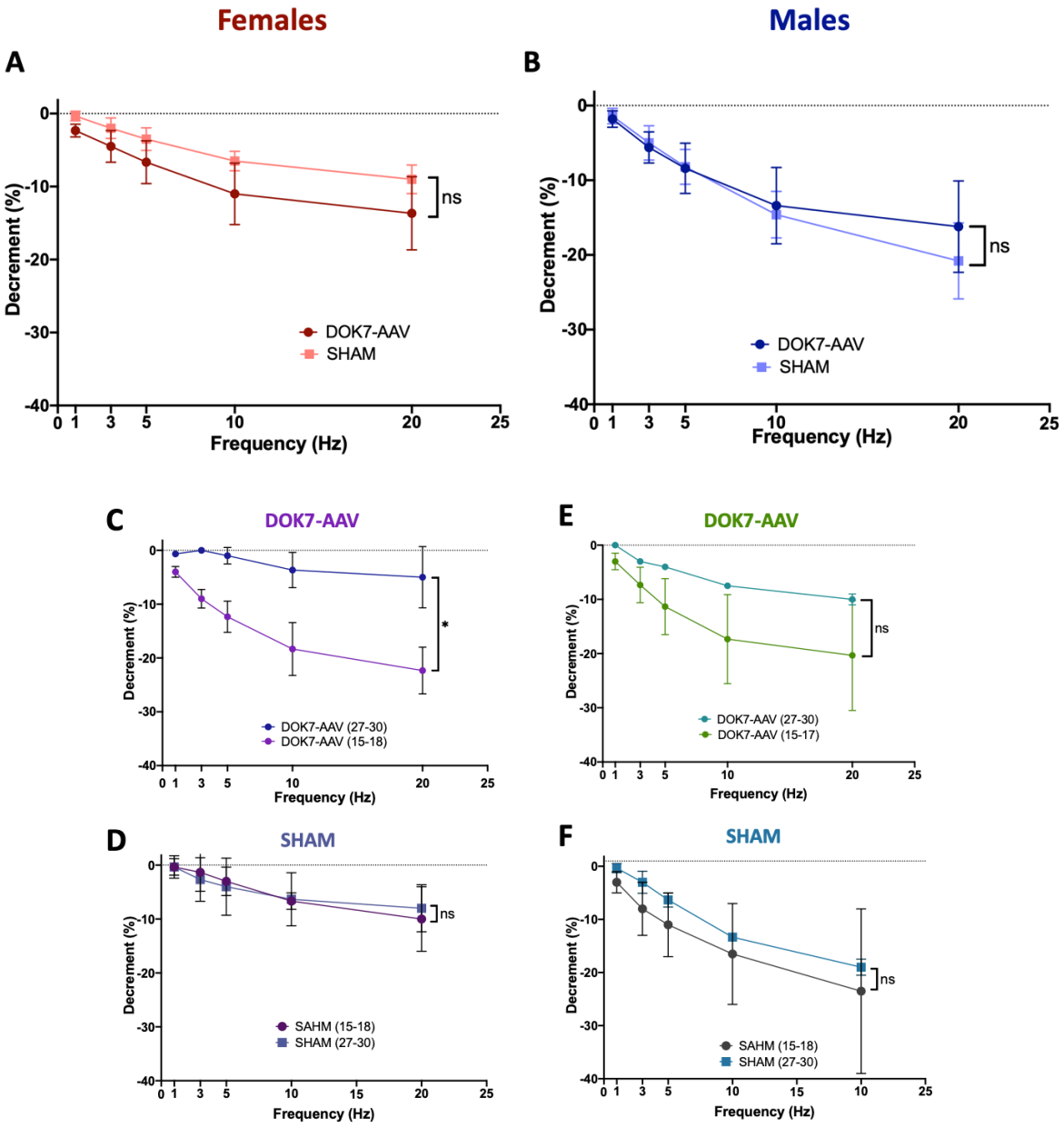

Figure 5.9. Decrement results of model mice during treatment trial. Mice from both the gene therapy treated and SHAM groups were anaesthetised and prepared for decrement test. Individual data points represent the mean ±SEM at different frequencies for females (**A**) and males (**B**). Comparison between younger and older mice are shown in panels **C** and **D** for females and in **E** and **F** for males. A two-way ANOVA repeated measurements with Sidak's multiple comparison tests were performed to compare overall between the SHAM and the gene therapy treated mice as well as between different frequencies timepoints (ns.- non-significant; *p<0.05; n=5 male and 6 female mice per treatment group; Age groups: males- n= 2 mice/SHAM and 3/DOK7-AAV treatment group and females- n=3 mice for each treatment group).

In conclusion, gene therapy model mice did not show significant improvement in muscle decrement, however, there was a difference within the gene therapy group between younger and older mice, with younger mice presenting higher decrement, and that was significant for females.

5.2.4. Ex vivo electrophysiological recordings of neuromuscular transmission following gene therapy treatment

To understand whether DOK7-AAV gene therapy leads to changes in neurotransmission, mice were sacrificed one week subsequent to the decrement test and *ex vivo* hemidiaphragm-phrenic nerve preparations were used to collect detailed recordings of endplate transmission. Miniature endplate potentials (mEPPs), endplate potentials (EPPs) and quantal content were measured upon μ-conotoxin blockage of muscle action potentials. 15 to 20 endplates per animal were analysed.

The small and spontaneous leakage from the nerve terminal of a single neurotransmitter containing vesicle results in small depolarisations that are called miniature endplate potentials (mEPPs). The depolarisation of the resting membrane potential is induced when the ACh (released from the vesicles) binds to the AChRs on the postsynaptic membrane. Since the mEPP amplitudes is thought to depend on AChR density, their measurements were used to compare between both genders and treatment groups. No differences in mEPP amplitudes were observed for any gender or treatment group (**Figure 5.10A**), suggesting the density of endplate AChR is not altered by DOK7-AAV. However, significantly higher frequencies of mEPPs were observed for DOK7-AAV treated model mice for both genders (2.6 times higher in males; 2.7 times higher in females) (**Figure 5.10B**)

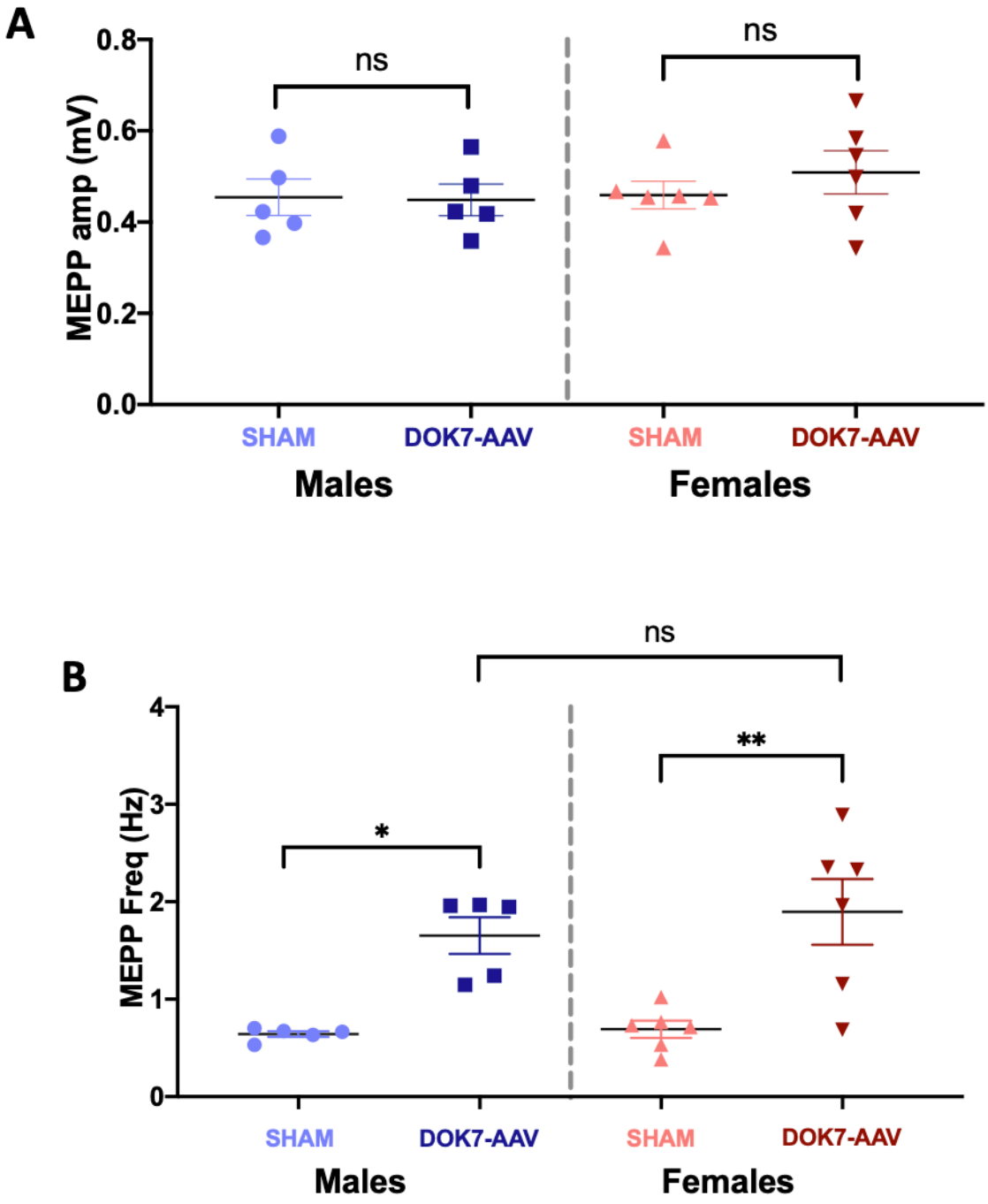

Figure 5.10. Amplitudes (A) and frequencies (B) of mEPPs recorded from diaphragm preparations of model mice following gene therapy treatment. Data points represent the mean ± SEM. A one-way ANOVA with Tukey's multiple comparison test was performed to understand the differences between treatment groups and gender (*p<0.05; **p<0.01; n=5 male and 6 female mice per treatment group).

EPPs were evoked by applying brief depolarising pulses to the phrenic nerve at 1 Hz. Each of the pulses resulted in neurotransmitter release from the nerve terminal, causing a large depolarisation at the postsynaptic membrane. **Figure 5.11.A** shows EPP amplitude for both SHAM and DOK7-AAv gene therapy mice for each gender. An approximate 52% increase was seen in the mean EPP amplitudes in males treated with DOK7-AAV in comparison to SHAM. Similarly, a 29% increase was observed for the females.

Quantal content is a measure of the number of quanta released per stimulation. It is calculated by dividing the EPP amplitudes (recorded at 1 Hz) by the mEPP amplitudes (with correction for non-linear summation). An increase was observed for both males and females DOK7-AAV treated model mice in comparison to control, of 80% and 53% respectively (**Figure 5.11B**).

In conclusion, mEPP frequencies, EPP amplitudes and quantal content were increased in DOK7-AAV gene therapy treated mice, suggesting an increased endplate size and a higher number of presynaptic vesicle release as evidenced by the change in quantal content, with no change in AChR density at the postsynaptic membrane as represented by the lack of change in mEPP amplitudes. No gender or age-dependent differences were observed.

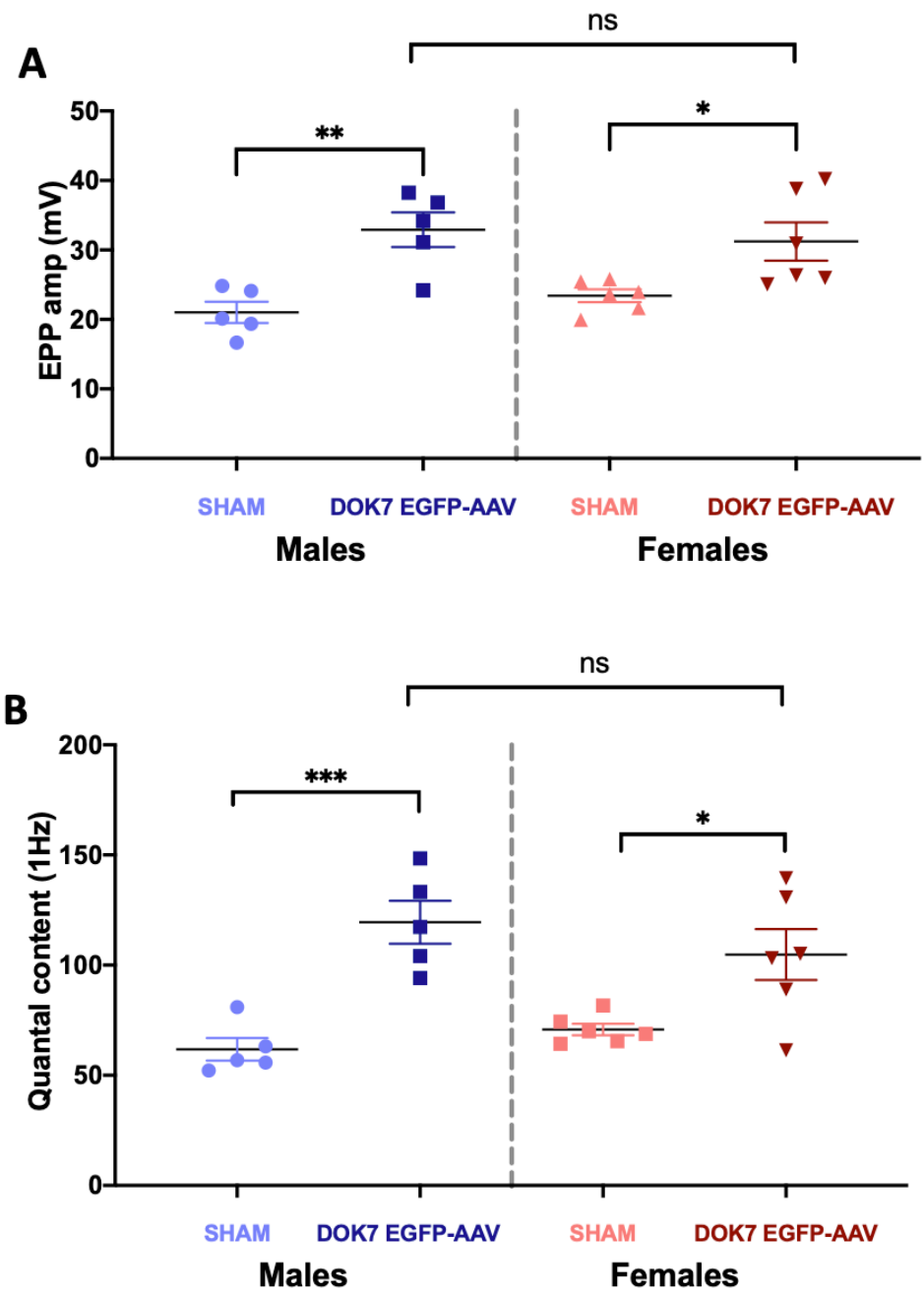

Figure 5.11. Amplitudes of EPPs (A) and Quantal content (B) recorded from diaphragm preparations of model mice following gene therapy treatment. Data points represent the mean ± SEM. A one-way ANOVA with Tukey's multiple comparison test was performed to understand the differences between treatment groups and gender**.** (*p<0.05; **p<0.01; ***p<0.001; n=5 male and 6 female mice per treatment group)

5.2.5. DOK7-AAV transduction efficiency in different muscles of treated model mice

Hitherto we have shown clear differences in fatigable muscle weakness as analysed by an inverted screen test and most of the electrophysiological parameters recorded for the DOK7-AAV gene therapy treated model mice. In **Chapters 3** and **4** we showed that DOK7-AAV gene therapy induced the formation of enlarged synapses in both wild-type mice and a DOK7 deficiency mouse model. Accordingly, in this chapter, electrophysiological changes pointed towards changes in the postsynaptic structure. Thus, we next examined for possible alterations of the NMJ structure by immunolabelling AChR clusters with fluorescent α-bungarotoxin.

In **Chapter 3**, we used the measurements of AChR clusters to quantify the AAV transduction efficiency in various muscles. Using the same technique, at least 75 individual NMJs per mouse were analysed for the extensor digitorum longus (EDL), soleus and diaphragm muscles. NMJs with an AChR cluster area larger than the upper limit of the 95% CI of the SHAM group were defined as enlarged. Fiji software was used to measure AChR areas for both genders and representative images are shown in **Figure 5.12**.

Diaphragm

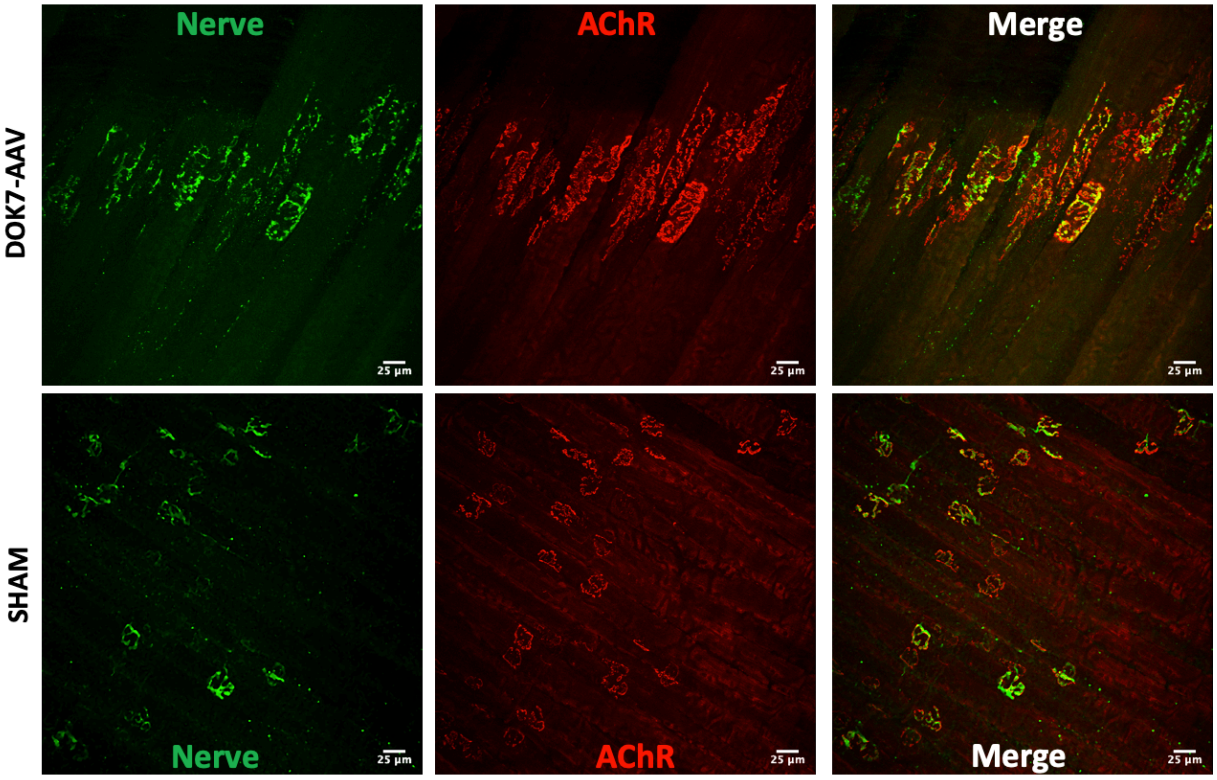

EDL

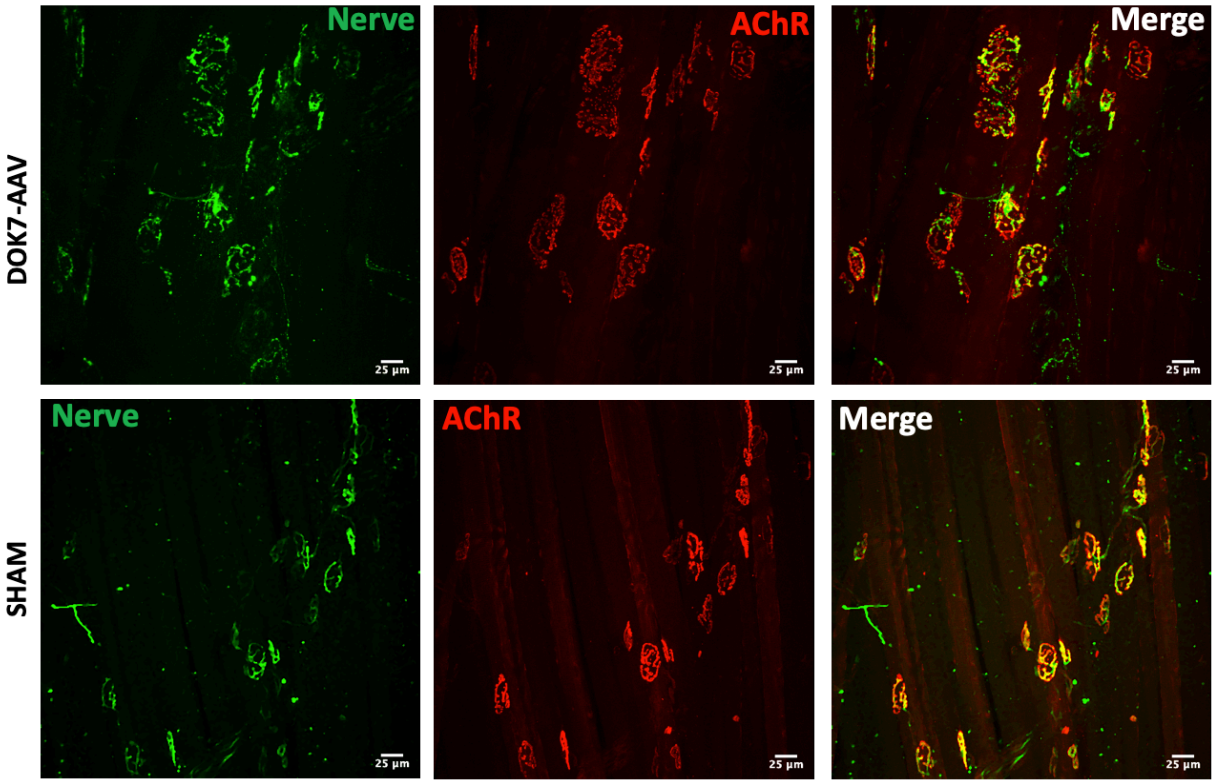

*Image continues on the next page

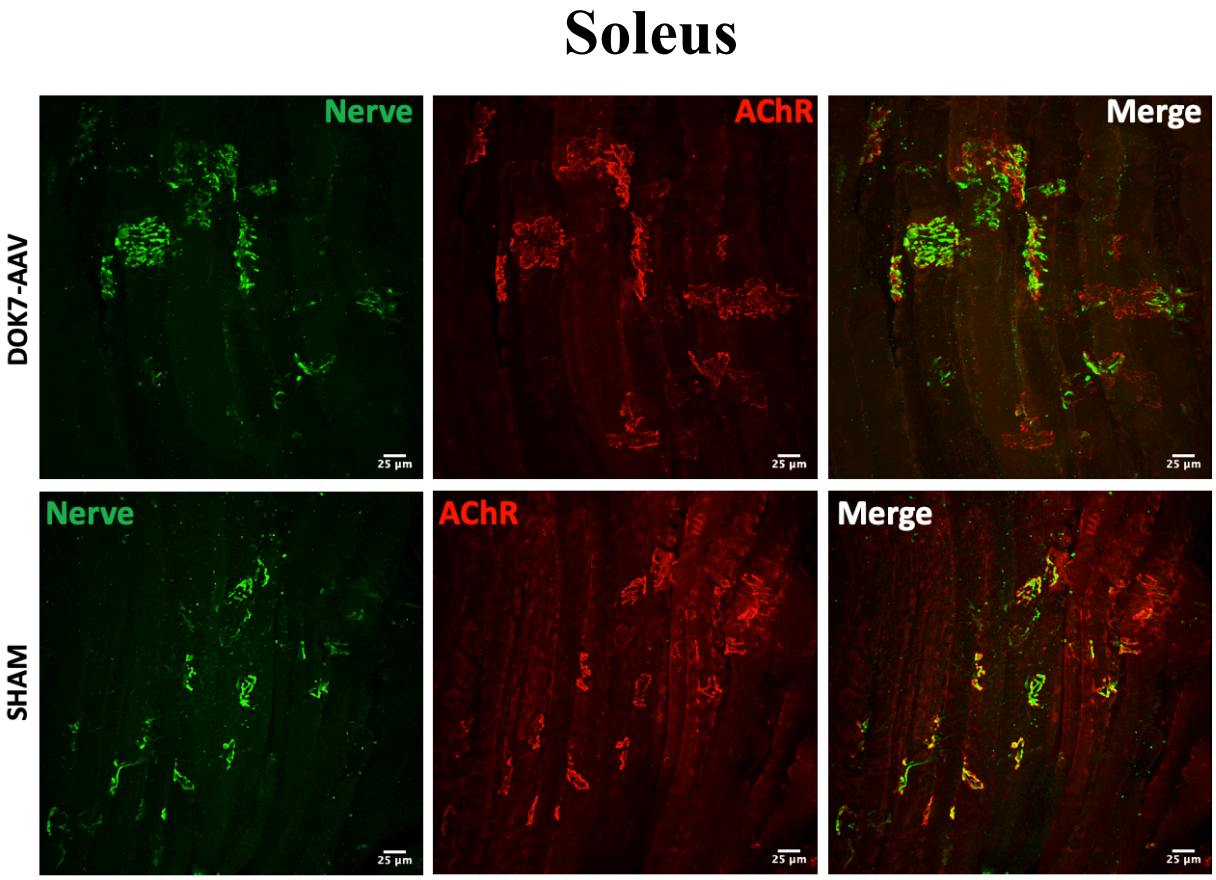

Figure 5.12. Fluorescent staining of model mice NMJs following DOK7-AAV gene therapy treatment trial. Dissected diaphragm, EDL and soleus muscles were stained with fluorescent α-bungarotoxin for the AChR (red) and neurofilament and synaptophysin for the nerve and presynaptic area (green). Merged pictures are shown in the panels on the right (Scale bar: 25µm).

Greater AChR cluster areas were seen in gene therapy treated mice for both males and females in all three muscles when compared to control. The increase was significant for females, with a 2.14-fold increase in the EDL, 2 in the soleus muscle and 2.85 in the diaphragm (**Figure 5.13A,C,E**). With a 3.25-fold increase in the EDL muscle, 2.25 in the soleus muscles and 3.7 in the diaphragm, males showed significant higher AChR areas in all three muscles as well (**Figure 5.13B,D,F**). No age-dependent differences were observed (data not shown).

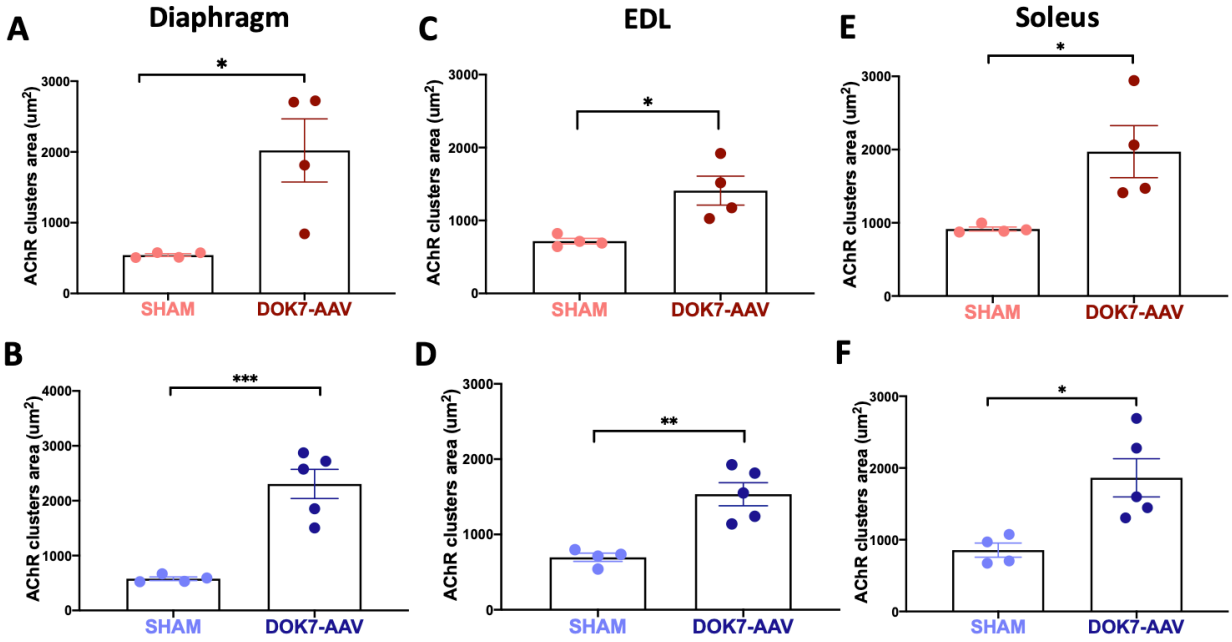

Figure 5.13. Areas of NMJs stained for AChR clusters in model mice following DOK7-AAV treatment. Tissue was collected and immunolabeled to visualize AChRs in both females (red) and males (blue) in diaphragm (**A, B**), EDL (**C, D**) and soleus (**E, F**) muscles. AChR area was measured for both treated (females- dark red; males- dark blue) and control (females- light red; males- light blue) mice. Individual data points represent the mean from at least 75 NMJ areas per mouse ± SEM. Unpaired t-tests were performed to compare between treatment groups (ns-not significant; *p<0.05; **p<0.01; ***p<0.001; n=4 female mice per treatment group; 4 male mice for the SHAM group and 5 male mice for the DOK7-AAV group).

All in all, the highest transduction efficiency was seen in the diaphragm muscle (females-89%; males- 97%) as shown in **Figure 5.14**. Also, a tendency for a lower efficiency was seen in the two leg muscles of male mice, however, this is not significant.

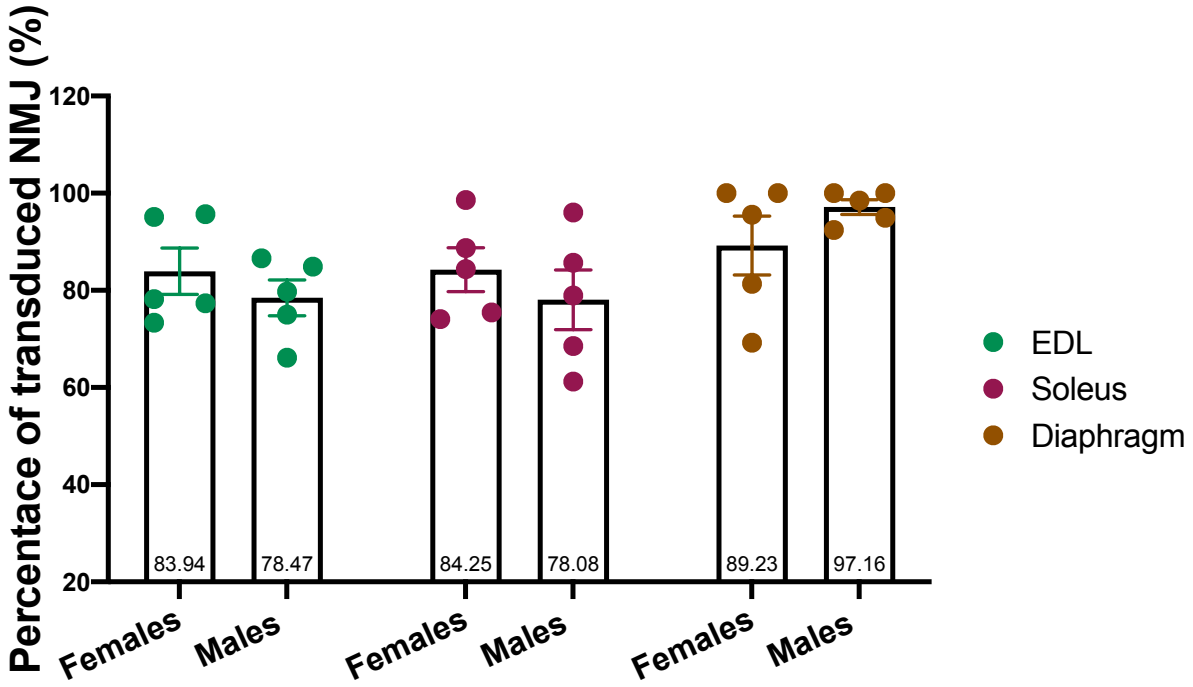

Figure 5.14. DOK7-AAV transduction efficiency in various muscles of low-dose model mice following gene therapy. Tissue was immunolabeled to visualize AChR areas in EDL (green), soleus (purple) and diaphragm (brown) muscles. The percentage of enlarged NMJs in the DOK7-AAV treated animals was calculated in both males (n=5) and females (n=4). Data points represent the mean ± SEM from 75 NMJs per mouse. Two-way ANOVA with Tukey's multiple comparison test was used to compare the differences between sexes for each muscle (not significant) and the overall differences between muscles (p=0.0053).

5.2.6. DOK7 expression levels in other muscles tissues

To further understand the AAV transduction efficiency, DOK7 EGFP protein expression was assessed in tibialis anterior (TA) and heart muscles (**Figure 5.15**). Tissue was homogenised and DOK7 tagged protein was purified by immunoprecipitation from whole muscle lysates. The samples were subjected to SDS PAGE and western blotting and the signal intensities were detected with a monoclonal Dok7 antibody and ultimately analysed by Fiji software. Robust DOK7 EGFP expression was detected in gene therapy treated model mice only and was similar for both muscles. However, some variability between mice was encountered.

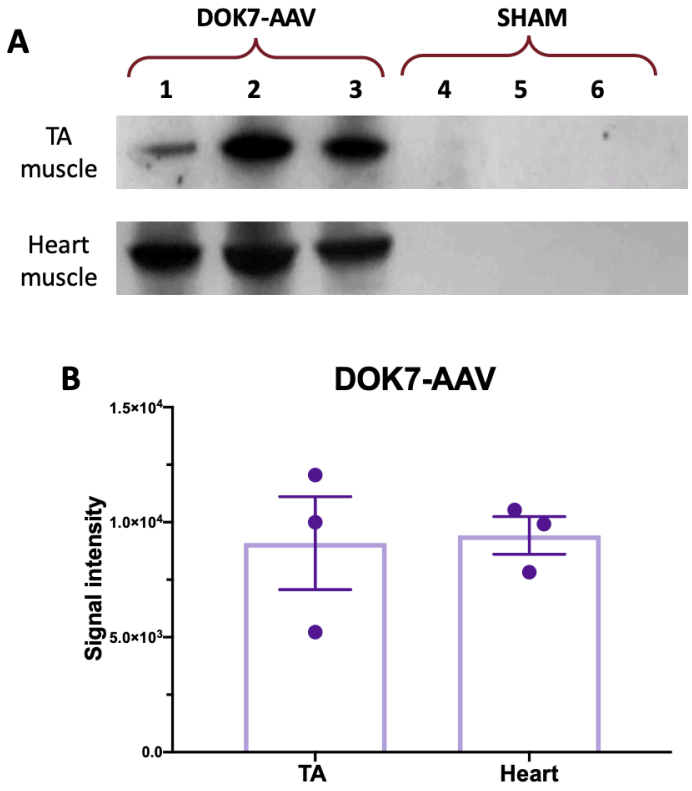

Figure 5.15. DOK7 EGFP expression in TA and heart muscles in model mice following DOK7-AAV treatment. Heart and TA muscles were dissected and homogenized in lysis buffer. Processed samples were analysed by western blotting (**A**) and an ~80.9 kDa DOK7 EGFP tagged protein was detected only in the gene therapy group (mouse number 1,2 and 3). Signal intensities were analysed using Fiji software (**B**) (mean ±SEM; n=3 mice per group).

5.3. A pilot study for high-dose DOK7-AAV gene therapy in AChR deficient model mice

To evaluate whether a higher dose of the DOK7-AAV gene therapy treatment could be more effective, a pilot study was next designed. During the course of this trial, lockdown restriction imposed due to COVID-19 led to institute closure for four months and restricted activity allowed in the Biomedical Services building where our mice were housed. Thus, the study is incomplete and analysis could not be performed. An overview of the study with representation of collected results are shown.

3 female and 5 male mice were injected intraperitoneally as follows: 3 males and 1 female with DOK7-AAV gene therapy at a dose of $1x10^{12}$vg/mouse, and 2 males and 2 females with saline solution as a negative control (SHAM) (**Figure 5.16**). From 6 weeks of age, their muscle strength was assessed once per week for a period of approximatively 10 weeks. Two mice (a male from the DOK7-AAV and a female from the SHAM group) had to be euthanised (as per Home License) around the end of the trial due to reasons unrelated to the treatment. Decrement tests were planned at three different timepoints: 6weeks, 10-12 weeks and 25 weeks. We were able to only assess for muscle decrement at 25 weeks for all mice. At the end of the trial, the mice were humanely euthanised for *ex vivo* electrophysiological recordings and tissue collection. Experiments were done in a blinded fashion.

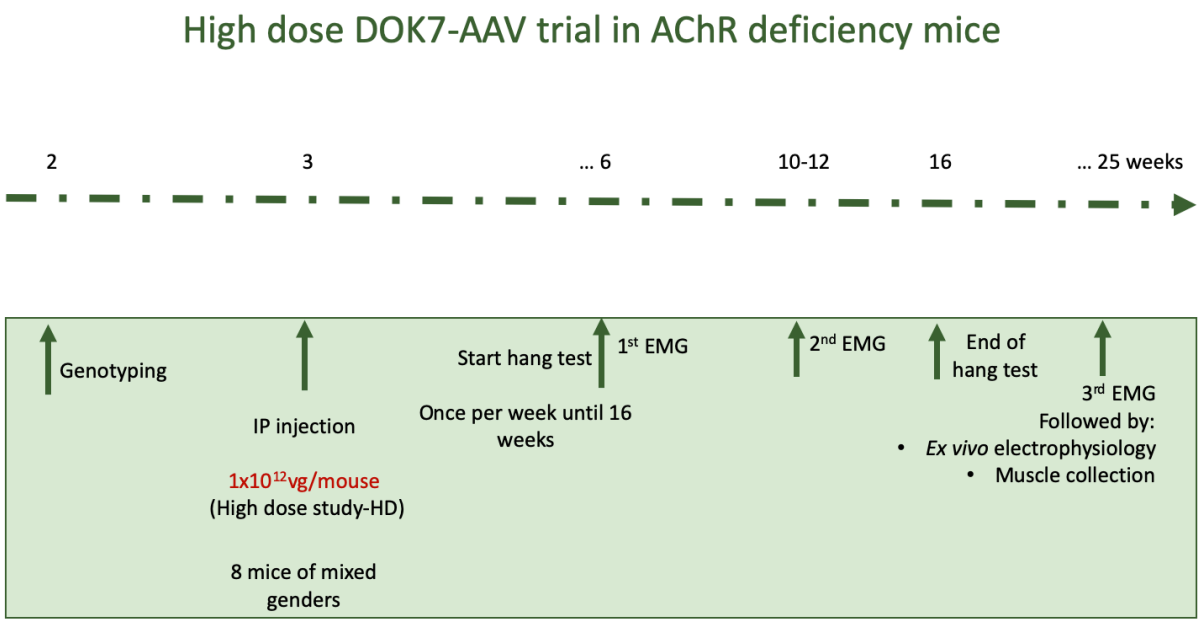

Figure 5.16. Schematic representation of study design for using high-dose DOK7-AAV gene therapy.

5.3.1. Evaluation of changes in body weight during high-dose treatment trial

DOK7-AAV treated mice seem to show increased body weight over the course of the trial in comparison to control mice, similar to the low-dose study (**Figure 5.17**). Body weight was assessed once per week and, for consistency, at the same time of the day.

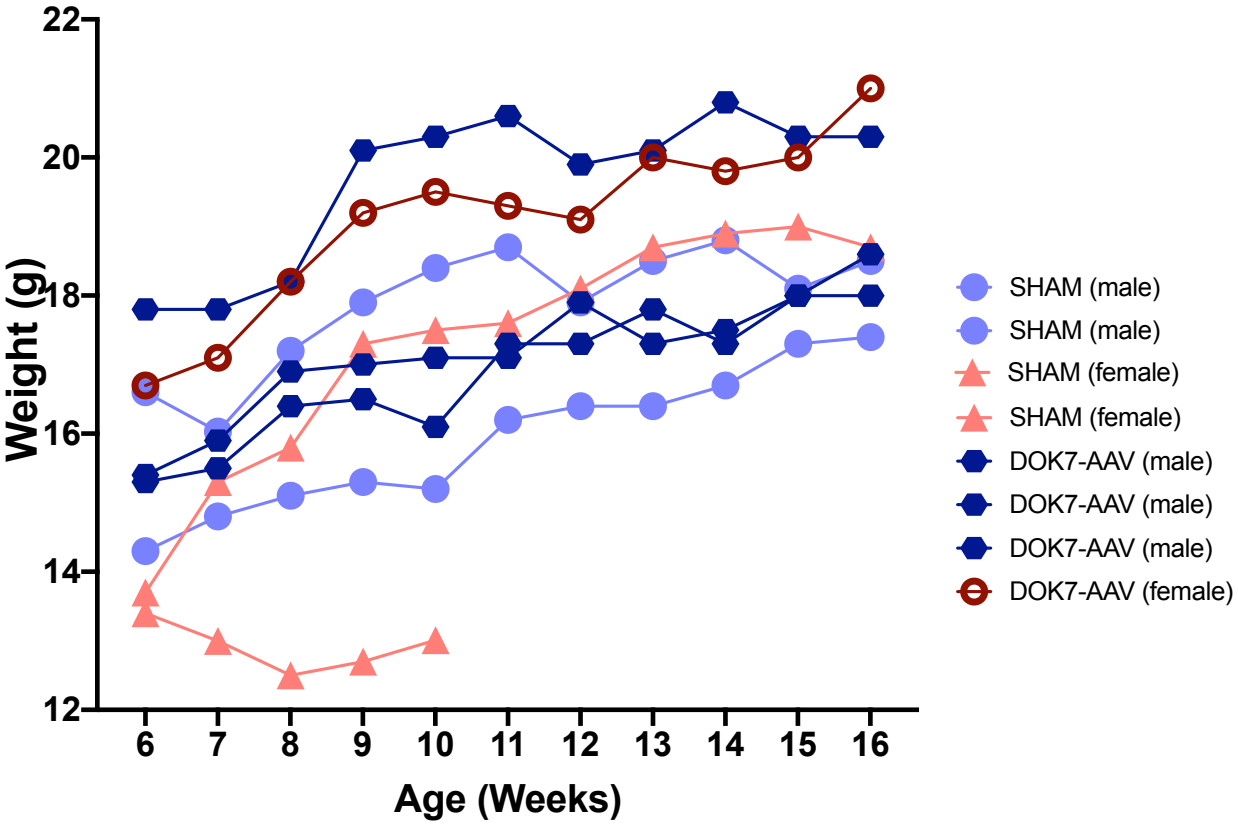

Figure 5.17. Body weight of model mice during high-dose treatment trial. Body weights of mice from both gene therapy treated (dark blue and red) and SHAM (light blue and red) groups were monitored for the whole period of treatment trial. Data was collected over a period of 10 weeks starting with 6 weeks of age. Each line represents one animal and data points are body weights recorded every week.

5.3.2. Evaluation of muscle fatigability of model mice during high-dose treatment trial

Muscle hang time on an inverted screen was measured once a week to investigate the clinical response to a higher dose of the DOK7-AAV gene therapy treatment (**Figure 5.18**). Unexpectedly, the DOK7-AAV treated mice appeared weaker than the control mice.

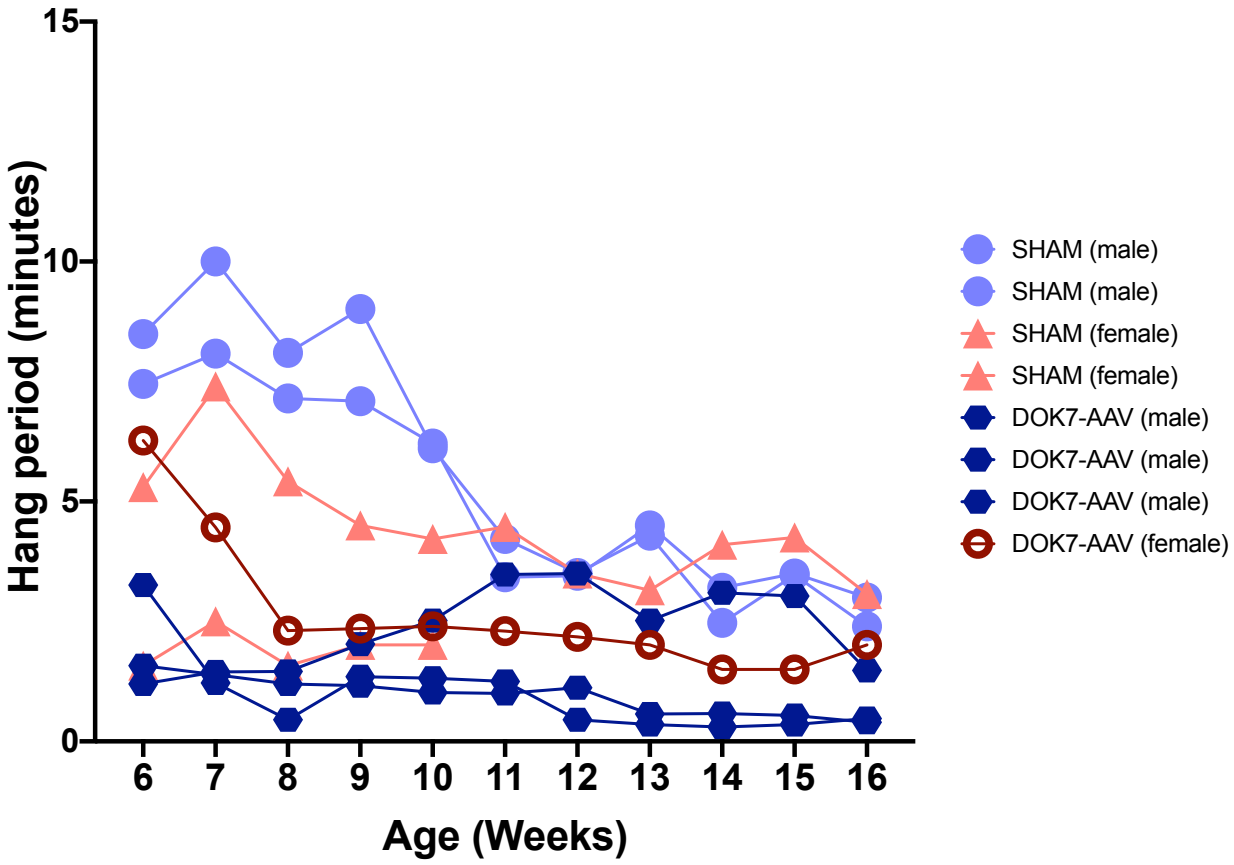

Figure 5.18. Muscle fatigability as assessed by inverted screen test in model mice during high-dose treatment trial. Mice from both the gene therapy treated (dark blue and red) and SHAM (light blue and red) groups were assessed for muscle fatigability using an inverted screen test. Data was collected over a period of 10 weeks starting with 6 weeks of age. Each line represents one animal and data points represent hang time recorded every week.

5.3.3. Decrement of compound muscle action potentials following repetitive nerve stimulation in model mice during high-dose treatment trial

Having shown increased muscle fatigability in DOK7-AAV gene therapy treated mice, we next examined muscle decrement as assessed by repetitive nerve stimulation. Decrement was calculated as the difference between the 1st and the 10th CMAP recordings, and was represented as the percentage of muscle decrement. Stimulation frequencies varied between 1 to 20 Hz (**Figure 5.19**).

At the beginning of the pilot study, three timepoints were planned for the decrement test:

- 6 weeks- before beginning the inverted screen tests
- 10-12 weeks- when the continuous decrease in muscle strength plateaus
- after 25 weeks old- when the mice in the previous study (low-dose) showed recovery from earlier increased muscle decrement

Due to Covid-19 lockdown, this was only possible for the later timepoint for all mice. Muscle decrement was observed in model mice of both treatment groups. However, increased decrement from ~20% to more than 40% was observed in gene therapy treated mice. High variability was observed between mice of the same treatment group.

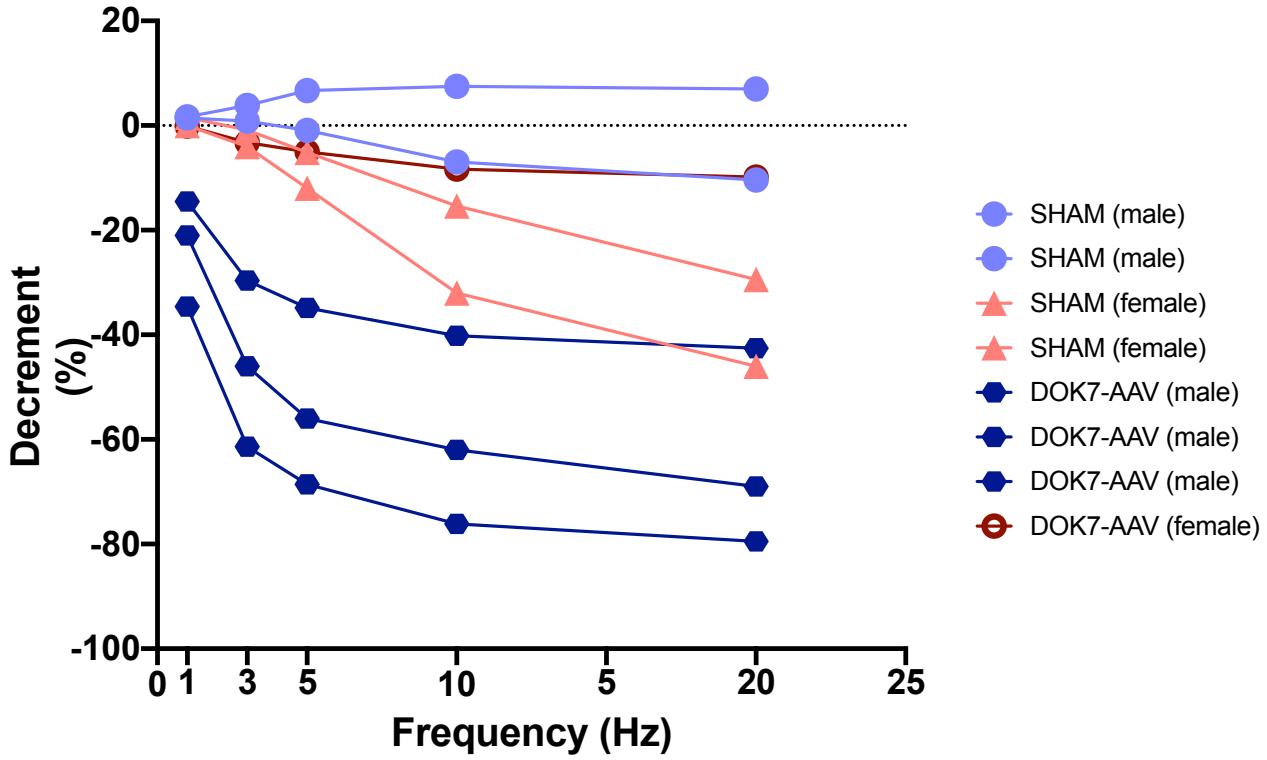

Figure 5.19. Decrement results of model mice during high-dose treatment trial. Mice from both the gene therapy treated (dark blue and red) and SHAM (light blue and red) groups were assessed for muscle fatigability using an inverted screen test. Each line represents one animal and data points represent stimulations at different frequencies.

5.3.4. Ex vivo electrophysiological recordings of neuromuscular transmission following high-dose gene therapy treatment

Neurotransmission parameters were analysed by *ex-vivo* electrophysiological recordings. A tendency for higher values for both presynaptic and postsynaptic measurements were observed for DOK7-AAV gene therapy mice in comparison to control (**Figure 5.20**).

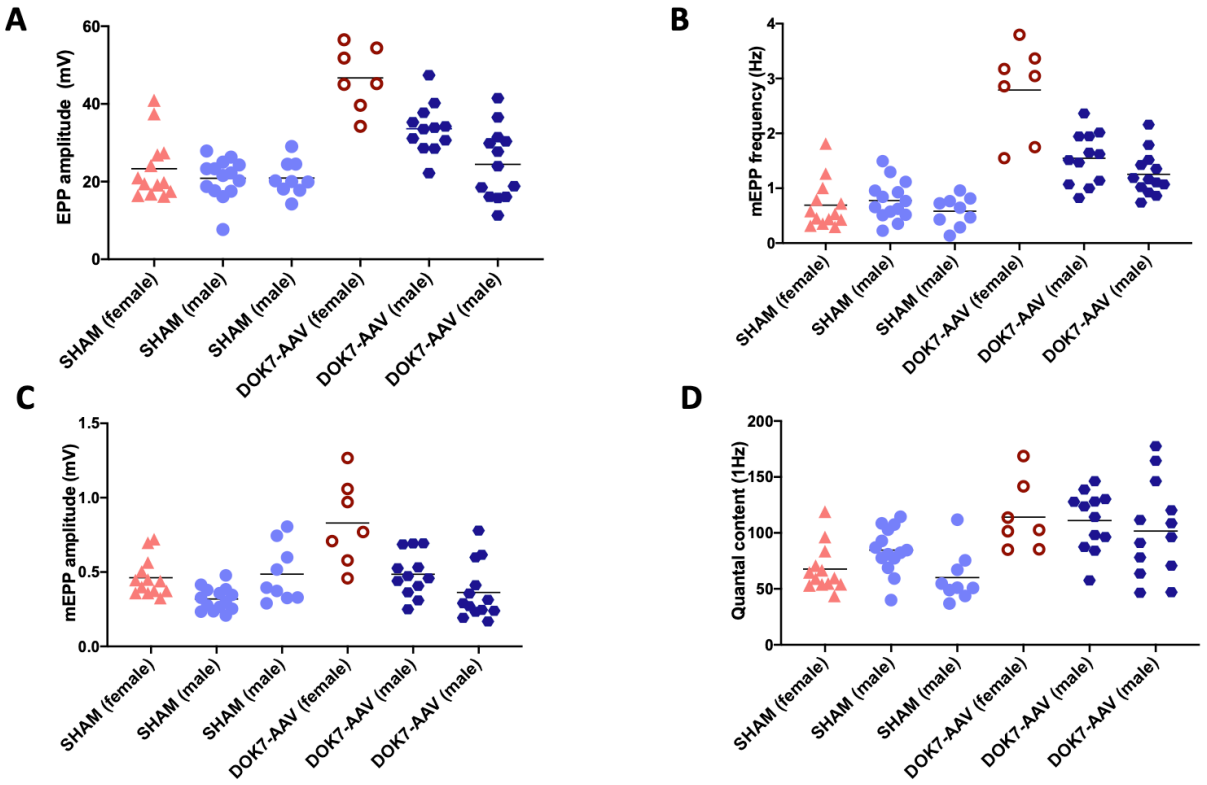

Figure 5.20. Electrophysiological parameters recorded from diaphragm preparations of model mice following high-dose gene therapy treatment. Data points represent individual recording for each mouse in the DOK7-AAV gene therapy group (dark blue and red) and SHAM (light blue and red).

5.3.5. Evaluation of NMJ structure following high-dose gene therapy treatment

To evaluate AVV transduction efficiency in high-dose treated mice, EDL, soleus and diaphragm muscles were immunolabelled with fluorescent α-bungarotoxin to stain for the AChR clusters area. At least 30 individual NMJs were analysed for each muscle per animal, and Fiji software was used to measure AChR areas.

Similar to the low-dose study, greater AChR areas were seen in DOK7-AAV gene therapy treated mice (**Figure 5.21**). Overall, the transduction efficiency in gene therapy treated mice (calculated as described in **Section 5.2.5**) appeared high as shown by percentages in **Figure 5.21D**. It seems clear that for one of the mice the viral infection was less efficient for the leg muscles.

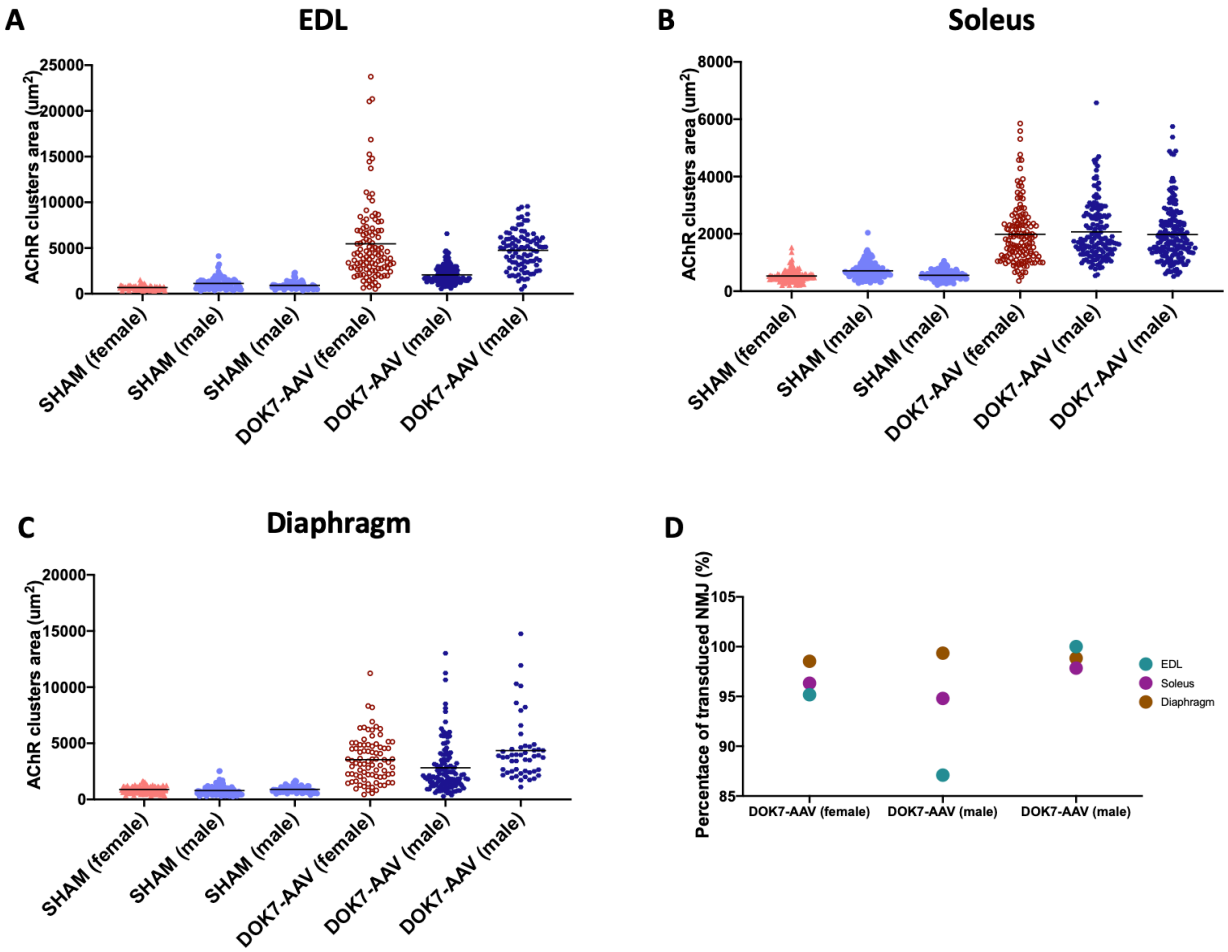

Figure 5.21. Areas of NMJs stained for AChR clusters in model mice following high-dose DOK7-AAV treatment. Tissue was collected and immunolabeled to visualize AChRs in EDL (**A**), soleus (**B**) and diaphragm (**C**) muscles. AChR area was measured for both DOK7-AAV treated (dark blue and red) and SHAM (light blue and red) mice. Individual data points represent the area of at least 30 NMJs per mouse. Percentages of transduction efficiency in each muscle are shown in panel **D** for individual mice.

5.3.6. DOK7 protein expression in muscle tissues of model mice following high-dose DOK7-AAV treatment

Similar to previous results, DOK7 EGFP robust expression was detected only in gene therapy treated mice for both TA and heart muscles by western blotting (**Figure 5.22**).

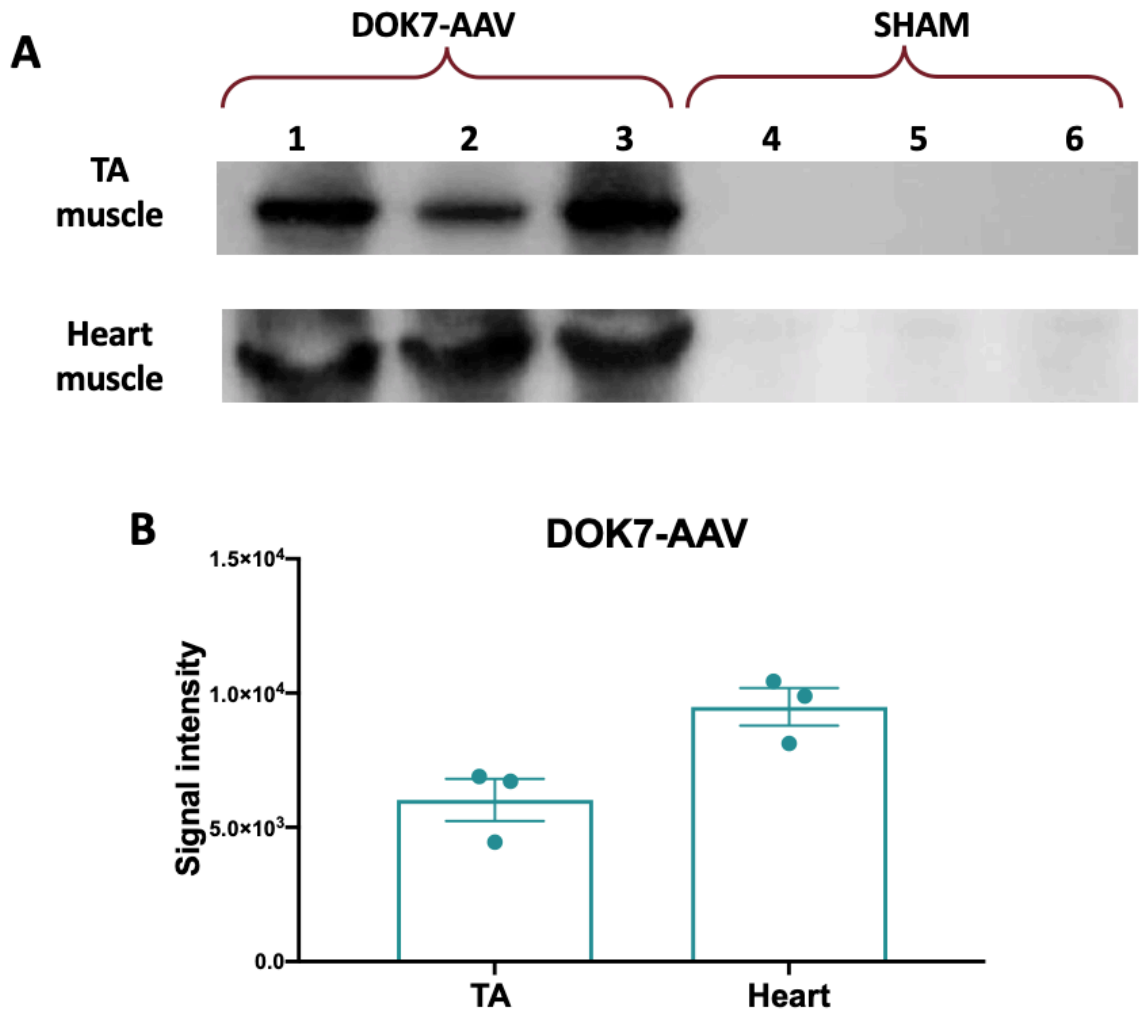

Figure 5.22. DOK7 EGFP expression in tibialis (TA) and heart muscles in model mice following high-dose DOK7-AAV treatment. Heart and tibialis muscles were dissected and homogenized in lysis buffer. Processed samples were analysed by western blotting (**A**) and an ~80.9 kDa DOK7 EGFP tagged protein was detected only in the gene therapy group (1, 2, 3). Signal intensities were analysed using Fiji software (**B**) (mean ±SEM; n=3 mice per group).

Also, to compare the expression of tagged DOK7 protein for the two gene therapy trials, whole lysate samples of TA muscles were subjected to SDS PAGE and analysed by western blotting in triplicates (**Figure 5.23**). Besides detecting the DOK7 EGFP tagged protein, α-tubulin was also detected on the same blot as a loading control. Signal intensities, analysed by Fiji, were normalised to the loading control and compared between the two studies. High variability was observed within separate dose groups.

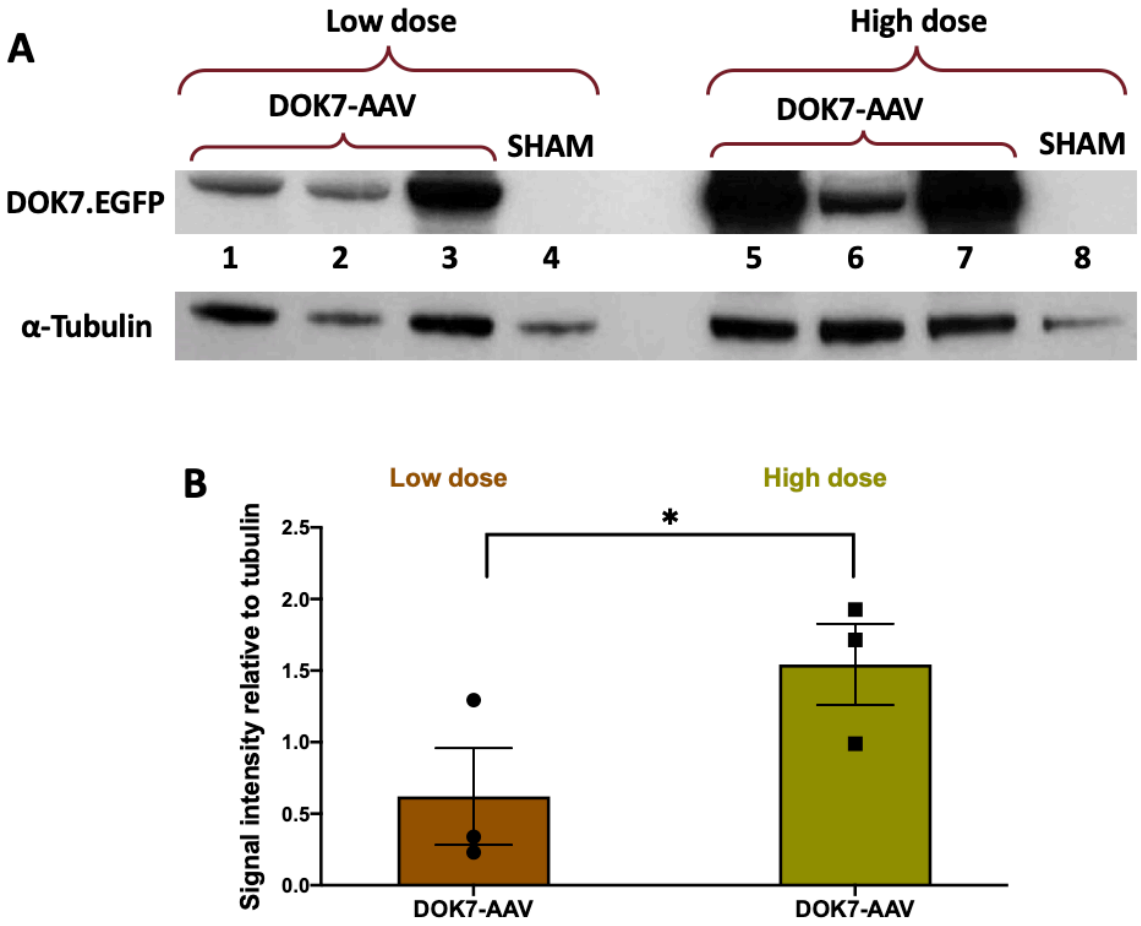

Figure 5.23. DOK7 EGFP expression in TA muscles on model mice following low-dose and high-dose DOK7-AAV treatment. TA muscles were dissected and homogenized in lysis buffer. Processed samples were analysed by western blotting (**A**) and an ~80.9 kDa DOK7 EGFP tagged protein was detected in the gene therapy groups. Signal intensities were analysed using Fiji software (**B**) An unpaired t-test was performed to compare between the two doses (*$p<0.05$; mean ±SEM; n=3 mice per group).

5.4. Discussion

This chapter presents the results of DOK7-AAV gene therapy treatment in a mouse model of AChR deficiency. The effects of this therapy were first described in a DOK7-CMS mouse model that showed improved lifespan and motor functions (Arimura et al. 2014). Also, the potential of DOK7 as a therapeutic target was shown by using the same technique in mouse models of autosomal dominant Emery-Dreifuss muscular dystrophy, Amyotrophic lateral sclerosis, and recently Spinal muscular atrophy (Arimura et al. 2014; Miyoshi et al. 2017; Kaifer et al. 2020). These mice showed overall reduced phenotypic severity with improved lifespan and grip strength. More recently, aged mice were also shown to present improved motor functions linked to supressed muscle denervation when treated with DOK7 gene therapy, demonstrating another therapeutic area that can benefit from DOK7 upregulation (Ueta et al. 2020). However, assessment of *in vivo* or *ex vivo* neurotransmission and detailed examination of size alterations at the NMJ have not been reported for using DOK7-AAV gene therapy in these disease models.

The gold standard treatment for AChR deficiency patients, based mainly on AChR inhibitors, can lose efficiency over time (Rodríguez Cruz et al. 2015). Also, pyridostigmine has been shown to have detrimental effects on the postsynaptic structure and function in rodents, and for long term therapy in a mouse model of AChR-deficiency (Engel et al. 1973; Vanhaesebrouck et al. 2019). We demonstrated that DOK7-AAV gene therapy could be beneficial as a one-time treatment for AChR deficiency, with the added potential for enhanced response to pyridostigmine. It may be that DOK7-AAV could be used in combination with pyridostigmine without the need to introduce β-adrenergic receptor agonists, thus reducing medication and the accompanying side effects.

In a disease model that mimics the clinical situation of human patients, we found that DOK7-AAV gene therapy partially ameliorates the myasthenic phenotype. There were improvements of motor function and neurotransmission as well as evidence of morphological changes of immunolabelled NMJs. The methods used in this chapter included inverted screen hang test, recordings of CMAP decrement, *ex* vivo electrophysiological recordings and immunostaining of NMJ. A stronger treatment effect was observed in males in comparison to females as shown by the longer hang time on the inverted screen test (**Figure 5.7**). Also, higher variability was observed during the treatment trial between female mice within one treatment group, especially for some of the *ex vivo* recorded electrophysiological parameters (**Figure 5.10B** and **Figure 5.11B**). The human γ-subunit transgene was integrated into the X-chromosome in the AChR-deficiency mouse model (J. Cossins, data not published). This is likely to have caused a gender effect on response to treatment. In female mammals, the majority of genes on one X chromosome are silenced due to X-chromosome inactivation, to achieve dosage compensation between XX females and XY males (Carrel and Willard 2005; Peeters et al. 2014; Balaton and Brown 2016). Some of the genes can escape the X-inactivation, being expressed from both X chromosomes in a process not fully understood. This suggests a remarkable degree of expression heterogeneity amongst females and the possibility of phenotypic variation between AChR deficiency female model mice treated with DOK7-AAV gene therapy.

In **Chapters 4** we confirmed that DOK7-AAV gene therapy can restore the myasthenic phenotype without having any obvious detrimental effects on the organism on DOK7-CMS mice, as has also been found by others (Arimura et al. 2014). With that in mind, we postulated that DOK7-AAV gene therapy could benefit other CMS types and potentially NMJ-related diseases. We undertook experiments using two different doses of the gene therapy treatment in an AChR-deficiency mouse model. The trial design is presented in **Table 5.1**. The study,

particularly for the higher viral treatment titre was not completed due to COVID-19 crisis. Only observation from the high-dose study have been reporter in this chapter.

Table 5.1. Experimental design for the two AAV studies.

Study	Amount of AAV injected	Age of injection	Number of mice		Age of first hang test	Decrement test			End of trial	
			SHAM	DOK7 - AAV						
Low-dose	$4x10^{11}$vg/ mouse	3 w	6 F	6 F	6 w	~one week before end of trial			young	old
			5 M	5 M					17-19 weeks	>26 weeks
High-dose	$1x10^{12}$vg/ mouse		1F	2F		Timepoints:			16 w*	
			3M	2F		6 w	10-12 w	~25 w		

**end of hang test; w-weeks; F-females; M-males;*

Body weight of DOK7-AAV treated mice was significantly increased, and the high-dose treatment trial supported what was seen for the low-dose treatment (**Figure 5.4**, **Figure 5.17**). This may be explained by the fact that improved muscle fatigability can lead to improved mobility and thus more food consumption. However, the observations done on the high-dose DOK7-AAV gene therapy treated mice do not necessarily support this statement, presenting similar or even potentially reduced hang time on the inverted screen test compared to control mice (**Figure 5.18**). Thus, increased body weight could be a direct effect of the gene therapy treatment that could influence changes in muscle mass. More investigations are needed to understand this effect. Considering that the gene therapy treated mice were heavier than the SHAM mice, hang time was normalised to body weight to account for this difference, and thus a higher significance was shown for the DOK7-AAV treated model female mice (**Figure 5.7A**).

Muscle fatigability was tested using an inverted screen test. Improved hang time was observed for both males and females in the low-dose study overall (**Figure 5.5**). Also, a decrease in hang time was observed for all mice independently of the treatment group or gender until it plateaued at around 10-12 weeks. This reduction in strength is likely related to the gradual loss of mouse γ-subunit. Transition from γ to ε subunit-containing AChRs occurs between P1 and P10 in wild-type mice (Engel 2013). In the ε-subunit knockout mice, γ subunit-containing AChRs were still detected long after their usual time of disappearance and their expression was shown to be downregulated over time (Missias et al. 1997). Also, male mice appeared stronger than female mice independent of the treatment group, and this likely relates to gender-based differences in the skeletal muscle fatigue, with females being more prone to having weaker muscle endurance (Milia et al. 2011). In rodents, a reason for that was shown to be that in females, oestrogen negatively regulates the expression of orosomucoid, an endogenous anti-fatigue protein that enhances muscle endurance (Sun et al. 2018).

Unexpectedly, the few high-dose gene therapy treated mice showed decreased hang time compared with mice just injected with saline. We are not sure what underlies this and it will require further investigation (**Figure 5.18**). Possible causes could be AAV immune- and off target-related toxicity in the high-dose mice, that interfere with the therapeutic efficacy and may end up worsening the myasthenic phenotype. A few studies with different tissue targets have reported observed toxicity in high-dose groups upon AAV mediated gene therapy in other species (Hinderer et al. 2018; Xiong et al. 2019). They showed systemic and sensory neuron toxicity related to the delivery of high-dose AAV vectors independent of transgene or capsid serotype. Another possible explanation for the observed reverse effect in the high-dose study could be the fact that enlargement of NMJ presenting foetal AChRs might

be detrimental. By all means, we need to consider that the high-dose study is incomplete and future investigations with more animals should be performed. It is of note that the mice in the SHAM group that were counterpart to the high-dose DOK7-AAV treatment showed surprisingly persistent inverted screen hang times for the typical AChR deficiency model mouse and this may be skewing the results for the small number of animals that we were able to assess.

We performed experiments where we added pyridostigmine medication to the treated mice. Pyridostigmine is a cholinesterase inhibitor and so increases the effective ACh concentration within the synaptic cleft. It is absorbed rapidly through the gut and has its beneficial effect within 30-60 minutes of ingestion. It is also metabolised quickly and so completely removed from the system within 24 hours. As expected, pyridostigmine improved hang time in low-dose and sham treatment groups, however the increase for time of the screen was far more marked for the DOK7-AAV groups than for the sham group (**Figure 5.8**). Potentially, the enlarged synapses enhance the effect of the pyridostigmine and so underlie this improvement.

Decrement of CMAP on repetitive nerve stimulation can be used to assess response to treatment for a disorder involving the NMJ, as it tests the ability of an individual NMJs to maintain effective neurotransmission (Ha and Richman 2015). It is a measure of the accumulation of multiple fibres muscular action potential stimulated by neurotransmission. If the number of fibres contributing to the CMAP falls due to individual neurotransmission failure, the overall CMAP amplitude will decrease. Even at high frequencies in wild-type mice there is little to no neurotransmission failure. Thus, CMAP decrement is a measure of neurotransmission failure. Muscle decrement tests did not show a significant improvement due

to the DOK7-AAV treatment, although when the DOK7-AAV treated mice were divided according to the length of time from the DOK7-AAV IP injection, the mice that have had the therapy for the longest time showed smaller decrement as compared to younger mice, indicating improved NMJ function over time (**Figure 5.9C,E**) (not observed for the control group as shown by **Figure 5.9,F**). This is supported by the observations shown on the high-dose gene therapy treated mice (**Figure 5.19)**. Some of these mice show a decremental response of more than 50% at 20Hz. These results suggest muscle fatigability which is opposite to what was seen for the inverted screen data. A possible explanation could be that the endplates containing foetal AChRs might get stabilised over time following DOK7-AAV gene therapy. We know that the foetal AChR gets turned over faster than the adult AChR, but in AChR deficiency CMS, this might be slowing down over time (Brenner and Rudin 1989; Engel 2013).

Increased mEPP frequencies, EPP amplitudes and quantal content were observed in the DOK7-AAV treated mice. This was significant for both low-dose treated males and females (**Figure 5.10**, **Figure 5.11**). These results support the inverted screen test data that showed improved hang time in mice for the low-dose study. The increased electrophysiology parameters are likely to reflect larger nerve terminal areas and thus availability of more vesicle release sites at the nerve terminal. Similar results were seen in **Chapter 3** in wild-type mice treated with the DOK7-AAV gene therapy.

No increase in mEPPs amplitudes was however observed in our study. mEPPs amplitudes could be relate to a variety of factors such as the number of neurotransmitter in each quantum, endplate organisation or the density and distribution of the AChR (Engel et al. 2015). Reduced AChR density has been shown before in ε-subunit null mice, and the continuous expression of γ-AChRs at low levels is not sufficient to maintain postsynaptic AChR density at the same

levels as found in wild-type mice (Missias et al. 1997; Schwarz et al. 2000; Cossins et al. 2004). Our results would suggest that even though the DOK7-AAV can induce enlarged synapses, the therapy is not able to enhance the tight aggregation of AChRs that is characteristic of endplates harbouring the adult AChRs.

To assess increased AChR cluster areas and investigate AAV transduction efficiency in different muscles, EDL, soleus and diaphragm muscles were fluorescently stained with Alexa Fluor 594 α-bungarotoxin, and AChR cluster areas were analysed. Significant increased AChR areas were seen in both low-dose treated females and males (**Figure 5.13**). AChR-deficient mice usually present fragmented NMJ with reduced AChR intensity staining and loss of "pretzel"-like shape (Cossins et al. 2004). DOK7-AAV gene therapy probably contributes to improved neurotransmission and increased muscle strength by inducing the formation of "enlarged" NMJ structures, and thus increasing the overall number of AChRs on the post-synaptic membrane (Arimura et al. 2014).

AAV transduction proved to be very efficient in all three muscles tested. For the low-dose study, the highest efficiency was observed in the diaphragm muscle: females- 89% +/-6.058 (n=5); males- 97% +/-1.506 (n=5) (**Figure 5.14**). The high-dose study showed more than 95% transduction efficiency for all three muscles (n=3 individual mice analysed: EDL- 95%, 87% and 100%; soleus- 96%, 95% and 98%; and diaphragm- 99%, 99% and 99%) (**Fig.21**), even though the therapeutic effect proved differently than expected (**Figure 5.18**). The observed slightly higher transduction efficiency for diaphragm muscles is likely linked to the IP route of administration. In preparation for potential applications in humans, additional investigations of different routes for treatment administration and different dosing regimens would be an important future step.

To assess transduction efficiency in other muscle tissue, western blotting was performed for a different leg muscle (TA) and the heart. Given the fact that no significant differences were seen between males and females in transduction efficiency, muscles harvested only from males were used for the low-dose study. Very high levels of expression were seen in the DOK7-AAV treated mice for both TA and the heart (**Figure 5.15**, **Figure 5.22**, **Figure 5.23**). Arimura et al. showed no effect of gene therapy on the heart tissue from a histology point of view (Arimura et al. 2014). It is not possible to directly correlate the increase in DOK7 expression on the western blots with expression at the NMJ. The DOK7-AAV expression is under control of the CMV promoter and therefore will express in many tissues and from nuclei all along the muscle fibre, whereas in a wild-type or sham-injected mouse the expression of endogenous Dok7 would be restricted to the subsynaptic nuclei beneath the endplate. Thus, the site of expression is very difficult to account for in a western blot. However, it is clear that the DOK7 protein is expressed very efficiently from this vector and that it does have a marked effect at the NMJ. It would be of interest to try a neuromuscular junction-specific promoter as shown by Webster and colleagues (Webster et al. 2013) to gauge if this is equally effective in generating 'super synapses' without potential side effects that might results from the global expression under the CMV promoter.

To compare protein expression in a leg muscle between the low- and high-dose viral titres, whole lysates of TA muscles were run through a western blot. Similar amounts were loaded, however, to account for technical variability between the samples, α-tubulin was used as a loading control. An approximatively 3-fold increase in protein expression was seen in the high dose study and that's reflective of the higher amount of virus delivered intraperitoneally (2.2 times more than the low-dose). Although there appeared to be considerable variability within each treatment group.

In conclusion, this chapter shows the effects and implications of using the DOK7-AAV gene therapy in a mouse model of AChR deficiency. We showed that DOK7-AAV gene therapy can improve muscle strength in disease model mice. Overall improved neurotransmission was also observed consistent with the presence of enlarged neuromuscular junctions. AAV transduction efficiency showed that the route of administration is effective and generates a therapeutic effect. Important, it was also clear that DOK7-AAV treatment enhanced the gold standard therapy used in AChR deficiency CMS and thus could provide an additional therapeutic avenue for treating patients. These early experiments suggest that DOK7-AAV has marked potential for modifying neuromuscular junction structure and thereby enhancing neuromuscular transmission in multiple myasthenic disorders.

Chapter 6

Screening for small molecules that can upregulate the expression of DOK7 protein

6.1. Introduction

Congenital myasthenic syndromes (CMS) are a group of rare heterogeneous inherited disorders for which neuromuscular transmission is compromised due to one or more genetic pathophysiological mechanisms (Engel 2015). Mutations in more than 30 genes have been linked to CMS so far, and these can be classified according to the site at the neuromuscular junction where function is impaired: pre-synaptic, synaptic or post-synaptic (Finsterer 2019).

Current treatment repertoire includes drugs from the following categories:

- Potassium channel blockers (3,4-diaminopyridine) → increasing acetylcholine release and prolonging action potential duration (Palace et al. 1991)
- Acetylcholinesterase inhibitors (pyridostigmine) → inhibiting acetylcholinesterase form breaking down acetylcholine and thus increasing its concentrations and diffusion within the synaptic cleft to target more receptors (Schwab and Timberlake 1954)
- β2–adrenergic receptor agonists (ephedrine, salbutamol) → increasing structural stability of neuromuscular junctions in long-term (Lashley 2010; Burke et al. 2013; Lorenzoni et al. 2013)

- Acetylcholine receptor (AChR) open-channel blockers (fluoxetine, quinidine) → preventing excitotoxicity by terminating pathogenically prolonged AChR currents (Harper et al. 2003)

The response to treatment varies for each CMS subtype and depends on the underlying mechanism behind individual pathogenic mutations. An effective treatment requires a sustainable balance between enhancing neuromuscular transmission and maintaining a stable synaptic structure. While current treatments can be effective to some extent for many CMS subtypes, new pathogenic variants are constantly uncovered and the field is always in need for new treatment options. The use of next-generation sequencing is revealing mutations with even more complex disease phenotype in which myasthenia symptoms could represent only a minor component of the phenotype, highlighting thus the importance of exploring novel therapies.

Since the discovery of CMS caused by mutations in the *DOK7* gene, the encoded protein became a potential therapeutic target, especially once its importance at the NMJ had been highlighted in *DOK7* knock-out mice that are immobile and die shortly after birth (Okada et al. 2006; Palace et al. 2007). In a study that aimed to understand more in depth the function of DOK7 protein, it was shown that overexpression of DOK7 increased the activity of MuSK and enhanced mid-muscle synaptogenesis *in vivo* in mouse embryos (Inoue et al. 2009). Following these studies, Arimura and colleagues used an AAV gene therapy system to test the potential of DOK7 upregulation in restoring NMJ dysfunction in a DOK7-CMS mouse model carrying the equivalent of the common human DOK7 CMS frameshift mutation c.1124_1127dupTGCC (Arimura et al. 2014). Model mice showed prolonged lifespan and improved muscle strength with no detrimental effects on the body. Moreover, this therapy also proved to be effective by

improving muscle function in aged mice, as well as in restoring the phenotype of other neuromuscular diseases such as autosomal dominant Emery-Dreifuss muscular dystrophy (AD-EDMD), Amyotrophic lateral sclerosis (ALS), or Spinal muscular atrophy (SMA) (Arimura et al. 2014; Miyoshi et al. 2017; Kaifer et al. 2020; Ueta et al. 2020). By using a similar approach, we also showed improved neuromuscular transmission and muscle strength in a mouse model of AChR deficiency myasthenia in **Chapter 5**. The results highlight the potential of DOK7 gene therapy for CMS and many other neuromuscular disorders.

Despite the immense potential, apparent excellent safety profile, and high efficiency of transduction associated with the AAV gene therapy, many challenges are encountered on the way of translating gene therapy into clinic. These challenges include possible side effects linked to the modulation of the therapeutic gene, toxicity linked to high-dose AAV administration, or constraints related to host's immune response to the virus which imply limitations to a one-time application (Colella et al. 2018; Hinderer et al. 2018).

In this chapter we aimed to develop a model system to screen for small molecules that can upregulate the expression of DOK7 protein (**Figure 6.1**). The study was designed to first generate a mouse muscle cell line that can be used in the screening of small molecule compounds, to find molecules that upregulate the expression of DOK7, drive the formation of AChR clusters *in vitro* and ultimately induce the formation of enlarged synapses *in vivo*. This could be developed as a complementary treatment strategy alongside the DOK7 gene therapy previously mentioned, to be used in the field of CMS and potentially other neuromuscular diseases.

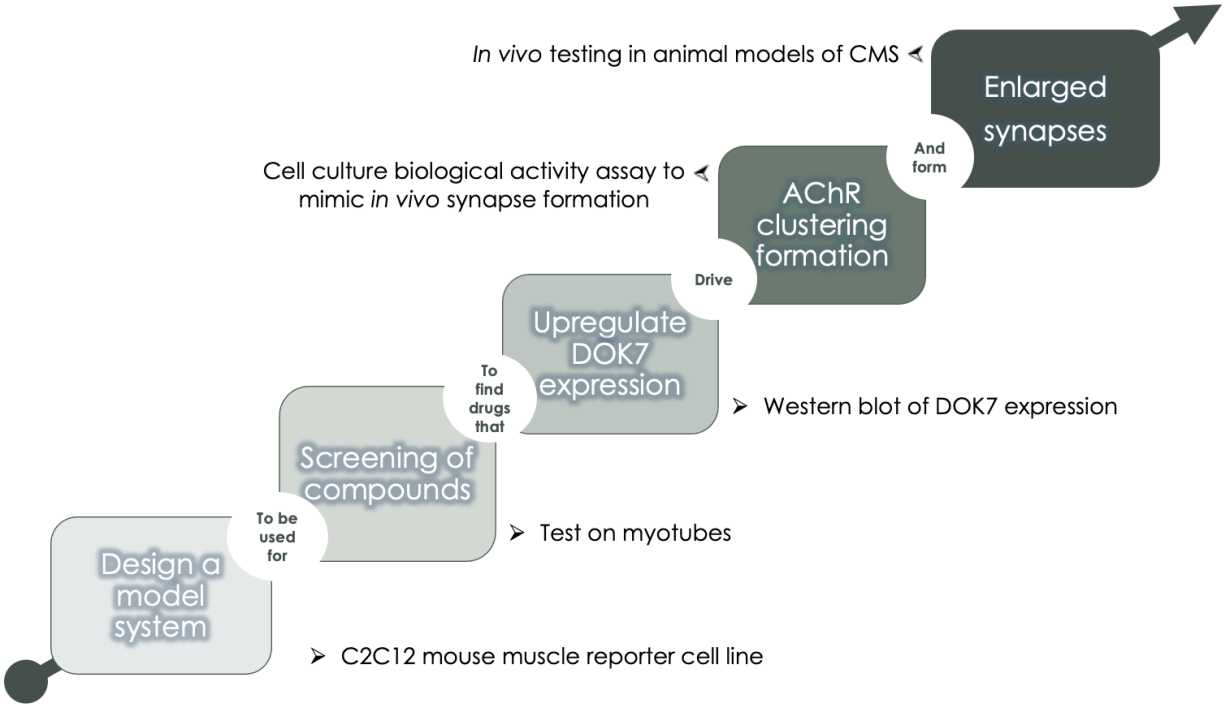

Figure 6.1 Small molecule screening study objectives and workflow. We first generated a physiologically relevant reporter cell line (differentiated myotubes) to be used in the screening of small molecules. We will be searching for compounds that can show upregulation of DOK7 protein and the ability to induce AChR clusters in our biological activity assay. We ultimately aim to find compounds that can induce the formation of enlarges NMJs.

6.1.1. Small molecule library used

Modulating protein expression as a therapy for human disease is a potential therapeutic avenue for many diseases. Dame Kay Davies and the colleagues have been exploring this approach to upregulate the expression of utrophin, a muscle protein, as a potential therapy for Duchenne Muscular Dystrophy (Babbs et al. 2020). They have identified a series of chemical compounds that can upregulate utrophin, with the most advanced utrophin modulator (ezutromid) successfully completing Phase I of clinical trials, although it failed a later trial (Ricotti et al. 2016).

We initiated a collaboration with Dr Graham M. Wynne and Dr Angela J. Russell from the Department of Chemistry, University of Oxford, who took part in the synthesis of the chemical libraries used to screen for compounds that were found to upregulate the utrophin protein. To identify small molecules capable of increasing the expression of DOK7 protein, they offered access to a focused set of compounds previously used for utrophin, which is known to be expressed at the NMJ as well (Blake et al. 1996; Chancellor et al. 2011). These compounds were mainly part of the EXPRESS-Pick library (ChemBridge), a collection of approximatively 500,000 small molecule compounds selected to have druglike properties. The primary screen was performed using 5341 of these small molecules.

6.1.2. Using a reporter system for compound screening

Using a cellular model system that is similar to the *in vivo* target tissue is of outstanding importance for the initial screenings. The first step in the experimental approach for screening compounds was to generate reporter cell lines that constitutively express luciferase under the control of the *DOK7* promoter (**Figure 6.2**).

Reporter genes represent an essential tool for studying gene expression and regulation (Bauer 2011). Their surrogate function allows for the analysis of key cellular processes and disease phenotypes, as well as for the analysis of treatment response. Here we use a firefly luciferase reporter fused to a sequence of the *DOK7* promoter, immediately after the start codon of the *DOK7* gene. Little is known about the *DOK7* promoter, with one study showing high promoter activity in myotubes for the 113bp 5'-flanking region of the mouse *Dok7* gene. This region contains two consensus sequences for the Sp1 transcription factor, conserved in the human *DOK7* gene as well (**Figure 6.3A**) (Hamuro et al. 2011).

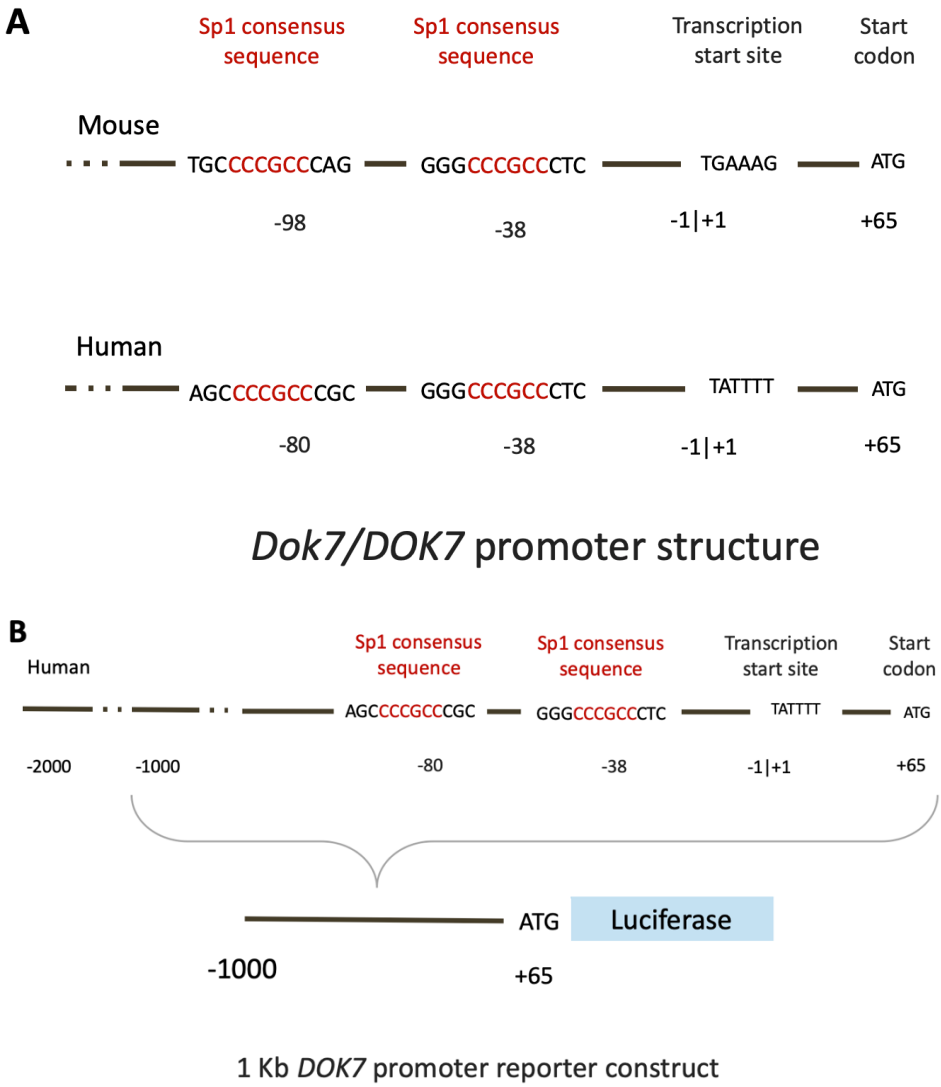

Figure 6.2. The structure of the *Dok7/DOK7* promoter. The ATG initiation codon of the *Dok7* gene is situated 65 bases downstream of the transcription start site (**A**). Two Sp1 consensus sequences are present in the 5'-flanking region of the mouse *Dok7* gene and are necessary for the Dok7 expression in both myoblasts and myotubes. The Sp1 transcription factor contributes to the expression of the *Dok7* gene by binding to these two sequences. The two Sp1 sequences are conserved between mice and humans, suggesting that Sp1 could be also important in the transcriptional regulation of the human *DOK7* gene. Usually, for muscle genes the majority of the control of gene expression is through transcription factors that act on promoter regions close to the ATG initiation codon. This is consistent with the fact that the two Sp1 consensus sequences are only 103 and 145 bases upstream of the start codon. The luciferase reporter cell line was designed to containing a 1 kb sequence of the human *DOK7* promoter (**B**).

The 1 kb upstream sequence of human *DOK7* gene was chosen for the generation of a stably transfected reporter cell line (**Figure 6.3**). The promoter sequence was amplified from genomic DNA and the construct was generated through molecular cloning and subjected to Sanger sequencing for confirmation of integrity. The generation of luciferase reporter construct was presented in more details in **Section 2.2.6.1**.

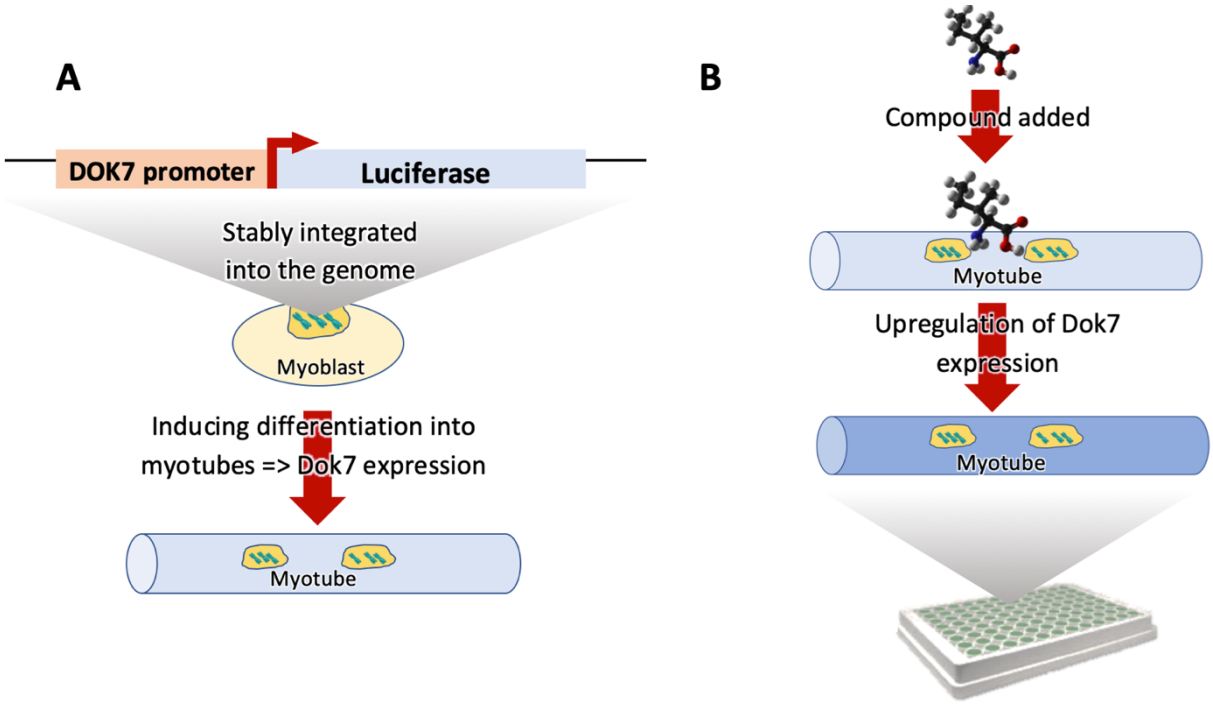

Figure 6.3. Schematic representation of luciferase reporter assay design. A 1 kb sequence of the *DOK7* promoter upstream of firefly luciferase was used to generate a C2C12 reporter cell line. Thus any compound potentially interacting with the promoter and inducing overexpression, would be detected in a luciferase readout. The reporter construct would be stably integrated into the genome and upon myoblast differentiation, the natural upregulation of DOK7 would give a baseline luciferase expression **(A)**. Thus the assay is designed in such way that potential hits would give a luciferase signal higher than the baseline (**B**).

6.2. Experimental design of screening assay

Transcriptional modulation of the DOK7 promoter with a bioavailable small molecule compound that can specifically target skeletal muscles represents an attractive strategy for most CMS subtypes. We designed an *in vitro* screening model system by using the C2C12 mouse muscle cell line carrying a sequence of the DOK7 promoter linked to a luciferase reporter gene. This model system was used in the primary screen of 5341 compounds, in triplicates.

A natural upregulation is observed in the expression of DOK7 protein when C2C12 mouse myoblasts are differentiated into myotubes, and so the screening assay was performed on mature myotubes to find compounds that can upregulate DOK7 above that level (Hamuro et al. 2011). To confirm the expression profile on differentiation, we used C2C12 cell lysates collected at different timepoints during differentiation (0, 2, 4, 6, 8, 10 days), that were subjected to SDS-PAGE and western blotting (**Figure 6.4A**). A gradual increase in DOK7 expression was observed in the first week until it plateaus between 8th to 10th day (**Figure 6.4B**).

For the library screen, C2C12 myotubes were differentiated in 96-well plates for ~8 days prior to performing the reporter assay. Following, cells were incubated with the compounds for ~24hr and the level of luciferase was determined by using a ONE-Glo Luciferase assay system on a GloMax Luminometer. Each plate contained a column of cells, assigned at random between triplicate screens, incubated with vehicle control (DMSO) used at the same dilution as the compounds. The primary screen was done at 100 μM. Because no positive control was available for this screen, compounds with a coefficient of variation higher than 15% were excluded (Sui and Wu 2007; Inglese et al. 2007).

Compound hits were then tested for their ability to induce AChR clustering and a dose-response curve was ultimately performed for the lead compounds.

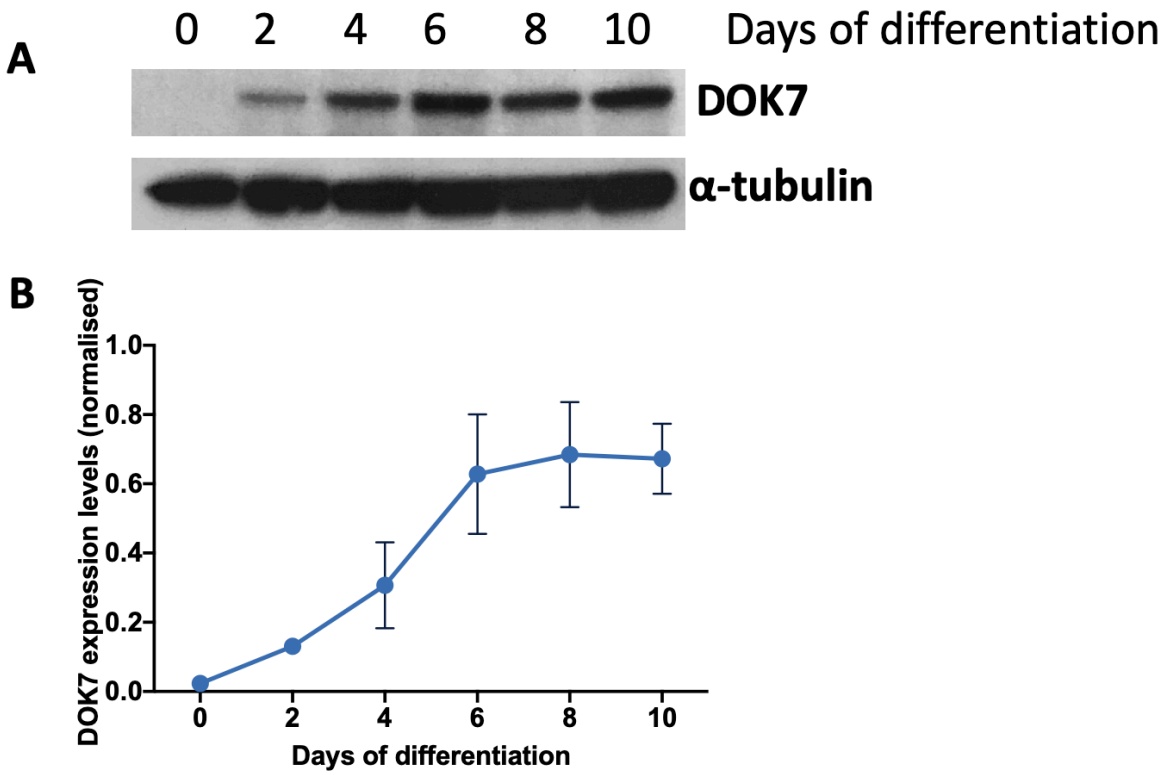

Figure 6.4. The natural upregulation of DOK7 protein upon myoblasts differentiation. C2C12 myoblasts cells were grown to confluency and the growth media was changed to differentiation media. Cell lysates were collected every 2 days until mature myotubes were fully formed. The samples were subjected to western blotting (**A**) and data from 3 individual experiments are represented as mean ±SEM relative to the loading control α-tubulin (**B**) (n=3).

6.3. Generation of DOK7 luciferase reporter cell line

The specificity of DOK7 luciferase construct was first tested in transiently transfected C2C12 cells, for the upregulation of DOK7 upon differentiation of myoblasts into myotubes (**Figure 6.5A**). C2C12 mouse muscle cells were transfected with the DOK7 luciferase construct. A control transfection using a construct containing the luciferase sequence but no promoter was also used. The cells were seeded the following day in 96-well plates, and the luciferase intensity was read the next day for myoblasts and after ~8 days for myotubes. A 14-fold increase in the luciferase activity was observed in differentiated myotubes compared to myoblasts.

DOK7 luciferase transfected C2C12 cells were further used to generate stably transfected cells harbouring the reporter construct (**Figure 6.5B**). The stable cell line shows a 10-fold increase in luciferase expression in differentiated myotubes.

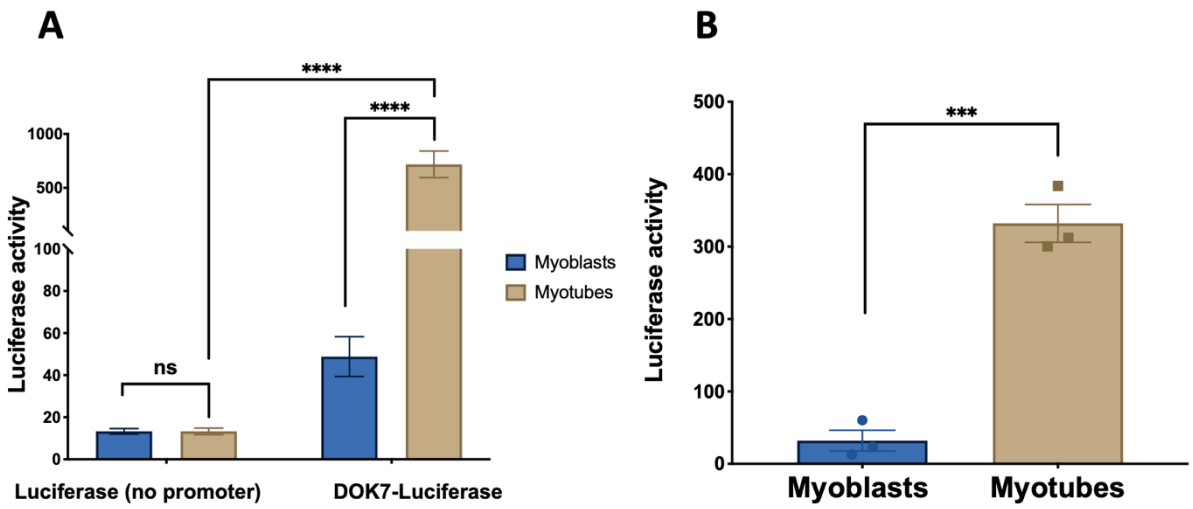

Figure 6.5. Generation of DOK7 luciferase reporter stable cell line. C2C12 cells were transiently transfected with the DOK7 luciferase reporter construct **(A)**. A construct containing the luciferase sequence but no promoter was used as negative control. The increased expression following myoblasts differentiation was used as a measurement of assay efficiency. Data is represented as mean ±SEM from 3 separate transfections. A two way ANOVA with Tukey's multiple comparisons test was performed to compare the luciferase expression between the reporter cell line and negative control. Following, a stable cell line was generated and an unpaired t test was used to assess the reliability of the assay by comparing luciferase levels in myoblasts and myotubes **(B)** (n=3; mean ±SEM).

6.3.1. Stable transfection and single clone selection

Variability in the ability of C2C12 cells to differentiate into myotubes was observed and to ultimately generate a stable cell line that, when differentiated, gave the strongest luciferase activity, single clones were further selected (**Figure 6.6**). Single clones were seeded in 96-well plates and after ~ 4 weeks, 18 clones were selected to be assayed for luciferase activity. The luciferase activity is represented as the ratio between myotubes and myoblasts, thus, a ratio above 1 implies increased luciferase expression upon differentiation into myotubes. 13 clones showed absent or minimal luciferase activity (~1). With the highest luciferase activity, shortest differentiation timespan, and lowest variability between triplicate experiments, clone number 16 was further chosen to be used in the small molecules screening assay.

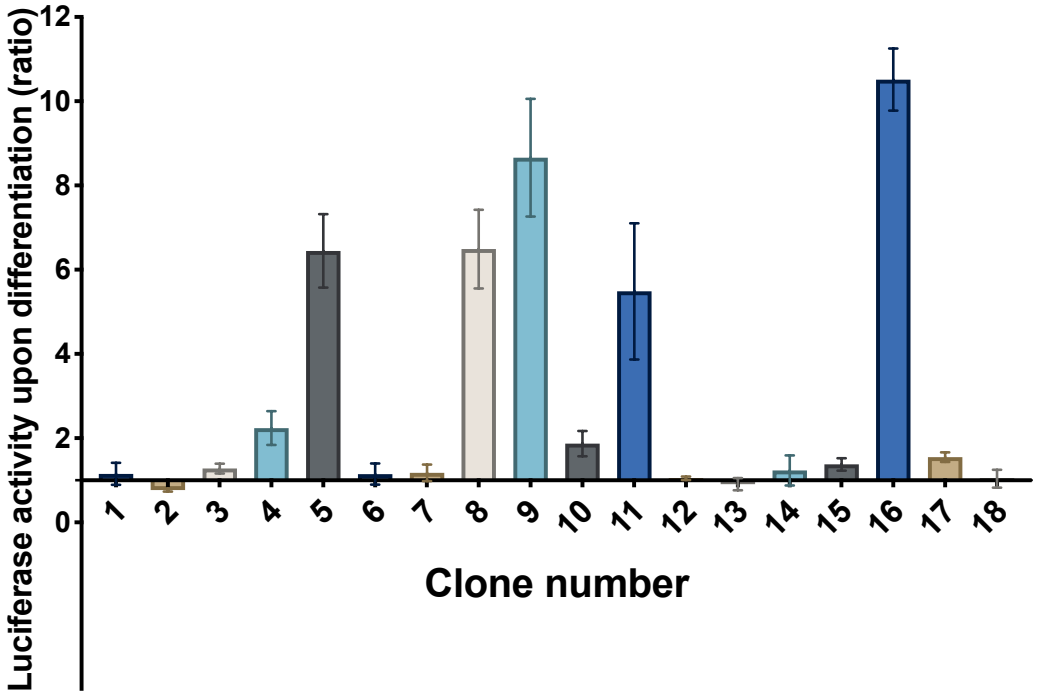

Figure 6.6. Single clone selection upon generation of stable luciferase reporter cell line. Cell lines from 18 individual clones were generated and each clone was assessed for their ability to induce luciferase expression following myotube differentiation. Data is represented as the mean ±SEM from 3 separate differentiation experiments.

6.4. Screening for enhanced DOK7 promoter activity using a luciferase reporter

The level of upregulation needed to generate the enlarged NMJs is undefined *in vitro*. In order to explore this, we used a retroviral vector harbouring a human *DOK7* expression cassette (**Section 2.5.7.1**) to infect wild-type C2C12 myoblasts and subsequently titrate the levels of DOK7 needed to generate AChR clusters. This is a way to mimic the generation of synaptic structures *in vitro*. Cells were infected with increasing percentages of DOK7 retrovirus as shown in **Figure 6.7** (the remaining amount to 100% was covered using an empty retrovirus). Lysates of mature myotubes infected with different percentages were subjected to SDS-PAGE and western blotting (**Figure 6.7A,B**). AChR clustering assays were also performed (**Figure 6.7C,D**). AChR clusters were visualised upon fluorescent α-bungarotoxin staining and analysed by Fiji software. A 2-fold increase in DOK7 protein expression levels, as shown by the analysis of western blotting intensity levels (**Figure 6.7B**), proved to be sufficient to induce a significant increase in the number of AChR clusters in DOK7 infected myotubes (**Figure 6.7D**). Representative images of AChR clusters at various DOK7 infection percentages are shown in **Figure 6.7C**.

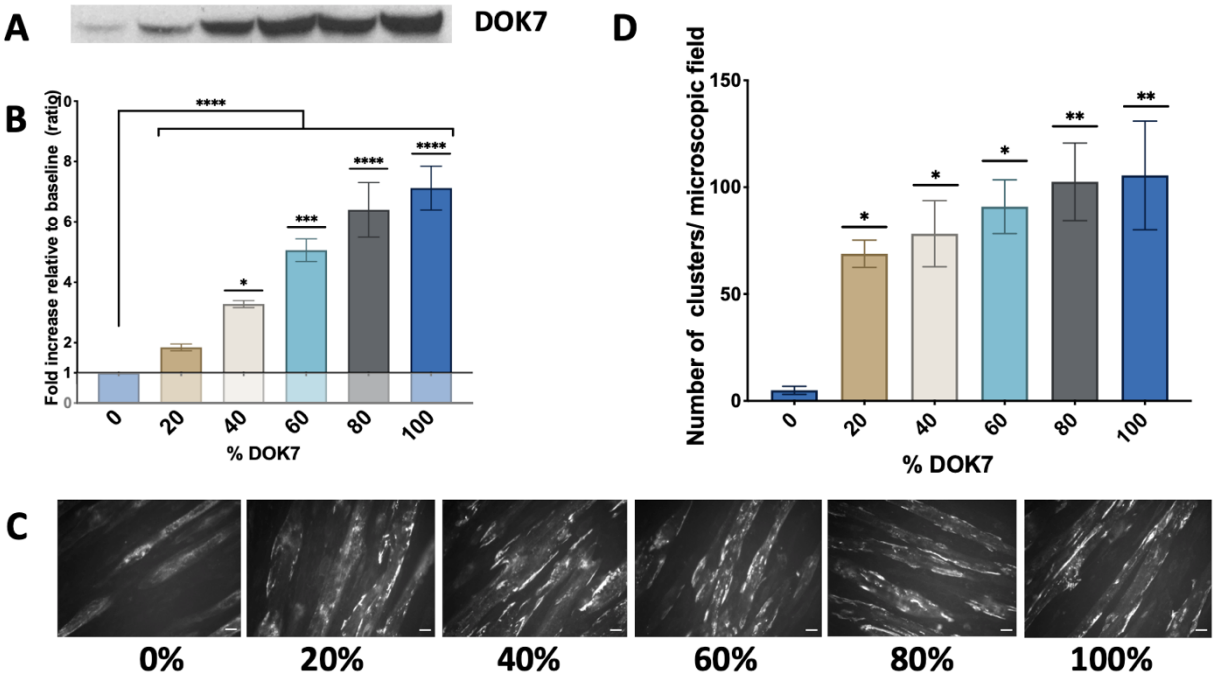

Figure 6.7. Understanding the level of DOK7 protein expression needed to induce AChR clusters on the surface of C2C12 myotubes. C2C12 cells were infected with various percentages (0, 20, 40, 60, 80, 100) of DOK7 WT retrovirus. The infections were completed with the corresponding amount of an empty retrovirus (up to 100%). After ~ 8 days of differentiation, myotubes were lysed and subjected to SDS-PAGE and western blotting **(A)**. The signal intensities of the bands on the western blotting membrane are represented as the ratio relative to the baseline control (0%) and were compared using a one way ANOVA with Dunnett's multiple comparisons test **(B)**. AChR clustering assay was performed on differentiated myotubes in the absence of Agrin **(C)**. A one way ANOVA with Dunnett's multiple comparison test was performed to compare the number of clusters between different infections **(D)**. Data is represented as the mean ±SEM from a minimum of 20 microscopic fields/infection of 3 separate retroviral infections (n=3 infections; mean ±SEM). Scale bar: 25μM.

6.4.1. Screening of small molecules

With an optimised *in vitro* model system for which the natural upregulation of DOK7 from myoblasts to myotubes can be used as a baseline control, 5430 small molecule compounds were tested. Myotubes were incubated with the compounds for ~24h prior to reading the luciferase activity. Since a 2-fold increase in DOK7 expression had been found sufficient to induce AChR clusters in myotubes, the lower cut-off for luciferase upregulation was chosen at a 2-fold increase. A representative graph with results from one plate containing 80 small molecules is shown in **Figure 6.8**. Data is represented as the ratio between the luciferase activity of each compound and the mean vehicle control (DMSO) for each plate. Small molecule compounds were stored as 10 mM stocks diluted in 100% DMSO and used at 100μM. The vehicle control was used at the same dilution with the compounds (e.g. 1% DMSO). 37 compound hits that showed at least a 2-fold increase in luciferase activity, and a coefficient of variation between triplicates of lower than 15%, were further chosen to be tested using a biological activity assay.

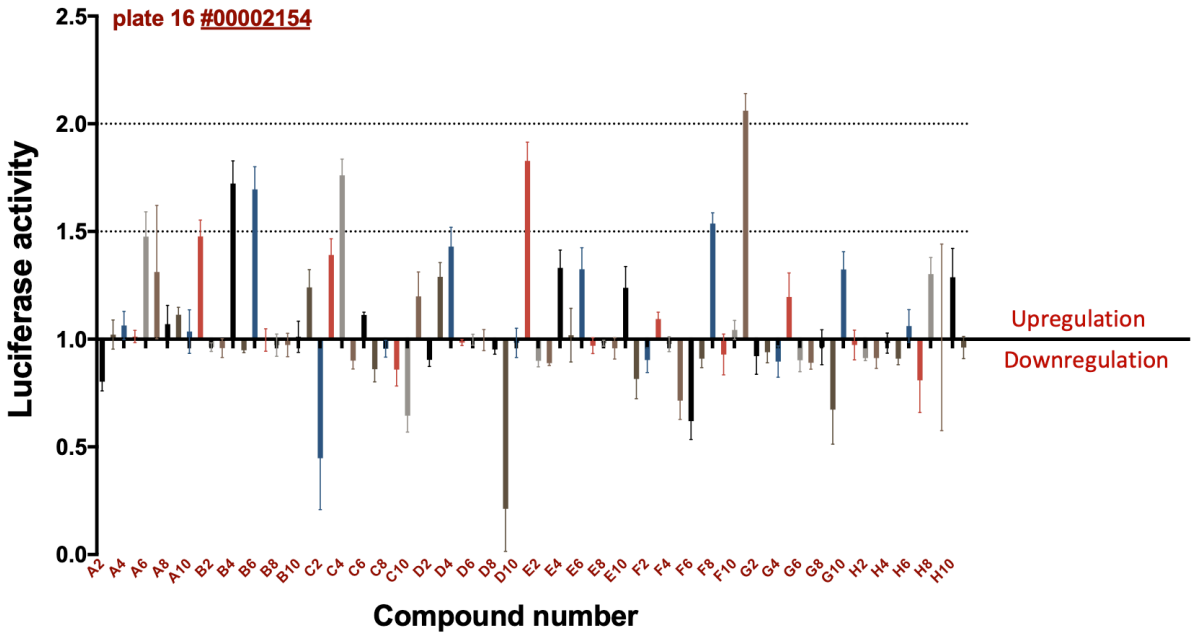

Figure 6.8. Screening for small molecule compounds using a stable luciferase-reporter cell line. 5430 small molecules were tested using our reporter assay. The compounds come as 80/plate in a 96 well format. The figure shows the results from one plate with the bar code presented in the left corner. For each plate one column was used to incubate cells with the vehicle control (DMSO) at the same dilution. This was assigned randomly in a different column between triplicates of the same plate. The data is represented as the ratio between the luciferase reading for each compound normalized to the mean vehicle control (mean ±SEM from 3 separate experiments).

6.5. Validation of compound hits using an assay of relevant biology

The AChR clustering assay was used as a secondary assay to confirm the activity and test the specificity of the 37 compounds hits that were found in the primary screen. C2C12 cells were differentiated into myotubes over the course of ~ 8 days. The compounds were added for ~24 hours at 100μM, and the same dilution of DMSO was used as a vehicle control. Since agrin is a natural instigator of AChR clustering and can be used to mimic the formation of a synaptic structure *in vitro* (**Section 1.6**), cells incubated with agrin overnight were used as positive control. Agrin was purified and titrated for the concentration that induced the highest number of AChR clusters as described in **Section 2.5.2**. Myotubes were stained using fluorescent α-bungarotoxin and imaged with a fluorescence microscope. The number of AChR clusters per field was analysed from 15-20 individual images. Data was normalised to the baseline control (DMEM).

Agrin induced on average 42 clusters per field (**Figure 6.9**), while the mean value of AChR clusters for the vehicle control (DMSO) was 3. Most of the compounds showed values similar to the vehicle control. Two of the compounds induced more than 5 clusters per field on average, and were further tested using a dose-response curve (**Figure 6.10**). Representative images for the positive control (Agrin), the vehicle control (DMSO) and the two compound hits are shown in **Figure 6.9A**.

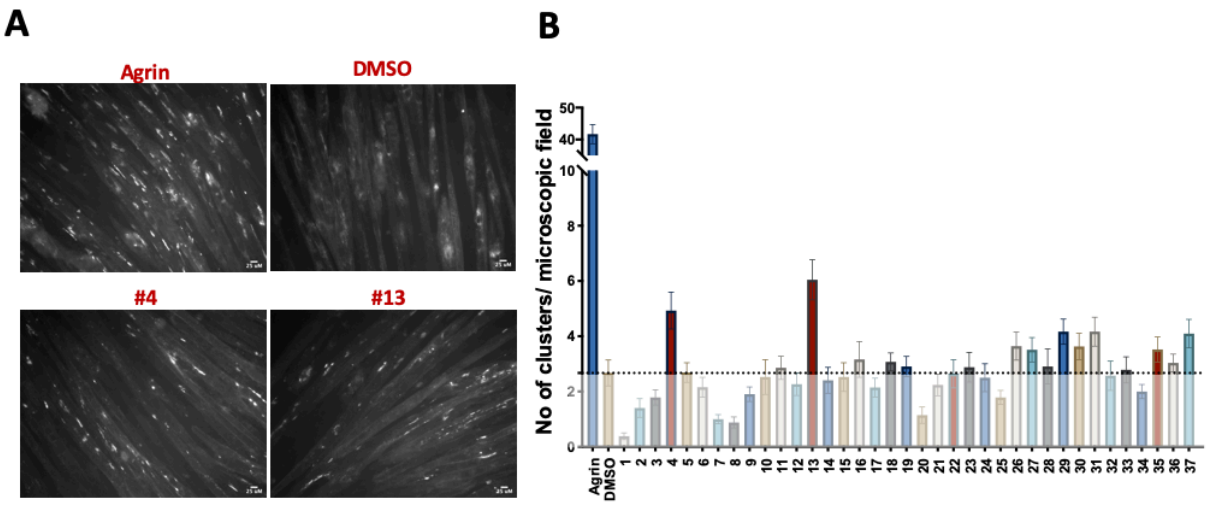

Figure 6.9. AChR clustering assay for the compound hits identified from the luciferase reporter assay screening. 37 compounds were tested in our clustering assay for their ability to induce the formation of AChR clusters on the surface of the myotubes **(A)**. Overnight incubation with Agrin was used as a positive control and the vehicle control (DMSO) incubation was used as the negative control. (**B**) Values shown above the dotted line are higher than the negative control. Data was normalized to the baseline control (incubation with DMEM) and was collected from 15-20 microscopic fields per compound from 3 separate experiments (n=3; mean ±SEM). Scale bar: 25 μM.

6.6. Determining dose-response patters for lead compounds

Having shown that compounds 4 and 13 induce the formation of clusters in C2C12 mature myotubes, we next performed a dose-response assay of each compound. For that, C2C12 myotubes were incubated with the compounds for ~24h at different concentration. Agrin was used as a positive control and DMSO as negative/vehicle control. AChR clusters were stained using fluorescent α-bungarotoxin and image acquisition was carried out using a fluorescence microscope. The ability of a compound to induce AChR clusters at various concentrations was assessed by the number of fluorescently stained AChR clusters per field from 15-20 microscopic fields. All data was normalised to the baseline control (DMEM).

Firstly, to get an idea of the range of concentrations that should be considered for dose-response analysis, C2C12 myotubes were incubated with 100 μM of each compound, as well as 3 lower concentration: 25 μM, 50 μM and 75μM (**Figure 6.10**). Compound 13 showed similar numbers of AChR clusters/field at all concentrations, while compound 4 showed increasing numbers of clusters at lower concentrations (**Figure 6.10B,C**). While both compounds showed significant increase in the number of clusters at most concentrations in comparison to the vehicle control (**C**), none of the compounds induced more than ~30% of the total number induced by Agrin (~10 clusters/field for compound 4 and ~7 clusters/field for compound 13). Representative images are shown in panel **A** of **Figure 6.10**.

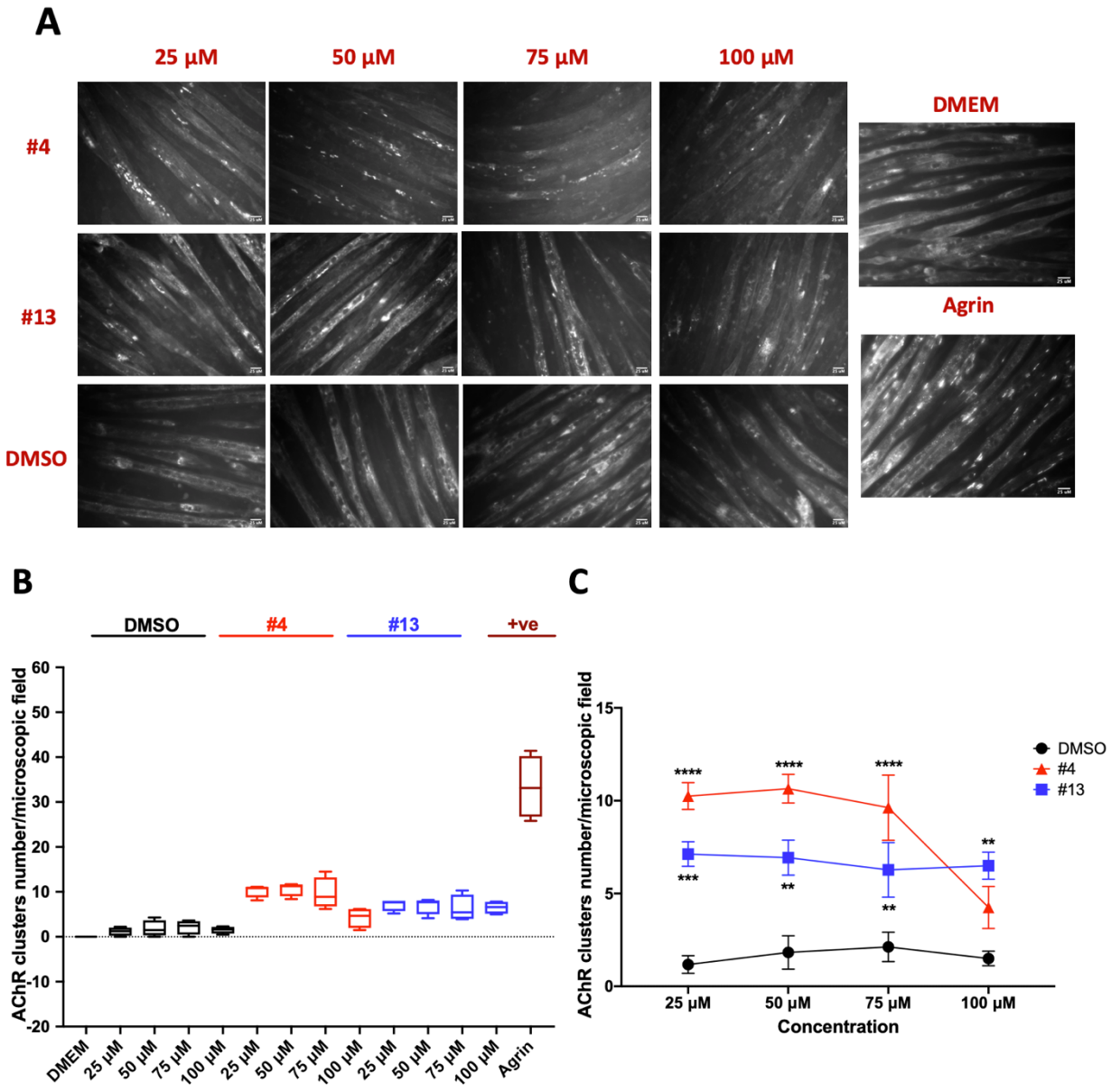

Figure 6.10. Titration of two hit compounds using the AChR clustering assay. C2C12 cells were incubated with compounds #4 and #13 at 100, 75, 50 and 25 µM and the vehicle control at respective dilutions (1%, 0.75%, 0.5% and 0.25%) (**A**). Agrin was used as the positive control and DMEM as the baseline control. 15-20 individual microscopic fields were collected from three different experiments and data is represented as mean ±SEM relative to the baseline control (**B**). A two-way ANOVA with Dunnett's multiple comparison test was performed to compare the number of clusters per field between each of the two compounds and the vehicle control at different concentrations (**C**) (n=3; mean ±SEM). Scale bar: 25 µM.

Following, a series of 2-fold dilutions starting with 200 μM was performed for each compound (**Figure 6.11**).

As shown by previous results, compound 4 shows increasing number of AChR clusters from an average of 4 at 100 μM to 11 at 12.5 μM and 6.25 μM (**Figure 6.11A**). The average number of clusters/fields decreases then to 8 at 3.125 μM and ~3 at 1.56 μM, resulting in significant changes for all concentrations except for 1.56 μM and 100 μM, when compound 4 was compared to DMSO of respective dilutions. Compound 13 showed significant results only for 25 μM, 50 μM, and 100 μM with ~7 clusters per field. The number of clusters per field decreased to an average of 3 at 6.25μM. A modest but visible degree of cell death was observed in cells incubated with 200 μM for compound 13 and this was higher for compound 4, which also presented no clusters (data not shown).

The concentration corresponding with the highest number of clusters per field for each compound was next chosen to compare to the positive control (**Figure 6.11B**). Compound 4 induced on average about 34% of the mean AChR clusters per field induced by agrin, while compound 13 induced an average of 25%.

Based on these results, a dose-response curve was generated for each of the two compounds (**Figure 6.11C**). The dose was represented as logarithm of concentration (log[dose]), and AChR cluster number was transformed in percentages with 100% being the highest average number of clusters in each data set. A higher potency was shown by compound 4, with a concentration of 2.9 μM corresponding to the half-maximum effective response (EC_{50}), in comparison to 14.4 μM as shown for compound 13.

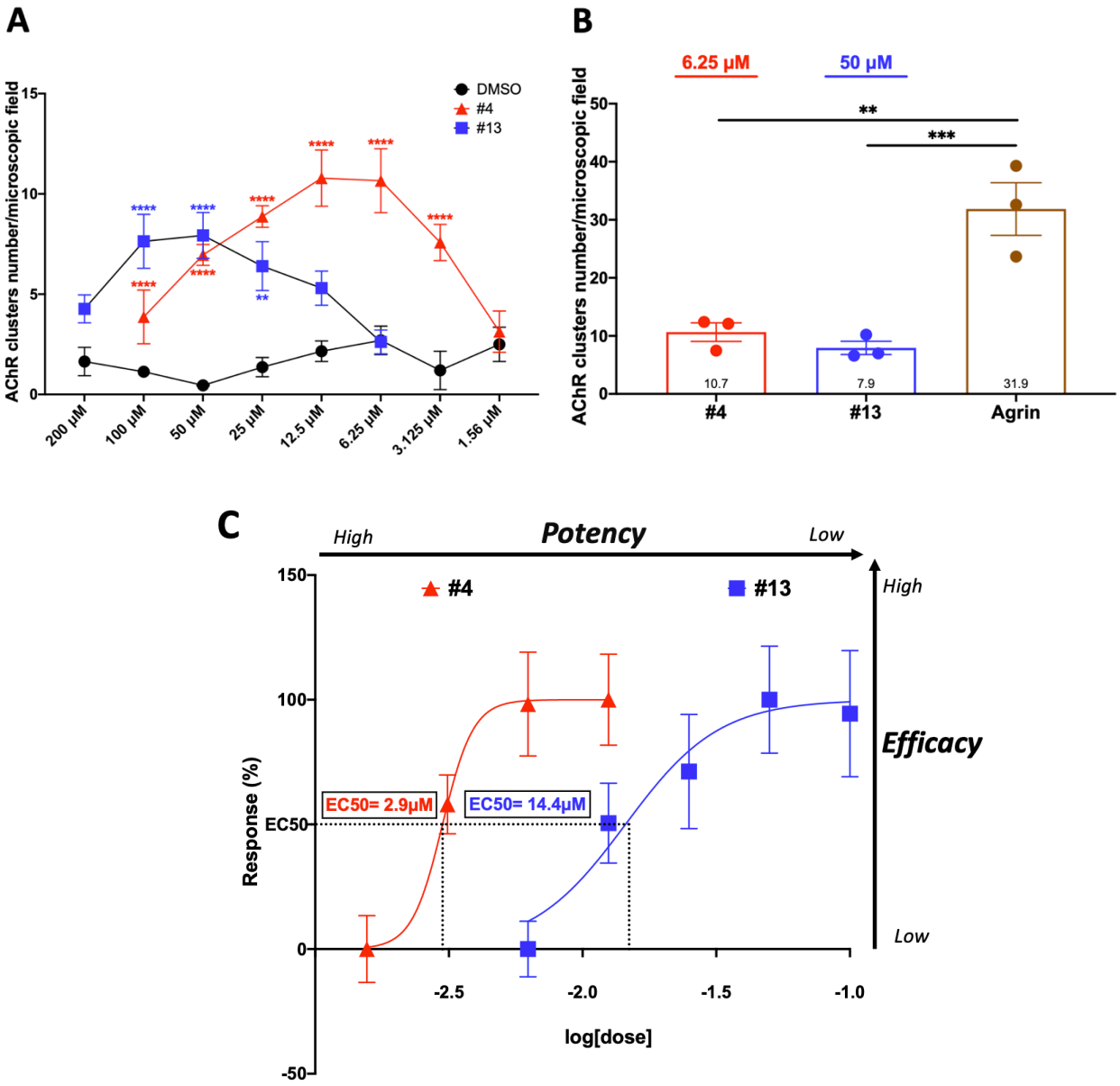

Figure 6.11. Dose-response curve of the two compound hits generated from a series of 2-fold dilutions. Dilutions were performed for compounds #4 and #13 starting with 200 µM until no AChR clusters were observed. Two-way ANOVA with Dunnett's multiple comparison tests were performed to compare each compound with the vehicle control (DMSO) at different concentration **(A)**. The concentration corresponding to the highest number of clusters observed for each compound were used to compare to the positive control (agrin) **(B)** (ordinary one-way ANOVA with Tukey's multiple comparison test). A dose-response curve was generated for each compound **(C)**. The response is represented as percentage and the dose was transformed to log[dose]. EC_{50} values were calculated in GraphPad prism and are represented here as the 50% response. Data was normalized to the baseline control (DMEM) (n=3 individual experiments, 10-15 microscopic fields/ experiment; mean ±SEM).

6.7. Discussion

In this study we aimed to screen for small molecules that can upregulate the expression of DOK7 protein in skeletal muscles. Upon screening of 5430 small molecule from a narrowed library of muscle-specific compounds, 2 hit compounds showed activity in our AChR clustering assay. They have the potential to form the basis of a novel therapy that could be applicable to many CMS patients and possibly other neuromuscular disorders. This idea is based on an extension of the AAV gene therapy described in the previous chapters.

A cell-based assay was first designed to allow for the assessment of DOK7 upregulation in a physiologically relevant environment. A 1 kb sequence of the human *DOK7* promoter followed by the luciferase reporter was integrated into the genome of C2C12 cells to provide a stable reporter cell line (**Figure 6.5**). A reporter construct with a 2 kb region of the *DOK7* promoter was also generated but showed no increase in luciferase activity over the reporter containing a 1 kb region (data not shown). A 3 kb sequence proved very difficult to amplify probably due to a high GC-content of the region of more than 60% which is linked to the formation of secondary intramolecular structures (McDowell et al. 1998; Assal and Lin 2020). However, this region of the promoter is likely not required since Cooper and colleagues showed that functional regions that are found within a sequence of ~250 bp upstream of the transcription start site positively contribute to the core promoter activity of 45 randomly selected human promoters (Cooper et al. 2006). More specifically, for many postsynaptic NMJ genes, such as *Musk*, AChR subunits encoding genes and also *Dok7,* regulatory sequences are located in close proximity of the transcription start site (Tang et al. 2006; Hamuro et al. 2011). Therefore we have chosen a 1 kb sequence for our assay.

Reporter genes can facilitate the study of gene expression. They are designed in such way that their signal is directly correlated with the actual expression of the gene of interest by being placed downstream of its promoter and regulatory elements. The advantage is that their activity is easier to measure as compared to direct measurements of transcription, and there are commercially available assays to do so. We used the firefly luciferase reporter gene, and the primary advantages over other reporter genes are their low background in mammalian cells (which do not naturally express light-generating enzymes), their high specific activity and their relatively rapid enzyme turnover (Bauer 2011). Also, the sensitivity and broad dynamic range linked to luciferase gene reporter assays, make them a suitable and convenient choice for cell-based high throughput screening of small molecules in the hunt for activators of drug targets. However, one of the drawback is that the reporter firefly luciferase is known to be modulated by low-molecular weight compounds such as the small molecules used in this study. Within the cell, this can lead to changes in the enzymatic activity of the luciferase enzyme and thus an increase in luciferase activity. In this case, the luciferase expression can be indistinguishable from the transcriptional activation of the reporter gene, and so generating false positives (Auld et al. 2008; Thorne et al. 2012; Ho et al. 2013; Auld and Inglese 2018). A perfect scenario of high-throughput screening would imply using a primary screen, a counter-screen to rule out false positives, an orthogonal screen and ultimately to use the compound hits in a functional assay (Inglese et al. 2007; Auld and Inglese 2018). However, negative results in counter-screen assays are not always as conclusive as an assay that reinforces evidence for target activity. A powerful assay for confirming activity of interest is the ‘orthogonal assay’ as it replicates the exact same biology but uses a different detection strategy.

During experimental design and assay optimisation, we developed and tested an orthogonal assay using an EGFP reporter to provide confirmatory readouts. The assay proved inefficient as the signals between the negative and positive control sample in the proof-of-principle experiments were indistinguishable, most likely linked to high background signal. It also showed no differences in reporter gene expression when myoblasts were differentiated into myotubes, which is clearly shown by our luciferase assay in **Figure 6.5** and **6.6**. This could be due to the type of fluorescence reading assay that was based on averaging of multipoint readings in a well of adherent C2C12 myotubes. Myoblasts can have varying degrees of fluorescent intensities depending on the efficiency of transfection. Moreover, even within a single well of a plate, individual myotubes can differentiate at various rates, and therefore present different levels of DOK7 natural upregulation, or in our case EGFP upregulation. A plate reader that uses a multipoint pattern could omit reading fully differentiated cells and thus give misleading results. Various attempts were made using different plate readers and methodologies such as quantification of fluorescence microscopy images or analysis of lysate samples by SDS-Page and western blotting, but with no success.

AChR clustering assay in C2C12 myotubes represents a true readout of genuine biological activity that results from overexpression of DOK7 or upon agrin incubation. Moreover, this robust and reliable assay has been developed and used in our group over many years. Thus, rather than using an orthogonal reporter assays which may be subject to a number of confounding factors, AChR cluster formation in the absence of agrin was chosen as an *in vitro* readout of biological function for the compound hits. 5430 compounds from a narrowed library were first tested in our DOK7 luciferase reporter assay. Having no positive control for our assay to be able to generate z scores, the screening was done in triplicates and compounds with

a coefficient of variation between triplicate reading higher than 15% were excluded (Inglese et al. 2007). Furthermore, by using a retroviral system we showed that a 2-fold increase in DOK7 expression relative to the baseline control was enough to generate significantly more AChR clusters as compared to the baseline control (**Figure 6.7**). Even though a 2-fold increase in expression might not be enough to generate 'super synapses', it is a good guidance for our screening and was set as the lower limit cut-off in selecting compound hits for the functional assay.

37 small molecule hits were further chosen to be tested in our biological activity assay. Two compounds showed their ability to induce AChR clusters in cultured myotubes at 100 μM (**Figure 6.9**). We further tested various concentrations for the two compound hits and ultimately generated dose-response curves. Compound number 4 induced overall more AChR clusters in comparison to compound 13, with 11 clusters per field as opposed to ~7 (**Figure 6.10** and **6.11**). Also, a higher potency was associated with compound 4, which induced the half maximum response at a dose approximatively five times lower than compound 13 (**Figure 6.11C**). Even though both compounds induced no more than 20-30% of the total number of AChR clusters per field induced by agrin, the two compounds show potential and may represent the springboard for further investigations.

Having shown that the two compounds can induce the formation of AChR clusters on the surface of mature myotubes to some extent, it is important to mention that in both cases the highest potency was observed at lower concentrations as compared to the primary screening which was done at 100 μM. This suggests the possibility of having missed potential hits that could have shown activity at lower concentrations in the primary screen. It would be important

to repeat the screening using the compound library at lower concentrations, and this time the compound 4 could be used as a positive control.

Having found two potential lead compounds (**Figure 6.12**), the next step would involve looking into the mechanism of action. This could help in understanding binding partners of the two hits and look into potential binding sites and ways of allowing better access to those for a stronger affinity and thus higher potency. Subsequently, lead compounds optimisation could involve structural modifications to avoid potential toxic and metabolically vulnerable groups. With the aid of computational tools this would then move towards predicting drug-like molecules and finally developing potential drugs. Small molecule drugs are primarily cleared either through hepatic metabolism or through renal/biliary excretion. Thus, *in vitro* metabolic profile would be next tested in both mouse and human liver cells and promising molecules will be chosen for further progression to preclinical studies (Silber 2010; Berdigaliyev and Aljofan 2020).

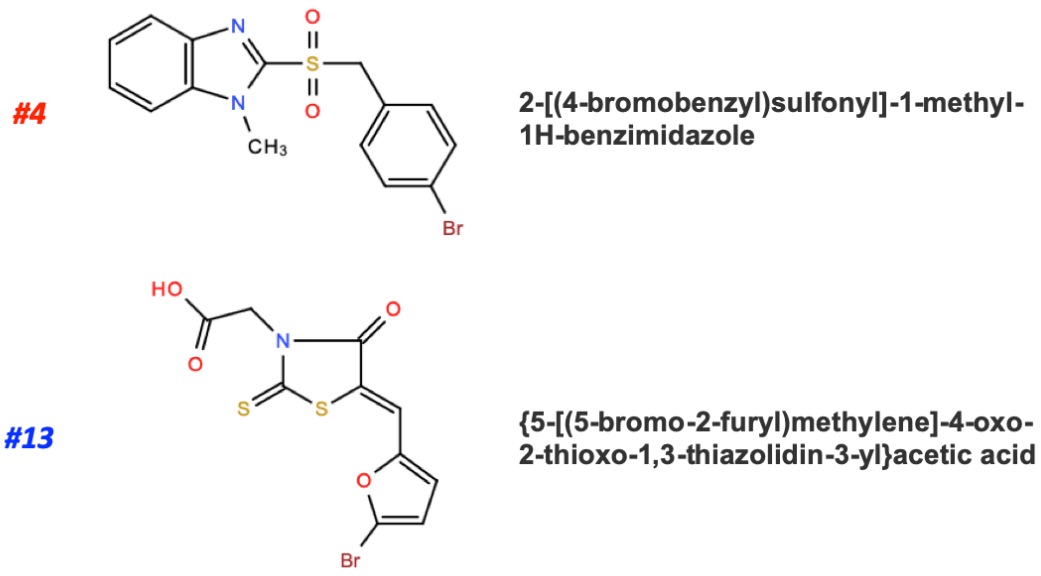

Figure 6.12. Chemical structures and names of compound hits.

Small molecules are relatively simple chemical compounds and their pharmacological activity, stability and permeability depend largely on their chemistry as opposed to structural interaction (Berdigaliyev and Aljofan 2020). In choosing a dosing route in the future, an orally bioavailable product to be taken at home would be the ideal preference for both CMS patients and manufacturers. While bioavailability is often a parameter of interest in drug development and delivery, efficient membrane permeation and solubility are likely necessary for the bioavailability of small molecule-drugs (Veber et al. 2002). A common issue encountered during clinical trials is achieving sufficient plasma levels to generate a substantial benefit (Silber 2010; Eder and Herrling 2016). This strongly supports the importance of early dose optimisation and testing of various formulations of the drug. Thus, early optimisation of oral bioavailability is essential and can be aided by the use of a specific list of guidelines which should emphasize:

1) the importance of maximised solubility and intestinal permeation for decent oral absorption
2) the benefit of using simple formulations to facilitate easier subsequent modifications
3) the attention required for early identification of specific functional groups that can influence poor bioavailability and first pass metabolism (Aungst 2017).

To summarise, this study shows the potential of screening small molecule compounds in the hunt for a novel drug that can upregulate the expression of DOK7 at the NMJ. This can potentially serve as a new therapy for many CMS subtypes, but would obviously exclude mutations in the *DOK7* gene.

Chapter 7

Conclusions and future perspectives

Rare genetic neuromuscular diseases comprise diverse musculoskeletal conditions ranging from ultra-orphan disorders to the more 'common' but rare orphan diseases such as spinal muscular atrophy (SMA) or Duchenne muscular dystrophy (DMD). Novel causative CMS-genes continue to be uncovered as next generation sequencing is taken into the clinic. Concomitant with genetic approaches being used more and more for the diagnosis of inherited muscle diseases, next generation sequencing is now viewed as part of the treatment strategies aimed at correcting the underlying pathology. Several promising genetic therapeutic approaches for DMD are currently at the preclinical or clinical stages, with the field of SMA benefiting from an already approved AAV-based gene therapy (Al-Zaidy and Mendell 2019; Babbs et al. 2020).

The potential of AAV vectors as a platform for gene therapy is enhanced by their excellent safety profile, high transduction efficiency and broad range of tissues that can be targeted (Colella et al. 2018). However, despite the significant progress being made, the field of neuromuscular disorders presents constraints, for example:

1) difficulties in targeting all muscle tissues at sufficiently high levels
2) the timing of gene therapy delivery is important considering that the efficiency can decrease during muscle growth
3) the effectiveness can be reduced by the host's immune response to the virus or the therapeutic gene (Babbs et al. 2020)

Moreover, to achieve clinical benefits, some disorders might need high titters of virus which in turn can lead to undesired adverse effects (Colella et al. 2018; Hinderer et al. 2018).

The aim of this thesis was to investigate potential novel therapies for congenital myasthenic syndromes and other neuromuscular junction diseases. Based on previous evidence demonstrating that increasing levels of the DOK7 protein could improve the myasthenic phenotype, we have tested two different approaches.

We have shown the potential of AAV-based gene therapy to upregulate the production of DOK7 protein in the first three results chapters. **Chapter 3** presents insights into the mechanism that induces the formation of enlarged synapses. We showed that DOK7 overexpression triggers upregulation of some NMJ-related genes (*Chrne*, *Chrna1*, *Chrnd*, *Colq*), but also of some genes potentially involved in cytoskeleton remodelling or neurotransmission. Next, we confirmed that the DOK7-CMS mouse model benefits from DOK7 overexpression with improved lifespan, motor activity and neurotransmission.

Following, in **Chapter 5** it was demonstrated that DOK7-AAV gene therapy lessens the impairment in neurotransmission in a mouse model of AChR deficiency and improves hang time on an inverted screen test. Overall, the efficiency of AAV transduction was monitored by analysing the number of enlarged synapses observed in the diaphragm and two leg muscles of treated mice. A lower transduction efficiency was observed in both leg muscles of wild-type mice (**Chapter 3**) as compared to the AChR deficiency model mice (**Chapter 5**). Perhaps the DOK7-AAV gene therapy effect was more accentuated in the deficient muscles that actually needed recovery and presented favourable circumstances for improvement. However, further

investigations are needed to understand these observations and to exclude the possibility of technical variability.

More work will be required to elucidate the pathway leading to structural enlargement of the NMJ, as well as long-term implications of these changes during health and disease. The enlarged synapses could be an intrinsic property of DOK7 overexpression at the NMJ, or it could simply be the consequence of DOK7 overexpression along the length of the muscle fibre. Also, it would be of interest to assess differences in transduction efficiency more in depth considering slow- and fast-twitch muscles, as it has been shown previously that AAV9 preferentially transduces fast-twitch muscles (Bostick et al. 2007). This could give insights into potential advantages and disadvantages of choosing other AAV serotypes over AAV9 to improve treatment response in the future. Lastly, an interesting approach to further understand the feasibility to transpose this therapy to other NMJ-related disease would be to test it in animal models of DMD.

This thesis also began to explore an alternative strategy of screening small-molecule drugs to potentially find novel therapies for CMS. This is based on the underling biology of the NMJ utilising the effect of overexpression of DOK7. It is also based on the approach used in finding the utrophin modulator ezutromid for DMD (Muntoni et al. 2019).

Upon reporter cell line generation and assay optimisation, we found two compound hits that proved their ability to induce AChR clusters *in vitro* in our biological active assay to a significant level when compared to the vehicle control. Having showed that, following steps would be to liaise with our collaborators form the Department of Chemistry to look into generating clusters of compounds with similar structures to be further tested in our assay, but

also discuss structural modification of these compounds. Studying the structure of the two lead compounds is of outstanding importance for future steps (**Figure 7.1**).

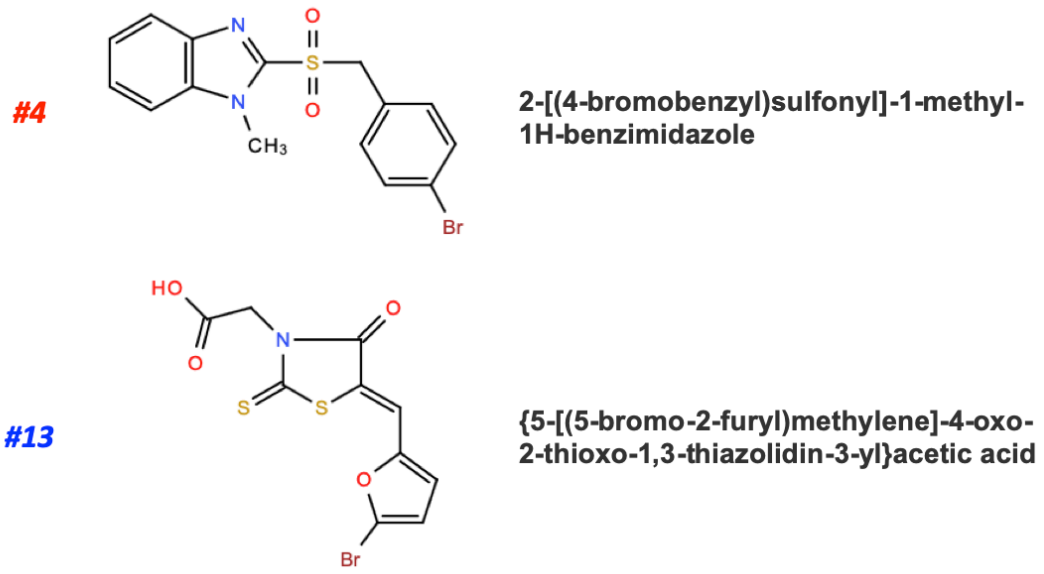

Figure 7.1. Chemical structures and names of compound hits.

Although both compounds present encouraging levels of potency *in vitro*, the presence of potential toxicophores or other structural features that could give cause for concern need to be discussed with our colleagues prior to developing similar libraries. For example the bromobenzene primary feature that we can observe in compound 4 has been linked to hepatotoxicity for two drugs that are now withdrawn from the market (bromfenac and ebrotidine) (**Figure 7.2**) (Singh et al. 2016). Also, the heteroaryl acetic acid feature present in the structure of compound 13 has been linked to hepatotoxicity (shown by approved drug-feclozic acid) but also potential anaphylaxis as shown by use of zomepirac (Singh et al. 2016).

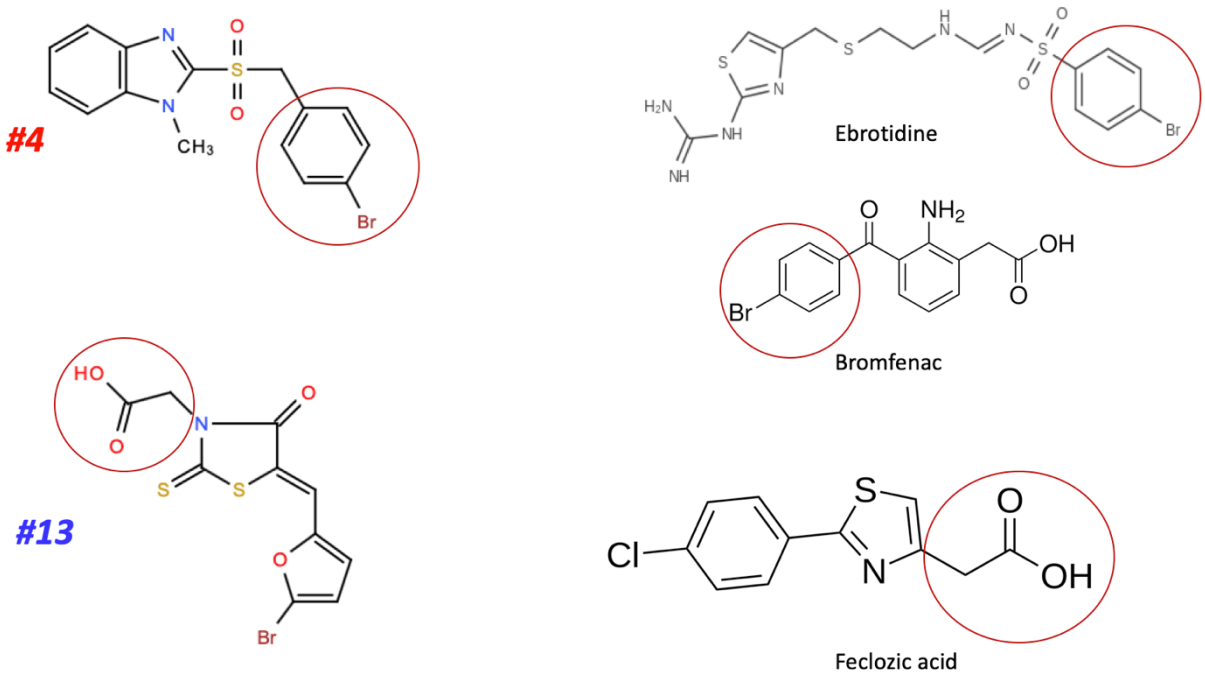

Figure 7.2. Structural similarities between our compound hits and previously approved drugs that showed side effects. The three drugs presented on the right are approved drugs that were withdrawn from the market due to concerns related to adverse effects. Note the similarities between these and our compounds (bromobenzene for #4 and the heteroaryl acetic acid feature for #13; red circles). These could potentially increase the toxicity *in vivo* and so would need to be modified.

Looking into possible metabolically vulnerable groups during early stages is also important. For example, one of the drawbacks in the utrophin upregulation project during Phase 2 clinical trials was that the initially observed positive effects were not sustainable in long-term. They later showed that this was due to the drug (ezutromid) being rapidly metabolised (Chatzopoulou et al. 2020). The main aim would be to focus on attempts to replace structures that raise concern while still retaining some level of biological activity. Also, the structural similarities between the two compounds (**Figure 7.3**), as well as the major differences that potentially induce a higher potency for compound 4, should be taken into consideration. Moreover, structural comparison between the two hits and other CMS approved drugs could give new insights into possible structural modification for these two and other similar families of compounds.

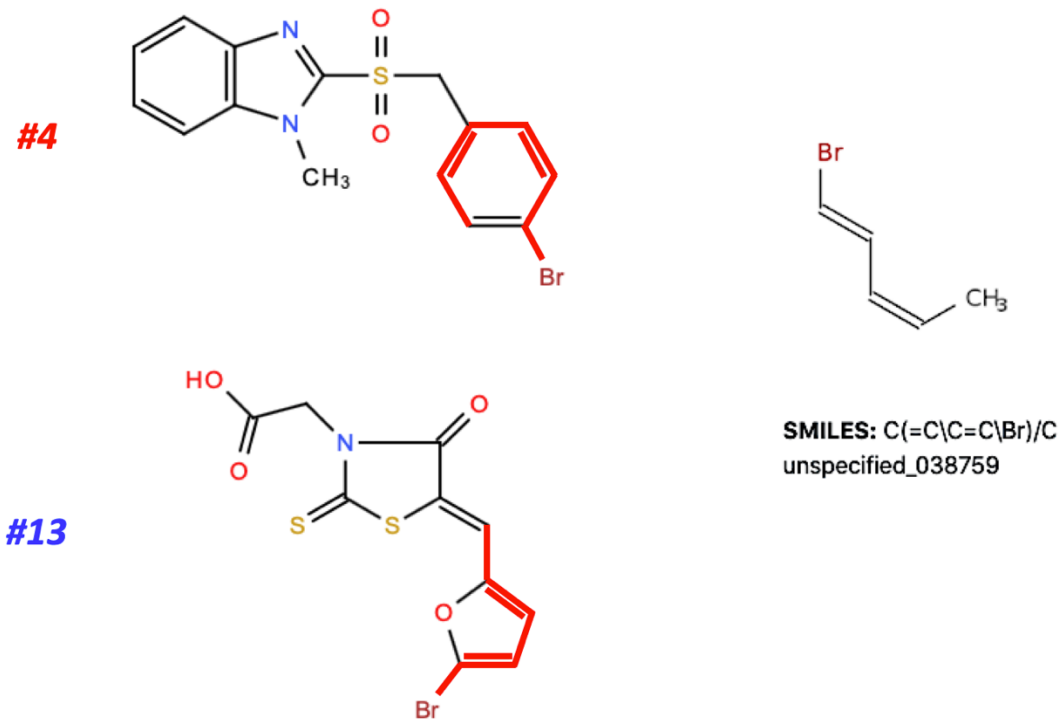

Figure 7.3. Similarities between the two compound hits. Using an online software for chemical structural comparison (ChemMine Tools), we revealed the similar features between the two compounds (the SMILES generated from the job is an unique tag of the feature to be able to compare with other compounds). This could help in designing a library of small molecule compounds that could be further tested in our functional assay in the hunt for a more potent drug that could be further used *in vivo* in animal models of CMS.

While no current treatments are actually able to "cure" CMS, but can only control and ameliorate the symptoms, tremendous progress has been made in understanding the disease mechanism and thus, identifying potential future therapeutic targets. The field is ripe for novel therapies that could eventually enter clinical trials, and current research advances are slowly heading in this direction.

Bibliography

Adams, Marvin E., Neal Kramarcy, Taku Fukuda, Andrew G. Engel, Robert Sealock, and Stanley C. Froehner. 2004. "Structural Abnormalities at Neuromuscular Synapses Lacking Multiple Syntrophin Isoforms." *Journal of Neuroscience* 24 (46): 10302–9. https://doi.org/10.1523/JNEUROSCI.3408-04.2004.

AG Engel, XM Shen, D Selcen, SM Sine. 2015. "Congenital Myasthenic Syndromes: Pathogenesis, Diagnosis, and Treatment." *Lancet Neurol* 14: 420–34.

Aguti, Sara, Alberto Malerba, and Haiyan Zhou. 2018. "The Progress of AAV-Mediated Gene Therapy in Neuromuscular Disorders." *Expert Opinion on Biological Therapy*. Taylor and Francis Ltd. https://doi.org/10.1080/14712598.2018.1479739.

Aittaleb, Mohamed, Isabel Martinez-Pena y Valenzuela, and Mohammed Akaaboune. 2017. "Spatial Distribution and Molecular Dynamics of Dystrophin Glycoprotein Components at the Neuromuscular Junction in Vivo." *Journal of Cell Science*. https://doi.org/10.1242/jcs.198358.

Akaaboune, Mohammed, Susan M. Culican, Stephen G. Turney, and Jeff W. Lichtman. 1999. "Rapid and Reversible Effects of Activity on Acetylcholine Receptor Density at the Neuromuscular Junction in Vivo." *Science* 286 (5439): 503–7. https://doi.org/10.1126/science.286.5439.503.

Al-Zaidy, Samiah A., and Jerry R. Mendell. 2019. "From Clinical Trials to Clinical Practice: Practical Considerations for Gene Replacement Therapy in SMA Type 1." *Pediatric Neurology*. Elsevier Inc. https://doi.org/10.1016/j.pediatrneurol.2019.06.007.

Albuquerque, Edson X, Edna F R Pereira, Manickavasagom Alkondon, and Scott W Rogers. 2009. "Mammalian Nicotinic Acetylcholine Receptors: From Structure to Function." https://doi.org/10.1152/physrev.00015.2008.

Antolik, C., D. H. Catino, A. M. O'Neill, W. G. Resneck, J. A. Ursitti, and R. J. Bloch. 2007.

"The Actin Binding Domain of ACF7 Binds Directly to the Tetratricopeptide Repeat Domains of Rapsyn." *Neuroscience*. https://doi.org/10.1016/j.neuroscience.2006.11.047.

Apel, Elizabeth D., Steven L. Roberds, Kevin P. Campbell, and John P. Merlie. 1995. "Rapsyn May Function as a Link between the Acetylcholine Receptor and the Agrin-Binding Dystrophin-Associated Glycoprotein Complex." *Neuron* 15 (1): 115–26. https://doi.org/10.1016/0896-6273(95)90069-1.

Arikawa-Hirasawa, Eri, Susana G. Rossi, Richard L. Rotundo, and Yoshihiko Yamada. 2002. "Absence of Acetylcholinesterase at the Neuromuscular Junctions of Perlecan-Null Mice." *Nature Neuroscience* 5 (2): 119–23. https://doi.org/10.1038/nn801.

Arimura, Sumimasa, Takashi Okada, Tohru Tezuka, Tomoko Chiyo, Yuko Kasahara, Toshiro Yoshimura, Masakatsu Motomura, Nobuaki Yoshida, David Beeson, Shin'ichi Takeda, et al. 2014. "DOK7 Gene Therapy Benefits Mouse Models of Diseases Characterized by Defects in the Neuromuscular Junction." *Science* 345 (6203): 1505–8. https://doi.org/10.1126/science.1250744.

Assal, Nadia, and Min Lin. 2020. "PCR Procedures to Amplify GC-Rich DNA Sequences of Mycobacterium Bovis." *BioRxiv*, February, 2020.02.18.953695. https://doi.org/10.1101/2020.02.18.953695.

Atchison, R. W., B. C. Casto, and W. McD. Hammon. 1965. "Adenovirus-Associated Defective Virus Particles." *Science*. https://doi.org/10.1126/science.149.3685.754.

Auld, Douglas S., and James Inglese. 2018. "Interferences with Luciferase Reporter Enzymes. 2016 Jul 1 [Updated 2018 Jul 1]. In: Sittampalam GS, Grossman A, Brimacombe K, et Al., Editors. Assay Guidance Manual [Internet]. Bethesda (MD): Eli Lilly & Company and the National Center for Advancing Tran" 1 (Md): 1–13. http://www.ncbi.nlm.nih.gov/pubmed/27478246.

Auld, Douglas S, Natasha Thorne, Dac-trung Nguyen, and James Inglese. 2008. "A Specific Mechanism for Nonspecific." *ACS Chemical Biology* 3 (8): 463–70.

Aungst, Bruce J. 2017. “Optimizing Oral Bioavailability in Drug Discovery: An Overview of Design and Testing Strategies and Formulation Options.” *Journal of Pharmaceutical Sciences*. Elsevier B.V. https://doi.org/10.1016/j.xphs.2016.12.002.

Awad, Suad S., Robert N. Lightowlers, Carol Young, Zofia M.A. Chrzanowska-Lightowlers, Terje Lømo, and Clarke R. Slater. 2001. “Sodium Channel MRNAs at the Neuromuscular Junction: Distinct Patterns of Accumulation and Effects of Muscle Activity.” *Journal of Neuroscience*. https://doi.org/10.1523/jneurosci.21-21-08456.2001.

Babbs, Arran, Maria Chatzopoulou, Ben Edwards, Sarah E. Squire, Isabel V.L. Wilkinson, Graham M. Wynne, Angela J. Russell, and Kay E. Davies. 2020. “From Diagnosis to Therapy in Duchenne Muscular Dystrophy.” *Biochemical Society Transactions*. Portland Press Ltd. https://doi.org/10.1042/BST20190282.

Badawi, Yomna, and Hiroshi Nishimune. 2018. “Presynaptic Active Zones of Mammalian Neuromuscular Junctions: Nanoarchitecture and Selective Impairments in Aging.” *Neuroscience Research*. Elsevier Ireland Ltd. https://doi.org/10.1016/j.neures.2017.11.014.

Balaton, Bradley P., and Carolyn J. Brown. 2016. “Escape Artists of the X Chromosome.” *Trends in Genetics*. Elsevier Ltd. https://doi.org/10.1016/j.tig.2016.03.007.

Balice-Gordon, R. J., and J. W. Lichtman. 1993. “In Vivo Observations of Pre- and Postsynaptic Changes during the Transition from Multiple to Single Innervation at Developing Neuromuscular Junctions.” *Journal of Neuroscience*. https://doi.org/10.1523/jneurosci.13-02-00834.1993.

Banks, Glen B., Christian Fuhrer, Marvin E. Adams, and Stanley C. Froehner. 2003. “The Postsynaptic Submembrane Machinery at the Neuromuscular Junction: Requirement for Rapsyn and the Utrophin/Dystrophin-Associated Complex.” *Journal of Neurocytology*. J Neurocytol. https://doi.org/10.1023/B:NEUR.0000020619.24681.2b.

Barefield, David Y., Megan J. Puckelwartz, Ellis Y. Kim, Lisa D. Wilsbacher, Andy H. Vo, Emily A. Waters, Judy U. Earley, et al. 2017. "Experimental Modeling Supports a Role for MyBP-HL as a Novel Myofilament Component in Arrhythmia and Dilated Cardiomyopathy." *Circulation* 136 (16): 1477–91. https://doi.org/10.1161/CIRCULATIONAHA.117.028585.

Bartoli, Marc, Manjunath K. Ramarao, and Jonathan B. Cohen. 2001. "Interactions of the Rapsyn RING-H2 Domain with Dystroglycan." *Journal of Biological Chemistry* 276 (27): 24911–17. https://doi.org/10.1074/jbc.M103258200.

Bauer, Paul. 2011. "Luciferase Reporter Gene Assays." In *Encyclopedia of Cancer*, 2077–81. Springer Berlin Heidelberg. https://doi.org/10.1007/978-3-642-16483-5_3430.

Beeson, David. 2016. "Congenital Myasthenic Syndromes: Recent Advances." *Current Opinion in Neurology* 29 (5): 565–71. https://doi.org/10.1097/WCO.0000000000000370.

Beeson, David, Osamu Higuchi, Jackie Palace, Judy Cossins, Hayley Spearman, Susan Maxwell, John Newsom-davis, et al. 2006. "Dok-7 Mutations Underlie a Neuromuscular Junction Synaptopathy," no. September.

Beeson, David, Osamu Higuchi, Jackie Palace, Judy Cossins, Hayley Spearman, Susan Maxwell, John Newsom-Davis, et al. 2006. "Dok-7 Mutations Underlie a Neuromuscular Junction Synaptopathy." *Science* 313 (5795): 1975–78. https://doi.org/10.1126/science.1130837.

Belaya, Katsiaryna, Sarah Finlayson, Clarke R. Slater, Judith Cossins, Wei Wei Liu, Susan Maxwell, Simon J. McGowan, et al. 2012. "Mutations in DPAGT1 Cause a Limb-Girdle Congenital Myasthenic Syndrome with Tubular Aggregates." *American Journal of Human Genetics* 91 (1): 193–201. https://doi.org/10.1016/j.ajhg.2012.05.022.

Belaya, Katsiaryna, Pedro M. Rodríguez Cruz, Wei Wei Liu, Susan Maxwell, Simon McGowan, Maria E. Farrugia, Richard Petty, et al. 2015. "Mutations in GMPPB Cause

Congenital Myasthenic Syndrome and Bridge Myasthenic Disorders with Dystroglycanopathies." *Brain*. https://doi.org/10.1093/brain/awv185.

Berdigaliyev, Nurken, and Mohamad Aljofan. 2020. "An Overview of Drug Discovery and Development." *Future Medicinal Chemistry*. Future Medicine Ltd. https://doi.org/10.4155/fmc-2019-0307.

Bergamin, Elisa, Peter T. Hallock, Steven J. Burden, and Stevan R. Hubbard. 2010. "The Cytoplasmic Adaptor Protein Dok7 Activates the Receptor Tyrosine Kinase MuSK via Dimerization." *Molecular Cell* 39 (1): 100–109. https://doi.org/10.1016/j.molcel.2010.06.007.

Berns, Kenneth I., and Nicholas Muzyczka. 2017. "AAV: An Overview of Unanswered Questions." *Human Gene Therapy*. Mary Ann Liebert Inc. https://doi.org/10.1089/hum.2017.048.

Bezakova, Gabriela, Johannes P. Helm, Maura Francolini, and Terje Lømo. 2001. "Effects of Purified Recombinant Neural and Muscle Agrin on Skeletal Muscle Fibers in Vivo." *Journal of Cell Biology* 153 (7): 1441–52. https://doi.org/10.1083/jcb.153.7.1441.

Blake, Derek J., Jonathon M. Tinsley, and Kay E. Davies. 1996. "Utrophin: A Structural and Functional Comparison to Dystrophin." *Brain Pathology*. Blackwell Publishing Ltd. https://doi.org/10.1111/j.1750-3639.1996.tb00781.x.

Bloch, R. J. 1986. "Actin at Receptor-Rich Domains of Isolated Acetylcholine Receptor Clusters." *Journal of Cell Biology* 102 (4): 1447–58. https://doi.org/10.1083/jcb.102.4.1447.

Borges, Lúcia S., and Michael Ferns. 2001. "Agrin-Induced Phosphorylation of the Acetylcholine Receptor Regulates Cytoskeletal Anchoring and Clustering." *Journal of Cell Biology* 153 (1): 1–11. https://doi.org/10.1083/jcb.153.1.1.

Borges, Lucia S., Sergey Yechikhov, Young I. Lee, John B. Rudell, Matthew B. Friese, Steven J. Burden, and Michael J. Ferns. 2008. "Identification of a Motif in the

Acetylcholine Receptor β Subunit Whose Phosphorylation Regulates Rapsyn Association and Postsynaptic Receptor Localization." *Journal of Neuroscience*. https://doi.org/10.1523/JNEUROSCI.2508-08.2008.

Bostick, B., A. Ghosh, Y. Yue, C. Long, and D. Duan. 2007. "Systemic AAV-9 Transduction in Mice Is Influenced by Animal Age but Not by the Route of Administration." *Gene Therapy*. https://doi.org/10.1038/sj.gt.3303029.

Brenner, H. R., and W. Rudin. 1989. "On the Effect of Muscle Activity on the End-plate Membrane in Denervated Mouse Muscle." *The Journal of Physiology*. https://doi.org/10.1113/jphysiol.1989.sp017546.

Bruneau, Emile, David Sutter, Richard I. Hume, and Mohammed Akaaboune. 2005. "Identification of Nicotinic Acetylcholine Receptor Recycling and Its Role in Maintaining Receptor Density at the Neuromuscular Junction in Vivo." *Journal of Neuroscience* 25 (43): 9949–59. https://doi.org/10.1523/JNEUROSCI.3169-05.2005.

Bulaklak, Karen, and Xiao Xiao. 2017. "Therapeutic Advances in Musculoskeletal AAV Targeting Approaches." *Current Opinion in Pharmacology*. Elsevier Ltd. https://doi.org/10.1016/j.coph.2017.07.001.

Burden, Steven J., Maartje G. Huijbers, and Leonor Remedio. 2018. "Fundamental Molecules and Mechanisms for Forming and Maintaining Neuromuscular Synapses." *International Journal of Molecular Sciences*. https://doi.org/10.3390/ijms19020490.

Burke, Georgina, Andrew Hiscock, Andrea Klein, Erik H Niks, Marion Main, Adnan Y Manzur, Joanne Ng, et al. 2013. "Salbutamol Benefits Children with Congenital Myasthenic Syndrome Due to DOK7 Mutations." https://doi.org/10.1016/j.nmd.2012.11.004.

Campanelll, James T., Steven L. Roberds, Kevin P. Campbell, and Richard H. Scheller. 1994. "A Role for Dystrophin-Associated Glycoproteins and Utrophin in Agrin-Induced AChR Clustering." *Cell*. https://doi.org/10.1016/0092-8674(94)90051-5.

Carr, Aisling S., Chris R. Cardwell, Peter O. McCarron, and John McConville. 2010. “A Systematic Review of Population Based Epidemiological Studies in Myasthenia Gravis.” *BMC Neurology* 10 (June): 46. https://doi.org/10.1186/1471-2377-10-46.

Carrel, Laura, and Huntington F. Willard. 2005. “X-Inactivation Profile Reveals Extensive Variability in X-Linked Gene Expression in Females.” *Nature* 434 (7031): 400–404. https://doi.org/10.1038/nature03479.

Cartaud, Annie, Sébastien Coutant, Tamara C. Petrucci, and Jean Cartaud. 1998. “Evidence for in Situ and in Vitro Association between β-Dystroglycan and the Subsynaptic 43k Rapsyn Protein: Consequence for Acetylcholine Receptor Clustering at the Synapse.” *Journal of Biological Chemistry*. https://doi.org/10.1074/jbc.273.18.11321.

Cartaud, Annie, Laure Strochlic, Manuel Guerra, Benoît Blanchard, Monique Lambergeon, Eric Krejci, Jean Cartaud, and Claire Legay. 2004. “MuSK Is Required for Anchoring Acetylcholinesterase at the Neuromuscular Junction.” *Journal of Cell Biology* 165 (4): 505–15. https://doi.org/10.1083/jcb.200307164.

Castillo, J. del, and B. Katz. 1954. “Quantal Components of the End-plate Potential.” *The Journal of Physiology*. https://doi.org/10.1113/jphysiol.1954.sp005129.

Chancellor, Daniel R., Kay E. Davies, Olivier De Moor, Colin R. Dorgan, Peter D. Johnson, Adam G. Lambert, Daniel Lawrence, et al. 2011. “Discovery of 2-Arylbenzoxazoles as Upregulators of Utrophin Production for the Treatment of Duchenne Muscular Dystrophy.” *Journal of Medicinal Chemistry* 54 (9): 3241–50. https://doi.org/10.1021/jm200135z.

Chaouch, Amina, Vito Porcelli, Daniel Cox, Shimon Edvardson, Pasquale Scarcia, Anna De Grassi, Ciro L. Pierri, et al. 2014. “Mutations in the Mitochondrial Citrate Carrier SLC25A1 Are Associated with Impaired Neuromuscular Transmission.” *Journal of Neuromuscular Diseases*. https://doi.org/10.3233/JND-140021.

Chatzopoulou, Maria, Tim D.W. Claridge, Kay E. Davies, Stephen G. Davies, David J.

Elsey, Enrico Emer, Ai M. Fletcher, et al. 2020. “Isolation, Structural Identification, Synthesis, and Pharmacological Profiling of 1,2- Trans-Dihydro-1,2-Diol Metabolites of the Utrophin Modulator Ezutromid.” *Journal of Medicinal Chemistry* 63 (5): 2547–56. https://doi.org/10.1021/acs.jmedchem.9b01547.

Chen, Fei, Lei Qian, Zhi Hua Yang, Ying Huang, Shyuan T. Ngo, Nan Jie Ruan, Jia Wang, et al. 2007. “Rapsyn Interaction with Calpain Stabilizes AChR Clusters at the Neuromuscular Junction.” *Neuron* 55 (2): 247–60. https://doi.org/10.1016/j.neuron.2007.06.031.

Chen, Jie, Takafumi Mizushige, and Hiroshi Nishimune. 2012. “Active Zone Density Is Conserved during Synaptic Growth but Impaired in Aged Mice.” *Journal of Comparative Neurology* 520 (2): 434–52. https://doi.org/10.1002/cne.22764.

Cheung, A K, M D Hoggan, W W Hauswirth, and K I Berns. 1980. “Integration of the Adeno-Associated Virus Genome into Cellular DNA in Latently Infected Human Detroit 6 Cells.” *Journal of Virology*. https://doi.org/10.1128/jvi.33.2.739-748.1980.

Chevessier, F., B. Faraut, A. Ravel-Chapuis, P. Richard, K. Gaudon, S. Bauché, C. Prioleau, et al. 2005. “Towards the Molecular Elucidation of Congenital Myasthenic Syndromes: Identification of Mutations in MuSK.” In *Acta Myologica*.

Chipman, Peter H., Melitta Schachner, and Victor F. Rafuse. 2014. “Presynaptic NCAM Is Required for Motor Neurons to Functionally Expand Their Peripheral Field of Innervation in Partially Denervated Muscles.” *Journal of Neuroscience* 34 (32): 10497–510. https://doi.org/10.1523/JNEUROSCI.0697-14.2014.

Christensen, B. N., and A. R. Martin. 1970. “Estimates of Probability of Transmitter Release at the Mammalian Neuromuscular Junction.” *The Journal of Physiology*. https://doi.org/10.1113/jphysiol.1970.sp009250.

Colella, Pasqualina, Giuseppe Ronzitti, and Federico Mingozzi. 2018a. “Emerging Issues in AAV-Mediated In Vivo Gene Therapy” 8 (March): 87–104.

Molecular Therapy - Methods and Clinical Development. Cell Press. https://doi.org/10.1016/j.omtm.2017.11.007.

"Compilation of CDER New Molecular Entity (NME) Drug and New Biologic Approvals | FDA." n.d. Accessed January 5, 2021. https://www.fda.gov/drugs/drug-approvals-and-databases/compilation-cder-new-molecular-entity-nme-drug-and-new-biologic-approvals.

Cooper, Sara J., Nathan D. Trinklein, Elizabeth D. Anton, Loan Nguyen, and Richard M. Myers. 2006. "Comprehensive Analysis of Transcriptional Promoter Structure and Function in 1% of the Human Genome." *Genome Research* 16 (1): 1–10. https://doi.org/10.1101/gr.4222606.

Cossins, Judith, Katsiaryna Belaya, Debbie Hicks, Mustafa A. Salih, Sarah Finlayson, Nicola Carboni, Wei Wei Liu, et al. 2013. "Congenital Myasthenic Syndromes Due to Mutations in ALG2 and ALG14." *Brain*. https://doi.org/10.1093/brain/awt010.

Cossins, Judith, Wei Wei Liu, Katsiaryna Belaya, Susan Maxwell, Michael Oldridge, Tracy Lester, Stephanie Robb, and David Beeson. 2012. "The Spectrum of Mutations That Underlie the Neuromuscular Junction Synaptopathy in DOK7 Congenital Myasthenic Syndrome" 21 (17): 3765–75. https://doi.org/10.1093/hmg/dds198.

Cossins, Judith, Richard Webster, Susan Maxwell, Pedro M Rodríguez Cruz, Ravi Knight, John Gareth Llewelyn, Ji-Yeon Shin, Jacqueline Palace, and David Beeson. 2020. "Congenital Myasthenic Syndrome Due to a TOR1AIP1 Mutation: A New Disease Pathway for Impaired Synaptic Transmission." *Brain Communications*. https://doi.org/10.1093/braincomms/fcaa174.

Cossins, Judy, Richard Webster, Susan Maxwell, Georgina Burke, Angela Vincent, and David Beeson. 2004. "A Mouse Model of AChR Deficiency Syndrome with a Phenotype Reflecting the Human Condition." *Human Molecular Genetics* 13 (23): 2947–57. https://doi.org/10.1093/hmg/ddh320.

Croxen, R. 2001a. “End-Plate Gamma- and Varepsilon-Subunit MRNA Levels in AChR Deficiency Syndrome Due to Varepsilon-Subunit Null Mutations.” *Brain*. https://doi.org/10.1093/brain/124.7.1362.

Cruz, Pedro M.Rodríguez, Jacqueline Palace, and David Beeson. 2014. “Congenital Myasthenic Syndromes and the Neuromuscular Junction.” *Current Opinion in Neurology* 27 (5): 566–75. https://doi.org/10.1097/WCO.0000000000000134.

Dai, Zhengshan, Xiaoyan Luo, Hongbo Xie, and H. Benjamin Peng. 2000. “The Actin-Driven Movement and Formation of Acetylcholine Receptor Clusters.” *Journal of Cell Biology* 150 (6): 1321–34. https://doi.org/10.1083/jcb.150.6.1321.

Dawkins, Hugh J.S., Ruxandra Draghia-Akli, Paul Lasko, Lilian P.L. Lau, Anneliene H. Jonker, Christine M. Cutillo, Ana Rath, et al. 2018. “Progress in Rare Diseases Research 2010–2016: An IRDiRC Perspective.” *Clinical and Translational Science*. Blackwell Publishing Ltd. https://doi.org/10.1111/cts.12501.

Daya, Shyam, and Kenneth I. Berns. 2008. “Gene Therapy Using Adeno-Associated Virus Vectors.” *Clinical Microbiology Reviews*. https://doi.org/10.1128/CMR.00008-08.

Denzer, A. J., D. M. Hauser, M. Gesemann, and M. A. Ruegg. 1997. “Synaptic Differentiation: The Role of Agrin in the Formation and Maintenance of the Neuromuscular Junction.” *Cell and Tissue Research* 290 (2): 357–65. https://doi.org/10.1007/s004410050941.

Denzer, Alain J., Ralph Brandenberger, Matthias Gesemann, Matthias Chiquet, and Markus A. Ruegg. 1997. “Agrin Binds to the Nerve-Muscle Basal Lamina via Laminin.” *Journal of Cell Biology*. https://doi.org/10.1083/jcb.137.3.671.

Deshaies, Raymond J., and Claudio A.P. Joazeiro. 2009. “RING Domain E3 Ubiquitin Ligases.” *Annual Review of Biochemistry*. https://doi.org/10.1146/annurev.biochem.78.101807.093809.

DN Herrmann, R Horvath, JE Sowden, M Gonzalez, A Sanchez-Mejias, Z Guan, RG

Whittaker, JL Almodovar, M Lane, B Bansagi, A Pyle, V Boczonadi, H Lochmüller, H Griffin, PF Chinnery, TE Lloyd, JT Littleton, S Zuchner. 2014. “Synaptotagmin 2 Mutations Cause an Autosomal-Dominant Form of Lambert-Eaton Myasthenic Syndrome and Nonprogressive Motor Neuropathy.” *Am J Hum Genet* 95: 332–39.

Dobin, Alexander, Carrie A. Davis, Felix Schlesinger, Jorg Drenkow, Chris Zaleski, Sonali Jha, Philippe Batut, Mark Chaisson, and Thomas R. Gingeras. 2013. “STAR: Ultrafast Universal RNA-Seq Aligner.” *Bioinformatics*. https://doi.org/10.1093/bioinformatics/bts635.

Domenger, Claire, and Dirk Grimm. 2019. “Next-Generation AAV Vectors-Do Not Judge a Virus (Only) by Its Cover.” *Human Molecular Genetics* 28 (R1): R3–14. https://doi.org/10.1093/hmg/ddz148.

Dreyer, F., K. Peper, K. Akert, C. Sandri, and H. Moor. 1973. “Ultrastructure of the ‘active Zone’ in the Frog Neuromuscular Junction.” *Brain Research* 62 (2): 373–80. https://doi.org/10.1016/0006-8993(73)90699-9.

Drouin, Lauren M., and Mavis Agbandje-Mckenna. 2013. “Adeno-Associated Virus Structural Biology as a Tool in Vector Development.” *Future Virology*. Future Medicine Ltd London, UK . https://doi.org/10.2217/fvl.13.112.

Earley, Lauriel F., Laura M. Conatser, Victoria M. Lue, Amanda L. Dobbins, Chengwen Li, Matthew L. Hirsch, and R. Jude Samulski. 2020. “Adeno-Associated Virus Serotype-Specific Inverted Terminal Repeat Sequence Role in Vector Transgene Expression.” *Human Gene Therapy* 31 (3–4): 151–62. https://doi.org/10.1089/hum.2019.274.

Eder, Jörg, and Paul L. Herrling. 2016. “Trends in Modern Drug Discovery.” In *Handbook of Experimental Pharmacology*, 232:3–22. Springer New York LLC. https://doi.org/10.1007/164_2015_20.

Eguchi, Takahiro, Tohru Tezuka, Takayasu Fukudome, Yuji Watanabe, Hiroshi Sagara, and Yuji Yamanashi. 2020. “Overexpression of Dok-7 in Skeletal Muscle Enhances

Neuromuscular Transmission with Structural Alterations of Neuromuscular Junctions: Implications in Robustness of Neuromuscular Transmission." *Biochemical and Biophysical Research Communications* 523 (1): 214–19. https://doi.org/10.1016/j.bbrc.2019.12.011.

Eisenberg, Brenda. 1983. "Muscles and Their Neural Control. Edited by Graham Hoyle, 689 Pp, John Wiley & Sons, Inc., New York, NY, 1983. $59.95." *Muscle & Nerve* 6 (8): 611–611. https://doi.org/10.1002/mus.880060814.

Engel, A G, X-M Shen, Andrew G Engel, Xin-Ming Shen, Duygu Selcen, and Steven M Sine. 2015. "Congenital Myasthenic Syndromes: Pathogenesis, Diagnosis, and Treatment." *Lancet Neurol*. Vol. 14. www.thelancet.com/neurology.

Engel, Andrew G. 2007. "The Therapy of Congenital Myasthenic Syndromes." *Neurotherapeutics*. https://doi.org/10.1016/j.nurt.2007.01.001.

Engel, Andrew G., Edward H. Lambert, and Tetsuji Santa. 1973. "Study of Long-Term Anticholinesterase Therapy: Effects on Neuromuscular Transmission and on Motor End-Plate Fine Structure." *Neurology*. https://doi.org/10.1212/wnl.23.12.1273.

Engel, Andrew G., Duygu Selcen, Xin Ming Shen, Margherita Milone, and C. Michel Harper. 2016. "Loss of MUNC13-1 Function Causes Microcephaly, Cortical Hyperexcitability, and Fatal Myasthenia." *Neurology: Genetics* 2 (5). https://doi.org/10.1212/NXG.0000000000000105.

Engel, Andrew G., Xin Ming Shen, and Duygu Selcen. 2018. "The Unfolding Landscape of the Congenital Myasthenic Syndromes." *Annals of the New York Academy of Sciences*. Blackwell Publishing Inc. https://doi.org/10.1111/nyas.13539.

Engel, Andrew G., Xin Ming Shen, Duygu Selcen, and Steven M. Sine. 2008. "Further Observations in Congenital Myasthenic Syndromes." In *Annals of the New York Academy of Sciences*, 1132:104–13. Blackwell Publishing Inc. https://doi.org/10.1196/annals.1405.039.

Ferns, Michael J., James T. Campanelli, Werner Hoch, Richard H. Scheller, and Zach Hall. 1993. “The Ability of Agrin to Cluster AChRs Depends on Alternative Splicing and on Cell Surface Proteoglycans.” *Neuron* 11 (3): 491–502. https://doi.org/10.1016/0896-6273(93)90153-I.

Finn, Alexander J., Guoping Feng, and Ann Marie Pendergast. 2003. “Postsynaptic Requirement for Abl Kinases in Assembly of the Neuromuscular Junction.” *Nature Neuroscience* 6 (7): 717–23. https://doi.org/10.1038/nn1071.

Finsterer, Josef. 2019a. “Congenital Myasthenic Syndromes.” *Orphanet Journal of Rare Diseases*. BioMed Central Ltd. https://doi.org/10.1186/s13023-019-1025-5.

Fischer, Lindsey R., Deborah G. Culver, Philip Tennant, Albert A. Davis, Minsheng Wang, Amilcar Castellano-Sanchez, Jaffar Khan, Meraida A. Polak, and Jonathan D. Glass. 2004. “Amyotrophic Lateral Sclerosis Is a Distal Axonopathy: Evidence in Mice and Man.” *Experimental Neurology* 185 (2): 232–40. https://doi.org/10.1016/j.expneurol.2003.10.004.

Fishman, Robert A. 1994. “Myology: Basic and Clinical, Second Edition, Vols 1 and 2.Edited by Andrew G. Engel and Clara Franzini-Armstrong, New York, McGraw-Hill, 1994, 1937 Pp. Illustrated. $350.00.” *Annals of Neurology* 36 (5): 808–808. https://doi.org/10.1002/ana.410360536.

Flucher, B. E., and M. P. Daniels. 1989. “Distribution of Na+ Channels and Ankyrin in Neuromuscular Junctions Is Complementary to That of Acetylcholine Receptors and the 43 Kd Protein.” *Neuron* 3 (2): 163–75. https://doi.org/10.1016/0896-6273(89)90029-9.

Forrest, Katharine, Jemima E. Mellerio, Stephanie Robb, Patricia J.C. Dopping-Hepenstal, John A. Mcgrath, Lu Liu, Stefan J.A. Buk, Safa Al-Sarraj, Elizabeth Wraige, and Heinz Jungbluth. 2010. “Congenital Muscular Dystrophy, Myasthenic Symptoms and Epidermolysis Bullosa Simplex (EBS) Associated with Mutations in the PLEC1 Gene Encoding Plectin.” *Neuromuscular Disorders*.

https://doi.org/10.1016/j.nmd.2010.06.003.

Frail, D. E., L. L. McLaughlin, J. Mudd, and J. P. Merlie. 1988. "Identification of the Mouse Muscle 43,000-Dalton Acetylcholine Receptor-Associated Protein (RAPsyn) by CDNA Cloning." *Journal of Biological Chemistry*. https://doi.org/10.1016/S0021-9258(19)37631-8.

Garcia-Osta, Ana, Panayiotis Tsokas, Gabriella Pollonini, Emmanuel M. Landau, Robert Blitzer, and Cristina M. Alberini. 2006. "MuSK Expressed in the Brain Mediates Cholinergic Responses, Synaptic Plasticity, and Memory Formation." *Journal of Neuroscience*. https://doi.org/10.1523/JNEUROSCI.1674-06.2006.

Gaudet, Pascale, Michael S. Livstone, Suzanna E. Lewis, and Paul D. Thomas. 2011. "Phylogenetic-Based Propagation of Functional Annotations within the Gene Ontology Consortium." *Briefings in Bioinformatics* 12 (5): 449–62. https://doi.org/10.1093/bib/bbr042.

Gautam, Medha, Peter G. Noakes, Jacqueline Mudd, Mia Nichol, Gerald C. Chu, Joshua R. Sanes, and John P. Merlie. 1995. "Failure of Postsynaptic Specialization to Develop at Neuromuscular Junctions of Rapsyn-Deficient Mice." *Nature* 377 (6546): 232–36. https://doi.org/10.1038/377232a0.

Gesemann, Matthias, Alain J. Denzer, and Markus A. Ruegg. 1995. "Acetylcholine Receptor-Aggregating Activity of Agrin Isoforms and Mapping of the Active Site." *Journal of Cell Biology* 128 (4): 625–36. https://doi.org/10.1083/jcb.128.4.625.

Ghedini, Paulo C., Tânia A. Viel, Luciana Honda, Maria Christina W. Avellar, Rosely O. Godinho, Maria Teresa R. Lima-Landman, Antônio J. Lapa, and Caden Souccar. 2008. "Increased Expression of Acetylcholine Receptors in the Diaphragm Muscle of *Mdx* Mice." *Muscle & Nerve* 38 (6): 1585–94. https://doi.org/10.1002/mus.21183.

Gilhus, Nils E. 2012. "Myasthenia and the Neuromuscular Junction." *Current Opinion in Neurology*. https://doi.org/10.1097/WCO.0b013e3283572588.

Gilhus, Nils Erik, Geir Olve Skeie, Fredrik Romi, Konstantinos Lazaridis, Paraskevi Zisimopoulou, and Socrates Tzartos. 2016. “Myasthenia Gravis - Autoantibody Characteristics and Their Implications for Therapy.” *Nature Reviews Neurology*. Nature Publishing Group. https://doi.org/10.1038/nrneurol.2016.44.

GL O’Grady, C Verschuuren, M Yuen, R Webster, M Menezes, JM Fock, N Pride, HA Best, T Benavides Damm, C Turner, M Lek, AG Engel, KN North, NF Clarke, DG MacArthur, EJ Kamsteeg, ST Cooper. 2016. “Variants in SLC18A3, Vesicular Acetylcholine Transporter, Cause Congenital Myasthenic Syndrome.” *Neurology* 87: 1442–48.

Glass, David J., David C. Bowen, Trevor N. Stitt, Czeslaw Radziejewski, Jo Anne Bruno, Terence E. Ryan, David R. Gies, et al. 1996. “Agrin Acts via a MuSK Receptor Complex.” *Cell* 85 (4): 513–23. https://doi.org/10.1016/S0092-8674(00)81252-0.

Green, William N. 1999. “Perspective: Ion Channel Assembly: Creating Structures That Function.” *Journal of General Physiology*. The Rockefeller University Press. https://doi.org/10.1085/jgp.113.2.163.

H Wang, CG Salter, O Refai, H Hardy, KES Barwick, U Akpulat, M Kvarnung, BA Chioza, G Harlalka, F Taylan, T Sejersen, J Wright, HH Zimmerman, M Karakaya, B Stüve, J Weis, U Schara, MA Russell, OA Abdul-Rahman, J Chilton, RD Blakely, EL Baple, S Cirak, AH Crosby. 2017. “Choline Transporter Mutations in Severe Congenital Myasthenic Syndrome Disrupt Transporter Localization.” *Brain* 140: 2838–50.

Ha, James C., and David P. Richman. 2015. “Myasthenia Gravis and Related Disorders: Pathology and Molecular Pathogenesis.” *Biochimica et Biophysica Acta - Molecular Basis of Disease*. https://doi.org/10.1016/j.bbadis.2014.11.022.

Haggerty, David L., Gregory G. Grecco, Kaitlin C. Reeves, and Brady Atwood. 2020. “Adeno-Associated Viral Vectors in Neuroscience Research.” *Molecular Therapy - Methods and Clinical Development*. Cell Press.

https://doi.org/10.1016/j.omtm.2019.11.012.

Hallock, Peter T., Chong Feng Xu, Tae Ju Park, Thomas A. Neubert, and Tom Curran Steven J. Burden. 2010. “Dok-7 Regulates Neuromuscular Synapse Formation by Recruiting Crk and Crk-L.” *Genes and Development* 24 (21): 2451–61. https://doi.org/10.1101/gad.1977710.

Hallock, Peter T, Chong-feng Xu, Tae-ju Park, Thomas A Neubert, Tom Curran, and Steven J Burden. 2010. “Dok-7 Regulates Neuromuscular Synapse Formation by Recruiting Crk and Crk-L,” 2451–61. https://doi.org/10.1101/gad.1977710.2006.

Hamuro, Johko, Osamu Higuchi, Kumiko Okada, Makiko Ueno, Shun-ichiro Iemura, and Tohru Natsume. 2008. “Mutations Causing DOK7 Congenital Myasthenia Ablate Functional Motifs in Dok-7 * □” 283 (9): 5518–24. https://doi.org/10.1074/jbc.M708607200.

Hamuro, Johko, Osamu Higuchi, Kumiko Okada, Makiko Ueno, Shun Ichiro Iemura, Tohru Natsume, Hayley Spearman, David Beeson, and Yuji Yamanashi. 2008. “Mutations Causing DOK7 Congenital Myasthenia Ablate Functional Motifs in Dok-7.” *Journal of Biological Chemistry* 283 (9): 5518–24. https://doi.org/10.1074/jbc.M708607200.

Hamuro, Johko, Yukihiro Hishida, Osamu Higuchi, and Yuji Yamanashi. 2011. “Biochemical and Biophysical Research Communications The Transcription Factor Sp1 Plays a Crucial Role in Dok-7 Gene Expression.” *Biochemical and Biophysical Research Communications* 408 (2): 293–99. https://doi.org/10.1016/j.bbrc.2011.04.020.

Hann, Michael M, Andrew R Leach, and Gavin Harper. 2001. “Molecular Complexity and Its Impact on the Probability of Finding Leads for Drug Discovery.” https://doi.org/10.1021/ci000403i.

Harper, C. Michel, Takayasu Fukodome, and Andrew G. Engel. 2003. “Treatment of Slow-Channel Congenital Myasthenic Syndrome with Fluoxetine.” *Neurology* 60 (10): 1710–13. https://doi.org/10.1212/01.WNL.0000061483.11417.1B.

Herlitze, S., A. Villarroel, V. Witzemann, M. Koenen, and B. Sakmann. 1996. “Structural Determinants of Channel Conductance in Fetal and Adult Rat Muscle Acetylcholine Receptors.” *Journal of Physiology*. https://doi.org/10.1113/jphysiol.1996.sp021345.

Hermonat, P. L., and N. Muzyczka. 1984. “Use of Adeno-Associated Virus as a Mammalian DNA Cloning Vector: Transduction of Neomycin Resistance into Mammalian Tissue Culture Cells.” *Proceedings of the National Academy of Sciences of the United States of America*. https://doi.org/10.1073/pnas.81.20.6466.

Hesselmans, L. F.G.M., F. G.I. Jennekens, C. J.M. Van Den Oord, H. Veldman, and A. Vincent. 1993. “Development of Innervation of Skeletal Muscle Fibers in Man: Relation to Acetylcholine Receptors.” *The Anatomical Record*. https://doi.org/10.1002/ar.1092360315.

Hettwer, Stefan, Shuo Lin, Stefan Kucsera, Monika Haubitz, Filippo Oliveri, Ruggero G. Fariello, Markus A. Ruegg, and Jan W. Vrijbloed. 2014. “Injection of a Soluble Fragment of Neural Agrin (NT-1654) Considerably Improves the Muscle Pathology Caused by the Disassembly of the Neuromuscular Junction.” Edited by Lin Mei. *PLoS ONE* 9 (2): e88739. https://doi.org/10.1371/journal.pone.0088739.

Hinderer, Christian, Nathan Katz, Elizabeth L. Buza, Cecilia Dyer, Tamara Goode, Peter Bell, Laura K. Richman, and James M. Wilson. 2018. “Severe Toxicity in Nonhuman Primates and Piglets Following High-Dose Intravenous Administration of an Adeno-Associated Virus Vector Expressing Human SMN.” *Human Gene Therapy* 29 (3): 285–98. https://doi.org/10.1089/hum.2018.015.

Ho, Pei I., Kimberley Yue, Pramod Pandey, Lyne Breault, Fred Harbinski, Aaron J. McBride, Brian Webb, et al. 2013. “Reporter Enzyme Inhibitor Study to Aid Assembly of Orthogonal Reporter Gene Assays.” *ACS Chemical Biology* 8 (5): 1009–17. https://doi.org/10.1021/cb3007264.

Hopf, Carsten, and Werner Hoch. 1998. “Dimerization of the Muscle-Specific Kinase

Induces Tyrosine Phosphorylation of Acetylcholine Receptors and Their Aggregation on the Surface of Myotubes." *Journal of Biological Chemistry* 273 (11): 6467–73. https://doi.org/10.1074/jbc.273.11.6467.

Hughes, Benjamin W., Linda L. Kusner, and Henry J. Kaminski. 2006. "Molecular Architecture of the Neuromuscular Junction." *Muscle and Nerve* 33 (4): 445–61. https://doi.org/10.1002/mus.20440.

Hughes, J. P., S. S. Rees, S. B. Kalindjian, and K. L. Philpott. 2011. "Principles of Early Drug Discovery." *British Journal of Pharmacology* 162 (6): 1239–49. https://doi.org/10.1111/j.1476-5381.2010.01127.x.

Huzé, Caroline, Stéphanie Bauché, Pascale Richard, Frédéric Chevessier, Evelyne Goillot, Karen Gaudon, Asma Ben Ammar, et al. 2009. "Identification of an Agrin Mutation That Causes Congenital Myasthenia and Affects Synapse Function." *American Journal of Human Genetics*. https://doi.org/10.1016/j.ajhg.2009.06.015.

Inagaki, Katsuya, Sally Fuess, Theresa A. Storm, Gregory A. Gibson, Charles F. Mctiernan, Mark A. Kay, and Hiroyuki Nakai. 2006. "Robust Systemic Transduction with AAV9 Vectors in Mice: Efficient Global Cardiac Gene Transfer Superior to That of AAV8." *Molecular Therapy* 14 (1): 45–53. https://doi.org/10.1016/j.ymthe.2006.03.014.

Inglese, James, Ronald L. Johnson, Anton Simeonov, Menghang Xia, Wei Zheng, Christopher P. Austin, and Douglas S. Auld. 2007. "High-Throughput Screening Assays for the Identification of Chemical Probes." *Nature Chemical Biology*. Nature Publishing Group. https://doi.org/10.1038/nchembio.2007.17.

Inoue, Akane, Kiyoko Setoguchi, Yosuke Matsubara, Kumiko Okada, Nozomi Sato, Yoichiro Iwakura, Osamu Higuchi, and Yuji Yamanashi. 2009a. "Dok-7 Activates the Muscle Receptor Kinase MuSK and Shapes Synapse Formation" 2 (59): 1–9.

Ito, Mikako, and Kinji Ohno. 2018. "Protein-Anchoring Therapy to Target Extracellular Matrix Proteins to Their Physiological Destinations." *Matrix Biology*. Elsevier B.V.

https://doi.org/10.1016/j.matbio.2018.02.014.

J Arredondo, M Lara, F Ng, DA Gochez, DC Lee, SP Logia, J Nguyen, RA Maselli. 2014. "COOH-Terminal Collagen Q (COLQ) Mutants Causing Human Deficiency of Endplate Acetylcholinesterase Impair the Interaction of ColQ with Proteins of the Basal Lamina." *Hum Genet* 133: 599–616.

Jacobson, Christian, Patrice D. Côté, Susana G. Rossi, Richard L. Rotundo, and Salvatore Carbonetto. 2001. "The Dystroglycan Complex Is Necessary for Stabilization of Acetylcholine Receptor Clusters at Neuromuscular Junctions and Formation of the Synaptic Basement Membrane." *Journal of Cell Biology*. https://doi.org/10.1083/jcb.152.3.435.

Jimsheleishvili, Sopiko, and Andrew l. Sherman. 2019. *Physiology, Neuromuscular Transmission*. *StatPearls*. StatPearls Publishing. http://www.ncbi.nlm.nih.gov/pubmed/31082177.

JR Parr, MJ Andrew, M Finnis, D Beeson, A Vincent, S Jayawant. 2014. "How Common Is Childhood Myasthenia? The UK Incidence and Prevalence of Autoimmune and Congenital Myasthenia." *Arch Dis Child* 99: 539–42.

JS Müller, SK Baumeister, U Schara, J Cossins, S Krause, M Hagen, A Huebner, R Webster, D Beeson, H Lochmüller, A Abicht. 2006. "CHRND Mutation Causes a Congenital Myasthenic Syndrome by Impairing Co-Clustering of the Acetylcholine Receptor with Rapsyn." *Brain* 129: 2784–93.

K Hoffmann, JS Muller, S Stricker, A Megarbane, A Rajab, TH Lindner, M Cohen, E Chouery, L Adaimy, I Ghanem, V Delague, E Boltshauser, B Talim, R Horvath, PN Robinson, H Lochmüller, C Hübner, S Mundlos. 2006. "Escobar Syndrome Is a Prenatal Myasthenia Caused by Disruption of the Acetylcholine Receptor Fetal Gamma Subunit." *Am J Hum Genet* 79: 303–12.

Kaifer, Kevin A., Eric Villalón, Caley E. Smith, Madeline E. Simon, Jose Marquez, Abigail

E. Hopkins, Toni I. Morcos, and Christian L. Lorson. 2020. “AAV9-DOK7 Gene Therapy Reduces Disease Severity in Smn2B/- SMA Model Mice.” *Biochemical and Biophysical Research Communications*. https://doi.org/10.1016/j.bbrc.2020.07.031.

Kaplan, Mehmet Mahsum, Nasreen Sultana, Ariane Benedetti, Gerald J. Obermair, Nina F. Linde, Symeon Papadopoulos, Anamika Dayal, Manfred Grabner, and Bernhard E. Flucher. 2018. “Calcium Influx and Release Cooperatively Regulate AChR Patterning and Motor Axon Outgrowth during Neuromuscular Junction Formation.” *Cell Reports*. https://doi.org/10.1016/j.celrep.2018.05.085.

Kariya, Shingo, Gyu Hwan Park, Yuka Maeno-Hikichi, Olga Leykekhman, Cathleen Lutz, Marc S. Arkovitz, Lynn T. Landmesser, and Umrao R. Monani. 2008. “Reduced SMN Protein Impairs Maturation of the Neuromuscular Junctions in Mouse Models of Spinal Muscular Atrophy.” *Human Molecular Genetics* 17 (16): 2552–69. https://doi.org/10.1093/hmg/ddn156.

Kim, Natalie, and Steven J. Burden. 2008. “MuSK Controls Where Motor Axons Grow and Form Synapses.” *Nature Neuroscience* 11 (1): 19–27. https://doi.org/10.1038/nn2026.

Kim, Natalie, Amy L. Stiegler, Thomas O. Cameron, Peter T. Hallock, Andrea M. Gomez, Julie H. Huang, Stevan R. Hubbard, Michael L. Dustin, and Steven J. Burden. 2008. “Lrp4 Is a Receptor for Agrin and Forms a Complex with MuSK.” *Cell* 135 (2): 334–42. https://doi.org/10.1016/j.cell.2008.10.002.

Kinch, Michael S., Austin Haynesworth, Sarah L. Kinch, and Denton Hoyer. 2014. “An Overview of FDA-Approved New Molecular Entities: 1827-2013.” *Drug Discovery Today*. Elsevier Ltd. https://doi.org/10.1016/j.drudis.2014.03.018.

Korneliussen, H., and J. K.S. Jansen. 1976. “Morphological Aspects of the Elimination of Polyneuronal Innervation of Skeletal Muscle Fibres in Newborn Rats.” *Journal of Neurocytology*. https://doi.org/10.1007/BF01175572.

Kotterman, Melissa A., Thomas W. Chalberg, and David V. Schaffer. 2015. “Viral Vectors

for Gene Therapy: Translational and Clinical Outlook." *Annual Review of Biomedical Engineering*. https://doi.org/10.1146/annurev-bioeng-071813-104938.

Kozera, Bartłomiej, and Marcin Rapacz. 2013. "Reference Genes in Real-Time PCR." *Journal of Applied Genetics*. https://doi.org/10.1007/s13353-013-0173-x.

Kummer, Terrance T., Thomas Misgeld, Jeff W. Lichtman, and Joshua R. Sanes. 2004. "Nerve-Independent Formation of a Topologically Complex Postsynaptic Apparatus." *Journal of Cell Biology* 164 (7): 1077–87. https://doi.org/10.1083/jcb.200401115.

Kummer, Terrance T., Thomas Misgeld, and Joshua R. Sanes. 2006. "Assembly of the Postsynaptic Membrane at the Neuromuscular Junction: Paradigm Lost." *Current Opinion in Neurobiology*. https://doi.org/10.1016/j.conb.2005.12.003.

Lacazette, Eric, Sophie Le Calvez, Nadesan Gajendran, and Hans Rudolf Brenner. 2003. "A Novel Pathway for MuSK to Induce Key Genes in Neuromuscular Synapse Formation." *Journal of Cell Biology* 161 (4): 727–36. https://doi.org/10.1083/jcb.200210156.

Lampe, Sara E.Gombash, Brian K. Kaspar, and Kevin D. Foust. 2014. "Intravenous Injections in Neonatal Mice." *Journal of Visualized Experiments*, no. 93 (November): 52037. https://doi.org/10.3791/52037.

Lanuza, Maria A., Neus Garcia, Manel Santafé, Carmen M. González, Immaculada Alonso, Phillip G. Nelson, and Josep Tomàs. 2002. "Pre- and Postsynaptic Maturation of the Neuromuscular Junction during Neonatal Synapse Elimination Depends on Protein Kinase C." *Journal of Neuroscience Research*. https://doi.org/10.1002/jnr.10122.

Lashley, D. 2010. "Ephedrine Treatment in Congenital Myasthenic Syndrome Due to Mutations in DOK7," 1517–23.

Lech, P., and N. Somia. 2008. "Retrovirus Vectors." *Contributions to Nephrology*. Contrib Nephrol. https://doi.org/10.1159/000125574.

Lee, Y., J. Rudell, and M. Ferns. 2009. "Rapsyn Interacts with the Muscle Acetylcholine Receptor via α-Helical Domains in the α, β, and ε Subunit Intracellular Loops."

Neuroscience 163 (1): 222–32. https://doi.org/10.1016/j.neuroscience.2009.05.057.

Li, Chengwen, and R. Jude Samulski. 2020. "Engineering Adeno-Associated Virus Vectors for Gene Therapy." *Nature Reviews Genetics*. Nature Research. https://doi.org/10.1038/s41576-019-0205-4.

Li, Lei, Yu Cao, Haitao Wu, Xinchun Ye, Zhihui Zhu, Guanglin Xing, Chengyong Shen, et al. 2016. "Enzymatic Activity of the Scaffold Protein Rapsyn for Synapse Formation." *Neuron*. https://doi.org/10.1016/j.neuron.2016.10.023.

Li, Lei, Wen-cheng Xiong, and Lin Mei. 2018. "Neuromuscular Junction Formation , Aging , and Disorders."

Lin, Weichun, Bertha Dominguez, Jiefei Yang, Prafulla Aryal, Eugene P. Brandon, Fred H. Gage, and Kuo Fen Lee. 2005. "Neurotransmitter Acetylcholine Negatively Regulates Neuromuscular Synapse Formation by a Cdk5-Dependent Mechanism." *Neuron*. https://doi.org/10.1016/j.neuron.2005.04.002.

Linder, T. M., and D. M. Quastel. 1978. "A Voltage-clamp Study of the Permeability Change Induced by Quanta of Transmitter at the Mouse End-plate." *The Journal of Physiology*. https://doi.org/10.1113/jphysiol.1978.sp012438.

Lippincott-Schwartz, Jennifer, Erik Snapp, and Anne Kemvorthy. 2001. "Studying Protein Dynamics in Living Cells." *Nature Reviews Molecular Cell Biology*. Nat Rev Mol Cell Biol. https://doi.org/10.1038/35073068.

Lisowski, Leszek, Szun Szun Tay, and Ian Edward Alexander. 2015. "Adeno-Associated Virus Serotypes for Gene Therapeutics." *Current Opinion in Pharmacology*. Elsevier Ltd. https://doi.org/10.1016/j.coph.2015.07.006.

Logan, Clare V., Judith Cossins, Pedro M. Rodríguez Cruz, David A. Parry, Susan Maxwell, Pilar Martínez-Martínez, Joey Riepsaame, et al. 2015. "Congenital Myasthenic Syndrome Type 19 Is Caused by Mutations in COL13A1, Encoding the Atypical Non-Fibrillar Collagen Type XIII A1 Chain." *American Journal of Human Genetics*.

https://doi.org/10.1016/j.ajhg.2015.10.017.

Lorenzoni, Paulo J., Rosana H. Scola, Cláudia S.K. Kay, Luciane Filla, Anna P.P. Miranda, João M.R. Pinheiro, Amina Chaouch, Hanns Lochmüller, and Lineu C. Werneck. 2013. "Salbutamol Therapy in Congenital Myasthenic Syndrome Due to DOK7 Mutation." *Journal of the Neurological Sciences* 331 (1–2): 155–57. https://doi.org/10.1016/j.jns.2013.05.017.

Lotfinia, Majid, Meghdad Abdollahpour-Alitappeh, Behzad Hatami, Mohammad Reza Zali, and Morteza Karimipoor. 2019. "Adeno-Associated Virus as a Gene Therapy Vector: Strategies to Neutralize the Neutralizing Antibodies." *Clinical and Experimental Medicine* 19 (3): 289–98. https://doi.org/10.1007/s10238-019-00557-8.

Lyons, Gary E., Robert Moore, Osamu Yahara, Margaret E. Buckingham, and Frank S. Walsh. 1992. "Expression of NCAM Isoforms during Skeletal Myogenesis in the Mouse Embryo." *Developmental Dynamics* 194 (2): 94–104. https://doi.org/10.1002/aja.1001940203.

Maimone, Margaret M., and John P. Merlie. 1993. "Interaction of the 43 Kd Postsynaptic Protein with All Subunits of the Muscle Nicotinic Acetylcholine Receptor." *Neuron*. https://doi.org/10.1016/0896-6273(93)90270-2.

Mann, C. J. 2001. "Antisense-Induced Exon Skipping and Synthesis of Dystrophin in the Mdx Mouse." *Proceedings of the National Academy of Sciences*. https://doi.org/10.1073/pnas.011408598.

Marchand, Sophie, Anne Devillers-Thiéry, Stéphanie Pons, Jean Pierre Changeux, and Jean Cartaud. 2002. "Rapsyn Escorts the Nicotinic Acetylcholine Receptor along the Exocytic Pathway via Association with Lipid Rafts." *Journal of Neuroscience* 22 (20): 8891–8901. https://doi.org/10.1523/jneurosci.22-20-08891.2002.

Marques, Maria Julia, José Angel Conchello, and Jeff W. Lichtman. 2000. "From Plaque to Pretzel: Fold Formation and Acetylcholine Receptor Loss at the Developing

Neuromuscular Junction." *Journal of Neuroscience*. https://doi.org/10.1523/jneurosci.20-10-03663.2000.

Martinez-Pena y Valenzuela, Isabel, Marcelo Pires-Oliveira, and Mohammed Akaaboune. 2013. "PKC and PKA Regulate AChR Dynamics at the Neuromuscular Junction of Living Mice." Edited by Lin Mei. *PLoS ONE* 8 (11): e81311. https://doi.org/10.1371/journal.pone.0081311.

Massoulié, Jean, Leo Pezzementi, Suzanne Bon, Eric Krejci, and François Marie Vallette. 1993. "Molecular and Cellular Biology of Cholinesterases." *Progress in Neurobiology*. Pergamon. https://doi.org/10.1016/0301-0082(93)90040-Y.

Mazhar, Sania, and Ruth Herbst. 2012. "The Formation of Complex Acetylcholine Receptor Clusters Requires MuSK Kinase Activity and Structural Information from the MuSK Extracellular Domain." *Molecular and Cellular Neuroscience* 49 (4): 475–86. https://doi.org/10.1016/j.mcn.2011.12.007.

McDowell, David G., Nigel A. Burns, and Helen C. Parkes. 1998. "Localised Sequence Regions Possessing High Melting Temperatures Prevent the Amplification of a DNA Mimic in Competitive PCR." *Nucleic Acids Research* 26 (14): 3340–47. https://doi.org/10.1093/nar/26.14.3340.

McLachlan, E. M., and A. R. Martin. 1981. "Non-linear Summation of End-plate Potentials in the Frog and Mouse." *The Journal of Physiology*. https://doi.org/10.1113/jphysiol.1981.sp013586.

McMahan, U. J. 1990. "The Agrin Hypothesis." In *Cold Spring Harbor Symposia on Quantitative Biology*, 55:407–18. https://doi.org/10.1101/SQB.1990.055.01.041.

McMahan, U.J., and B.G. Wallace. 1989. "Molecules in Basal Lamina That Direct the Formation of Synaptic Specializations at Neuromuscular Junctions." *Developmental Neuroscience* 11 (4–5): 227–47. https://doi.org/10.1159/000111903.

McMahon, Harvey T., and David G. Nicholls. 1991. "The Bioenergetics of Neurotransmitter

Release." *BBA - Bioenergetics*. Elsevier. https://doi.org/10.1016/S0005-2728(05)80210-5.

Mendell, Jerry R., S. Al-Zaidy, R. Shell, W. D. Arnold, L. R. Rodino-Klapac, T. W. Prior, L. Lowes, et al. 2017. "Single-Dose Gene-Replacement Therapy for Spinal Muscular Atrophy." *New England Journal of Medicine*. https://doi.org/10.1056/NEJMoa1706198.

Mendell, Jerry R., Zarife Sahenk, Vinod Malik, Ana M. Gomez, Kevin M. Flanigan, Linda P. Lowes, Lindsay N. Alfano, et al. 2015. "A Phase 1/2a Follistatin Gene Therapy Trial for Becker Muscular Dystrophy." *Molecular Therapy*. https://doi.org/10.1038/mt.2014.200.

Mihaylova, V., R. H. Scola, B. Gervini, P. J. Lorenzoni, C. K. Kay, L. C. Werneck, R. Stucka, et al. 2010. "Molecular Characterisation of Congenital Myasthenic Syndromes in Southern Brazil." *Journal of Neurology, Neurosurgery and Psychiatry*. https://doi.org/10.1136/jnnp.2009.177816.

Milia, Lee Di, Michael H. Smolensky, Giovanni Costa, Heidi D. Howarth, Maurice M. Ohayon, and Pierre Philip. 2011. "Demographic Factors, Fatigue, and Driving Accidents: An Examination of the Published Literature." *Accident Analysis and Prevention*. https://doi.org/10.1016/j.aap.2009.12.018.

Misgeld, Thomas, Terrance T. Kummer, Jeff W. Lichtman, and Joshua R. Sanes. 2005. "Agrin Promotes Synaptic Differentiation by Counteracting an Inhibitory Effect of Neurotransmitter." *Proceedings of the National Academy of Sciences of the United States of America*. https://doi.org/10.1073/pnas.0504806102.

Mishina, Masayoshi, Toshiyuki Takai, Keiji Imoto, Masaharu Noda, Tomoyuki Takahashi, Shosaku Numa, Christoph Methfessel, and Bert Sakmann. 1986. "Molecular Distinction between Fetal and Adult Forms of Muscle Acetylcholine Receptor." *Nature*. https://doi.org/10.1038/321406a0.

Missias, Andrea C., Gerald C. Chu, Barbara J. Klocke, Joshua R. Sanes, and John P. Merlie. 1996. "Maturation of the Acetylcholine Receptor in Skeletal Muscle: Regulation of the

AChR γ-to-ε Switch." *Developmental Biology*. https://doi.org/10.1006/dbio.1996.0253.

Missias, Andrea C., Jacqueline Mudd, Jeanette M. Cunningham, Joseph H. Steinbach, John P. Merlie, and Joshua R. Sanes. 1997. "Deficient Development and Maintenance of Postsynaptic Specializations in Mutant Mice Lacking an 'adult' Acetylcholine Receptor Subunit." *Development*.

Miyoshi, Sadanori, Tohru Tezuka, Sumimasa Arimura, Taro Tomono, Takashi Okada, and Yuji Yamanashi. 2017. " DOK 7 Gene Therapy Enhances Motor Activity and Life Span in ALS Model Mice ." *EMBO Molecular Medicine* 9 (7): 880–89. https://doi.org/10.15252/emmm.201607298.

Miyoshi, Sadanori, Yuji Yamanashi, Tohru Tezuka, Sumimasa Arimura, Taro Tomono, and Takashi Okada. 2017. "DOK 7 Gene Therapy Enhances Motor Activity and Life Span in ALS Model Mice" 9 (7): 880–89.

Muntoni, Francesco, Bina Tejura, Stefan Spinty, Helen Roper, Imelda Hughes, Gary Layton, Kay E Davies, Shawn Harriman, and Jonathon Tinsley. 2019. "A Phase 1b Trial to Assess the Pharmacokinetics of Ezutromid in Pediatric Duchenne Muscular Dystrophy Patients on a Balanced Diet." *Clinical Pharmacology in Drug Development* 8 (7): 922–33. https://doi.org/10.1002/cpdd.642.

Muriel, Joaquin M., Andrea O'Neill, Jaclyn P. Kerr, Emily Kleinhans-Welte, Richard M. Lovering, and Robert J. Bloch. 2020. "Keratin 18 Is an Integral Part of the Intermediate Filament Network in Murine Skeletal Muscle." *American Journal of Physiology - Cell Physiology* 318 (1): C215–24. https://doi.org/10.1152/ajpcell.00279.2019.

Murray, Christopher W., and David C. Rees. 2009. "The Rise of Fragment-Based Drug Discovery." *Nature Chemistry* 1 (3): 187–92. https://doi.org/10.1038/nchem.217.

Musil, L. S., C. Carr, J. B. Cohen, and J. P. Merlie. 1988. "Acetylcholine Receptor-Associated 43K Protein Contains Covalently Bound Myristate." *The Journal of Cell Biology*. https://doi.org/10.1083/jcb.107.3.1113.

O'Connor, Emily, Ana Töpf, Juliane S. Müller, Daniel Cox, Teresinha Evangelista, Jaume Colomer, Angela Abicht, et al. 2016. "Identification of Mutations in the MYO9A Gene in Patients with Congenital Myasthenic Syndrome." *Brain*. https://doi.org/10.1093/brain/aww130.

Ohkawara, Bisei, Macarena Cabrera-Serrano, Tomohiko Nakata, Margherita Milone, Nobuyuki Asai, Kenyu Ito, Mikako Ito, et al. 2014. "LRP4 Third β-Propeller Domain Mutations Cause Novel Congenital Myasthenia by Compromising Agrin-Mediated MuSK Signaling in a Position-Specific Manner." *Human Molecular Genetics*. https://doi.org/10.1093/hmg/ddt578.

Ohno, Kinji, Joan Brengman, Akira Tsujino, and Andrew G. Engel. 1998. "Human Endplate Acetylcholinesterase Deficiency Caused by Mutations in the Collagen-like Tail Subunit (ColQ) of the Asymmetric Enzyme." *Proceedings of the National Academy of Sciences of the United States of America*. https://doi.org/10.1073/pnas.95.16.9654.

Ohno, Kinji, Polly A Quiram, Margherita Milone, Hai-Long Wang, Michel C Harper, J Ned Pruitt, Joan M Brengman, et al. 1997. "Congenital Myasthenic Syndromes Due to Heteroallelic Nonsense/Missense Mutations in the Acetylcholine Receptor ε Subunit Gene: Identification and Functional Characterization of Six New Mutations." *Human Molecular Genetics*. Vol. 6. Oxford University Press.

Ohno, Kinji, Menachem Sadeh, Ilan Blatt, Joan M. Brengman, and Andrew G. Engel. 2003. "E-Box Mutations in the RAPSN Promoter Regions in Eight Cases with Congenital Myasthenic Syndrome." *Human Molecular Genetics*. https://doi.org/10.1093/hmg/ddg089.

Ohno, Kinji, Akira Tsujino, Joan M. Brengman, C. Michel Harper, Zeljko Bajzer, Bjarne Udd, Roger Beyring, Stephanie Robb, Fenella J. Kirkham, and Andrew G. Engel. 2001. "Choline Acetyltransferase Mutations Cause Myasthenic Syndrome Associated with Episodic Apnea in Humans." *Proceedings of the National Academy of Sciences of the*

United States of America. https://doi.org/10.1073/pnas.98.4.2017.

Okada, Kumiko, Akane Inoue, Momoko Okada, Yoji Murata, Shigeru Kakuta, Takafumi Jigami, Sachiko Kubo, et al. 2006. "The Muscle Protein Dok-7 Is Essential for Neuromuscular Synaptogenesis." *Science* 312 (5781): 1802–5. https://doi.org/10.1126/science.1127142.

Oprea, Tudor I., and John P. Overington. 2015. "Computational and Practical Aspects of Drug Repositioning." *Assay and Drug Development Technologies* 13 (6): 299–306. https://doi.org/10.1089/adt.2015.29011.tiodrrr.

Palace, J., C. M. Wiles, and J. Newsom-Davis. 1991. "3,4-Diaminopyridine in the Treatment of Congenital (Hereditary) Myasthenia." *Journal of Neurology, Neurosurgery and Psychiatry* 54 (12): 1069–72. https://doi.org/10.1136/jnnp.54.12.1069.

Palace, Jacqueline, Daniel Lashley, John Newsom-Davis, Judy Cossins, Susan Maxwell, Robin Kennett, Sandeep Jayawant, Yuji Yamanashi, and David Beeson. 2007. "Clinical Features of the DOK7 Neuromuscular Junction Synaptopathy." *Brain*. https://doi.org/10.1093/brain/awm072.

Parr, Jeremy Ross, Morag Jane Andrew, Maria Finnis, David Beeson, Angela Vincent, and Sandeep Jayawant. 2014. "How Common Is Childhood Myasthenia? The UK Incidence and Prevalence of Autoimmune and Congenital Myasthenia." *Archives of Disease in Childhood*. https://doi.org/10.1136/archdischild-2013-304788.

Peeters, Samantha B., Allison M. Cotton, and Carolyn J. Brown. 2014. "Variable Escape from X-Chromosome Inactivation: Identifying Factors That Tip the Scales towards Expression." *BioEssays* 36 (8): 746–56. https://doi.org/10.1002/bies.201400032.

R Brugnoni, L Maggi, E Canioni, I Moroni, C Pantaleoni, S D'Arrigo, D Riva, F Cornelio, P Bernasconi, R Mantegazza. 2010. "Identification of Previously Unreported Mutations in CHRNA1, CHRNE and RAPSN Genes in Three Unrelated Italian Patients with Congenital Myasthenic Syndromes." *J Neurol* 257: 1119–23.

RA Maselli, J Arredondo, J Vázquez, JX Chong, MJ Bamshad, DA Nickerson, M Lara, F Ng, VL Lo, P Pytel, CM McDonald. 2017. “Presynaptic Congenital Myasthenic Syndrome with a Homozygous Sequence Variant in LAMA5 Combines Myopia, Facial Tics, and Failure of Neuromuscular Transmission.” *Am J Med Genet A* 173: 2240–45.

RA Maselli, JJ Ng, JA Anderson, O Cagney, J Arredondo, C Williams, HB Wessel, H Abdel-Hamid, RL Wollmann. 2009. “Mutations in LAMB2 Causing a Severe Form of Synaptic Congenital Myasthenic Syndrome.” *J Med Genet* 46: 203–8.

Rabinowitz, Joseph E., Fabienne Rolling, Chengwen Li, Hervè Conrath, Weidong Xiao, Xiao Xiao, and R. Jude Samulski. 2002. “Cross-Packaging of a Single Adeno-Associated Virus (AAV) Type 2 Vector Genome into Multiple AAV Serotypes Enables Transduction with Broad Specificity.” *Journal of Virology* 76 (2): 791–801. https://doi.org/10.1128/jvi.76.2.791-801.2002.

Ramarao, Manjunath K., Michael J. Bianchetta, Jonathan Lanken, and Jonathan B. Cohen. 2001. “Role of Rapsyn Tetratricopeptide Repeat and Coiled-Coil Domains in Self-Association and Nicotinic Acetylcholine Receptor Clustering.” *Journal of Biological Chemistry*. https://doi.org/10.1074/jbc.M009888200.

Ramarao, Manjunath K., and Jonathan B. Cohen. 1998. “Mechanism of Nicotinic Acetylcholine Receptor Cluster Formation by Rapsyn.” *Proceedings of the National Academy of Sciences of the United States of America*. https://doi.org/10.1073/pnas.95.7.4007.

Régal, Luc, Xin Ming Shen, Duygu Selcen, Chantal Verhille, Sandra Meulemans, John W.M. Creemers, and Andrew G. Engel. 2014. “PREPL Deficiency with or without Cystinuria Causes a Novel Myasthenic Syndrome.” *Neurology*. https://doi.org/10.1212/WNL.0000000000000295.

RIBCHESTER, R R. 1988. “Competitive Elimination of Neuromuscular Synapses.” *Nature* 331 (6151): 21. https://doi.org/10.1038/331021a0.

Richards, David A., Cristina Guatimosim, Silvio O. Rizzoli, and William J. Betz. 2003. "Synaptic Vesicle Pools at the Frog Neuromuscular Junction." *Neuron* 39 (3): 529–41. https://doi.org/10.1016/S0896-6273(03)00405-7.

Ricotti, Valeria, Stefan Spinty, Helen Roper, Imelda Hughes, Bina Tejura, Neil Robinson, Gary Layton, Kay Davies, Francesco Muntoni, and Jonathon Tinsley. 2016. "Safety, Tolerability, and Pharmacokinetics of SMT C1100, a 2-Arylbenzoxazole Utrophin Modulator, Following Single-and Multiple-Dose Administration to Pediatric Patients with Duchenne Muscular Dystrophy." *PLoS ONE* 11 (4). https://doi.org/10.1371/journal.pone.0152840.

Rodríguez Cruz, Pedro M., Judith Cossins, David Beeson, and Angela Vincent. 2020. "The Neuromuscular Junction in Health and Disease: Molecular Mechanisms Governing Synaptic Formation and Homeostasis." *Frontiers in Molecular Neuroscience*. https://doi.org/10.3389/fnmol.2020.610964.

Rodríguez Cruz, Pedro M., Jacqueline Palace, and David Beeson. 2018a. "The Neuromuscular Junction and Wide Heterogeneity of Congenital Myasthenic Syndromes." *International Journal of Molecular Sciences* 19 (6). https://doi.org/10.3390/ijms19061677.

Rodríguez Cruz, Pedro M., Jacqueline Palace, Hayley Ramjattan, Sandeep Jayawant, Stephanie A. Robb, and David Beeson. 2015. "Salbutamol and Ephedrine in the Treatment of Severe AChR Deficiency Syndromes." *Neurology*. https://doi.org/10.1212/WNL.0000000000001952.

Rose, J. A., K. I. Berns, M. D. Hoggan, and F. J. Koczot. 1969. "Evidence for a Single-Stranded Adenovirus-Associated Virus Genome: Formation of a DNA Density Hybrid on Release of Viral DNA." *Proceedings of the National Academy of Sciences of the United States of America*. https://doi.org/10.1073/pnas.64.3.863.

Rotundo, Richard L., Susana G. Rossi, Lewis M. Kimbell, Carlos Ruiz, and Emilio Marrero.

2005. “Targeting Acetylcholinesterase to the Neuromuscular Synapse.” In *Chemico-Biological Interactions*. https://doi.org/10.1016/j.cbi.2005.10.007.

Rudolf, Rüdigger, Julius Bogomolovas, Siegfried Strack, Kyeong Rok Choi, Muzamil Majid Khan, Anika Wagner, Kathrin Brohm, et al. 2013. “Regulation of Nicotinic Acetylcholine Receptor Turnover by MuRF1 Connects Muscle Activity to Endo/Lysosomal and Atrophy Pathways.” *Age* 35 (5): 1663–74. https://doi.org/10.1007/s11357-012-9468-9.

Ruegg, Markus A., and John L. Bixby. 1998. “Agrin Orchestrates Synaptic Differentiation at the Vertebrate Neuromuscular Junction.” *Trends in Neurosciences* 21 (1): 22–27. https://doi.org/10.1016/S0166-2236(97)01154-5.

Salpeter, M. M., and R. Harris. 1983. “Distribution and Turnover Rate of Acetylcholine Receptors throughout the Junction Folds at a Vertebrate Neuromuscular Junction.” *Journal of Cell Biology* 96 (6): 1781–85. https://doi.org/10.1083/jcb.96.6.1781.

Salpeter, Miriam M, and Mohyee E Eldefrawi. 1973. “SIZES OF END PLATE COMPARTMENTS, DENSITIES OF ACETYLCHOLINE RECEPTOR AND OTHER QUANTITATIVE ASPECTS OF NEUROMUSCULAR TRANSMISSION’.” Vol. 21.

Salpietro, W Lin, A Delle Vedove, M Storbeck, Y Liu, S Efthymiou, A Manole, S Wiethoff, Q Ye, A Saggar, K McElreavey, SS Krishnakumar, M Pitt, OD Bello, JE Rothman, L Basel-Vanagaite, MW Hubshman, S Aharoni, AY Manzur, B Wirth, H Houlden V. 2017. “Homozygous Mutations in VAMP1 Cause a Presynaptic Congenital Myasthenic Syndrome.” *Ann Neurol* 81: 597–603.

Sanes, Joshua R. 1995. “The Synaptic Cleft of the Neuromuscular Junction.” *Seminars in Developmental Biology* 6 (3): 163–73. https://doi.org/10.1016/S1044-5781(06)80026-5.

Schmittgen, Thomas D., and Kenneth J. Livak. 2008. “Analyzing Real-Time PCR Data by the Comparative CT Method.” *Nature Protocols* 3 (6): 1101–8. https://doi.org/10.1038/nprot.2008.73.

Schorling, David C., Astrid Pechmann, and Janbernd Kirschner. 2020. “Advances in Treatment of Spinal Muscular Atrophy - New Phenotypes, New Challenges, New Implications for Care.” *Journal of Neuromuscular Diseases*. IOS Press. https://doi.org/10.3233/JND-190424.

Schwab, Robert S., and William H. Timberlake. 1954. “Pyridostigmin (Mestinon) in the Treatment of Myasthenia Gravis.” *New England Journal of Medicine* 251 (7): 271–72. https://doi.org/10.1056/nejm195408122510706.

Schwarz, Holger, Günter Giese, Holger Müller, Michael Koenen, and Veit Witzemann. 2000. “Different Functions of Fetal and Adult AChR Subtypes for the Formation and Maintenance of Neuromuscular Synapses Revealed in ε-Subunit-Deficient Mice.” *European Journal of Neuroscience* 12 (9): 3107–16. https://doi.org/10.1046/j.1460-9568.2000.00195.x.

Selcen, Duygu, Margherita Milone, Xin Ming Shen, C. Michel Harper, Anthony A. Stans, Eric D. Wieben, and Andrew G. Engel. 2008. “Dok-7 Myasthenia: Phenotypic and Molecular Genetic Studies in 16 Patients.” *Annals of Neurology* 64 (1): 71–87. https://doi.org/10.1002/ana.21408.

Senderek, Jan, Juliane S. Müller, Marina Dusl, Tim M. Strom, Velina Guergueltcheva, Irmgard Diepolder, Steven H. Laval, et al. 2011. “Hexosamine Biosynthetic Pathway Mutations Cause Neuromuscular Transmission Defect.” *American Journal of Human Genetics*. https://doi.org/10.1016/j.ajhg.2011.01.008.

Shaberman, Ben. 2017. “A Retinal Research Nonprofit Paves the Way for Commercializing Gene Therapies.” In *Human Gene Therapy*, 28:1118–21. Mary Ann Liebert Inc. https://doi.org/10.1089/hum.2017.29058.bsh.

Shen, Xin Ming, Duygu Selcen, Joan Brengman, and Andrew G. Engel. 2014. “Mutant SNAP25B Causes Myasthenia, Cortical Hyperexcitability, Ataxia, and Intellectual Disability.” *Neurology*. https://doi.org/10.1212/WNL.0000000000001079.

Shoyaib, Abdullah Al, Sabrina Rahman Archie, and Vardan T. Karamyan. 2020. "Intraperitoneal Route of Drug Administration: Should It Be Used in Experimental Animal Studies?" *Pharmaceutical Research*. Springer. https://doi.org/10.1007/s11095-019-2745-x.

Sieb, Jörn P., Simone Kraner, Michael Rauch, and Ortrud K. Steinlein. 2000. "Immature End-Plates and Utrophin Deficiency in Congenital Myasthenic Syndrome Caused by ε-AChR Subunit Truncating Mutations." *Human Genetics*. https://doi.org/10.1007/s004390000359.

Sigoillot, Séverine M., Francine Bourgeois, Monique Lambergeon, Laure Strochlic, and Claire Legay. 2010. "ColQ Controls Postsynaptic Differentiation at the Neuromuscular Junction." *Journal of Neuroscience* 30 (1): 13–23. https://doi.org/10.1523/JNEUROSCI.4374-09.2010.

Silber, B. Michael. 2010. "Driving Drug Discovery: The Fundamental Role of Academic Labs." *Science Translational Medicine*. American Association for the Advancement of Science. https://doi.org/10.1126/scitranslmed.3000169.

Simon, A.M., P. Hoppe, and S.J. Burden. 1992. "Spatial Restriction of AChR Gene Expression to Subsynaptic Nuclei." *Development* 114 (3).

Singh, Pankaj Kumar, Arvind Negi, Pawan Kumar Gupta, Monika Chauhan, and Raj Kumar. 2016. "Toxicophore Exploration as a Screening Technology for Drug Design and Discovery: Techniques, Scope and Limitations." *Archives of Toxicology*. Springer Verlag. https://doi.org/10.1007/s00204-015-1587-5.

Slater, C. R., P. R.W. Fawcett, T. J. Walls, P. R. Lyons, S. J. Bailey, D. Beeson, C. Young, and D. Gardner-Medwin. 2006. "Pre- and Post-Synaptic Abnormalities Associated with Impaired Neuromuscular Transmission in a Group of Patients with 'Limb-Girdle Myasthenia.'" *Brain*. https://doi.org/10.1093/brain/awl200.

Slater, Clarke R. 2008. "Chapter 2 Reliability of Neuromuscular Transmission and How It Is

Maintained." *Handbook of Clinical Neurology*. Elsevier. https://doi.org/10.1016/S0072-9752(07)01502-3.

"Small Molecules Lead in Recent New Drug Approvals." n.d. Accessed January 5, 2021. https://www.dcatvci.org/6326-small-molecules-lead-in-recent-new-drug-approvals.

Smith, Cynthia L., Peggy Mittaud, Elizabeth D. Prescott, Christian Fuhrer, and Steven J. Burden. 2001. "Src, Fyn, and Yes Are Not Required for Neuromuscular Synapse Formation but Are Necessary for Stabilization of Agrin-Induced Clusters of Acetylcholine Receptors." *Journal of Neuroscience*. https://doi.org/10.1523/jneurosci.21-09-03151.2001.

Snapp, Erik. 2005. "Design and Use of Fluorescent Fusion Proteins in Cell Biology." *Current Protocols in Cell Biology* 27 (1): Unit. https://doi.org/10.1002/0471143030.cb2104s27.

Soitu, Cristian, Alexander Feuerborn, Cyril Deroy, Alfonso A. Castrejón-Pita, Peter R. Cook, and Edmond J. Walsh. 2019. "Raising Fluid Walls around Living Cells." *Science Advances* 5 (6): 8002–7. https://doi.org/10.1126/sciadv.aav8002.

Söllner, Thomas, and James E. Rothman. 1994. "Neurotransmission: Harnessing Fusion Machinery at the Synapse." *Trends in Neurosciences*. https://doi.org/10.1016/0166-2236(94)90178-3.

Souto, Eliana B., Bernardo Lima, Joana R. Campos, Carlos Martins-Gomes, Selma B. Souto, and Amélia M. Silva. 2019. "Myasthenia Gravis: State of the Art and New Therapeutic Strategies." *Journal of Neuroimmunology*. Elsevier B.V. https://doi.org/10.1016/j.jneuroim.2019.577080.

Spillane, Jennifer, David J. Beeson, and Dimitri M. Kullmann. 2010. "Myasthenia and Related Disorders of the Neuromuscular Junction." *Journal of Neurology, Neurosurgery and Psychiatry*. https://doi.org/10.1136/jnnp.2008.169367.

Strack, Siegfried, Yvonne Petersen, Anika Wagner, Ira V. Röder, Marina Albrizio, Markus Reischl, Irene U. Wacker, Christoph Wilhelm, and Rüdiger Rudolf. 2011. "A Novel

Labeling Approach Identifies Three Stability Levels of Acetylcholine Receptors in the Mouse Neuromuscular Junction in Vivo." *PLoS ONE* 6 (6). https://doi.org/10.1371/journal.pone.0020524.

Strochlic, Laure, Annie Cartaud, Alexandre Mejat, Régis Grailhe, Laurent Schaeffer, Jean Pierre Changeux, and Jean Cartaud. 2004. "14-3-3 γ Associates with Muscle Specific Kinase and Regulates Synaptic Gene Transcription at Vertebrate Neuromuscular Synapse." *Proceedings of the National Academy of Sciences of the United States of America* 101 (52): 18189–94. https://doi.org/10.1073/pnas.0406905102.

Sui, Yunxia, and Zhijin Wu. 2007. "Alternative Statistical Parameter for High-Throughput Screening Assay Quality Assessment." https://doi.org/10.1177/1087057106296498.

Sun, Yang, Zhen Qin, Jing Jing Wan, Peng Yuan Wang, Yi Li Yang, Jian Guang Yu, Bo Han Hu, Ding Feng Su, Zhu Min Luo, and Xia Liu. 2018. "Estrogen Weakens Muscle Endurance via Estrogen Receptor-P38 MAPK-Mediated Orosomucoid (ORM) Suppression." *Experimental and Molecular Medicine*. https://doi.org/10.1038/emm.2017.307.

Tang, Huibin, Matthew B. Veldman, and Daniel Goldman. 2006. "Characterization of a Muscle-Specific Enhancer in Human MuSK Promoter Reveals the Essential Role of Myogenin in Controlling Activity-Dependent Gene Regulation." *Journal of Biological Chemistry* 281 (7): 3943–53. https://doi.org/10.1074/jbc.M511317200.

Taylor, Palmer, and Joan Heller Brown. 1999. "Synthesis, Storage and Release of Acetylcholine." https://www.ncbi.nlm.nih.gov/books/NBK28051/.

Thien, Christine B.F., Francesca Walker, and Wallace Y. Langdon. 2001. "RING Finger Mutations That Abolish C-Cbl-Directed Polyubiquitination and Downregulation of the EGF Receptor Are Insufficient for Cell Transformation." *Molecular Cell*. https://doi.org/10.1016/S1097-2765(01)00183-6.

Thorne, Natasha, Min Shen, Wendy A. Lea, Anton Simeonov, Scott Lovell, Douglas S. Auld,

and James Inglese. 2012. “Firefly Luciferase in Chemical Biology: A Compendium of Inhibitors, Mechanistic Evaluation of Chemotypes, and Suggested Use as a Reporter.” *Chemistry and Biology* 19 (8): 1060–72. https://doi.org/10.1016/j.chembiol.2012.07.015.

Tsujino, Akira, Chantal Maertenst, Kinji Ohno, Xin Ming Shen, Taku Fukuda, C. Michael Harper, Stephen C. Cannon, and Andrew G. Engel. 2003. “Myasthenic Syndrome Caused by Mutation of the SCN4A Sodium Channel.” *Proceedings of the National Academy of Sciences of the United States of America*. https://doi.org/10.1073/pnas.1230273100.

Tuček, S. 1983. “Acetylcoenzyme A and the Synthesis of Acetylcholine in Neurones: Review of Recent Progress.” *Gen. Physiol. Biophys*. Vol. 2.

Ueta, Ryo, Satoshi Sugita, Yoshihiko Minegishi, Noboru Ogiso, Takahiro Eguchi, and Yuji Yamanashi. 2020. “DOK7 Gene Therapy Enhances Neuromuscular Junction Innervation and Motor Function in Aged Mice.” *ISCIENCE* 23: 101385. https://doi.org/10.1016/j.isci.2020.101385.

Ueta, Ryo, Tohru Tezuka, Yosuke Izawa, Sadanori Miyoshi, Satoru Nagatoishi, Kouhei Tsumoto, and Yuji Yamanashi. 2017. “The Carboxyl-Terminal Region of Dok-7 Plays a Key, but Not Essential, Role in Activation of Muscle-Specific Receptor Kinase MuSK and Neuromuscular Synapse Formation.” *Journal of Biochemistry*. https://doi.org/10.1093/jb/mvw073.

Valenzuela, David M., Trevor N. Stitt, Peter S. DiStefano, Eduardo Rojas, Karen Mattsson, Debra L. Compton, Lorna Nunez, et al. 1995. “Receptor Tyrosine Kinase Specific for the Skeletal Muscle Lineage: Expression in Embryonic Muscle, at the Neuromuscular Junction, and after Injury.” *Neuron*. https://doi.org/10.1016/0896-6273(95)90146-9.

Vanhaesebrouck, An E., and David Beeson. 2019. “The Congenital Myasthenic Syndromes: Expanding Genetic and Phenotypic Spectrums and Refining Treatment Strategies.”

Current Opinion in Neurology. Lippincott Williams and Wilkins. https://doi.org/10.1097/WCO.0000000000000736.

Vanhaesebrouck, An E., Richard Webster, Susan Maxwell, Pedro M. Rodriguez Cruz, Judith Cossins, James Wickens, Wei Wei Liu, et al. 2019. "B2-Adrenergic Receptor Agonists Ameliorate the Adverse Effect of Long-Term Pyridostigmine on Neuromuscular Junction Structure." *Brain* 142 (12): 3713–27. https://doi.org/10.1093/brain/awz322.

Vaughan, Kevin T., Franz E. Weber, Thomas Ried, David C. Ward, Fernando C. Reinach, and Donald A. Fischman. 1993. "Human Myosin-Binding Protein H (MyBP-H): Complete Primary Sequence, Genomic Organization, and Chromospinal Localization." *Genomics* 16 (1): 34–40. https://doi.org/10.1006/geno.1993.1136.

Veber, Daniel F., Stephen R. Johnson, Hung Yuan Cheng, Brian R. Smith, Keith W. Ward, and Kenneth D. Kopple. 2002. "Molecular Properties That Influence the Oral Bioavailability of Drug Candidates." *Journal of Medicinal Chemistry* 45 (12): 2615–23. https://doi.org/10.1021/jm020017n.

Vogt, J., N. V. Morgan, T. Marton, S. Maxwell, B. J. Harrison, D. Beeson, and E. R. Maher. 2009. "Germline Mutation in DOK7 Associated with Fetal Akinesia Deformation Sequence." *Journal of Medical Genetics*. https://doi.org/10.1136/jmg.2008.065425.

Wade, Robert, Roger Eddy, Thomas B. Shows, and Larry Kedes. 1990. "CDNA Sequence, Tissue-Specific Expression, and Chromosomal Mapping of the Human Slow-Twitch Skeletal Muscle Isoform of Troponin I." *Genomics* 7 (3): 346–57. https://doi.org/10.1016/0888-7543(90)90168-T.

Wang, Dan, Phillip W.L. Tai, and Guangping Gao. 2019a. "Adeno-Associated Virus Vector as a Platform for Gene Therapy Delivery." *Nature Reviews Drug Discovery*. Nature Publishing Group. https://doi.org/10.1038/s41573-019-0012-9.

Wang, Dan, Phillip W L Tai, and Guangping Gao. 2019b. "Adeno-Associated Virus Vector as a Platform for Gene Therapy Delivery." *Nature Reviews. Drug Discovery* 18 (5):

358–78. https://doi.org/10.1038/s41573-019-0012-9.

Wang, Dan, Li Zhong, M. Abu Nahid, and Guangping Gao. 2014. “The Potential of Adeno-Associated Viral Vectors for Gene Delivery to Muscle Tissue.” *Expert Opinion on Drug Delivery*. https://doi.org/10.1517/17425247.2014.871258.

Wang, Xueyong, Kathrin L. Engisch, Yingjie Li, Martin J. Pinter, Timothy C. Cope, and Mark M. Rich. 2004. “Decreased Synaptic Activity Shifts the Calcium Dependence of Release at the Mammalian Neuromuscular Junction in Vivo.” *Journal of Neuroscience* 24 (47): 10687–92. https://doi.org/10.1523/JNEUROSCI.2755-04.2004.

Weatherbee, Scott D., Kathryn V. Anderson, and Lee A. Niswander. 2006. “LDL-Receptor-Related Protein 4 Is Crucial for Formation of the Neuromuscular Junction.” *Development* 133 (24): 4993–5000. https://doi.org/10.1242/dev.02696.

Webster, R. G., J. Cossins, D. Lashley, S. Maxwell, W. W. Liu, J. R. Wickens, P. Martinez-Martinez, M. de Baets, and D. Beeson. 2013a. “A Mouse Model of the Slow Channel Myasthenic Syndrome: Neuromuscular Physiology and Effects of Ephedrine Treatment.” *Experimental Neurology*. https://doi.org/10.1016/j.expneurol.2013.06.012.

Webster, Richard G., An E. Vanhaesebrouck, Susan E. Maxwell, Judith A. Cossins, Weiwei Liu, Ryo Ueta, Yuji Yamanashi, and David M.W. Beeson. 2020. “Effect of Salbutamol on Neuromuscular Junction Function and Structure in a Mouse Model of DOK7 Congenital Myasthenia.” *Human Molecular Genetics* 29 (14): 2325–36. https://doi.org/10.1093/hmg/ddaa116.

Webster, Richard G. 2018. “Molecular Sciences Animal Models of the Neuromuscular Junction, Vitally Informative for Understanding Function and the Molecular Mechanisms of Congenital Myasthenic Syndromes.” https://doi.org/10.3390/ijms19051326.

Weinberg, Marc S., R. Jude Samulski, and Thomas J. McCown. 2013. “Adeno-Associated Virus (AAV) Gene Therapy for Neurological Disease.” *Neuropharmacology*.

https://doi.org/10.1016/j.neuropharm.2012.03.004.

Willmann, Raffaella, San Pun, Lena Stallmach, Gayathri Sadasivam, Alexandre Ferrao Santos, Pico Caroni, and Christian Fuhrer. 2006. “Cholesterol and Lipid Microdomains Stabilize the Postsynapse at the Neuromuscular Junction.” *EMBO Journal*. https://doi.org/10.1038/sj.emboj.7601288.

Witzemann, V., H. Schwarz, M. Koenen, C. Berberich, A. Villarroel, A. Wernig, H. R. Brenner, and B. Sakmann. 1996. “Acetylcholine Receptor ε-Subunit Deletion Causes Muscle Weakness and Atrophy in Juvenile and Adult Mice.” *Proceedings of the National Academy of Sciences of the United States of America*. https://doi.org/10.1073/pnas.93.23.13286.

Wood, S. J., and C. R. Slater. 1997. “The Contribution of Postsynaptic Folds to the Safety Factor for Neuromuscular Transmission in Rat Fast- and Slow-Switch Muscles.” *Journal of Physiology*. https://doi.org/10.1113/jphysiol.1997.sp022007.

Wood, Sarah J., and Clarke R. Slater. 2001. “Safety Factor at the Neuromuscular Junction.” *Progress in Neurobiology*. https://doi.org/10.1016/S0301-0082(00)00055-1.

Wu, Haitao, Wen C. Xiong, and Lin Mei. 2010. “To Build a Synapse: Signaling Pathways in Neuromuscular Junction Assembly.” *Development*. Oxford University Press for The Company of Biologists Limited. https://doi.org/10.1242/dev.038711.

Xing, Guanglin, Wen Cheng Xiong, and Lin Mei. 2020. “Rapsyn as a Signaling and Scaffolding Molecule in Neuromuscular Junction Formation and Maintenance.” *Neuroscience Letters*. Elsevier Ireland Ltd. https://doi.org/10.1016/j.neulet.2020.135013.

Xiong, Wenjun, David M Wu, Yunlu Xue, Sean K Wang, Michelle J Chung, Xuke Ji, Parimal Rana, Sophia R Zhao, Shuyi Mai, and Constance L Cepko. n.d. “AAV Cis-Regulatory Sequences Are Correlated with Ocular Toxicity.” Accessed November 16, 2020. https://doi.org/10.1073/pnas.1821000116.

XM Shen, D Selcen, J Brengman, AG Engel. 2014. “Mutant SNAP25B Causes Myasthenia, Cortical Hyperexcitability, Ataxia, and Intellectual Disability.” *Neurology* 83: 2247–55.

Xu, Jiqing, Koji Tsutsumi, Kiyotaka Tokuraku, Katherine A. Estes, Shin Ichi Hisanaga, and Tsuneya Ikezu. 2011. “Actin Interaction and Regulation of Cyclin-Dependent Kinase 5/P35 Complex Activity.” *Journal of Neurochemistry* 116 (2): 192–204. https://doi.org/10.1111/j.1471-4159.2010.06824.x.

Yang, Xia, Silvia Arber, Christopher William, Li Li, Yasuto Tanabe, Thomas M. Jessell, Carmen Birchmeier, and Steven J. Burden. 2001. “Patterning of Muscle Acetylcholine Receptor Gene Expression in the Absence of Motor Innervation.” *Neuron* 30 (2): 399–410. https://doi.org/10.1016/S0896-6273(01)00287-2.

Yumoto, Norihiro, Shuji Wakatsuki, and Atsuko Sehara-Fujisawa. 2005. “The Acetylcholine Receptor γ-to-ε Switch Occurs in Individual Endplates.” *Biochemical and Biophysical Research Communications*. https://doi.org/10.1016/j.bbrc.2005.04.081.

Zhang, Bin, Shiwen Luo, Qiang Wang, Tatsuo Suzuki, Wen C Xiong, and Lin Mei. 2008. “LRP4 Serves as a Co-Receptor of Agrin.” https://doi.org/10.1016/j.neuron.2008.10.006.

Zhang, H. G., Y. M. Wang, J. F. Xie, X. Liang, H. C. Hsu, X. Zhang, J. Douglas, D. T. Curiel, and J. D. Mountz. 2001. “Recombinant Adenovirus Expressing Adeno-Associated Virus Cap and Rep Proteins Supports Production of High-Titer Recombinant Adeno-Associated Virus.” *Gene Therapy*. https://doi.org/10.1038/sj.gt.3301454.

Zhang, Jing, Julie L. Lefebvre, Shuxia Zhao, and Michael Granato. 2004. “Zebrafish Unplugged Reveals a Role for Muscle-Specific Kinase Homologs in Axonal Pathway Choice.” *Nature Neuroscience*. https://doi.org/10.1038/nn1350.

Zhu, Dan, Wen C. Xiong, and Lin Mei. 2006. “Lipid Rafts Serve as a Signaling Platform for Nicotinic Acetylcholine Receptor Clustering.” *Journal of Neuroscience*. https://doi.org/10.1523/JNEUROSCI.2807-05.2006.

Publications

Co-author in a publication resulted from a collaboration for part of the study presented in **Chapter 6**. The aim was to develop a screening system for the EGFP-reporter cell line using an innovative method of creating microfluidic walls around differentiated myotubes (Soitu et al. 2019).

Cristian Soitu, **Mirela Panea**, Alfonso A. Castrejón-Pita, Peter R. Cook, and Edmond J. Walsh. Creating wounds *in vitro* using micro-jets
Manuscript approved for publication (cleared for editor assignment).

Appendix

1.1. List of buffers

- Krebs solution
  - 118 mM (6.896 g) NaCl,
  - 4.7 mM (0.350 g) KCl,
  - 1.2 mM (0.296 g) $MgSO_4.7H_2O$,
  - 1.2 mM (0.164 g) KH_2PO_4,
  - 24.9 mM (2.1 g) $NaHCO_3$,
  - 11.1 mM (0.9 g) D-glucose,
  - 2.5 mM (1.25 ml) $CaCl_2$,
  - in 1 L dH_2O

- LB (lysogeny broth) agar solution to make agar plates
  - 2.5 g NaCl,
  - 2.5 g Bacto Tryptone,
  - 1.25 g Bacto Yeast Extract,
  - 3.75 g Bacto Agar
  - dH_2O up to a total of 250 ml
  - autoclaved

- LB (lysogeny broth) medium
  - 5 g NaCl,
  - 5 g Bacto Tryptone,
  - 2.5 g Bacto Yeast Extract
  - dH_2O up to a total of 500 ml
  - (autoclaved)

- Lysis buffer
  - 1 ml Tris-HCl (1M, pH 7.5),
  - 2 ml NaCl solution (5M),
  - 0.2 ml EDTA (0.5M),
  - 1 ml 1% Triton X-100,
  - 95.8ml dH_20

- PBS (phosphate-buffered saline)
  - 10 phosphate buffered saline tablets
    - 3.2 mM Na2HPO4, 0.5 mM KH2PO4, 1.3 mM
    - KCl, 135 mM NaCl, pH 7.4
  - dH2O up to 1L (autoclaved)

- PBS-Tween 0.05%
  - 10 phosphate buffered saline tablets
  - 0.5ml in 1L Tween 20
  - dH2O up to 1L

- PEI (polyethylenimine) - linear MW 25,000 Da (Cat. No. 11460630; Fischer Scientific)
  - 45 mg pure PEI
  - dH_2O up to 10 ml
  - pH 7.2

- TBE (Tris-Borate-EDTA) electrophoresis buffer (5x)
  - 54 g Tris base,
  - 27.5 g boric acid,
  - 20 ml EDTA (pH8, 0.5M)
  - dH2O up to 1L

1.2. Reagents

- 36% w/v formaldehyde EM, 100 ml (TAAB; Cat. No. F003)
- Alexa Fluor-594 conjugated bungarotoxin (Invitrogen; Cat. No. B13423)
- μ-conotoxin GIIIB (Peptide Institute Inc.)
- DirectPCR Extraction Reagent (ViagenBiotech; Cat. No. 401-E (ear))
- EDTA (Fluka; 03690)
- SlowFade™ Diamond Antifade Mountant (Thermo Fischer Scientific; Cat no. S36967)
- Goat serum (Sigma-Aldrich; Cat no. G9023)
- DNA molecular weight marker VI (Roche; Cat no. 11062590001)
- Loading dye (Gelpilot 5x) (Qiagen; Cat no. 239901)
- MegaMix~Blue PCR master mix (Microzone; Cat no. 2MMB-25)
- Methanol for HPLC (Sigma-Aldrich; Cat no. 34885)
- Oxoid Phosphate Buffered Saline Tablets (Thermo Scientific; Cat no. BR0014G)
- Triton X-100 (Sigma-Aldrich; Cat no. T8532)
- Tris base (Sigma-Aldrich; Cat no. T1503)

- Tween 20 (Sigma-Aldrich; Cat no. P1379)
- UltraPure Agarose (Invitrogen; Cat no. 15510-027)

1.3. Drugs used in mice

- DOK7-AAV Vigene Biosciences custom-made large-scale production
  - ◊ packaging of AAV9
  - ◊ check individual study for dosage (IP* administered)
- Pyridostigmine bromide Sigma-Aldrich P9797
  - ◊ 14 mg/kg/day po**
- Sodium Chloride for Injections 0.9% w/v Hameln
  - ◊ To use in control animals and to dilute drugs

*Intraperitoneal injection (IP) were given in the lower right quadrant of the abdomen using a 30G needle (BD Micro-Fine 0.3 mm x 8 mm).

**Drugs administered per os (po) were dissolved in drinking water.

1.4. Antibodies used in immunohistochemistry

Antibody	Dilution	Company	Cat. No.
chicken polyclonal anti-neurofilament antibody	1:1000	Thermo Fisher Scientific	ab-4680
rabbit polyclonal anti-synaptophysin antibody	1:100		ab-4
Alexa Fluor® 488 goat anti chicken secondary antibody		Invitrogen	A-11039
Alexa Fluor® 488 conjugated goat anti-rabbit secondary antibody			R37116

1.5. List of software programmes used

Fiji version 2		https://imagej.nih.gov/nih-image/index.html
Prism, version 8	GraphPad Software Inc., California, USA	http://www.graphpad.com
Simple PCI imaging software	Compix Inc Imaging Systems, Cranberry Township, PA, USA	https://hcimage.com/simple-pci-legacy
SnapGene, version 3.3.1	GSL Biotech	https://www.snapgene.com
VisionWorks LS Image Acquisition Software	Ultra-Violet Products Ltd., Cambridge, USA	https://www.uvp.com/visionworks.html
ZEN Microscope and Imaging Software (2.1 LSM)	Zeiss	https://www.zeiss.com/microscopy/int/downloads/zen.html

1.6. Fiji macro used for the analysis of NMJ parameters

Semi-automated macro used to measure areas and staining intensities of neuromuscular junctions in Chapters 3, 4 and 5

```
roiManager("reset");
run("Add to Manager");
title = getTitle();
run("Duplicate...", "duplicate channels=2");
run("8-bit");
waitForUser( "Pause","select rectangle ROI and press ok");
run("Gaussian Blur...", "sigma=20");
setAutoThreshold("Moments dark");
setThreshold(22, 255);
run("Create Mask");
setOption("BlackBackground", false);
run("Dilate");
run("Fill Holes");
run("Dilate");
run("Watershed");
run("Analyze Particles...", "size=250.00-Infinity circularity=0.00-0.90 display exclude add");
selectWindow("Results");
run("Close");
selectWindow(image_title);
roiManager("Show All");
roiManager("Measure");
```